ISBN 978-82-326-6463-4 (printed ver.)
ISBN 978-82-326-5379-9 (electronic ver.)
ISSN 1503-8181 (printed ver.)
ISSN 2703-8084 (electronic ver.)

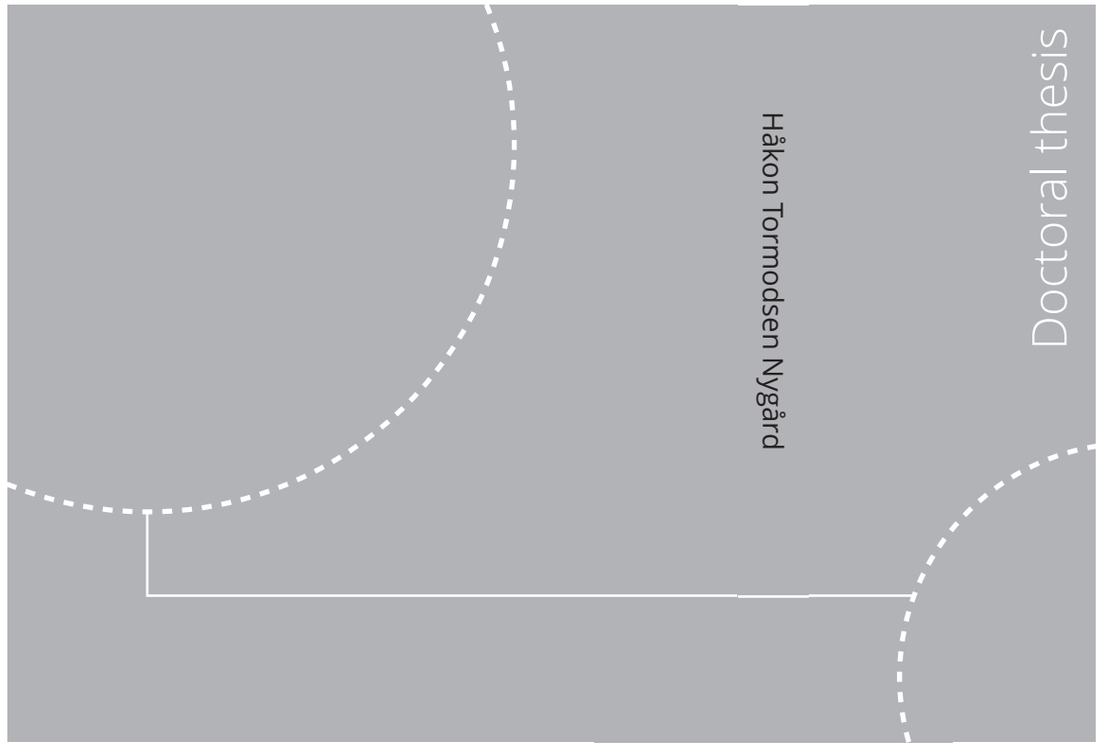

Doctoral theses at NTNU, 2021:178

Håkon Tormodsen Nygård

Experimental Measurement of Flame Describing Functions in an Azimuthally Forced Annular Combustor

NTNU
Norwegian University of
Science and Technology
Thesis for the degree of
Philosophiae Doctor
Faculty of Engineering
Department of Energy and Process Engineering

NTNU
Norwegian University of
Science and Technology

Doctoral theses at NTNU, 2021:178

NTNU

NTNU
Norwegian University of
Science and Technology

Håkon Tormodsen Nygård

Experimental Measurement of Flame Describing Functions in an Azimuthally Forced Annular Combustor

Thesis for the degree of Philosophiae Doctor

Trondheim, June 2021

Norwegian University of Science and Technology
Faculty of Engineering
Department of Energy and Process Engineering

NTNU
Norwegian University of
Science and Technology

NTNU
Norwegian University of Science and Technology

Thesis for the degree of Philosophiae Doctor

Faculty of Engineering
Department of Energy and Process Engineering

ISBN 978-82-326-6463-4 (printed ver.)
ISBN 978-82-326-5379-9 (electronic ver.)
ISSN 1503-8181 (printed ver.)
ISSN 2703-8084 (electronic ver.)

Doctoral theses at NTNU, 2021:178

PRINTED IN NORWAY
NO - 1598

NORDIC SWAN ECOLABEL
Printed matter
2041 0731

Printed by Skipnes Kommunikasjon AS

Abstract

Thermoacoustic instabilities have become an increasingly relevant issue in the search for lower emissions in gas turbines, both for power production and transportation. Adoption of alternative fuels in land based gas turbines can reduce CO_2 emissions, and NO_x emissions can be reduced by operating in a lean burn regime. Both approaches can make gas turbine engines more prone to exhibit self-excited thermoacoustic instabilities. Therefore, to increase the fuel and operational flexibility of gas turbines, a better understanding of thermoacoustic instabilities is required.

A promising approach to predict the stability of a new gas turbine design is to use low order models in conjunction with experimentally obtained flame transfer functions on axially perturbed single flame setups. This approach would greatly reduce the cost of the design process, allowing for a range of geometries to be numerically evaluated. However, practical configurations often have an annular geometry, where the azimuthal pressure mode is commonly the unstable mode. This is in contrast to the axially forced single flames used for defining the flame transfer function. Therefore, it is important to know if there are potential differences between the response of a single flame to axial perturbations and flames arranged in an annulus subjected to azimuthal pressure modes.

The aim of this thesis is to improve our understanding of the flame response in an annular combustor. The first step to achieve this is to create a reference case equivalent to a conventional axially perturbed single flame. One of the flames from an annular combustor is therefore isolated and studied in detail for a large range of operating conditions in an enclosure similar to one sector in the annular combustor. The response of the flame is characterised over a large range of frequencies, and the relevant time scales are extracted by fitting distributed time delay models. The response is observed to depend on the effective confinement of the flame, suppressing the expected dip behaviour for sufficiently long flames.

The second step is to study the response of an annular combustor to different azimuthal pressure modes in detail. To be able to study this, azimuthal forcing is applied to vary the amplitude, spinning state, and the orientation of the first azi-

muthal mode. The first method to exhibit good control over the full parameter space is developed in the current work. Additionally, a novel rotation averaging technique and the concept of Azimuthal Flame Describing Functions are introduced, allowing for efficient isolation of the flame response to different forced states and clear description of the main features. The different pressure mode types are shown to produce different responses for an annular combustor with co-swirling flames. The differences are attributed to the local symmetry breaking created by the finite width annulus in combination with swirling flames. By removing the swirl, the local reflectional symmetry is restored, and the heat release rate pattern is observed to have reflectional symmetry for the two spinning directions. The difference in response for the annular combustor with swirling flames resulted in several interesting features, including a non-negligible heat release rate at the pressure node. Additionally, numerical simulations showed the difference in response results in a strong spinning direction preference for the pressure mode under self-excited conditions. The understanding gained here will help the development of practical combustors, enabling the wider use of low emission technology.

Preface

This thesis is submitted for partial fulfilment of the requirements for the degree of Philosophiae Doctor (Ph.D.) to the Norwegian University of Science and Technology (NTNU). The research has been carried out at the Department of Energy and Process Engineering (EPT) from October 2016 to March 2021. The work has been supervised by Associate Professor Nicholas A. Worth, and Professor James R. Dawson has been the co-supervisor.

The Ph.D. has been part of the project *Breaking the paradigm: A new approach to understanding and controlling combustion instabilities*, funded by the European Research Council (ERC) under grant agreement 677931 TAIAC.

The thesis consists of 6 chapters and 5 scientific articles. The chapters give an introduction to thermoacoustic instabilities, the experimental setups and the theory required for the data analysis. The articles are summarised in Chapter 5, and the full texts are included at the end of the thesis, after the concluding remarks in Chapter 6.

Article I

Flame transfer functions and dynamics of a closely confined premixed bluff body stabilized flame with swirl.
Håkon T. Nygård, Nicholas A. Worth (2021). *Journal of Engineering for Gas Turbines and Power*, 143(4):041011.

Author's constributions: Håkon T. Nygård conducted the experiments, performed the data analysis, wrote the majority of the article and presented the results at the ASME Turbo Expo 2020. Nicholas A. Worth read and reviewed the manuscript, and provided technical and editorial guidance. The research work was conceptualised by Håkon T. Nygård and Nicholas A. Worth.

Article II

Flame dynamics of azimuthal forced spinning and standing modes in an annular combustor.
Håkon T. Nygård, Marek Mazur, James R. Dawson, Nicholas A. Worth (2019). *Proceedings of the Combustion Institute*, 37(4):5113–5120.

Author's constributions: Håkon T. Nygård and Marek Mazur conducted the experiments. Håkon T. Nygård performed the data analysis, wrote the majority of the article and presented the results at the 37th International Symposium on Combustion. Marek Mazur, James R. Dawson, and Nicholas A. Worth read and reviewed the

manuscript, and provided technical and editorial guidance. The research work was conceptualised by Håkon T. Nygård, James R. Dawson, and Nicholas A. Worth.

Article III

Characteristics of self-excited spinning azimuthal modes in an annular combustor with turbulent premixed bluff-body flames.
Marek Mazur, Håkon T. Nygård, James R. Dawson, Nicholas A. Worth (2019). *Proceedings of the Combustion Institute*, 37(4):5129–5136.

Author's constributions: Marek Mazur and Håkon T. Nygård conducted the experiments. Marek Mazur performed the data analysis, wrote the majority of the article and presented the results at the 37th International Symposium on Combustion. Håkon T. Nygård, James R. Dawson, and Nicholas A. Worth read and reviewed the manuscript, and provided technical and editorial guidance. The research work was conceptualised by Marek Mazur, James R. Dawson, and Nicholas A. Worth.

Article IV

Azimuthal flame response and symmetry breaking in a forced annular combustor.
Håkon T. Nygård, Giulio Ghirardo, Nicholas A. Worth (2021). *Under consideration for publication in Combustion and Flame*.

Author's constributions: Håkon T. Nygård conducted the experiments, performed the data analysis, and wrote the majority of the article. Giulio Ghirardo and Nicholas A. Worth read and reviewed the manuscript, and provided technical and editorial guidance. The research work was conceptualised by Håkon T. Nygård and Nicholas A. Worth.

Article V

Symmetry breaking modelling for azimuthal combustion dynamics.
Giulio Ghirardo, Håkon T. Nygård, Alexis Cuquel, Nicholas A. Worth (2021). *Proceedings of the Combustion Institute*, 38(4):5953–5962.

Author's constributions: Giulio Ghirardo performed the analytical and numerical analysis, and wrote the majority of the article. Håkon T. Nygård provided the experimental data and figures to the article, and presented the results at the 38th International Symposium on Combustion. Håkon T. Nygård, Alexis Cuquel, and Nicholas A. Worth read and reviewed the manuscript, and provided technical and editorial guidance. The research work was conceptualised by Giulio Ghirardo.

Acknowledgements

First and foremost, I would like to express my gratitude to my supervisor, Nicholas Worth. Your continuous support, patient guidance, insights and frequent discussions have been invaluable on this journey. It has been a great privilege to be part of the research group, and it has been truly fascinating to see how the combustion facility has evolved since starting out in the basement of VATL. I also want to thank my co-supervisor James Dawson, both for getting me into this field of research and for all the support and guidance throughout the years. My other close collaborators, Marek Mazur and Giulio Ghirardo, deserves a special thanks for their contributions on experimental knowledge and analytical insights.

Thank you to the supporting staff at EPT, and Arnt Egil, Paul and Stein Kristian in particular for putting up with all my requests, usually with impossibly short deadlines.

Furthermore, I would like to thank all the great friends and colleagues at EPT. Thank you for all the social events and the daily lunch break. I want to give a special thanks to Anna, Dhiren, Eirik, Franz, José, Marek, Philip, Thomas and Øyvind, who have had an immeasurable impact on my time here. The Friday porridge lunch with David has also been one of the weekly highlights.

Last, but not least, I want to thank my family for the endless support and understanding.

Trondheim, March 2021

Håkon T. Nygård

Contents

Abstract i

Preface iii

Acknowledgements v

Contents vii

List of Figures xi

Nomenclature xiii

1 Introduction 1
- 1.1 Thermoacoustic instabilities . . . 2
- 1.2 Flame Transfer Functions . . . 4
  - 1.2.1 Experimental determination . . . 7
  - 1.2.2 Effect of swirling flow . . . 9
  - 1.2.3 Time delay models . . . 11
- 1.3 Flame Describing Functions . . . 13
- 1.4 Transverse instabilities . . . 14
- 1.5 Annular combustors . . . 17
  - 1.5.1 Self-excited instabilities and modal dynamics . . . 18
  - 1.5.2 Acoustically forced annular configurations . . . 20
  - 1.5.3 Acoustic modelling of azimuthal instabilities . . . 21
- 1.6 Research goals . . . 22
- 1.7 Thesis outline . . . 23

2 Experimental setups 25
- 2.1 Annular combustor . . . 25
  - 2.1.1 Injectors . . . 30
- 2.2 Single sector . . . 32

2.3 Heat release rate measurements . . . 34
2.3.1 Synchronisation . . . 37

3 Development and application of azimuthal acoustic forcing 39
3.1 Axial forcing . . . 39
3.2 Azimuthal forcing . . . 41
3.2.1 Theoretical considerations . . . 42
3.2.2 Thermoacoustic stability and thermal equilibrium . . . 44
3.2.3 Monitoring the mode . . . 45
3.2.4 Setting up standing and spinning modes . . . 47
3.2.5 Potential improvements . . . 49

4 Processing methods 51
4.1 Flame Describing Function . . . 51
4.1.1 Heat release rate . . . 52
4.2 Acoustic mode in the injector tubes . . . 54
4.2.1 Determining the mode . . . 55
4.2.2 Contraction and expansion . . . 56
4.2.3 Swirler . . . 57
4.3 Distributed time delay model . . . 59
4.4 Acoustic mode in the annulus . . . 62
4.4.1 C-indicator . . . 64
4.4.2 Quaternion formalism . . . 65
4.5 Phase averaging . . . 68
4.6 Rotation averaging . . . 69
4.6.1 Temporal mean . . . 70
4.6.2 Azimuthal fluctuations . . . 72
4.6.3 Alternative description of rotational averaging . . . 75
4.6.4 Reconstruction of the phase average . . . 77
4.6.5 Azimuthal axial velocity components . . . 78
4.6.6 Reconstructed Flame Describing Function . . . 80
4.7 Azimuthal Flame Describing Functions . . . 81
4.7.1 Azimuthal heat release rate mode . . . 83
4.7.2 Processing steps to obtain Azimuthal FDF . . . 85

5 Summary of research articles 87

6 Conclusions 91
6.1 Future outlook . . . 93

Bibliography 95

Article I - Flame transfer functions and dynamics of a closely confined premixed bluff body stabilized flame with swirl **109**

Article II - Flame dynamics of azimuthal forced spinning and standing modes in an annular combustor **121**

Article III - Characteristics of self-excited spinning azimuthal modes in an annular combustor with turbulent premixed bluff-body flames **131**

Article IV - Azimuthal flame response and symmetry breaking in a forced annular combustor **141**

Article V - Symmetry breaking modelling for azimuthal combustion dynamics **167**

List of Figures

1.1 Feedback loop of thermoacoustic instabilities. Adapted from Candel (2002) . . . 3
1.2 Analytical FTF for laminar ducted flame. Source: Dowling (1999) 6
1.3 Forcing setups of Balachandran et al. (2005) and Palies et al. (2010) 8
1.4 Effect of swirl on the FTF. Adapted from Gatti et al. (2018) 10
1.5 Gaussian distributed time delay model. Source: Polifke (2020) . . 12
1.6 Example of Flame Describing Function. Source: Noiray et al. (2008) 14
1.7 Transverse forcing setups of Lespinasse et al. (2013) and O'Connor and Acharya (2013) . . . 15
1.8 Simultaneous axial and transverse forcing rig. Source: Saurabh and Paschereit (2017) . . . 16
1.9 Annular combustors of Worth and Dawson (2013a), Bourgouin et al. (2013) and Roy et al. (2020) . . . 18
1.10 Annular forcing setups of Moeck et al. (2010) and Worth et al. (2017) 21

2.1 Schematic side view of the annular combustor . . . 26
2.2 Downstream view of the dump plane of the annular combustion chamber . . . 27
2.3 Annular combustor with the new forcing array mounted . . . 29
2.4 Simplified injector tube schematics and a render of the swirler design 31
2.5 Single sector setup with the front facing camera and the schematic side view . . . 33
2.6 Imaging setup for the single sector rig . . . 35
2.7 Imaging setup for the annular combustor . . . 37
2.8 Example of the sampled and the reconstructed camera trigger signal 38

3.1 Schematic presentation of the forcing array . . . 41
3.2 Relation between signal generator phase offset and nature angle . 44
3.3 Example of the time dependence of the forcing amplitude in the annular combustor . . . 45

3.4 Example screenshot from the annular forcing program 46

4.1 Example of FDF obtained experimentally in the annular combustor 53
4.2 Measured pressure amplitudes and the corresponding fitted pressure mode in an injector tube 56
4.3 Approximation of contraction caused by the bluff body and injector geometry 57
4.4 Transfer matrix $\boldsymbol{T}$ of the swirler 59
4.5 Example of distributed time delay model with two time scales . . 61
4.6 Frequency spectrum for a forced azimuthal mode 63
4.7 Example pressure time series of a standing and a spinning azimuthal mode 64
4.8 Example C-indicator time series of a standing and a spinning azimuthal mode 65
4.9 Poincaré sphere definition and example for different forced states . 67
4.10 Comparison of phase average and instantaneous heat release rate . 69
4.11 Temporal mean and corresponding rotation average of the heat release rate in the annular combustor 71
4.12 Phase average and the corresponding ACW and CW components of the rotation average for a standing mode 73
4.13 Illustration of using the ACW rotation average on a purely ACW mode 75
4.14 Illustration of using the ACW rotation average on a purely CW mode 76
4.15 Example of phase average and corresponding reconstruction for a standing pressure mode 78
4.16 Experimentally determined axial velocity and corresponding reconstruction from rotation averaging 79
4.17 Example of the reconstructed FDF, based on a FDF obtained experimentally in the annular combustor 81
4.18 Example of the two Azimuthal FDF components obtained experimentally 82
4.19 Nature angle of the pressure and the heat release rate modes for select Azimuthal FDF magnitude ratios 84
4.20 Process diagram of how to calculate the Azimuthal FDF from the sampled data 86

Nomenclature[1]

Latin Symbols

$\mathcal{A}$	Cross sectional area. Eq. (4.13) $[\mathbb{R}, \mathrm{m}^2]$
A	Amplitude of azimuthal pressure fluctuations (quaternion description). Fig. 3.3 $[\mathbb{R}, \mathrm{Pa}]$
$A_\pm$	Amplitude of the spinning azimuthal pressure fluctuation components. Eq. (3.1) $[\mathbb{C}, \mathrm{Pa}]$
$A^\perp$	Amplitude of azimuthal pressure fluctuations (orthogonal description). Eq. (4.23) $[\mathbb{R}, \mathrm{Pa}]$
$A^\perp_{\mathrm{imposed}}$	Amplitude of azimuthal pressure fluctuations imposed by all speaker pairs (orthogonal description). Eq. (3.5) $[\mathbb{R}, \mathrm{Pa}]$
$A^\perp_{\mathrm{pair}}$	Amplitude of azimuthal pressure fluctuations imposed by one speaker pair (orthogonal description). Eq. (3.2) $[\mathbb{R}, \mathrm{Pa}]$
$B_\pm$	Amplitude of pressure fluctuation components in the injector tube. Fig. 2.4 $[\mathbb{C}, \mathrm{Pa}]$
b	Bloch wavenumber. Eq. (4.44) $[\mathbb{N}, -]$
C	C-indicator of the azimuthal mode. Eq. (4.25) $[\mathbb{R}, \mathrm{Pa}]$
c	Speed of sound. Eq. (4.3) $[\mathbb{R}, \mathrm{m/s}]$
$\mathrm{DTL_T}, \mathrm{DTL}_i$	Total distributed time delay model (T) and individual components (i). Eq. (4.21) $[\mathbb{C}, -]$
E_i	Gaussian distributed time delay model i. Eq. (4.21) $[\mathbb{C}, -]$
FDF	Conventional Flame Describing Function. Eq. (4.1) $[\mathbb{C}, -]$
FDF_j	Conventional Flame Describing Function of the jth flame. Eq. (4.2) $[\mathbb{C}, -]$
$\mathrm{FDF}^\pm$	ACW $(-)$ and CW $(+)$ Azimuthal Flame Describing Function. Eq. (4.59) $[\mathbb{C}, -]$
g_i	Amplitude of Gaussian distributed time delay model i. Eq. (4.21) $[\mathbb{R}, -]$
H	Characteristic flame height. Eq. (4.20) $[\mathbb{R}, \mathrm{m}]$
$k_\pm$	Wavenumber of component propagating with/against flow direction. Eq. (4.6) $[\mathbb{R}, \mathrm{m}^{-1}]$

[1] Symbols from Chapter 1 are excluded for brevity.

L	Swirler vane trailing edge to dump plane distance. Eq. (4.20) $[\mathbb{R}, \mathrm{m}]$
Ma	Mach number. Eq. (4.6) $[\mathbb{R}, -]$
N	Number of injectors. §2.1 $[\mathbb{N}^+, -]$
N^*	Number of instrumented injectors. Eq. (4.25) $[\mathbb{N}^+, -]$
N_{im}	Number of images in a phase average bin. Eq. (4.35) $[\mathbb{N}^+, -]$
n	Order of the azimuthal mode. Eq. (4.23) $[\mathbb{N}^+, -]$
p'	Azimuthal pressure fluctuations. Eq. (3.1) $[\mathbb{R}, \mathrm{Pa}]$
p'_{tube}	Axial pressure fluctuations in the injector tube. Eq. (4.4) $[\mathbb{R}, \mathrm{Pa}]$
$\mathscr{Q}^{\pm}$	Normalised amplitudes of the heat release rate mode based on Azimuthal FDFs. Eq. (4.62) $[\mathbb{C}, -]$
q	Heat release rate. Eq. (4.1) $[\mathbb{R}, \mathrm{W}]$
q'	Phase dependent heat release rate fluctuations. Eq. (4.1) $[\mathbb{R}, \mathrm{W}]$
q'_{s}	Stochastic heat release rate fluctuations. Eq. (4.36) $[\mathbb{R}, \mathrm{W}]$
r	Radial distance from combustion chamber centre line. Eq. (4.37) $[\mathbb{R}, \mathrm{m}]$
$\boldsymbol{S}, S_{ij}$	Acoustic scattering matrix. Eq. (4.15) $[\mathbb{C}, -]$
SR	Spin ratio of azimuthal pressure fluctuations. Eq. (4.29) $[\mathbb{R}, -]$
$\boldsymbol{T}, T_{ij}$	Acoustic transfer matrix. Eq. (4.18) $[\mathbb{C}, -]$
T	Oscillation period. Eq. (4.34) $[\mathbb{R}, \mathrm{s}]$
t	Time. Eq. (3.1) $[\mathbb{R}, \mathrm{s}]$
t_0	Chosen start time of phase average. Eq. (4.36) $[\mathbb{R}, \mathrm{s}]$
t_l	Time relative to the chosen phase average start time t_0. Eq. (4.49) $[\mathbb{R}, \mathrm{s}]$
$\boldsymbol{U}, U$	Temporal mean bulk velocity. Eq. (4.3) $[\mathbb{R}, \mathrm{m/s}]$
U_{bulk}	Temporal mean bulk velocity in injector tube evaluated at the dump plane. Eq. (4.1) $[\mathbb{R}, \mathrm{m/s}]$
U_{prop}	Mean propagation velocity in the injector tube. Eq. (4.20) $[\mathbb{R}, \mathrm{m/s}]$
u'_{axial}	Axial acoustic velocity at the dump plane location. Eq. (4.1) $[\mathbb{R}, \mathrm{m/s}]$
$u'_{\mathrm{axial},j}$	Axial acoustic velocity at the dump plane location at azimuthal injector location θ_j. Eq. (4.2) $[\mathbb{R}, \mathrm{m/s}]$
$u'^{,\mathrm{rec}}_{\mathrm{axial},j}$	Rotation average reconstructed axial acoustic velocity at the dump plane for the jth injector. Eq. (4.57) $[\mathbb{R}, \mathrm{m/s}]$
$\langle u'_{\mathrm{axial}} \rangle_j$	Rotation averaged axial acoustic velocity component at the dump plane for the jth injector. Eq. (4.57) $[\mathbb{R}, \mathrm{m/s}]$
u'_{d}	Axial acoustic velocity fluctuations in the injector tube. Eq. (4.8) $[\mathbb{R}, \mathrm{m/s}]$
x	Axial location in the injector tube. Fig. 2.4 $[\mathbb{R}, \mathrm{m}]$
x_{lower}	Axial location of the lower pressure transducer. Fig. 2.4 $[\mathbb{R}, \mathrm{m}]$
x_{upper}	Axial location of the upper pressure transducer. Fig. 2.4 $[\mathbb{R}, \mathrm{m}]$
z	Impedance linking pressure and axial velocity fluctuations. Eq. (4.52) $[\mathbb{C}, \mathrm{kg/m^2 s}]$

Greek Symbols

β_i	Centre frequency of Gaussian distributed time delay model i. Eq. (4.21) $[\mathbb{R}, \mathrm{rad/s}]$
$\Delta\theta$	Azimuthal angle between adjacent injectors. Fig. 2.2 $[\mathbb{R}, \mathrm{rad}]$
$\Delta\bar{q}$	Flame to flame differences in temporal mean heat release rate. Eq. (4.38) $[\mathbb{R}, \mathrm{W}]$
$\epsilon\Delta q'_{\mathrm{a}}$	Flame to flame differences in heat release rate fluctuations. Eq. (4.39) $[\mathbb{C}, \mathrm{W}]$
θ	Azimuthal angle in the combustion chamber. Fig. 2.2 $[\mathbb{R}, \mathrm{rad}]$
θ_0	Orientation angle of the azimuthal pressure fluctuations. Eq. (4.27) $[\mathbb{R}, \mathrm{rad}]$
θ_j	Azimuthal centre angle of the injector corresponding to the jth flame. Eq. (4.25) $[\mathbb{R}, \mathrm{rad}]$
θ_{p}	Azimuthal angle between two speaker pairs. Eq. (3.1) $[\mathbb{R}, \mathrm{rad}]$
λ	Wavelength. §2.3 $[\mathbb{R}, \mathrm{m}]$
ξ_{a}	Function used to express the pressure as a quaternion function. Eq. (4.30) $[\mathbb{H}, \mathrm{Pa}]$
ξ_i	Functions used to express ξ_{a} in terms of real valued functions. Eq. (4.31) $[\mathbb{R}, \mathrm{Pa}]$
ρ	Gas density. Eq. (4.8) $\left[\mathbb{R}, \mathrm{kg/m^3}\right]$
τ	Time delay. Eq. (4.20) $[\mathbb{R}, \mathrm{s}]$
φ	Temporal phase of the azimuthal pressure mode. Eq. (4.27) $[\mathbb{R}, \mathrm{rad}]$
ϕ_0	Phase offset for distributed time delay model. Eq. (4.21) Eq. (3.1) $[\mathbb{R}, \mathrm{rad}]$
ϕ_{sg}	Phase offset between signal generator channels. Eq. (3.1) $[\mathbb{R}, \mathrm{rad}]$
σ_i	The reciprocal of the standard deviation of the Gaussian distributed time delay model i. Eq. (4.21) $[\mathbb{R}, \mathrm{s/rad}]$
χ	Nature angle of the azimuthal pressure fluctuations. Eq. (3.4) $[\mathbb{R}, \mathrm{rad}]$
χ_q	Nature angle of sector integrated heat release rate fluctuations. Eq. (4.64) $[\mathbb{R}, \mathrm{rad}]$
$\psi_{\pm 1}$	Heat release rate fluctuation Bloch kernels of the first azimuthal mode. Eq. (4.39) $[\mathbb{C}, \mathrm{W}]$
$\psi^u_{\pm 1}$	Amplitude of azimuthal axial velocity component. Eq. (4.52) $[\mathbb{C}, \mathrm{m/s}]$
ω	Angular oscillation frequency. Eq. (3.1) $[\mathbb{R}, \mathrm{rad/s}]$

Modifiers

$(\cdot)_{\mathrm{a}}$	Analytical signal of $(\cdot)$. Eq. (3.1)
$(\cdot)_{\mathrm{d}}$	Downstream value. Eq. (4.13)
$(\cdot)_{\mathrm{u}}$	Upstream value. Eq. (4.13)
$(\cdot)^{\mathrm{rec}}$	Reconstruction of $(\cdot)$ from rotation average components. The resulting values regain the full spatial dependence. Eq. (4.49)

$(\cdot)^*$	Complex conjugate of $(\cdot)$. Eq. (4.26)
$\hat{(\cdot)}$	Fourier amplitude of $(\cdot)$ at peak frequency. Removes the time dependence. Eq. (4.1)
$\bar{(\cdot)}$	Temporal mean of $(\cdot)$. Removes time dependence. Eq. (4.1)
$\langle(\cdot)\rangle$	Spatial average of $(\cdot)$. Removes all spatial dependence. Eq. (4.1)
$\langle(\cdot)\rangle_{\text{annulus}}$	Spatial average of $(\cdot)$ over the whole annulus. Removes all spatial dependence. Fig. 4.12
$\langle(\cdot)\rangle_j$	Spatial average of $(\cdot)$ over the jth flame sector. Removes spatial dependence within the jth flame sector. Eq. (4.2)
$\langle(\cdot)\rangle_{\text{sectors}}$	Rotation average of the temporal mean quantity $(\cdot)$. Reduces the spatial r and θ dependence from the full annulus to a single flame sector. Eq. (4.37)
$\langle(\cdot)\rangle^{\pm}$	Rotation average in the ACW $(-)$ and CW $(+)$ direction of $(\cdot)$. Reduces the spatial r and θ dependence from the full annulus to a single flame sector. Eq. (4.42)
$\lvert(\cdot)\rvert$	Absolute value of $(\cdot)$. §3.2.1
$\mathcal{H}[(\cdot)]$	Hilbert transform of the time dependent argument $(\cdot)$. Eq. (4.5)
$\Re\{(\cdot)\}$	Real part of $(\cdot)$. Eq. (4.5)

Abbreviations

c. c.	Complex conjugate of the preceding term
q. c.	Quaternion conjugate of the preceding term
ACW	Anti-clockwise
CW	Clockwise
FDF	Flame Describing Function
FTF	Flame Transfer Function
HRR	Heat release rate
IRO	Intensified relay optics
PMT	Photomultiplier tube
UV	Ultraviolet

Chapter 1

Introduction

Climate change due to emissions from human activity is a huge challenge. In an effort to combat this ever stricter emission guidelines are set in action, including those which restrict the emission of both carbon dioxide (CO_2) and nitrogen oxides (NO_x). Both are produced in typical means of transportation and power generation, for example in aviation and in natural gas power plants. While electric cars have become a viable option for personal transportation by road, there will still be a need for air travel and power production from non-renewable sources in the foreseeable future. Therefore, it is of great importance to reduce the emissions from those sources as much as possible.

One way to drastically reduce the amount of NO_x is to lower the temperature of the combustion process (Docquier and Candel, 2002). This can be achieved by running in a lean regime, where there is more air than required for the complete combustion process of the given amount of fuel. To ensure the emissions are kept at a minimum, the fuel and air have to be well mixed before entering the combustion chamber, reducing the chance of having zones with rich mixtures where NO_x can be more easily produced. Therefore, it is desired to run in the regime denoted lean premixed. However, in this regime the combustors have been shown to be more susceptible to thermoacoustic instabilities (Candel, 2002). This can result in a narrower range of viable operating conditions, and therefore thermoacoustic instabilities can indirectly lead to reduced power or increased emissions, when operating at unoptimal conditions. In the most extreme cases, the instabilities can grow sufficiently large to significantly shorten the operational life span of the engine, or destroy its structural integrity.

The reduction in combustion temperature does not significantly influence the production of CO_2. CO_2 emissions can however be reduced by using alternative fuels that are not based on hydrocarbons, for example hydrogen (H_2) (Bothien et al., 2019) or a mix of hydrogen and ammonia (NH_3) (Valera-Medina et al., 2018;

Wiseman et al., 2020). CO_2 emissions can be reduced completely by fully replacing the hydrocarbon fuel, or partially by replacing some of the hydrocarbon based fuel with an alternative. Combustion with hydrogen has been observed to exhibit significant thermoacoustic instabilities for some operating conditions (Lieuwen et al., 2008; Zhang et al., 2011; Indlekofer et al., 2021b), posing a potential problem for the adaption in gas turbines. Both the adoption of alternative fuels for reduction of CO_2 and the reduction of NO_x emissions through lean burn regimes are therefore hindered by the presence of thermoacoustic instabilities. To be able to increase the fuel and operational flexibility of gas turbines, a better understanding of thermoacoustic instabilities is required.

1.1 Thermoacoustic instabilities

The phenomenon of thermoacoustic instability has been known for well over two centuries, and was first discovered in the late 18th century according to Schimmer and Vortmeyer (1977). However, the large scientific push to understand the nature of these instabilities did not start before the mid 20th century (Candel, 2002; Poinsot, 2017). The race to space, starting in the 1950's, required a very high power density from rocket engines. However, rocket engines famously experienced troubles with thermoacoustic instabilities. One high profile example is the Rocketdyne F-1 engine used in the first stage of the Saturn-V launch vehicle from NASA's famous Apollo space program (Oefelein and Yang, 1993). During the development of this engine several thousand full scale tests were performed in a relatively short period of time, before the engine finally obtained complete qualifications for manned flight in 1966 (Oefelein and Yang, 1993). More recently, another driving factor for the study of thermoacoustic instabilities is the increasingly stringent emission requirements for gas turbines in both transport and power generation.

A very early and simple example of a system that can exhibit thermoacoustic instabilities is the Rijke tube (Rijke, 1859). This consists of a vertically oriented open ended tube, with a non-blocking heat source in the lower part. There exist several different variations of systems operating on the same basic principle, and a good overview can be found in Raun et al. (1993). The Rijke tube is a good example to showcase the basic principle behind thermoacoustic instabilities. The heating element in the bottom half of the tube heats up the air in the bottom of the tube, which is then convected towards the top of the tube due to buoyancy (Raun et al., 1993). Perturbations in the flow across the heating element affect the heat release rate, adding energy to pressure fluctuations in the tube at the correct phase, which in turn leads to more flow perturbations, as schematically presented in Fig. 1.1.

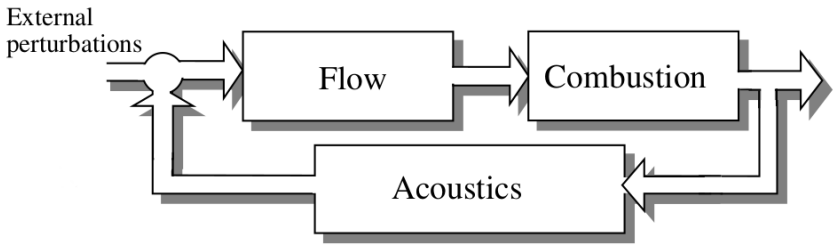

Figure 1.1: Typical feedback loop for thermoacoustic instabilities in combustion systems. Flow perturbations result in heat release rate perturbations, which in turn lead to acoustic perturbations in the system. The acoustic perturbations are driving the flow perturbations together with any external perturbations to the system. Adapted from Candel (2002).

While the Rijke tube is not very representative for more practical configurations, the main principles are the same. Practical systems typically consist of a heat source, a flow through the heat source, and an enclosing geometry. Perturbations in the flow cause perturbations in the heat release rate, which can result in excitation of acoustic modes in the enclosure that are again causing additional flow perturbations (Candel, 2002). A gas turbine is one example of a practical system, where the turbulent flames act as the heat source, the incoming air and fuel are the flow, and the enclosing geometry is the combustion chamber.

Thermoacoustic instabilities occur when this feedback loop is able to sustain the oscillation amplitude over time. The necessary condition for the instabilities to be self-excited is the famous Rayleigh criterion (Rayleigh, 1878) from the late 19th century. The condition requires the pressure and heat release rate oscillations to be in phase for it to be possible to have self-sustained oscillations. Similar to a pendulum, as discussed as a similar system by Rayleigh (1878), the applied force to the system has to be working with the oscillation, not against it, to add energy to the resulting oscillations. While Rayleigh himself presented the theory behind the criterion in a written argument, there have later been several mathematical derivations of this condition. A step by step version of the derivation of the generalised Rayleigh criterion is given by Schuller et al. (2020)

$$\mathcal{R} = \int_V \int_0^T \frac{\gamma - 1}{\gamma \bar{p} T} p' q' \mathrm{d}t \mathrm{d}V > \mathcal{D}\,. \tag{1.1}$$

Here γ is the specific heat ratio, $\bar{p}$ is the mean pressure and T is the oscillation period. The pressure fluctuations are given by p' and the heat release rate oscillations are denoted q'. Equation (1.1) states that the energy added to the system has to be greater than the acoustic losses $\mathcal{D}$ of the system. The left hand side of

Eq. (1.1) ($\mathcal{R}$) is often called the *Rayleigh index*, and the original Rayleigh criterion was $\mathcal{R} > 0$. This was a necessary condition, but not always sufficient. However, the generalised criterion $\mathcal{R} > \mathcal{D}$ is sufficient to have thermoacoustic instabilities.

The generalised Rayleigh criterion in Eq. (1.1) is a relatively simple looking equation, but it is not trivial to calculate analytically in most cases. For some very simple laminar flame shapes it is possible to derive a relationship between the acoustic mode and the heat release rate (Fleifil et al., 1996; Dowling, 1999; Schuller et al., 2003). However, in practical configurations with swirling turbulent flames in more complex geometries this is not a feasible approach. Therefore, significant effort has been put into understanding the relationship between the pressure and the heat release rate for a range of different types of flames in different geometries.

1.2 Flame Transfer Functions

A solution for how to link the acoustic and spatially integrated heat release rate fluctuations was proposed by Merk (1957)

$$\frac{\langle \hat{q}' \rangle}{\langle \bar{q} \rangle} = Tr_p \frac{\hat{p}'}{\bar{p}} + Tr_u \frac{\hat{u}'_{\text{axial}}}{U_{\text{ref}}} \,. \tag{1.2}$$

Here prime denotes the fluctuating quantities, the hat $\hat{(\cdot)}$ denotes the complex valued Fourier amplitude of oscillations, $\langle (\cdot) \rangle$ denotes spatial averaging, $\bar{p}$ is the temporal mean pressure, and U_{ref} is a temporal mean reference velocity. Merk (1957) relates the relative heat release rate fluctuations to the relative pressure and axial velocity fluctuations through the two transfer functions Tr_p and Tr_u respectively. It is here assumed that the pressure and axial velocity quantities are evaluated in the cold gas just upstream of the heat source. The two transfer functions are unknown, but depend on the frequency of oscillation in general.

Equation (1.2) was the first implementation of what is known as the Flame Transfer Function (*FTF*). The conventional modern FTF definition has dropped the explicit pressure dependence, and is defined as

$$\text{FTF}\,(\omega) = \frac{\langle \hat{q}'(\omega) \rangle \,/\, \langle \bar{q} \rangle}{\hat{u}'_{\text{axial}}(\omega)/U_{\text{ref}}} \,. \tag{1.3}$$

Compared to the original definition of Merk (1957), the reference location of the acoustic velocity perturbations is not always taken to be just upstream of the flame in practice (Komarek and Polifke, 2010; Palies et al., 2010). The pressure term is dropped, as premixed gaseous flames are more sensitive to velocity perturbations compared to the corresponding pressure perturbations (Polifke, 2020). The acoustic velocity perturbations result in direct flow perturbations, which is the main

driving mechanism in the heat release rate, as presented in Fig. 1.1. Additionally, the pressure and acoustic velocity at a given location can be linked through a system specific, frequency dependent impedance $z(\omega)$

$$\hat{p}'(\omega) = z(\omega)\hat{u}'_{\text{axial}}(\omega)\,, \tag{1.4}$$

where $\omega = 2\pi f$ is the angular frequency (Noiray et al., 2008; Gaudron et al., 2019). This means the FTF definition is also capable of capturing any potential direct effects of the pressure even though the explicit pressure dependence is lost. However, any direct pressure effects captured this way are dependent on the acoustic properties of the system due to the system specific impedance.

The major advantage of introducing the FTF is that the complex problem of thermoacoustic instabilities can be studied from a purely acoustic point of view when the FTF is known (Merk, 1957; Dowling, 1999; Schuller et al., 2020). This represents a major saving in computational complexity and cost compared to high fidelity large eddy simulations (Staffelbach et al., 2009; Fureby, 2009; Wolf et al., 2012) of more complex geometries or direct numerical simulations (Chen et al., 2009; Chen, 2011; Wiseman et al., 2020), which are currently unfeasible for parametric design studies due to the associated cost and lack of computational power. However, there still remains a large challenge for the acoustic approach in determining the FTF that is representative for the system of interest. For very simple geometries with simple flames it is possible to derive analytical models using level-set methods (Dowling, 1999; Schuller et al., 2003). An example of such analytical FTF expressions is given in Fig. 1.2. Level-set methods can also include more complex effects when paired with numerical solvers to obtain the transfer function (Lee and Lieuwen, 2003; Preetham and Lieuwen, 2007; Preetham et al., 2008; Hemchandra and Lieuwen, 2010; Hemchandra et al., 2011; Shin and Lieuwen, 2012, 2013). The methods also provide an explicit representation of the different effects on the transfer function, allowing for physical insight into the mechanisms contributing to the response. However, for flames and injectors representative of gas turbines, the response can usually not be derived easily by using analytic methods. In practice the FTF is therefore usually obtained either from experiments (Kunze et al., 2004; Hirsch et al., 2005; Komarek and Polifke, 2010; Schimek et al., 2012; Cuquel et al., 2013; Kim and Santavicca, 2013a; Gatti et al., 2017, 2018, 2019; Gaudron et al., 2019; Æsøy et al., 2020) or from high fidelity numerical simulations (Tay Wo Chong et al., 2010, 2011).

While Figure 1.2 is for an idealized flame, it does capture two general features of the FTF for perfectly premixed flames. The first feature is the unit gain in the low frequency limit, which is always the case for perfectly premixed flames (Polifke and Lawn, 2007). This is due to the slow perturbations in the inlet velocity being equivalent to slowly changing the inlet mass flow. For perfectly premixed

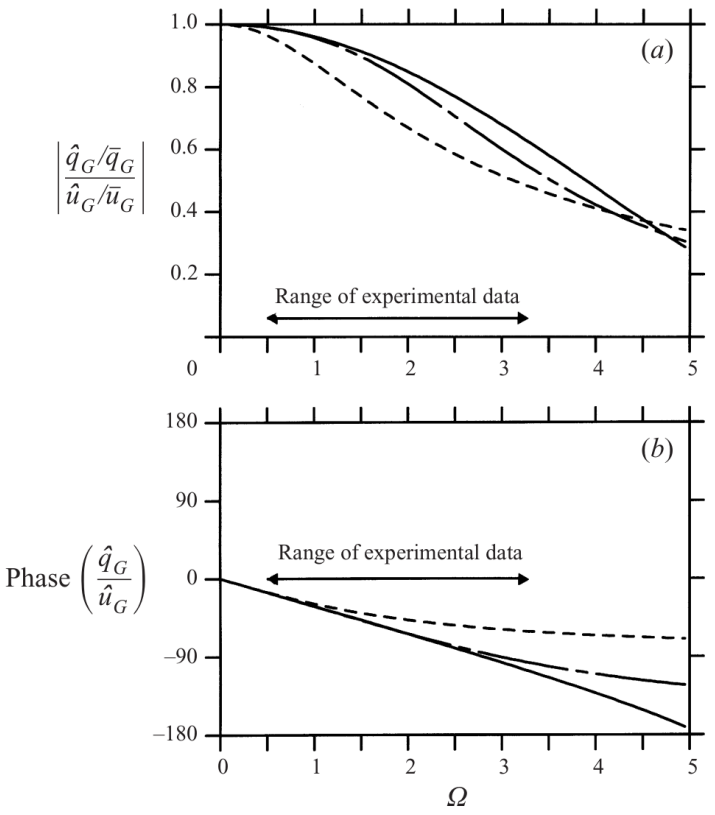

Figure 1.2: Analytical linearized FTF for a ducted flame anchored on a central rod (solid line) derived by Dowling (1999). The magnitude of the FTF is shown on top with the phase in the bottom, both plotted against a non-dimensional frequency Ω. The uniformly dashed and long-short dashed lines are from the first- and second-order lag laws of Bloxsidge et al. (1988) and Dowling (1997) respectively. Source: Dowling (1999).

flames the equivalence ratio is constant, and the relative change in mass flow is the same as the relative change in fuel mass flow and thus equal to the relative change in heat release rate. In the case of non-premixed flames with a separate fuel injection system, this does not hold as such systems exhibit equivalence ratio perturbations (Sattelmayer, 2003). Such systems can still be characterised by FTFs, but they will not be discussed in this work. The second feature is the low-pass filter behaviour of the FTF, meaning the magnitude of the FTF becomes negligible for sufficiently high frequencies (Fleifil et al., 1996; Schuller et al., 2003; Polifke, 2020). As the frequency is increasing, the wavelength, and conversely the scale, of the flame front wrinkles are reduced. The small-scale wrinkles of the flame front are dissipated faster than the larger ones, which are associated with lower frequencies, due to kinematic restoration, leading to a decreasing gain value for increasing frequencies (Shin and Lieuwen, 2012). Additionally, for sufficiently high frequencies, the wavelength of the convective perturbations causing the heat release rate fluctuations is short enough to cause both positive and negative contributions at the same time due to the finite length of the flame (Ducruix et al., 2000; Blumenthal et al., 2013). This can further reduce the spatially integrated heat release rate fluctuations as the frequency is increased.

The two general features of the FTFs for perfectly premixed flames are not sufficient to predict the stability of a given system. The information of how the magnitude of the FTFs goes from unity at low frequencies to zero at high frequency is of great interest to determine the system stability, as well as for the understanding of thermoacoustic instabilities. Therefore, an immense research effort has been put into understanding the behaviour of these functions, as well as their scaling and generality (Hirsch et al., 2005; Komarek and Polifke, 2010; Palies et al., 2010; Schimek et al., 2012; Kim and Santavicca, 2013a; Gatti et al., 2018).

1.2.1 Experimental determination

A common approach to obtain the FTF experimentally is to impose external acoustic perturbations for a thermoacoustically stable flame configuration (Kunze et al., 2004; Hirsch et al., 2005; Komarek and Polifke, 2010; Schimek et al., 2012; Cuquel et al., 2013; Kim and Santavicca, 2013a; Gatti et al., 2017, 2018, 2019; Gaudron et al., 2019; Æsøy et al., 2020). In the case of thermoacoustically stable configurations, the feedback loop between the acoustics caused by the heat release rate perturbations and the flow, as shown in Fig. 1.1, is not strong enough to sustain the oscillations. Instead the external input, as shown on the left in Fig. 1.1, is the sole driving force in the system. This also means the frequency of oscillation can be imposed externally, enabling the study of the full frequency range of interest. Two example setups for obtaining FTFs experimentally are presented in Fig. 1.3.

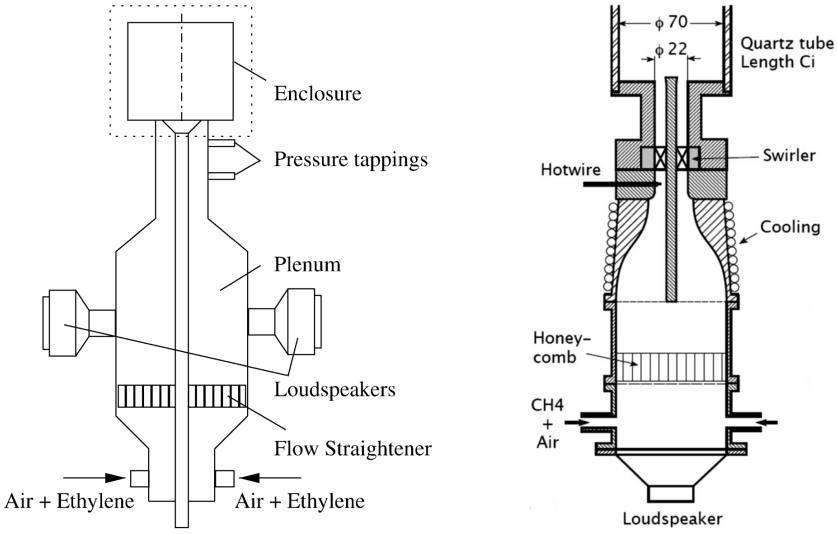

(a) Balachandran et al. (2005). (b) Palies et al. (2010).

Figure 1.3: Axial forcing setups of Balachandran et al. (2005) in (a) and Palies et al. (2010) in (b). Both setups use one or more loudspeakers upstream of the flame to impose axial acoustic velocity perturbations in the system. Both flames are attached to a central rod or bluff body, with the flame burning inside an open enclosure. Adapted from Balachandran et al. (2005) and Palies et al. (2010).

To obtain the FTF the velocity perturbations are captured through a technique of choice. Popular approaches include using multiple microphones to determine the acoustic velocity, hot wire measurements upstream of the flame or other direct measurement techniques of the flow at a reference position. The heat release rate is usually assumed to be proportional to the concentration of excited OH* or CH* radicals (Higgins et al., 2001; Hardalupas and Orain, 2004; Balachandran et al., 2005). This makes it possible to calculate the relative heat release rate perturbations as the relative fluctuations of the intensity of the light with wavelength corresponding to the de-excitation of the chosen radicals. This is usually captured by a camera or a photomultiplier tube (*PMT*) with a narrow band-pass filter. Then, the FTF is obtained for discrete frequencies by calculating the relative heat release rate fluctuations from the recorded light intensity, and the corresponding relative velocity perturbations are calculated with the technique of choice. An alternative method of calculating the transfer function based solely on acoustic measurements is outlined by Paschereit et al. (2002). This is great for systems where optical accessibility is limited, but comes at the loss of information on flame dynamics and spatial heat release rate distribution. Therefore, the method will not be used in the current work, where spatial information is of great interest.

1.2.2 Effect of swirling flow

A popular area of experimental investigation over the last couple of decades has been the effect of an upstream swirler on the gain and phase of the FTF, as upstream swirlers are a common approach to flame stabilisation in gas turbines. Several studies have examined the effect of the upstream location of the swirler relative to the flame location (Straub and Richards, 1999; Komarek and Polifke, 2010; Palies et al., 2010; Kim and Santavicca, 2013b). Other studies have looked at the difference between the two main ways of imposing a swirling motion on the inlet flow, namely axial swirlers and tangential swirlers (Hirsch et al., 2005). Gatti et al. looked at the influence of the injector geometry (Gatti et al., 2017) and of the swirl number (Gatti et al., 2018) on the FTF.

The swirler has been shown to introduce a convective flow perturbation as the acoustic wave impinges on the swirler (Komarek and Polifke, 2010; Palies et al., 2010, 2011). This introduces a time scale related to how long the convective perturbations take to travel from the swirler to the flame base compared to how long it takes the acoustic perturbation to travel the same distance. This results in interference at the flame base, resulting in modulations of both the gain and phase of the FTF as the interference switches between being positive or destructive (Komarek and Polifke, 2010; Palies et al., 2010), which is consistent with the observations of Preetham et al. (2008). An example of this is shown in Fig. 1.4, which is adapted

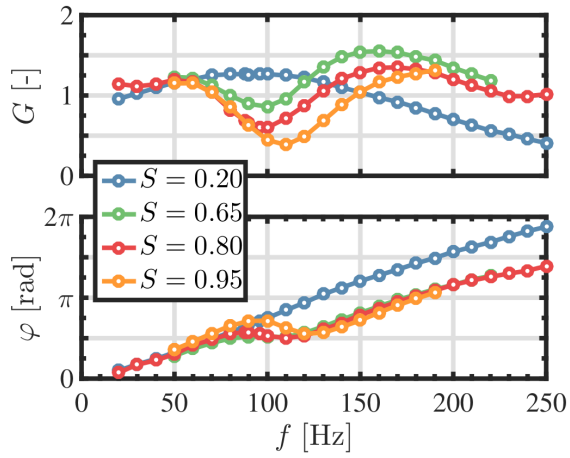

Figure 1.4: The effect of increasing the swirl number S, which is the ratio of the momentum flux in the tangential and the axial direction, is an increasing strength dip in the gain $G = |FTF|$ of the FTF according to Gatti et al. (2018). In the same frequency range a sharp modulation in the FTF phase φ is also observed. Adapted from Gatti et al. (2018).

from a comparison of different swirl levels by Gatti et al. (2018). In the case of very low swirl levels, $S = 0.20$, the convective perturbations from the swirler are shown to be negligible, and can be considered to be a good representation of the reference gain and phase of an unswirled flame. As the swirl level increases, there is a clear dip in the gain developing in the 100 Hz region. The dip is caused by the interference between the convective and acoustic perturbations at the flame base being destructive in this frequency range.

The location of the bottom of the dip in the response ω_{dip} is given by (Palies et al., 2010; Kim and Santavicca, 2013b)

$$\left(\frac{L}{U_{\text{prop}}} - \frac{L}{c}\right)\omega_{\text{dip}} = \pi\,, \tag{1.5}$$

where L is the distance between the dump plane and the swirler. U_{prop} is the mean velocity at which the convective perturbations are propagating. Equation (1.5) corresponds to the convective perturbations created at the swirler being in phase opposition to the acoustic perturbations at the base of the flame. The propagation velocity of the convective perturbations from the swirler U_{prop} was first assumed to be the local convective velocity (Palies et al., 2010; Kim and Santavicca, 2013b; Palies et al., 2017). However, there have been several studies suggesting the perturbations propagate faster than the convective speed (Komarek and Polifke, 2010;

Acharya and Lieuwen, 2014b). Albayrak et al. (2019) showed recently that the perturbations created at the swirler are actually behaving as inertial waves, which means the perturbations travel faster than the mean bulk flow in the injector. Values up to approximately $50\,\%$ have been reported (Albayrak et al., 2019). This is consistent with the faster velocity which has been observed to be necessary when modelling the FTF of systems with swirl (Komarek and Polifke, 2010).

To observe this interference phenomenon, it has been shown that two, or more, sources of convective or inertial wave perturbations are needed (Gatti et al., 2019). Typically, one source is the swirler used for flame stabilisation, and the other is the injector exit. Taking away either of these sources was shown by Gatti et al. (2019) to remove the interference observed when both are present in the system. Recently, Æsøy et al. (2020) made this more explicit by showing that the swirler can be replaced by round cylinders (grub screws) in the upstream flow. These generate convective perturbations that were shown to result in similar modulations of the gain and phase of the FTF, matching Eq. (1.5) well.

1.2.3 Time delay models

The Rayleigh criterion in Eq. (1.1) shows the phase between the pressure and heat release rate fluctuations is important to the stability of the system. To explain this phase difference, the concept of distributed time delay models can be used to characterise the response of the flame to incoming pressure fluctuations (Polifke, 2020). These assume there is one or more characteristic time delays in the system that determine the relation between the mass flow rate and the resulting heat release rate.

The first time delay model was the n-τ model introduced by Crocco (1951) for rocket engines. It assumed there is a fixed delay τ from when fuel is injected into the combustion chamber until it is converted to heat. The magnitude ratio of heat release rate and fuel mass injected is given by the constant n. The same principle can be applied to gas turbine combustion, where the time delay τ can be interpreted as the time it takes for the gas to reach the reaction zone of the flame (Polifke, 2020). This model is equivalent to an FTF of constant gain and a linear phase evolution $\angle\,\mathrm{FTF}\,(\omega) = \omega\tau$.

The constant magnitude of the n-τ model does not capture the low-pass filter behaviour, due to kinematic restoration (Shin and Lieuwen, 2012), observed for flames (Fleifil et al., 1996; Schuller et al., 2003). To fix this, models with a frequency dependent gain, equivalent to a frequency dependent n, have been applied to characterise the flame response. One such model is the gaussian distributed time delay model, which can be observed to have a characteristic low-pass behaviour in Fig. 1.5. As the name suggests, the gaussian distributed time delay model has

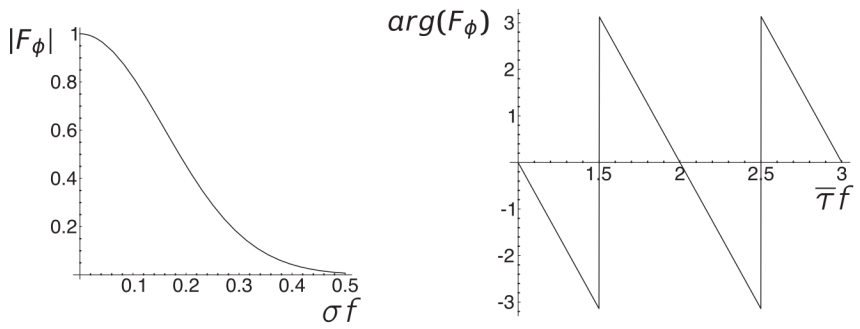

Figure 1.5: FTF of a Gaussian distributed time delay model with standard deviation σ and a mean time delay of $\overline{\tau}$. The phase evolution is observed to be determined solely by the mean time delay $\overline{\tau}$. Source: Polifke (2020).

a gaussian distribution of time delays. The distribution takes into account that the convective time from the base of the flame to the reaction zone is not the same for all parts of the flame. While the distributed time delay model contains a distribution of time delays, it is characterised by a single time scale, the mean time delay $\overline{\tau}$.

There are several configurations and setups where there might be more than a single characteristic time scale $\overline{\tau}$. The first time delay is usually the convective time from the base of the flame to the reaction zone. A second time scale can, for example, be introduced by an upstream swirler Komarek and Polifke (2010); Palies et al. (2010) or a turbulence generator (Æsøy et al., 2020). The perturbations created at this upstream location need to propagate to the base of the flame and continue to the reaction zone, making the time delay longer than the first one. Another potential source for a second time delay is operating in non-premixed conditions (Schuermans et al., 2004; Schimek et al., 2012), but that will not be the main focus here.

In the presence of multiple time scales, several time delay models can be summed to describe the response, which is assumed to be linear for FTFs. Successful application of several distributed time delay models include Sattelmayer (2003), Schuermans et al. (2004), Schimek et al. (2012), and Æsøy et al. (2020). In particular, the model of Æsøy et al. (2020) is used to model two spatially separated sources of convective perturbations in a flame without swirl. The approach uses two identical models with different parameters, where each model either acts as a low-pass or a band-pass filter around a model specific frequency. While Æsøy et al. (2020) used the model to capture the response of an unswirled flame, the model should also be suited to swirled flames with two time delays. For the case of swirled flames, which have two distinct time delays, the location of the dip in the

FTF is effectively determined by the difference in the two time delays in the low Mach number limit. This can be seen from Eq. (1.5), where the expression in the parenthesis on the left hand side can be approximated as L/U_{prop}, corresponding to the convective time from the swirler to the dump plane.

1.3 Flame Describing Functions

The Flame Transfer Function, or FTF, has proven to be a very useful tool to predict the *linear* stability of systems (Kopitz et al., 2005; Tay Wo Chong et al., 2011; Schuller et al., 2020). However, the sustained oscillations associated with thermoacoustic instabilities are a limit cycle phenomenon, meaning it is non-linear in nature (Langhorne, 1988). To predict the limit cycle behaviour of a combustion system, the FTF is not sufficient, as it is linear in nature, and will predict the system to either grow to infinite amplitudes or be damped to zero response after some time.

The non-linear nature of the heat release rate response can be included by generalising the FTF to the Flame Describing Function (*FDF*) (Dowling, 1997)

$$\text{FDF}\left(\omega, \hat{u}'_{\text{axial}}/U_{\text{ref}}\right) = \frac{\langle \hat{q}'(\omega, \hat{u}'_{\text{axial}}/U_{\text{ref}})\rangle \,/\, \langle \bar{q}\rangle}{\hat{u}'_{\text{axial}}(\omega)/U_{\text{ref}}}\,. \tag{1.6}$$

Compared to the FTF, the FDF includes an explicit velocity dependence on the heat release rate fluctuations. For sufficiently low velocity amplitudes, the FDF will be the same as the FTF, while at sufficiently high amplitudes, the gain of the FDF will be lower than the gain of the linear FTF. This accounts for the saturation of the heat release rate, and allows for the prediction of the limit cycle amplitude for a given saturation level of the heat release rate (Dowling, 1997; Stow and Dowling, 2004; Noiray et al., 2008).

The FDF can be obtained experimentally on the same setups as used to obtain the FTF, following the same procedure described in §1.2.1. The main difference is the heat release rate response is obtained at several perturbation levels for each frequency, up to an amplitude where the heat release rate fluctuations saturate. Similar to the FTF, the FDF is usually either obtained experimentally (Balachandran et al., 2005; Boudy et al., 2011; Gaudron et al., 2019) or through high-fidelity simulations (Krediet et al., 2012; Han and Morgans, 2015; Xia et al., 2019). Additionally, the FDF can also be captured through level-set approaches, where the equations are solved for increasing perturbation levels (Preetham and Lieuwen, 2007; Preetham et al., 2008). The obtained FDF can then be used in acoustic solvers to capture the limit cycle behaviour of the studied system, and not only the linear stability (Stow and Dowling, 2004). An example of an experimentally determined FDF is shown in Fig. 1.6. A framework on how experimentally obtained

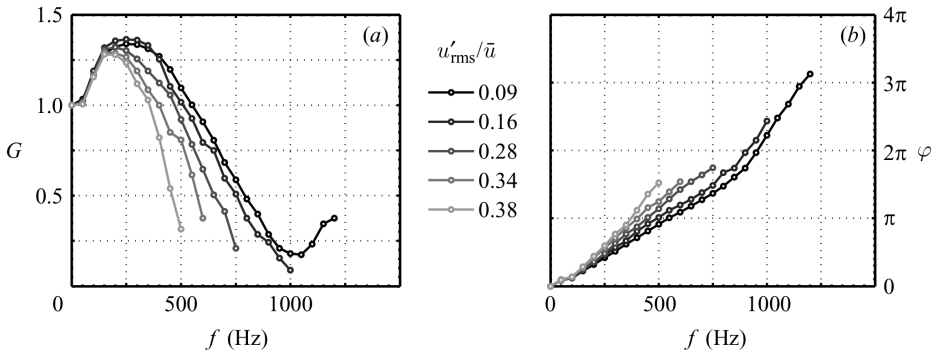

Figure 1.6: Example of an experimentally obtained FDF. The gain is observed to decrease for increasing perturbation levels, indicating a saturating level of heat release rate fluctuations. Source: Noiray et al. (2008).

FDFs can be utilised in an acoustic solver to predict the limit cycle behaviour of a flame can be found in Noiray et al. (2008).

The approach of using the FDF in modelling the response of a flame is of significant interest in the case of annular combustors, where there exists a rich range of pressure modes which can occur with the same frequency. To model the behaviour and time evolution of such systems, it is paramount that the limit cycle nature of the oscillations are captured in the model. How to model the time evolution of such systems will be discussed in more detail in §1.5.3.

1.4 Transverse instabilities

The FTF is often determined by imposing axial perturbations on the system, as described in §1.2.1. It is also the axial velocity perturbations that are considered in the FTF definition in Eq. (1.3). However, in gas turbines with an annular combustion chamber geometry, the acoustic modes that are excited are predominantly azimuthal in nature. Another feature of these configurations is the high aspect ratio of the combustion chamber length to the radial width compared to the typically cylindrical or square enclosures used on single flame experiments. Therefore, it is of great interest to ascertain whether there are any significant differences when the flames are subjected to transverse perturbations in a high aspect ratio configuration compared to the conventional axially perturbed configurations. A comprehensive review of recent research on transverse instabilities in air-breathing systems can be found in O'Connor et al. (2015).

Full annular setups are relatively expensive to build compared to single flame setups, and the process of applying forcing to such systems is, in general, more

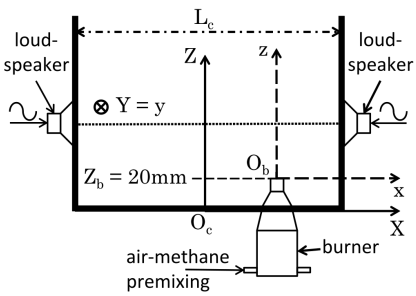

(a) Source: Lespinasse et al. (2013).

(b) Source: O'Connor and Acharya (2013).

Figure 1.7: Examples of two long aspect transverse forcing setups. Both setups have downstream speakers which impose a transverse pressure mode in the combustion chamber. (a) is the setup of Lespinasse et al. (2013) with a transversely offset burner, and (b) is the setup of O'Connor and Acharya (2013) with a centred burner inlet, marked by the white arrow.

complicated than for single flame setups. Additionally, in annular setups there are typically flame to flame interactions, which might complicate the response. Therefore, in an effort to study the isolated differences between transverse and axial forcing, researchers have very recently started to build long aspect ratio single flame setups with transverse forcing capabilities (Hauser et al., 2011; O'Connor and Lieuwen, 2011; Lespinasse et al., 2013; Saurabh and Paschereit, 2013). Some examples of such setups are shown in Figure 1.7. These setups approximate an annular setup by unwrapping it, removing all the curvature of the geometry. This allows the study of the direct effect of transverse forcing on the response of a single flame.

Such transverse forcing setups are typically excited by either standing waves, where different positions in the standing wave can be examined (O'Connor and Lieuwen, 2011, 2012; Lespinasse et al., 2013), or by travelling waves (Saurabh et al., 2014). It was observed that the response in the pressure node and anti-node of a standing wave differ in general, and the response to a travelling wave is similar to that of a flame located in the pressure anti-node of a standing wave.

Another significant result from the high aspect transverse forcing setups is that the *direct* effects of the transverse perturbations on the global heat release rate response is small for axisymmetric flames (Acharya et al., 2012; O'Connor et al., 2015). The transverse acoustic velocity perturbations were shown to lead to significant wrinkling of the local flame front, but the effect on the globally integrated heat release rate of the flame was small. However, the pressure distributions associated with the transverse acoustic modes induce acoustic velocity perturbations

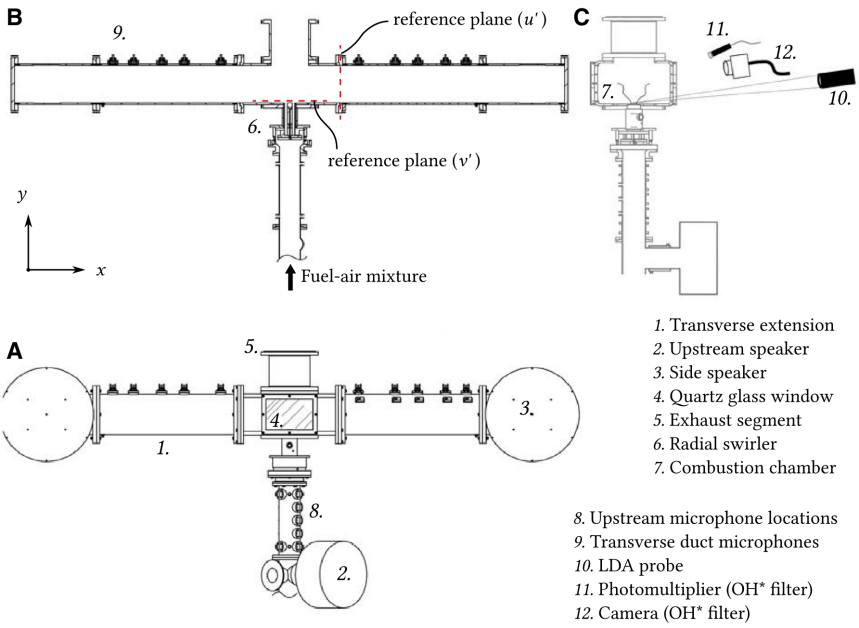

Figure 1.8: Experimental rig with the capability of applying simultaneous axial and transverse forcing. Using both at the same time allows for variability in the timing of the transverse and axial velocity perturbations. Source: Saurabh and Paschereit (2017).

in the injector tube. The resulting axial acoustic velocity perturbations have been observed to be the main driving factor of the global heat release rate response (O'Connor et al., 2015). The transverse acoustic mode therefore plays an important role in the response, but mostly indirectly through the induced axial velocity perturbations.

In the case of non-axisymmetric flames, the transverse perturbations can have a direct effect on the global heat release rate response. Acharya and Lieuwen (2014a, 2016, 2019) showed that the globally integrated contribution of the non-axisymmetric helical modes do not cancel in the case of a non-axisymmetric flame. While common injectors are designed to produce axisymmetric flames, small imperfections in manufacturing and assembly, or in the approach flow, can create small asymmetries. The symmetry of the flames can also be broken in multi flame geometries, for example an annular combustor, by the flames directly interacting with the adjacent flames. The sum of these effects is that in most practical configurations, the flames will not be completely axisymmetric.

Recently Saurabh and Paschereit (2017, 2019) studied the response to simultaneous axial and transverse acoustic forcing for different phases between the two

forcing directions. The setup used is presented in Fig. 1.8, where the axial and transverse speakers can be tuned individually. This simulates the conditions in an annular combustor, where the timing between the axial velocity perturbations and the transverse velocity perturbations depends on both the mode orientation and the nature of the mode. Interestingly, Saurabh and Paschereit (2017, 2019) found that when the transverse acoustic mode was changed from 0° phase difference to 180° phase difference relative to the axial mode, the global heat release rate response was not the same. Introducing that phase shift is equivalent to changing the spinning direction of the transverse mode in an annular combustor, suggesting the two spinning directions are not necessarily the same. The effect was attributed to small asymmetries in the single studied flame, which is consistent with the observations of Acharya et al. (2012) and Acharya and Lieuwen (2016, 2019) that asymmetries in the flame can lead to the transverse acoustic mode having a direct effect on the heat release rate response.

1.5 Annular combustors

Annular combustors, together with can-annular combustors, are the most widely used geometries for gas turbines used in both transport and power generation (Poinsot, 2017). One of the most prevalent modes encountered in annular combustors is azimuthal in nature, as the azimuthal length scale is typically of the same order as the length of the combustion chamber (Poinsot, 2017). Without an acoustic boundary in the azimuthal direction, the azimuthal mode in the combustion chamber is degenerate. The degenerate modes result in a rich parameter space of resulting azimuthal modes when combined, which are not possible to observe on the transverse setups described in the previous section. Therefore, to understand the dynamics of such modes, experiments on true annular configurations are needed to be able to improve the understanding of such modes. Some initial data was acquired on full scale commercial gas turbines (Seume et al., 1988; Krebs et al., 2002; Paschereit et al., 2006). However, these configurations are geometrically very complex and expensive to run. Motivated by this, simplified annular combustion chambers, capable of exhibiting self-excited thermoacoustic instabilities, for use in a laboratory were developed in the last decade (Worth and Dawson, 2013b; Bourgouin et al., 2013; Roy et al., 2020). Figure 1.9 presents an external view of these three different combustor designs.

The combustor of Worth and Dawson (2013b) and the MICCA combustor (Bourgouin et al., 2013) were developed independently at about the same time, and both have been shown to be capable of exhibiting self-excited azimuthal modes. In addition to exciting azimuthal thermoacoustic instabilities, the MICCA combustor has been shown to excite longitudinal (Bourgouin et al., 2013) and slanted

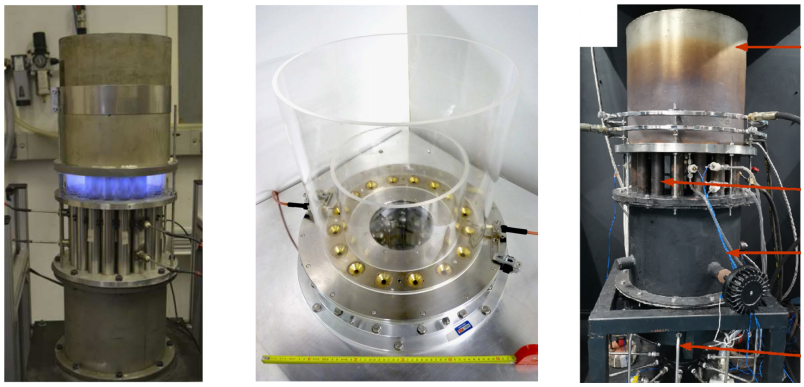

(a) (b) (c)

Figure 1.9: The annular combustor of Worth and Dawson (2013a) in (a) and the MICCA combustor (Bourgouin et al., 2013) in (b) were the two first annular lab scale combustors to exhibit self-excited thermoacoustic instabilities. Very recently a hybrid between the two was created at IIT Madras by Roy et al. (2020), which is shown in (c). Figures are adapted from Worth and Dawson (2013a), Bourgouin et al. (2013) and Roy et al. (2020) respectively.

(Bourgouin et al., 2015) modes for some configurations and operating conditions. The slanted mode is a combination of a longitudinal and an azimuthal mode of the same frequency, where both are excited at the same time. The combustor of Roy et al. (2020) is a combination of the design of the two former combustors, and has so far only been shown to excite longitudinal modes. A comprehensive review of experimental research on annular combustors can be found in Vignat et al. (2020). In this work, azimuthal modes will be the main focus, and the discussion will be limited to the combustor of Worth and Dawson (2013b) and the MICCA combustor at operating conditions featuring azimuthal instabilities (Bourgouin et al., 2013).

1.5.1 Self-excited instabilities and modal dynamics

The degenerate behaviour of the azimuthal modes in annular configurations results, as described, in a rich set of possible resulting azimuthal modes. The azimuthal mode can be spinning in either direction, standing, or a combination of the two. The exact combination of these can be described as the nature of the mode. Initially, the azimuthal mode was described by using an orthogonal description of two counter propagating waves (Wolf et al., 2012; Worth and Dawson, 2013b; Bourgouin et al., 2013; Vignat et al., 2019) or two standing waves (Ghirardo and Bothien, 2018). While the standing mode decomposition is mostly used in model-

ling efforts, the two spinning wave decomposition has been the most popular for experimental studies. In the latter case, the nature of the mode has typically been characterised using the spin ratio introduced by Bourgouin et al. (2013)

$$\mathrm{SR} = \frac{|A_+| - |A_-|}{|A_+| + |A_-|}\,. \tag{1.7}$$

Here, A_+ and A_- are the amplitudes of the ACW spinning and CW spinning plane waves respectively. The spin ratio of any standing mode is zero, while ACW and CW spinning modes have spin ratios $+1$ and -1 respectively. Everything in between is often denoted as a mixed mode, as such modes have both a spinning and a standing component.

Experiments have shown that the nature of the azimuthal mode can change over time, both in real gas turbines (Krebs et al., 2002) and in lab scale combustors (Worth and Dawson, 2013a; Bourgouin et al., 2013). This phenomenon is often called modal dynamics, and means it is of great interest to study the behaviour of the limit cycles over time. The dependence of the modal dynamics on the equivalence ratio was investigated by Worth and Dawson (2017). Worth and Dawson have also studied the effect of inserting baffles in the combustion chamber on the acoustic mode (Dawson and Worth, 2015), and the structural differences in the individual flames for the two spinning directions (Dawson and Worth, 2014). Prieur et al. (2017) showed that the MICCA combustor equipped with laminar matrix burners (Bourgouin et al., 2014) has regions of operating conditions where a single mode was stable over time, with a smaller region where both standing and spinning modes could be observed.

In the effort to model the modal dynamics, the nature of the mode has proven hard to implement directly in the models using the spin ratio, as it is a derived quantity. Recently, Ghirardo and Bothien (2018) solved this problem by introducing the hypercomplex quaternion formalism, where the nature of the mode is a state space parameter. Any azimuthal mode of order n can be described as (Ghirardo and Bothien, 2018)

$$\begin{aligned} p'(\theta, t) =& A\cos\left(n(\theta - \theta_0)\right)\cos\left(\chi\right)\cos\left(\omega t + \varphi\right) + \\ & A\sin\left(n(\theta - \theta_0)\right)\sin\left(\chi\right)\sin\left(\omega t + \varphi\right). \end{aligned} \tag{1.8}$$

The nature of the mode is characterised by the nature angle χ in this formalism, which is a state space parameter. The spin ratio and the nature angle are directly related through $\mathrm{SR} = \tan\left(\chi\right)$. The amplitude A, azimuthal orientation of the anti-node θ_0, nature angle χ, and temporal phase φ can all vary in time. Most importantly, the four variables are all state space variables, which can be used directly in models. The state space variables are assumed to be slowly varying compared to the period of the fast oscillations ω.

1.5.2 Acoustically forced annular configurations

Modal dynamics are a highly interesting phenomenon in itself, but they also pose a problem for the study of how flames respond to a given azimuthal mode. The constantly changing nature of the modes makes it hard to study a single mode during self-excited instability. One possible approach is to employ conditional phase averaging, as performed by Worth and Dawson (2013a); Bourgouin et al. (2013); Dawson and Worth (2014). However, this requires very long measurements to study a single mode, as both orientation and nature of the mode change over time. This is also complicated by the preference for certain modes (Noiray et al., 2011; Worth and Dawson, 2013a; Bourgouin et al., 2013; Ghirardo et al., 2015; Bauerheim et al., 2015), meaning some modes are practically impossible to study in self-excited conditions due to the rarity of their occurrence.

For single flame setups similar complications, caused by the limited frequency range of self-excited modes due to the geometry, were overcome by imposing acoustic modes via acoustic forcing techniques. It is natural to extend similar principles to annular setups. However, this is more complicated compared to the more conventional axial or transverse forcing setups. Kunze et al. (2004) excited the flow upstream of the injectors using a speaker array, but this is not equivalent to exciting the modes directly in the annular combustion chamber. Moeck et al. (2010) used a novel technique with speakers distributed around an annular Rijke tube rig to impose the acoustic mode of the system downstream of the injectors and heating elements. The setup and speaker placement can be seen in Figure 1.10. With this setup both standing, spinning and mixed modes can be excited in the annular chamber. The same setup was later used with more advanced feedback control of the speakers by Gelbert et al. (2012) and Humbert et al. (2020a,b) to excite the desired modes of interest.

Worth et al. (2017) used a similar approach to Moeck et al. (2010) to excite standing modes of the first azimuthal order by using two opposing speakers driven out of phase, as shown in Figure 1.10. This enabled the study of well controlled standing modes, where the amplitude and orientation of the mode was controlled by the forcing array. A similar forcing array was used by Allison et al. (2017) to excite a range of frequencies, but due to the large frequency range the excited azimuthal mode was not explicitly controlled, making the interpretation of the results harder.

The forcing array imposes an excited mode which is approximately constant in time, making it possible to study the response without conditioning on the mode. Imposing the acoustic mode on the combustion chamber can also give the possibility of obtaining the FTF/FDF of flames in true annular configurations, similar to what is obtained on single flame setups. However, due to the geometric constraint of the azimuthal mode, the response would be limited to a single frequency for any

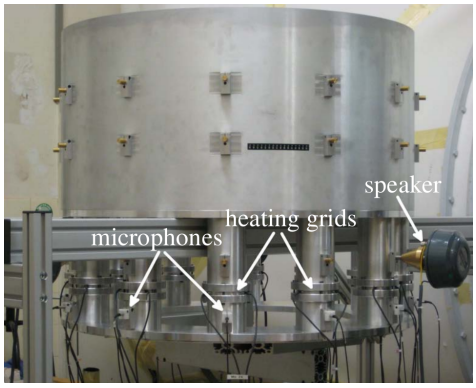

(a) Adapted from Moeck et al. (2010).

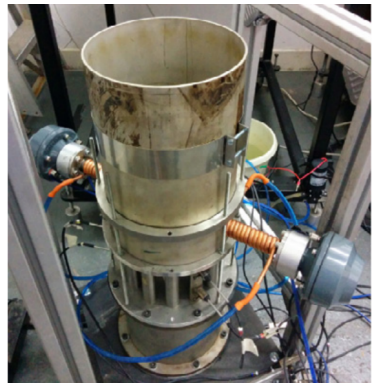

(b) Adapted from Worth et al. (2017).

Figure 1.10: Annular forcing setups of Moeck et al. (2010) in (a) and of Worth et al. (2017) in (b). The setups utilise the geometry of the problem with speakers to excite the desired acoustic modes. Adapted from Moeck et al. (2010) and Worth et al. (2017) respectively.

given operating condition. Additionally, imposing the acoustic mode would allow the exploration of the full state space of Eq. (1.8) up to a finite amplitude limit.

1.5.3 Acoustic modelling of azimuthal instabilities

A common approach to model thermoacoustic instabilities and the stability of systems is to use acoustic models, where the connection between pressure fluctuations and heat release rate is reduced to either a FTF or a FDF. For very simple geometries, acoustic network models can be used (Noiray et al., 2011), but for more complex geometries, Helmholtz solvers are a popular approach (Wolf et al., 2012; Silva et al., 2013; Bauerheim et al., 2014; Mensah and Moeck, 2015; Laera et al., 2017; Yang et al., 2019). To reduce the computational domain of the Helmholtz solvers, Mensah and Moeck (2015) recently applied Bloch theory (Bloch, 1929) to thermoacoustic instabilities in annular configurations. For an annular setup with N equidistantly spaced injectors, the computational domain is reduced to $1/N$ of the full annular geometry. This approach has recently gained traction in modelling efforts (Haeringer and Polifke, 2019; von Saldern et al., 2020), but Bloch theory has not been applied to experiments yet. The acoustic Helmholtz solvers and network model solvers find the stability and growth rate of the systems, but do not capture the time evolution of the state space variables describing the unstable azimuthal modes.

Another approach is to significantly simplify the geometry down to an infin-

itely thin annulus, with no injectors and plenum to take into account, while allowing for more nonlinear features by using the FDF to describe the coupling between pressure and heat release rate. Some of the earliest models on this for annular gas turbines are Noiray et al. (2011) and Ghirardo and Juniper (2013). In addition to allowing the use of the FDF response, the effects of the model can often be studied directly from the equations, compared to the more involved Helmholtz solvers which are solving an eigenvalue problem. With the introduction of the quaternion formalism of Ghirardo and Bothien (2018), described briefly in §1.5.1, a new model based on this pressure description was developed (Ghirardo and Gant, 2019; Faure-Beaulieu and Noiray, 2020; Ghirardo and Gant, 2021). Using the quaternion formalism, the models open up the potential for the heat release rate to depend on the nature of the mode. It has also allowed the direct assessment of the effect of the nature angle on the mode. The new models also show that for increasing noise levels relative the amplitude of the mode, the mode is, in general, pushed away from the spinning states and towards the standing modes (Ghirardo and Gant, 2019, 2021; Faure-Beaulieu and Noiray, 2020).

All of the aforementioned models assume the FTF and FDF defined by axially perturbing a single flame setup are representative for an annular configuration. Due to a lack of well controlled experiments on full annular configurations for the full state space, it has been assumed that the heat release rate is not dependent on the nature of the azimuthal mode. Whether the mode is spinning in either direction, or the mode is standing, the response is assumed to be the same. For the pressure mode, it has been shown that the azimuthal acoustic mode might split the degenerate eigenvalues when the symmetry is broken (Hummel et al., 2016), leading to different growth rates of the acoustic mode (Bauerheim et al., 2015; Faure-Beaulieu and Noiray, 2020). This was taken into account by Faure-Beaulieu and Noiray (2020) in the case of a mean azimuthal flow in the system, showing it affects the acoustic mode of the system. However, this does not account for a direct nature angle dependence of the heat release rate. For that additional experimental, or modelling, results are required.

1.6 Research goals

The aim of the current work is to better understand flame describing functions in annular combustion chambers. The FDF, or the FTF, plays a defining role in determining the stability of a system when performing acoustic analysis, and it is of the utmost importance that the function is representative of the system. Currently, the functions used have been obtained on axially forced single flame setups, even when applied to predict the stability of a full annular combustor (Silva et al., 2013; Laera et al., 2017). It is currently unknown if these functions are directly applic-

able, and one of the objectives of this thesis is therefore to change that by studying the response of the flames in an annulus to well controlled azimuthal modes. To be able to study the difference compared to the response obtained in the conventional axially perturbed single flame systems, it is required to have a representative reference case from such a system. Therefore, an additional goal is to characterise the response of a single flame from the annular combustor when subjected to axial acoustic forcing.

The main objectives of this thesis are summarised in the following:

i) Obtain the FTF of an axially forced single flame setup which is representative of a single burner sector in the annular combustor.

ii) Extend the forcing technique of Worth et al. (2017) to be able to force an arbitrary mode of the first azimuthal order in an annular combustor.

iii) Study for the first time the potential dependence of heat release rate on the nature of the azimuthal mode.

1.7 Thesis outline

This thesis is organised as 6 chapters followed by 5 research articles. Chapter 1 is the current chapter, and gives an introduction to the field of thermoacoustic instabilities, with a focus on transverse instabilities. The experimental setups are presented in detail in Chapter 2, followed by an extensive description of the development of the azimuthal acoustic forcing in Chapter 3. Chapter 4 discusses the difference processing methods required for the data analysis performed in the articles included in this thesis. The articles are summarised in Chapter 5, and included in full length at the back of this thesis. The main conclusions are presented in Chapter 6, detailing how the aims and objectives of the project have been met.

Chapter 2

Experimental setups

Two different experimental setups have been used in the current work. The main experimental setup is the annular combustor developed by Worth and Dawson (2013b). A copy of the original rig was made at NTNU, with the original still located in Cambridge. The combustor is described in detail in §2.1. The second experimental setup is a single flame setup made to resemble a single sector in the annular setup, which is described in §2.2. This setup is used to obtain the response of an axially perturbed flame which is similar to the individual flames in the annular combustor. Both setups use similar imaging setups, described in §2.3, to measure the heat release rate.

2.1 Annular combustor

The annular combustor is presented schematically in Fig. 2.1. The plenum is fed with a perfectly premixed air-ethylene mixture through two impinging jets at the upstream end of the plenum. The air and fuel flow rates are controlled separately by Alicat mass flow controllers. The flow rate is chosen to match the required flow range, with a higher flow rate for the air supply compared to the fuel supply. The air and ethylene lines are merged in a T junction sufficiently upstream of the plenum to be considered perfectly premixed as the mixture enters the plenum. The impinging jets feeding the plenum further enhances the mixing and are beneficial for the flow distribution.

The plenum consists of a rapid expansion before a cylindrical section with diameter $212\,\mathrm{mm}$ and length $200\,\mathrm{mm}$. At the upstream end of the cylindrical section a perforated grid is inserted for flow conditioning, followed by a honeycomb flow straightener. The grid has a $5\,\mathrm{mm}$ centre to centre hole spacing, with either $2.7\,\mathrm{mm}$ or $3.0\,\mathrm{mm}$ holes (porosity $46\,\%$ and $57\,\%$ respectively). The downstream end of the plenum is terminated by the injector base plate, which has a centrally

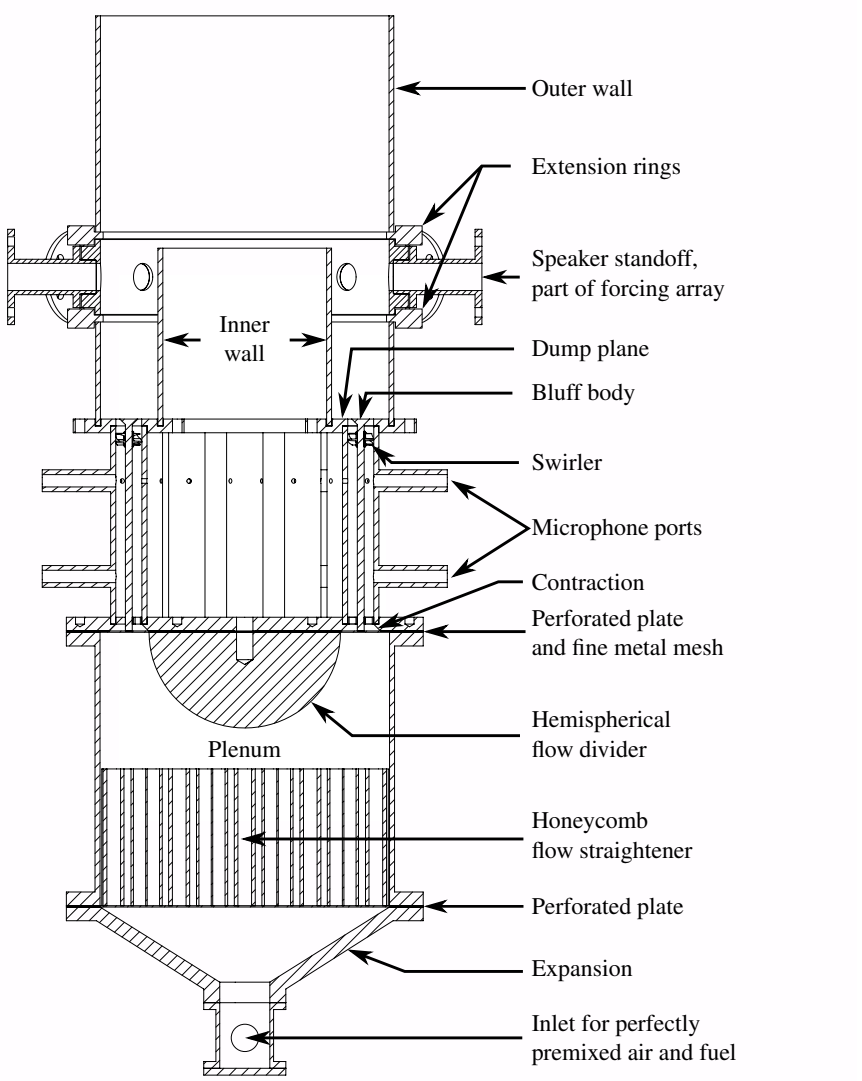

Figure 2.1: Schematic side view of the annular combustor, cut through the vertical centre line of the combustion chamber. The shown configuration, with $N = 12$ injectors and the newest forcing array raised above the dump plane, was used in Article IV.

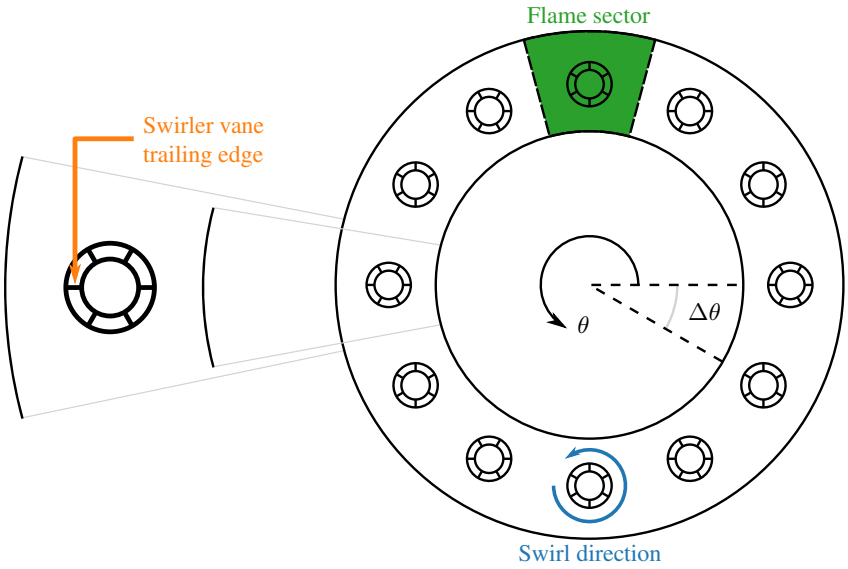

Figure 2.2: Downstream view of the dump plane of the annular combustion chamber. Each swirler is rotated to have a pair of swirler vane trailing edges aligned with the radial direction. The injectors are separated by $\Delta\theta = 2\pi/N$, and the flame sectors are defined to span an angle $\Delta\theta$, centred at the different injectors.

mounted hemispherical body of diameter $140\,\mathrm{mm}$ to enhance flow distribution. The injector base plate has machined chamfers on the upstream side to further aid smooth flow distribution to the injectors. An additional layer of perforated grids is mounted in the intersection between the plenum and the chamfered base plate. The upstream grid is made of the same material as the perforated plate in the bottom of the plenum with $3\,\mathrm{mm}$ holes, and the downstream grid is a fine square metal mesh ($0.1\,\mathrm{mm}$ wire, centre to centre distance $0.5\,\mathrm{mm}$, porosity $64\,\%$), both providing further flow conditioning. The N injectors are mounted equidistantly distributed along a circle of diameter $170\,\mathrm{mm}$ on the injector base plate. A set of rubber gaskets ensures the interface is not introducing gas leakages and accounts for small differences in injector tube lengths. Each injector tube has a centrally mounted bluff body with a nominally identical swirler attached, and this geometry will be described in detail in §2.1.1.

The injectors are held in place by a top retention plate, which also acts as the dump plane. Similar to the base plate, the retention plate has N equidistantly distributed holes arranged in a circle of diameter $170\,\mathrm{mm}$. A downstream view of the resulting dump plane is presented in Fig. 2.2. The injector holes are of the

same diameter as the inner diameter of the injector tube and have a sharp edge at the top and bottom, essentially extending the injector tubes by $5\,\mathrm{mm}$. The injector base plate and the retention plate are connected using threaded rods. Clamping pressure is applied from these rods, keeping the injectors securely in place.

The combustion chamber consists of the dump plane created by the retention plate and two concentric cylinders, which are used for the inner and outer wall. The stainless steel inner wall is $130\,\mathrm{mm}$ long and $129\,\mathrm{mm}$ in diameter. The diameter of the outer stainless steel wall is $212\,\mathrm{mm}$, and the length is approximately $300\,\mathrm{mm}$ depending slightly on the experiment. These scales are chosen to be consistent with the ones observed to give rise to unstable modes by Worth and Dawson (2013b). Even though this work focus on the azimuthally forced response of the combustor, the decision to follow these lengths was two-fold. First, the amplitude of the imposed pressure oscillations is higher with the relatively long outer wall, but to avoid exciting longitudinal modes the wall length was not extended further. Secondly, the inner wall length followed the one used by Worth and Dawson (2013b), providing better optical access to all the flames when imaging from above compared to matching the outer wall length.

The outer wall of the combustion chamber is constructed from a combination of a forcing array and extension tubes to make up the total length. Initially the forcing array was placed directly on the injector retention plate, with an extension ring and cylindrical duct on top to extend to the desired $300\,\mathrm{mm}$ length. This approach was first used by Worth et al. (2017), and then in Article II. The initial forcing array consisted of 8 standoff tubes, equidistantly distributed in the azimuthal direction. In this configuration the standoff tubes were centred $35\,\mathrm{mm}$ above the dump plane, and each standoff tube is $105\,\mathrm{mm}$ long.

The first forcing array was manufactured by welding standoff tubes to section of $2\,\mathrm{mm}$ thick stainless steel tube. This resulted in a deformation of the cylindrical shape, and the standoff tubes were not fully equidistantly distributed and not perfectly radially oriented. Therefore, a precision machined forcing array was produced from a much thicker piece of stainless steel to improve the ease of forcing. The new forcing array also consisted of 8 standoffs, but a shorter standoff length of $68\,\mathrm{mm}$ was chosen to be able to fine tune the length with spacers if required. The new forcing array also ensured all the standoff tubes were equidistantly distributed and pointing radially to the center, removing one complicating factor of the forcing setup. Additionally, to avoid any potential direct interaction between the forcing array and the flames, the forcing array was raised by inserting an extension tube below the forcing array in addition to the top section. This brought the centre of the standoffs approximately $104\,\mathrm{mm}$ above the dump plane, and the total outer wall length to $287\,\mathrm{mm}$. An example of this setup is shown in Fig. 2.3, with the lower extension piece replaced by glass for optical accessibility. The glass was not

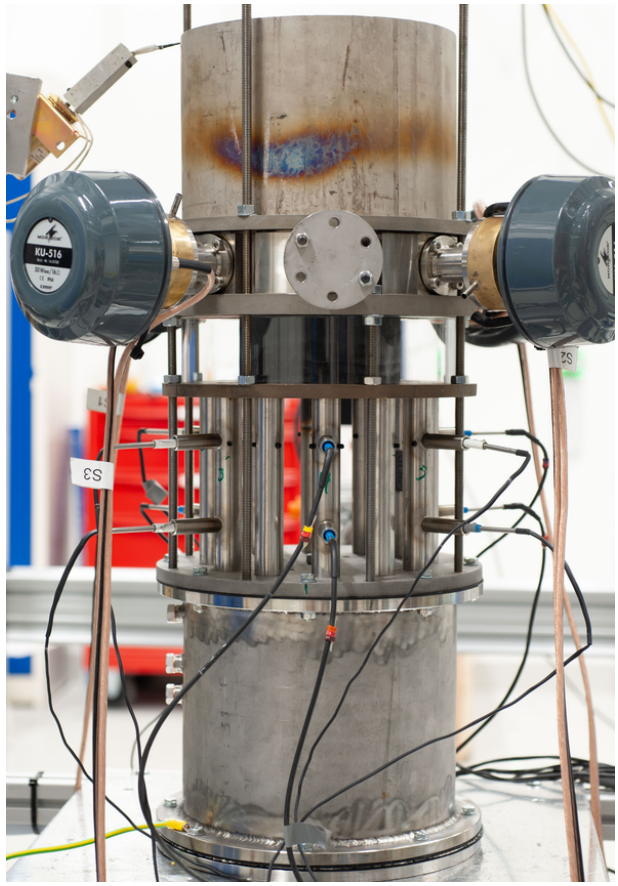

Figure 2.3: Annular combustor with the new forcing array mounted. Note the glass section was exchanged for a stainless steel section in the current work.

Table 2.1: Overview of the annular combustor configurations studied in the different articles included at the end of this thesis.

Parameter	*Article II*	*Article III*	*Article IV*	*Article V*
Fuel	C_2H_4	C_2H_4	C_2H_4	C_2H_4
Forced	Yes	No	Yes	No
Swirlers	Yes	No	Yes	Yes
No. injectors	18	12	12	18
Bulk velocity	$20\,\mathrm{m/s}$	$18 - 21\,\mathrm{m/s}$	$18\,\mathrm{m/s}$	$20\,\mathrm{m/s}$
Equivalence ratio	0.75	$0.85 - 1.00$	0.70	0.75

used for any experiments in the current work. A short overview of the different configurations used in the current work is presented in Tab. 2.1.

Both iterations of the forcing array were populated by four Adastra HD60 horn drivers, and later by Monacor KU-516 horn drivers due to a lack of Adastra HD60 stock. The horn drivers are powered by a pair of QTX PRO1000 power amplifiers, with a signal produced by an Aim-TTi TGA1244 four channel signal generator. How these components are used to set up the azimuthal pressure mode is described in detail in §3.2.

2.1.1 Injectors

The injector tubes used in the annular setup are shown schematically in Fig. 2.4a. Each injector tube is $145\,\mathrm{mm}$ long and has an internal diameter of $19\,\mathrm{mm}$ above the top microphone port and an internal diameter of $18\,\mathrm{mm}$ elsewhere. A bluff body of final diameter of $13\,\mathrm{mm}$ and half angle $45°$ is mounted concentrically in the injector. It is mounted to be flush with the dump plane of the combustor, giving an injector exit blockage of approximately $47\,\%$. To be able to centre the bluff body, it is mounted to a $5\,\mathrm{mm}$ diameter rod, spanning the whole length of the injector. A six vane swirler, shown in Fig. 2.4b, with a trailing edge angle of $60°$ to the axial direction is affixed to the central rod. The distance between the trailing edge of the swirler and the dump plane is chosen to be $10\,\mathrm{mm}$, providing a strong ACW swirl when viewed from downstream. Geometrically the swirl number before the contraction caused by the bluff body is 1.22 (Worth and Dawson, 2013a). The actual swirl value has been measured to be 0.65 a distance of $10\,\mathrm{mm}$ downstream of the dump plane in an unconfined setup. The swirlers are mounted in the injector tubes such that two of the swirler vane trailing edges are pointing radially towards the center of the annulus, as illustrated in Fig. 2.2. This is done in an effort to not break the discrete rotational symmetry of the combustor.

The bluff body and the swirler are centred in the tube by a webbed insert in

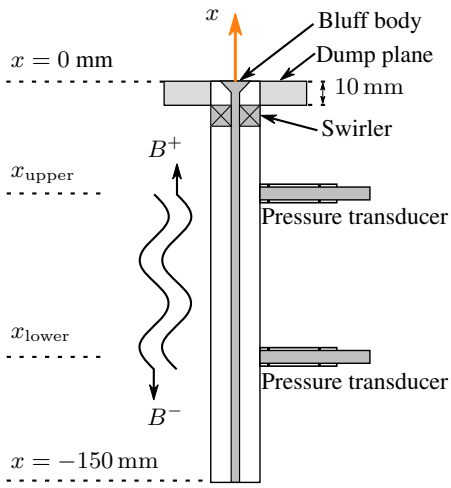

(a) Injector with microphone ports.

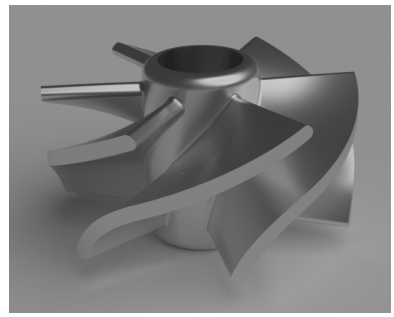

(b) Rendered swirler.

Figure 2.4: Simplified schematics of an injector tube with microphone ports (a) and a rendering of the swirler design (b) used in each injector. The acoustic mode in the injector tube is characterised by two components B_+ and B_- propagating with and against the flow direction respectively.

the bottom of the tube and three M4 grub screws at the same axial location as the upper microphone port. These grub screws have been observed to create convective perturbations by Æsøy et al. (2020), but due to the swirler downstream it is assumed the effect is small compared to the effect of the swirler, which is shown to be the case in Article I. The choice of three grub screws ensures the bluff body assembly is securely fastened, while also providing the opportunity to fine tune the centring. However, in ideal circumstances the grub screws should be of a smaller diameter to reduce any potential effect on the response.

There are two injector tube designs, as shown in Fig. 2.3. The first design is the one shown in Fig. 2.4a with two microphone ports, and the second design is exactly the same except the microphone ports are removed. The two microphone ports on the instrumented injectors are spatially separated by approximately $65\,\mathrm{mm}$ in the axial direction, providing two locations to measure the pressure fluctuations. The instrumented injectors have a pair of Kulite XCS-093-0.35D differential pressure transducers mounted flush with the inner wall. The transducers are mounted in a plastic tube and O-rings to provide a seal and to electrically insulate the transducers from the rest of the combustor and reduce vibrations. The electrical signals from the transducers are amplified by a pair of Fylde FE-579-TA bridge amplifiers. The amplified signals are then digitised by a set of NI-9234 24-bit DAQ modules. The

DAQ modules are sampling the data at the full $51.2\,\mathrm{kHz}$ sampling rate, well above the Nyquist frequency of the frequencies of interest. The same system is also used to sample the forcing signal from the signal generator, which is used for cross power spectrum analysis in some cases.

2.2 Single sector

The single sector setup, shown schematically in Fig. 2.5b, is made to resemble a single flame in the annular setup described above and they thus share several features. The plenum is fed by the same air-fuel system feeding the annular combustor, and the perfectly premixed air-fuel mixture enters the plenum through two impinging jets. After an expansion a honeycomb grid is used to straighten the flow inside the plenum. The cylindrical part of the plenum is $200\,\mathrm{mm}$ long and has an inner diameter of $94\,\mathrm{mm}$. A set of $60\,\mathrm{mm}$ long speaker standoff tubes is mounted to the middle of the cylindrical plenum section, each with a horn driver mounted as a speaker. The horn drivers are used to impose axial acoustic velocity perturbations with the technique described in §3.1, using the same equipment as the annular forcing array. In the downstream end of the cylindrical plenum section the flow is contracted by a conic section, which is similar to the upstream expansion. A similar perforated plate to the one used in the annular combustor is used for flow conditioning in the upstream end of the injector.

Downstream of the plenum one of the instrumented injectors from the annular combustor is mounted, kept in place by compression through a similar retention plate to the annular combustor. The top of the retention plate is again forming the dump plane of the combustion chamber, with the bluff body flush mounted with the dump plane. The combustion chamber is chosen to have a square cross section of $41\,\mathrm{mm} \times 41\,\mathrm{mm}$ with a height of $50\,\mathrm{mm}$. The square cross section is chosen over a circular cross section as a single flame sector in the annulus has a cross section which is closer to a square than a circle. The dimensions of $41\,\mathrm{mm} \times 41\,\mathrm{mm}$ is chosen to be similar to the inner to outer wall distance of $41.5\,\mathrm{mm}$ in the annular combustor. It is also close to the $44.5\,\mathrm{mm}$ arc length between burner centres in the $N = 12$ injectors configuration of the annular combustor. The square combustion chamber is constructed from four separate flat pieces of quartz glass. They are kept in place by a machined track in the injector retention plate at the bottom, and a top plate with a similar track, and a square hole of matching dimensions on top. A layer of Insulfrax ceramic wool between the injector retention plate and the quartz walls provides slight cushioning and accounts for thermal expansion of the quartz walls. No insulation was placed on top of the walls to prevent the insulation from slowly burning away in the presence of a flame. The $50\,\mathrm{mm}$ height of the combustion chamber is chosen to ensure the flames did not become thermoacoustically

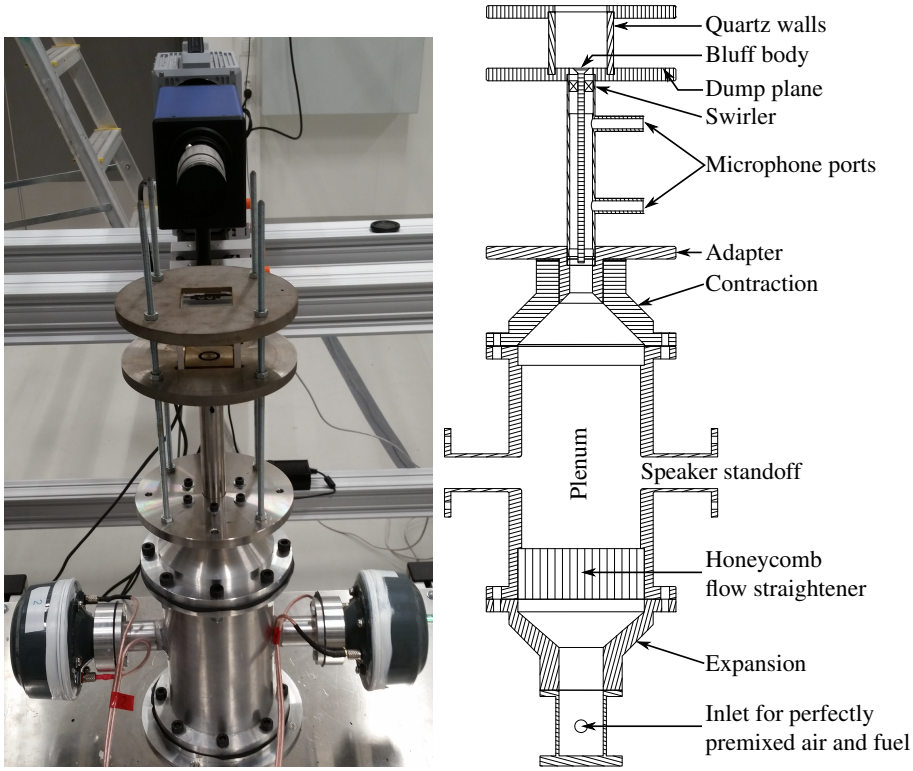

(a) Setup with front camera.

(b) Schematic side view.

Figure 2.5: Single sector setup with the front facing camera (a) and the schematic side view (b). The blue box in front in (a) is an Intensified Relay Optics (IRO) unit attached to the front of the high speed camera.

Table 2.2: Overview of the parameters for the single flame study in *Article I*.

Parameter	*Article I*
Fuel	C_2H_4
Frequencies	$50 - 2000\,\mathrm{Hz}$
Bulk velocity	$12 - 20\,\mathrm{m/s}$
Equivalence ratio	$0.6 - 1.0$
Combustion chamber	$41 \times 41 \times 50\,\mathrm{mm}$

unstable for any of the operating conditions considered. While the combustion chamber height is $50\,\mathrm{mm}$ the optical access from the side is restricted to $40\,\mathrm{mm}$ due to the construction of the top plate. The parameter combinations investigated in the single sector setup are summarised in Tab. 2.2.

2.3 Heat release rate measurements

The heat release rate is obtained by measuring the intensity of light corresponding to OH* radicals de-exciting. Perfectly premixed flames have been observed to excite a concentration of OH* radicals proportional to the heat release rate (Higgins et al., 2001; Hardalupas and Orain, 2004; Balachandran et al., 2005). This process is called OH* chemiluminescence, and the wavelength of the de-exciting OH* radicals is close to $305\,\mathrm{nm}$ (Higgins et al., 2001), corresponding to the ultraviolet part of the spectrum.

The light intensity from the OH* chemiluminescence is measured by a either a Phantom V2012 high speed camera equipped with a LaVision Intensified Relay Optics (IRO) unit, or by a Photron Fastcam SA1.1 high speed camera connected to the same IRO model. Due to the short wavelength of the light a UV specific Cerco 2178 lens is mounted to the IRO. To ensure only the light from the chemiluminescence is captured an narrow band-pass filter (centre wavelength $310\,\mathrm{nm}$, full width half maximum $10\,\mathrm{nm}$) is placed in front of the lens. The imaging system is operating at a sampling rate of $10\,\mathrm{kHz}$. Due to the low light intensity and low exposure time the IRO is required to amplify the light intensity for the camera.

The single sector rig has optical access both horizontally and vertically from downstream of the combustion chamber. Therefore, one camera is set up with the lens level with the middle of the $40\,\mathrm{mm}$ optical gap to capture the side view of the flame. Another camera is placed higher than the combustion chamber, but still level with the horizon. A first surface mirror, either regular (Edmund Optics $102 \times 127\,\mathrm{mm}$, 4-6$\lambda$) or UV enhanced (Edmund Optics $100 \times 100\,\mathrm{mm}$, $\lambda/4$), is placed directly above the flame and in the line of sight of the camera. The mirror is angled

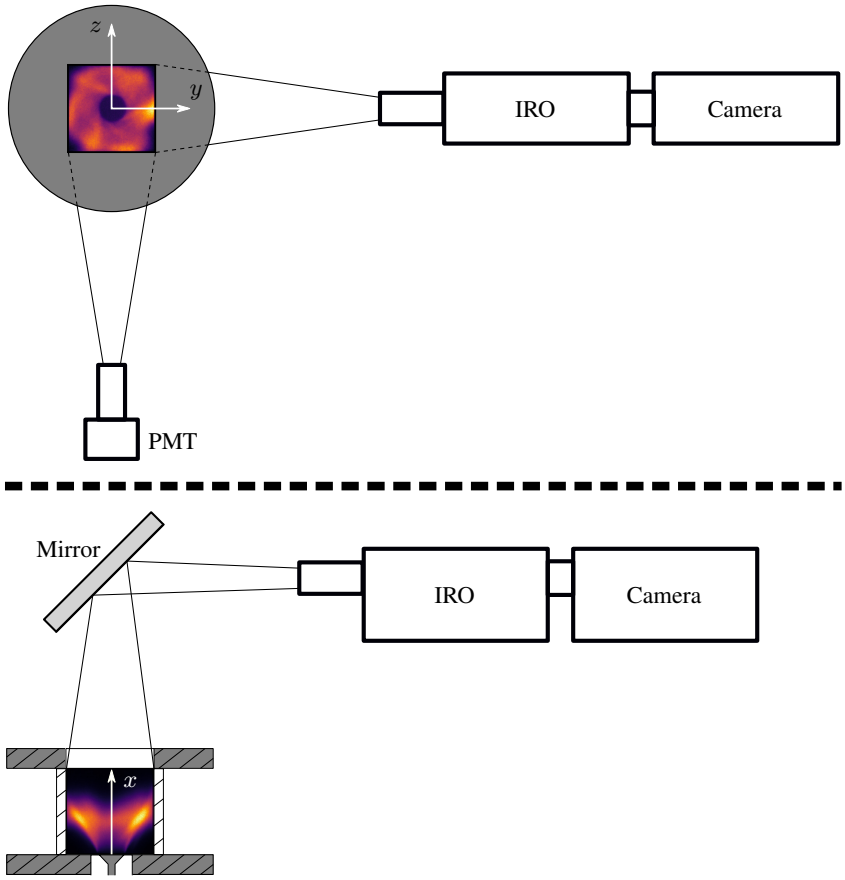

Figure 2.6: Imaging setup for the single sector rig, with both side (*top*) and overhead (*bottom*) imaging. The PMT and side camera is pointing directly at the combustion chamber, while the overhead view is achieved through using a first surface mirror at a 45° angle. Note all dimensions are not to scale to keep the figure relatively compact.

45° with the horizon, providing a view of the flame for the camera and minimal distortion of the image. The full camera setup is shown schematically in Fig. 2.6. To ensure the mirror is not damaged by the temperature of the exhaust gas, a set of air jets was pointing at the surface of the mirror. This provides both direct cooling to the mirror, while also creating an air barrier between the hot exhaust gases and the mirror surface. The distance between the combustion chamber, mirror and camera is adjusted to obtain the desired resolution of the setup while ensuring all the relevant areas are in frame.

Additionally a photomultiplier tube (PMT) is used to measure the OH* chemiluminescence for the single sector rig. The PMT integrates all the the light in its field of view, which is chosen to be larger than the flame to ensure the heat release rate from the entire flame is captured. Similar to the first camera, the PMT is pointed directly at the flame from the side, as illustrated in Fig. 2.6. The PMT is a Hamamatsu H11902-113, and it is amplified by a Hamamatsu C7169 amplifier. The same band-pass optical filter used on the cameras is inserted before the PMT to ensure only the desired wavelengths of light are captured. Compared to the cameras, the PMT creates a continuous signal, which is digitised on the same NI-9234 24-bit DAQ modules as the pressure signals. This ensures the heat release rate measurements and pressure measurements are perfectly synchronised. The sampled signal from the PMT was compared to the numerically integrated response from the cameras to ensure both captured the same region of heat release rate. Good quantitative agreement between the PMT and camera setups was observed.

The annular setup does not have optical access from the side of the combustion chamber in the configuration used in this work, only from the downstream direction. The same setup as the overhead view on the single sector rig is used to obtain the heat release rate of the annular combustor. Instead of centring the mirror on a single flame, the mirror is centred in the centre of the concentric combustion chamber walls, as shown schematically in Fig. 2.7. The inner wall will block some of the light close to the inner wall in this configuration. To reduce the effect of this the the inner wall is kept as short as possible at $130\,\mathrm{mm}$. This placement of the mirror is considered the most beneficial due to the additional processing described in §4.6 and §4.7 made possible by the central view. Due to the larger dimensions of the combustion chamber the mirror is located further downstream of the dump plane to be able to fit the whole combustion chamber in frame.

The different studies used different techniques for spatial calibration of the camera. In the single sector study in Article I, the combustion chamber was centred in the frame and it was relatively small. Due to the low distortion and optical arrangement, a simple linear scaling was applied to dimension the images. The two first azimuthal studies, Article II and Article III, were spatially calibrated using

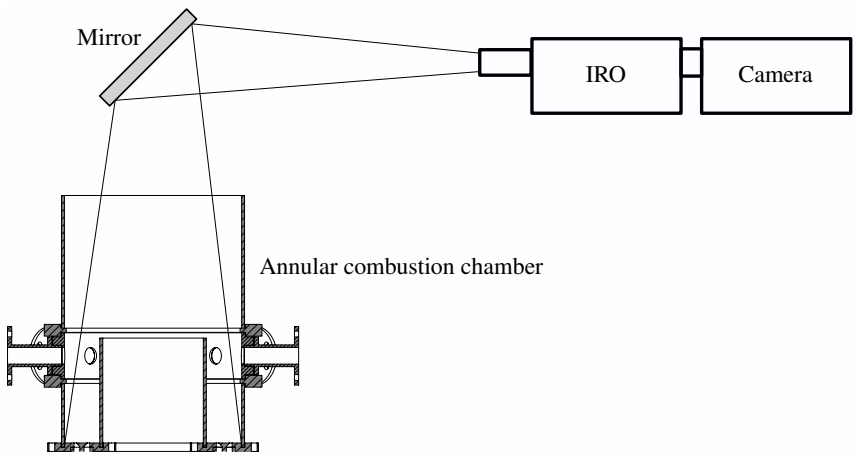

Figure 2.7: Overhead imaging setup for the annular combustor, with first surface mirror. Note all dimensions are not to scale to keep the figure relatively compact.

the inner combustor wall as a reference length scale. Minor distortion was caused by having a mirror slightly off from the ideal angle of $45°$, and the images were stretched to fix the aspect ratio. Finally, in Article IV a $200\,\mathrm{mm} \times 200\,\mathrm{mm}$ double layer calibration plate was imaged, and a spatial correction was applied by LaVision's DaVis software.

2.3.1 Synchronisation

The camera system and the DAQ system, sampling the pressure and PMT signals, operate independently. To be able to relate the measured pressure to the images obtained from the cameras, the two sampling systems are synchronised after the data have been acquired. The IRO is provided an external trigger signal to open the gate for each image, which is either in a high ($5\,\mathrm{V}$) or a low ($0\,\mathrm{V}$) state. The recorded trigger signal therefore corresponds to the start of the exposure of each image, which is used for synchronisation. This signal is lengthened and then sampled by the DAQ system used for the rest of the signals. The signal lengthening is required to ensure the trigger signal is captured for each frame, as the raw trigger signal is shorter than the time delta between two consecutive samples on the $51.2\,\mathrm{kHz}$ DAQ system. The signal is lengthened to span half the time delta between two consecutive frames using the Aim-TTi TGA1244 signal generator also used for the acoustic forcing.

The synchronisation between the images and the camera is obtained by fitting the measured trigger time series to the known shape of the trigger signal from the signal generator, using a least squares method. An example of this is shown

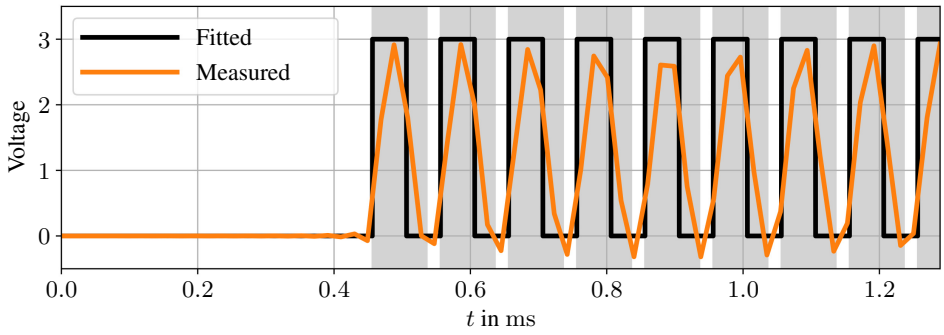

Figure 2.8: Example of the sampled and the reconstructed camera trigger signal. The IRO is activated when the trigger signal rises, and it kept open for a given duration. The IRO is active for $80\,\mu s$ for each exposure in this example, illustrated by the shaded regions.

in Fig. 2.8. The measured trigger signal, shown in orange, is observed to not have a perfect pulse train shape and the amplitude is lower than the expected $5\,V$. This difference is however not observed when the trigger signal is monitored on an oscilloscope. The effect is caused by the digitising method in the NI DAQ system in combination with the rapidly changing trigger signal, which switches state from high to low to high again in approximately 5 samples. The amplitude difference is accounted for by setting a lower amplitude for the theoretical signal. The synchronisation between the actual and measured triggers is found by using a least squares solver to minimize the difference between the two signals. The IRO is active for a chosen time delta for each exposure, as illustrated by the shaded regions in Fig. 2.8, and the camera is effectively averaging the heat release rate over this time delta. Therefore, the image time is considered to be in the middle of this interval.

Chapter 3

Development and application of azimuthal acoustic forcing

A common approach to obtain the transfer and describing functions of turbulent flames is to impose acoustic perturbations by some form of speakers, as described in §1.2.1. Here the axial forcing approach is used to obtain the conventional flame transfer functions. Due to the widespread use of the technique, and the relatively simple nature of it compared to the annular forcing, the strategy used in this work is explained relatively briefly in §3.1. The annular forcing technique used to obtain arbitrary azimuthal modes of the first order is however much more novel, with a successful strategy for annular combustors under reactive conditions developed for the first time in the current work. The full procedure is therefore presented in detail in §3.2, along with some observations from the development process.

3.1 Axial forcing

The schematic of the single flame setup is presented in Fig. 2.5b. The combustion chamber is chosen to be sufficiently short to make the geometry thermoacoustically stable for all the operating conditions of interest, which is important to ensure good control over the acoustic mode. Similar to previous studies (Balachandran et al., 2005; Worth and Dawson, 2012), both speakers mounted on the plenum section are driven in phase, creating an in phase push and pull motion on the flow. This results in an acoustic mode, where the mode amplitude in the injector tube depends on the geometry of the setup and the forcing frequency. Some frequencies are more damped than others, giving rise to different perturbation amplitudes for the same electric power provided to the speakers. The injector tube is open to the atmosphere, resulting in an acoustic mode with an acoustic velocity anti-node

located close to the injector exit, where the flame is anchored.

To obtain the FTF, or the FDF, it is important to set the amplitude of the acoustic axial velocity perturbations to a fixed value at the dump plane location. Due to the frequency dependent damping of the combined plenum and injector geometry, the voltage sent to the speakers has to be tuned for each frequency. For a given frequency the tuning is performed by setting an initial speaker voltage and calculating the velocity amplitude at the dump plane based on the upstream pressure measurements, and then adjusting the voltage based on this. Fortunately, the horn drivers used in the current study have a response that leads to a very close to linear relationship between the speaker voltage and the axial velocity amplitude at the dump plane. This is true from zero voltage and up to the limit of the speakers, meaning an iterative approach to finding the voltage is converging fast, usually within a couple of iterations. After the amplitude is set, the data is sampled for the desired time interval before moving to the next frequency of interest.

The sampling time for this data was usually $10\,\mathrm{s}$ in the current work, resulting in the manual amplitude tuning being the most time consuming part. An automatic program, which changes frequency, tunes the amplitude and samples the data was developed to greatly increase the efficiency of obtaining the transfer functions. The program was made possible by the ability to adjust the signal generator (Aim-TTi TGA1244) through serial communication. The main logic of the LabVIEW program is described in the following:

- Create a list of frequencies.
- For each frequency:
  - Set frequency on signal generator.
  - Tune amplitude:
    - Set initial voltage and take a short sample of the pressure signals.
    - Calculate current perturbation amplitude based on sampled signals.
    - Calculate the new voltage to obtain desired amplitude.
    - Set the new voltage and take a new sample.
    - Calculate the current perturbation amplitude. If the amplitude is not the desired amplitude, repeat the steps above until it is.
  - Sample the data for the desired length of time.

This made it possible to obtain a transfer function with 40 points in approximately 10 minutes, making it feasible to investigate a large range of operating conditions quickly. A live update of the transfer function was added later, enabling direct assessment of which frequencies to investigate further.

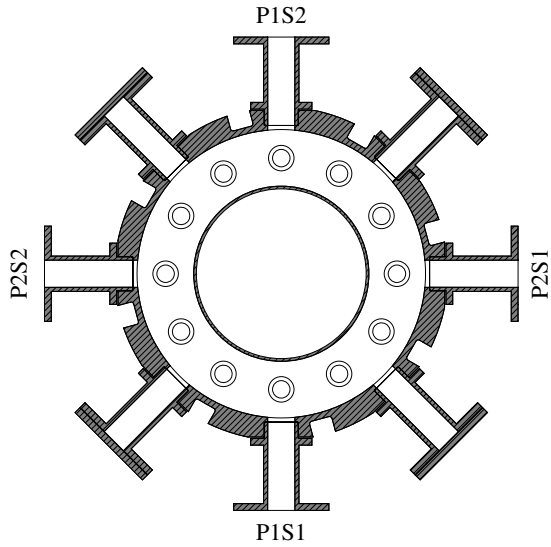

Figure 3.1: Schematic presentation of the forcing array. The four speakers are divided into pairs (P1 and P2), each consisting of two speakers (S1 and S2). The four remaining standoff tubes are blocked at the outer end.

3.2 Azimuthal forcing

Setting up azimuthal modes is a more complicated process compared to setting up the axial perturbations in the single sector setup. More speakers are required to set up well controlled modes, and it is highly dependent on how the different speakers are driven in relation to each other. Additionally, the temperature in the combustion chamber, the effect of the flames on the acoustic mode, the self-excited nature of the combustor all have to be accounted for. This will be discussed in more detail in §3.2.2 and subsequent subsections. However, an ideal case with perfect geometry and perfect electrical components is considered first.

The forcing array and annular combustor are presented in detail in §2.1. Additionally, the geometry created by the forcing array and inner wall is shown schematically in Fig. 3.1. There are eight equidistantly placed speaker standoff tubes, where every other is populated by a speaker and the rest are blocked off on the outer end by a solid stainless steel plate. The decision to make eight speaker tubes was to ensure enough speakers could be mounted to control the mode well, which was an unknown number in the beginning, and to ensure a sufficiently high amplitude could be achieved. The choice of not populating every standoff tube with a speaker was later made as a compromise between the ease of tuning and hav-

ing good control of the mode. The four equidistantly spaced speakers form two speaker pairs, where the two speakers in each pair are located diametrically opposite to each other. The two speakers in a pair are driven π out of phase, achieved by providing the same signal to both speakers while reversing the polarity for one speaker. Then the two speakers in a pair are pushing and pulling in the same direction. Since the speaker standoff tubes point in the radial direction, the velocity and and pressure perturbations are distributed in the ACW and CW direction as the perturbations impinge on the inner wall, resulting in an azimuthal mode shape. For a perfect geometry this will result in a perfectly standing mode, where the amplitude of both components is equal. This could also be theoretically achieved by a single speaker, but in practice it would introduce an unwanted asymmetry and lower the amplitude. Both speaker pairs are setting up independent standing modes, where the pressure anti-nodes are located at the speaker locations. Worth et al. (2017) have shown this for a single speaker pair, setting up perfectly standing modes. In the following the nature of the resulting azimuthal mode will be shown to depend on the phase between the driving of the two speaker pairs.

3.2.1 Theoretical considerations

The acoustic modes are linear in nature, which enables the description of the total pressure distribution as a super position of the azimuthal modes set up by the speaker pairs. Temporarily relaxing the assumption that the mode set up by each speaker pair is a standing azimuthal mode, the mode can be described as a general azimuthal mode of the form introduced later in Eq. (4.23). The first speaker pair is then assumed to be at $\theta = 0$ for simplicity, and the second pair is located at $\theta = \theta_\mathrm{p}$. Then the independent pressure modes set up by first ($p'_{1,\mathrm{a}}$) and second ($p'_{2,\mathrm{a}}$) pair are given by

$$p'_{1,\mathrm{a}}(\theta,t) = \left[A_{+,1}\exp\left(-\mathrm{i}\theta\right) + A_{-,1}\exp\left(\mathrm{i}\theta\right)\right]\exp\left(\mathrm{i}(\omega t - \phi_\mathrm{sg})\right), \tag{3.1a}$$

$$p'_{2,\mathrm{a}}(\theta,t) = \left[A_{+,2}\exp\left(-\mathrm{i}(\theta+\theta_\mathrm{p})\right) + A_{-,2}\exp\left(\mathrm{i}(\theta+\theta_\mathrm{p})\right)\right]\exp\left(\mathrm{i}\omega t\right), \tag{3.1b}$$

where ϕ_sg is the temporal phase difference between the second and first horn driver pair set up by the signal generator. The spatial phase offset θ_p for the second pair is due to the physical location of the two speaker pairs.

Since each speaker pair is setting up a standing mode, the magnitude of the two amplitudes are assumed to be equal ($|A_{+,i}| = |A_{-,i}|$). Due to how the mode is set up, the two amplitudes $A_{\pm,i}$ are assumed to be the complex conjugate of each other. For simplicity the phase is chosen to be zero, making the amplitudes $A_{\pm,i}$ real valued. A further simplification is to assume all the amplitudes are equal

$$A_{+,1} = A_{-,1} = A_{+,2} = A_{-,2} = \frac{A^{\perp}_{\mathrm{pair}}}{\sqrt{2}}\,. \tag{3.2}$$

The superposition of the two components in Eq. (3.1) is then given by

$$\begin{aligned}\frac{p'_{\mathrm{a}}(\theta,t)}{\sqrt{2}A^{\perp}_{\mathrm{pair}}\exp\left(\mathrm{i}\omega t\right)} = &\cos\left(\frac{1}{2}(\theta_{\mathrm{p}}-\phi_{\mathrm{sg}})\right)\exp\left(-\frac{\mathrm{i}}{2}(2\theta+\theta_{\mathrm{p}}+\phi_{\mathrm{sg}})\right)+\\ &\cos\left(\frac{1}{2}(\theta_{\mathrm{p}}+\phi_{\mathrm{sg}})\right)\exp\left(+\frac{\mathrm{i}}{2}(2\theta+\theta_{\mathrm{p}}-\phi_{\mathrm{sg}})\right).\end{aligned} \tag{3.3}$$

This corresponds to two plane waves propagating in opposite directions, where the relative amplitudes are determined by the cosine terms. The nature angle χ, defined later in Eq. (4.29), of the mode in Eq. (3.3) is given by

$$\tan\left(\chi\right) = \frac{\left|\cos\left(\frac{1}{2}(\theta_{\mathrm{p}}-\phi_{\mathrm{sg}})\right)\right| - \left|\cos\left(\frac{1}{2}(\theta_{\mathrm{p}}+\phi_{\mathrm{sg}})\right)\right|}{\left|\cos\left(\frac{1}{2}(\theta_{\mathrm{p}}-\phi_{\mathrm{sg}})\right)\right| + \left|\cos\left(\frac{1}{2}(\theta_{\mathrm{p}}+\phi_{\mathrm{sg}})\right)\right|}. \tag{3.4}$$

The total acoustic amplitude of the mode is given by

$$A^{\perp}_{\mathrm{imposed}} = A^{\perp}_{\mathrm{pair}}\sqrt{2(1+\cos\left(\theta_{\mathrm{p}}\right)\cos\left(\phi_{\mathrm{sg}}\right))}, \tag{3.5}$$

highlighting the advantage of using two diametrically opposite speakers ($\theta_{\mathrm{p}} = \pi$) in opposite phase ($\phi_{\mathrm{sg}} = \pi$) as a pair, due to factor 2 amplitude increase compared to using a single speaker ($A^{\perp}_{\mathrm{imposed}} = 2A^{\perp}_{\mathrm{pair}}$). Equation (3.4) also indicates the diametrically opposite speakers operating at the same level can only create a standing mode, where the amplitude is given by Eq. (3.5) with $\theta_{\mathrm{p}} = \pi$.

The even number of speakers are therefore always chosen to be distributed equidistantly in the azimuthal direction, with a physical azimuthal phase difference $\theta_{\mathrm{p}} = \pi/2$. Then modes of all possible nature angles ($-\pi/4 \leq \chi \leq \pi/4$) can be set up, and the nature angle expression in Eq. (3.4) reduces to

$$2\chi = \begin{cases}\phi_{\mathrm{sg}} - \pi & \text{for} \quad -\pi \leq \phi_{\mathrm{sg}} < -\pi/2\\ \phi_{\mathrm{sg}} & \text{for} \quad -\pi/2 \leq \phi_{\mathrm{sg}} \leq \pi/2\\ \pi - \phi_{\mathrm{sg}} & \text{for} \quad \pi/2 < \phi_{\mathrm{sg}} \leq \pi\end{cases}. \tag{3.6}$$

This is illustrated in Fig. 3.2 for all the unique signal generator phase offsets ϕ_{sg}. Outside the range $|\phi_{\mathrm{sg}}| < \pi/2$ the anti-node location of the pressure mode is rotated by an angle $\pi/2$. The choice of $\theta_{\mathrm{p}} = \pi/2$ also results in a constant total acoustic amplitude for all signal generator phase offsets ϕ_{sg}

$$A^{\perp}_{\mathrm{imposed}} = \sqrt{2}A^{\perp}_{\mathrm{pair}}, \tag{3.7}$$

at the expense of a slightly lower peak amplitude for predominantly standing modes. Since the nature angle of the mode is solely determined by the signal generator phase offset ϕ_{sg}, the amplitude of the mode is independent of the nature angle for a given speaker pair amplitude $A^{\perp}_{\mathrm{pair}}$.

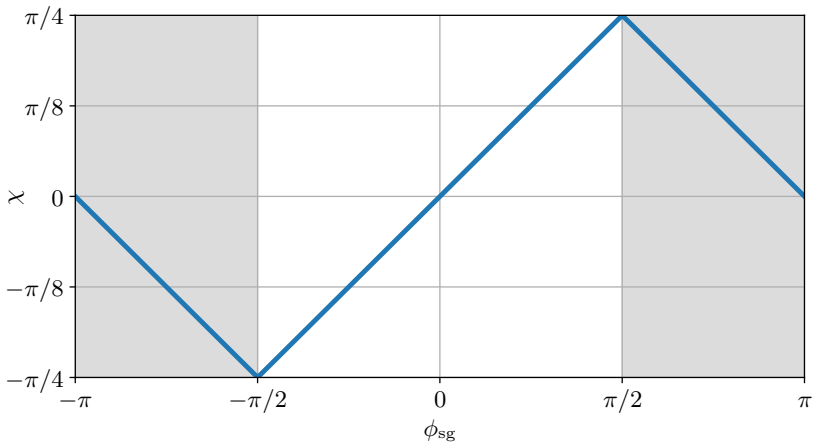

Figure 3.2: Relation between the signal generator phase offset ϕ_{sg} and the nature angle χ of the pressure mode in an ideal case. The two speaker pairs are separated by an azimuthal angle $\theta_{\mathrm{p}} = \pi/2$.

3.2.2 Thermoacoustic stability and thermal equilibrium

To be able to impose the acoustic mode the combustion geometry has to be thermoacoustically stable. Single flame studies with axial forcing usually achieve this by choosing an enclosure that is sufficiently short to not excite axial modes. However, the relevant length scale for azimuthal modes in an annular combustor is the azimuthal length of the combustion chamber, which is not easy to change. Instead the operating condition has to be chosen carefully to ensure the combustor is thermoacoustically stable. For the two configurations used in the current work this is achieved by having a sufficiently low equivalence ratio, with equivalence ratio 0.75 and 0.70 in Article II and Article IV respectively.

Another difference between the single sector forcing and the azimuthal forcing is the choice of excitation frequencies. While the single sector can be excited at a range of frequencies, the azimuthal forcing frequency is determined by the geometry for a given operating condition. The design of the combustion chamber and forcing array makes it impossible to achieve a total thermal equilibrium, as the speakers and rig are not able to survive the thermal equilibrium temperature. Therefore, the experimental data has to be obtained before the combustor has achieved a total thermal equilibrium, as in previous work (Worth and Dawson, 2013a,b; Dawson and Worth, 2014). While the frequency is mainly determined from the geometry and the flame temperature, the heating of the combustion chamber introduces a slight time dependence on the forcing frequency. In practice this results in a time dependence on the amplitude for a given forcing frequency, as il-

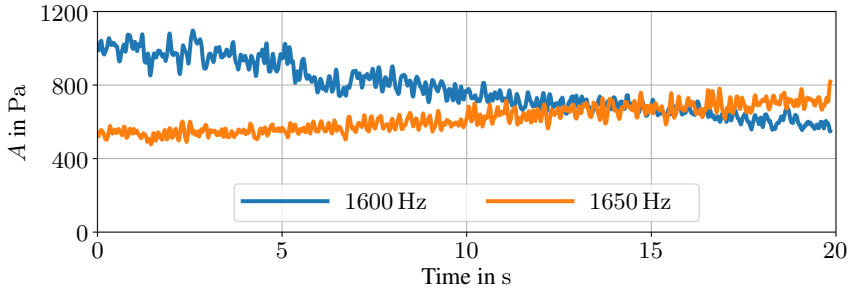

Figure 3.3: Example of the time dependence of the forcing amplitude in the annular combustor. The combustor is ignited approximately at the start of the time series, and the power supplied to the speakers is kept constant in time. The drift in the amplitude is caused by the increasing temperature of the combustion chamber. Note a moving average with a $62.5\,\mathrm{ms}$ window has been applied to the data.

lustrated in Fig. 3.3. To simplify the process of setting up a well controlled mode, and to achieve a mode which is as constant in time as possible during the sampling interval, the frequency is chosen such that the amplitude saturates slightly before the data acquisition is started. In the example in Fig. 3.3, this corresponds to the $1650\,\mathrm{Hz}$ case, even though the maximum amplitude is slightly lower and slightly off the resonant frequency. This is chosen to yield better control, and is consistent with the observations of Worth et al. (2017).

3.2.3 Monitoring the mode

The initial approach to setting up the desired azimuthal mode in the combustion chamber was to set the amplitudes and signal generator phase offsets ϕ_{sg} with the combustor turned off. In this case the assumptions in Eq. (3.3) are relatively good, and an arbitrary azimuthal mode can easily be set up using Eq. (3.6) and Eq. (3.7). In theory only the frequency needs to be changed when the combustor is ignited to account for the higher temperature. However, this approach was observed to not necessarily yield the desired mode when the combustor was turned on. The amplitude changed significantly, and more importantly the nature of the mode was also changed. Nevertheless standing modes were relatively easy to set up, but obtaining highly spinning modes proved to be hard using this approach.

To be able to impose well controlled spinning modes a constant monitoring of the mode was deemed to be required and essential. Therefore the logging program was expanded and developed to also perform near real-time post processing of the acquired pressure signals. The most important parameter to monitor is the nature of the mode, meaning the pressure measurements do not need to be propagated to

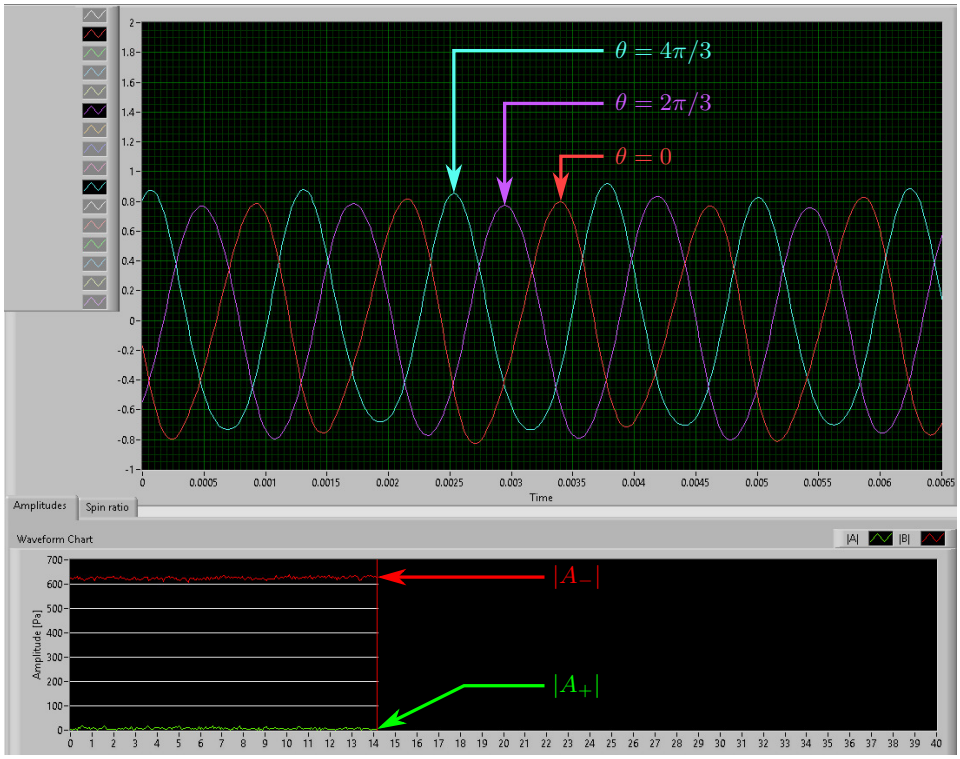

Figure 3.4: An example screenshot from the annular forcing program with additional annotations. In the top part the latest sample points are presented, while the bottom part displays the magnitude of the two azimuthal acoustic wave components in near real-time. In the current example the mode is a highly spinning CW pressure mode.

the dump plane before calculating the mode. This is possible as the pressure at the dump plane and a given microphone location are related through a system and frequency dependent impedance, which should be the same for all the injector tubes. Assuming the mode is constant over the short time interval, the mode is therefore calculated at the upper microphone locations using a least squares solver for the discrete time Fourier transform of the signals at the forcing frequency. Not having to propagate the pressure signals, assuming the mode is constant, and only evaluating the forcing frequency allows for very fast calculations of the mode, making it possible to provide fast updates. The final program updates the calculated mode 16 times a second, which is sufficiently fast to be perceived as real-time when tuning the mode. The program provides both the amplitude of the two spinning components and the spin ratio, which is directly related to the nature angle of the mode. In the example in Fig. 3.4 a screen shot of the logging program is shown. The program is started when the burner is ignited and the mode is then fine tuned. No adjustments were performed during the image acquisition to ensure no influence from changing forcing signals.

3.2.4 Setting up standing and spinning modes

Most of the equations introduced in §3.2.1 are only directly applicable in theory, and not in practice. However, the practical approach used in this work is very similar and builds on the same idea, but with some extra considerations. The amplitudes assumption in Eq. (3.2) does not hold perfectly in practice due to the imperfect geometry, but it is still a relatively good approximation. Therefore the two speaker pairs are independently tuned to result in standing modes of approximately the same amplitude. While the nature angle and signal generator phase difference shown in Fig. 3.2 does not hold perfectly in this case, the desired mode can be obtained by tuning the phase in the region close to the theoretical phase difference. This works well for standing modes and for mixed modes with a sufficiently small nature angle, where exact amplitude cancellation is not required.

The most challenging modes to force are the highly spinning ones, with nature angles close to $\chi = \pm\pi/4$. There are several possible reasons behind this. To be able to set up a perfectly spinning mode, one of the two components of the standing modes set up by each speaker pair has to be cancelled by perfect destructive interference. To be able to achieve this, the amplitudes of the two components interfering destructively must match perfectly. It is no longer possible to overcome small amplitude differences by compensating with signal generator offset. Furthermore, it has been observed in low-order modelling that combustion noise pushes the self-excited acoustic mode away from the spinning solutions (Ghirardo and Gant, 2019; Faure-Beaulieu and Noiray, 2020; Ghirardo and Gant, 2021). The

higher the non-dimensional noise level is, the more the mode is pushed away from the spinning solutions. The non-dimensional noise is inversely proportional to the amplitude of the mode, which makes it even harder to set up spinning modes at lower amplitude levels. This was also observed in practice, where it is very hard to set up spinning modes under a certain amplitude threshold even though the mode is not self-excited.

The best strategy that was found in the current work to overcome these complications is described in the following:

- The combustor is ignited from cold with only the first speaker pair on, and the amplitude is adjusted to the desired level at the time images will be acquired later.
- The amplitude of either the A_- or the A_+ component is noted at this point depending on whether an ACW ($A_+ \neq 0$) or a CW ($A_- \neq 0$) spinning mode is desired.
- The combustor is ignited from cold again, with only the second speaker pair on. Now the amplitude is adjusted so the amplitude of the component noted in the previous step match the value of the first speaker pair at the same point in time.
- The previous step is repeated until a closely matching amplitude is found.
- An initial signal generator phase offset ϕ_{sg} based on Fig. 3.2 is set.
- The combustor is ignited from cold with the initial phase offset, and up to the time of planned image acquisition the phase is adjusted based on the near real-time reconstruction to get the lowest possible amplitude of the spinning component that should be cancelled by destructive interference.
- If the magnitude of the nature angle is not as high as desired, either more fine tuning of the phase offset or readjusting the amplitude of the speaker pairs are required.
- When the nature angle is at the desired level at the correct time after ignition the images are acquired.

It is worth noting that it is the undesired component that is matched in the third to last step, as that component has to be removed by destructive interference. The process for the standing and mixed modes is similar, but the additional freedom of not having to perfectly cancel acoustic waves by destructive interference means that the very delicate amplitude tuning is not required. Therefore, most of the standing and mixed modes can be obtained in a single ignition. This highlights

Table 3.1: Overview of the different studies of forced azimuthal pressure modes.

Parameter	*Article II*	*Article IV*
Pressure definition location	$x = x_{\text{upper}}$	$x = 0\,\text{mm}$
No. injectors (N)	18	12
No. forced states	3	123
No. orientation angles	1	4
Amplitudes in Pa	$870 \lessapprox A^{\perp} \lessapprox 940$	$40 \lessapprox A \lessapprox 1100$
Nature angles	$-0.7 \lessapprox 4\chi/\pi \lessapprox 0.9$	$-0.9 \lessapprox 4\chi/\pi \lessapprox 0.9$

how much harder and time consuming it is to impose highly spinning acoustic modes. The different forced studies in the current work are summarised briefly in Tab. 3.1.

3.2.5 Potential improvements

A solution that could potentially make the tuning process significantly simpler and faster would be to water cool the combustion chamber and the forcing array. This would enable thermal equilibrium to be reached, relaxing the time dependency of the forcing. Such a combustion chamber without forcing array was used by Indlekofer et al. (2021b). However, the inclusion of a precision machined and water cooled forcing array is more technically challenging.

An automatic tuning program, similar to the single sector program discussed in §3.1, was developed in the current work in an attempt to set up the spinning modes. While this set up very well controlled modes relatively fast when the combustor was turned off, it was not sufficiently fast to tune the mode under reactive conditions. The drift in frequency and the mode due to the increasing temperature proved to be too fast for the program to work accurately with the current setup. With a combustion chamber in thermal equilibrium this would likely not be a problem, and using such automatic tuning approaches could potentially be used to explicitly set up the modes.

Chapter 4

Processing methods

The processing procedures used in each of the articles included in this thesis are briefly explained in each article. The aim of this chapter of the thesis is to provide a more comprehensive version of the methods used for processing the data, expanding the description from the different articles. First the flame describing function is presented in §4.1, followed by the techniques required to calculate the velocity and pressure at the dump plane in §4.2. The time delay model used to describe the flame transfer function of the single flame setup is presented in §4.3. The annular pressure mode is described in §4.4, followed by phase averaging in §4.5, rotation averaging in §4.6, and finally the Azimuthal Flame Describing Function is discussed in §4.7.

4.1 Flame Describing Function

The Flame Describing Function (FDF) relates the normalised heat release rate fluctuations to the normalised acoustic velocity fluctuations. The general FDF definition was described in §1.3, but there are some choices in how to define the relevant quantities in the FDF definition in Eq. (1.6). The definition chosen for the current work is given by

$$\mathrm{FDF}\left(\omega, \hat{u}'_{\mathrm{axial}}/U_{\mathrm{bulk}}\right) = \frac{\langle \hat{q}'(\omega, \hat{u}'_{\mathrm{axial}}/U_{\mathrm{bulk}})\rangle \,/\, \langle \bar{q}\rangle}{\hat{u}'_{\mathrm{axial}}(\omega)/U_{\mathrm{bulk}}}\,. \tag{4.1}$$

The temporal mean heat release rate is given by $\bar{q}$ and the Fourier amplitude of the phase dependent heat release rate fluctuations is given by $\hat{q}'$. The angle brackets $\langle(\cdot)\rangle$ denote the spatial average over the spatial distribution of the heat release rate from the flame of interest. The domain of the averaging depends on the experimental setup, and is described in detail in §4.1.1. The reference location for both the Fourier amplitude of the axial acoustic velocity perturbations $\hat{u}'_{\mathrm{axial}}$ and the

bulk velocity U_{bulk} is chosen to be the dump plane, defined in Fig. 2.5b. The axial acoustic velocity at the dump plane is calculated based on the signals from the pressure transducers in Fig. 2.4a due to the difficulty of obtaining a direct measurement. To be able to calculate the velocity, the acoustic mode in the injector tube has to be characterised. This is described in the next section, §4.2.

It is also worth noting the Flame Transfer Function (FTF) described in §1.2 is just a special case of FDF where the velocity amplitude is sufficiently low. Therefore, the equations and techniques described for the FDF in Eq. (4.1) are used to obtain the FTF as well. However, different amplitude levels are tested experimentally to ensure the response is in the linear regime for the FTF.

4.1.1 Heat release rate

The normalised heat release rate fluctuations are obtained, as described in §1.2.1, by measuring the light intensity of the wavelength corresponding to the concentration of OH* radicals. The concentration is assumed to be proportional to the heat release rate (Higgins et al., 2001; Hardalupas and Orain, 2004; Balachandran et al., 2005), and the light intensity is either capture by a PMT or a camera as described in §2.3.

A camera provides a line of sight measurement of the heat release rate in the direction normal to the image plane. To get the spatially averaged quantities in Eq. (4.1), the pixels in the image plane are averaged. For a single flame, as shown in Fig. 2.6, the averaging is performed over the full image. Since the flame of interest is the only source of heat release rate, there is no need to restrict the averaging domain further. A photomultiplier tube (PMT), which integrates over the field of view, can also be used without careful restriction of the field of view to capture the already integrated heat release rate in these configurations.

The response of annular combustors is often modelled based on FDFs obtained for a single, axially perturbed flame, as described in §1.5.3. Therefore, it is of great interest to measure the conventional FDF in an annular geometry subjected to azimuthal acoustic forcing. In the annular setup the camera is imaging from directly downstream of the combustion chamber, as shown in Fig. 2.7. This captures all the flames simultaneously, and it is no longer possible to integrate over the full image plane to obtain the normalised heat release rate in Eq. (4.1). Numbering the N different flames in the annulus from $j = 0$ to $j = N - 1$, the FDF of the jth flame is chosen to be defined as

$$\text{FDF}_j\left(\hat{u}'_{\text{axial},j}/U_{\text{bulk}}\right) = \frac{\langle \hat{q}' \rangle_j \,/\, \langle \bar{q} \rangle_j}{\hat{u}'_{\text{axial},j}/U_{\text{bulk}}}\,, \tag{4.2}$$

where the explicit amplitude dependence on the right hand side has been dropped for notational compactness. It is worth noting the frequency dependence is com-

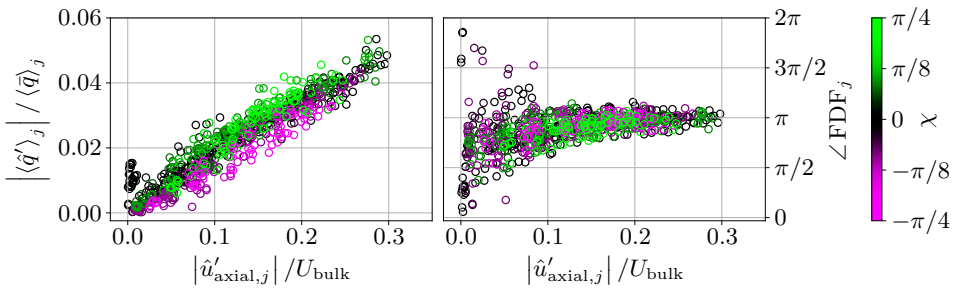

Figure 4.1: Example of the FDF obtained experimentally in an annular combustor with $N = 12$ injector tubes with swirl at frequency $f = 1650\,\mathrm{Hz}$. The heat release rate magnitude is presented on the left and the phase of the FDFs is presented on the right. Each instrumented injector is represented by a point for each forced state. Interpretation of the figure is presented in Article IV.

pletely dropped, as the first azimuthal mode can only be excited at discrete frequencies for a given operating point. Compared to the definition for the single flame in Eq. (4.1) the subscript j has been introduced for the different flames. The axial acoustic velocity at the dump plane evaluated in injector j is given by $\hat{u}'_{\mathrm{axial},j}$. The most important change is the spatial averaging operator $\langle(\cdot)\rangle_j$ which is defined to be the average over a sector spanning an angle $2\pi/N$ of the full annulus. Each sector is centred at an injector centre, as illustrated in Fig. 2.2. This ensures the heat release rate response is averaged over a single flame, similar to the FDF definition for the single flame setup. Figure 4.1 shows an example of how the FDFs of an annular combustor might be represented.

Adjacent flames in the annular combustor might have significant merging depending on the flame spacing, potentially complicating the extraction of the response of a single flame. However, due to the discrete rotational symmetry of the setup, the exact location of the dividing line between adjacent masks should not play a large role, as long as all the sectors are defined equally. Since all the flames are assumed to be nominally identical, any potential response of the flame cut off from one side of the sector will be included on the other side by a similar cutting of the adjacent flame. The masks may also introduce a slight increase or decrease of the response of a particular flame, but this will be removed when averaging flames together in §4.7.

4.2 Acoustic mode in the injector tubes

The pressure disturbances $p'(\boldsymbol{x}, t)$ in a general geometry with a mean flow $\boldsymbol{U}$ is given by the convected wave equation (Dowling and Stow, 2003)

$$\left(\frac{1}{c^2}\frac{\mathrm{D}^2}{\mathrm{D}t^2} - \nabla^2\right)p' = 0\,, \tag{4.3a}$$

$$\frac{\mathrm{D}}{\mathrm{D}t} = \frac{\partial}{\partial t} + (\boldsymbol{U}\cdot\nabla)\,, \tag{4.3b}$$

where c is the speed of sound. The injector tubes, described in §2.1.1, are long ($L_{\mathrm{tube}} = 145\,\mathrm{mm}$) compared to the diameter ($D = 19\,\mathrm{mm}$). Therefore, each tube can be approximated as being one dimensional (1D) for the frequencies of interest, reducing Eq. (4.3) to

$$\frac{\partial^2 p'_{\mathrm{tube}}}{\partial x^2} = \frac{1}{c^2}\left(\frac{\partial}{\partial t} + U\frac{\partial}{\partial x}\right)^2 p'_{\mathrm{tube}}\,, \tag{4.4}$$

where x is the axial position in the tube. The pressure in the axial direction of the duct is denoted p'_{tube} and U is the bulk flow in the axial direction.

To solve equations of the form of Eq. (4.4) it is beneficial to apply complex analysis instead of restricting the calculations to real valued expressions. Therefore, the complex valued *analytical* signal $p'_{\mathrm{tube,a}}$ is introduced as the complex valued equivalent to the real valued signal p'_{tube}. The two are related through

$$2p'_{\mathrm{tube}}(x,t) = \Re\left\{2p'_{\mathrm{tube,a}}(x,t)\right\} = p'_{\mathrm{tube,a}}(x,t) + \mathrm{c.\,c.}\,, \tag{4.5a}$$

$$p'_{\mathrm{tube,a}}(x,t) = p'_{\mathrm{tube}}(x,t) + \mathrm{i}\mathcal{H}\left[p'_{\mathrm{tube}}(x,t)\right]\,, \tag{4.5b}$$

where c. c. denotes the complex conjugate of the preceding term and $\mathcal{H}\left[(\cdot)\right]$ is the Hilbert transform of $(\cdot)$. The solution to Eq. (4.4) is then given by

$$p'_{\mathrm{tube,a}}(x,t) = \left[B_+\exp\left(-\mathrm{i}k_+x\right) + B_-\exp\left(\mathrm{i}k_-x\right)\right]\exp\left(\mathrm{i}\omega t\right)\,, \tag{4.6}$$

which describes two plane waves propagating in the downstream and upstream direction for the first and second component respectively. The complex valued amplitude of each component is given by $B_\pm$, and the positive, real valued wavenumbers $k_\pm$ are given by

$$k_\pm = \frac{\omega/c}{1 \pm Ma}\,, \tag{4.7}$$

where $Ma = U/c$ is the Mach number.

The acoustic axial velocity perturbations corresponding to the pressure fluctuations in Eq. (4.6) are governed by the 1D linearised fluctuating momentum equation (Dowling and Stow, 2003)

$$\frac{\partial u'_{\mathrm{tube}}}{\partial t} + U\frac{\partial u'_{\mathrm{tube}}}{\partial x} + \frac{1}{\rho}\frac{\partial p'_{\mathrm{tube}}}{\partial x} = 0\,. \tag{4.8}$$

Here ρ is the density of the fluid in the system and the velocity is given by

$$u'_{\mathrm{tube,a}}(x,t) = \frac{1}{\rho c}\left[B_+ \exp\left(-\mathrm{i}k_+ x\right) - B_- \exp\left(\mathrm{i}k_- x\right)\right] \exp\left(\mathrm{i}\omega t\right). \tag{4.9}$$

The expression is of the same form as the pressure in Eq. (4.6), only with a sign change in the second term and the introduction of the factor $1/\rho c$. Therefore, the acoustic velocity can be calculated based on the unknown coefficients $B^{\pm}$ shared with the pressure definition in Eq. (4.6). The reference acoustic velocity $\hat{u}'_{\mathrm{axial}}$ in the FDF definition in Eq. (4.1) is the velocity amplitude $\hat{u}'_{\mathrm{tube}}(x)$ in Eq. (4.9) evaluated at the dump plane

$$\hat{u}'_{\mathrm{axial}} = u'_{\mathrm{tube,a}}(x=0, t=0) = \hat{u}'_{\mathrm{tube}}(x=0). \tag{4.10}$$

4.2.1 Determining the mode

The acoustic mode in the tube is determined by the two unknown amplitudes $B_{\pm}$ and the imposed angular frequency ω. The speed of sound c, density ρ and bulk velocity U_{bulk} are all known from the flow rates and fluid properties. A common approach to determining the amplitudes based on pressure measurements is the multiple microphone technique (Seybert and Ross, 1977). Since there are two unknowns to be determined, two or more pressure measurements at unique axial locations are required. Then the amplitudes are determined from

$$\begin{bmatrix} \hat{p}'_{\mathrm{tube}}(x_0) \\ \hat{p}'_{\mathrm{tube}}(x_1) \\ \vdots \end{bmatrix} = \begin{bmatrix} \exp\left(-\mathrm{i}k_+ x_0\right) & \exp\left(\mathrm{i}k_- x_0\right) \\ \exp\left(-\mathrm{i}k_+ x_1\right) & \exp\left(\mathrm{i}k_- x_1\right) \\ \vdots & \vdots \end{bmatrix} \begin{bmatrix} B_+ \\ B_- \end{bmatrix}, \tag{4.11}$$

where the amplitudes are assumed constant in time and x_j is the axial location of the jth microphone. An example of the fitting in Eq. (4.11) is shown in Fig. 4.2 for one of the injectors in the annular combustor when a standing mode is forced. The measured and fitted signals match perfectly by definition, as there are two spatially separated measurements and two unknowns. The Fourier amplitudes $\hat{p}'_{\mathrm{tube}}(x_j)$ in Eq. (4.11) are related to the pressure signals through $p'_{\mathrm{tube,a}}(x_j, t) = \hat{p}'_{\mathrm{tube}}(x_j)\exp\left(\mathrm{i}\omega t\right)$, and are determined from either direct FFT or from cross power spectral analysis with the forcing signal. The cross power spectrum approach is used for the single flame setup, where the heat release rate, pressure and forcing signals are all sampled on the same system and at the same rate. By splitting the recorded data into several shorter sections and averaging the results, the influence of random turbulent fluctuations on the Fourier amplitude is reduced. However, in the cases where a camera is used to capture the heat release rate this is not as straight forward due to the large difference in sampling rates.

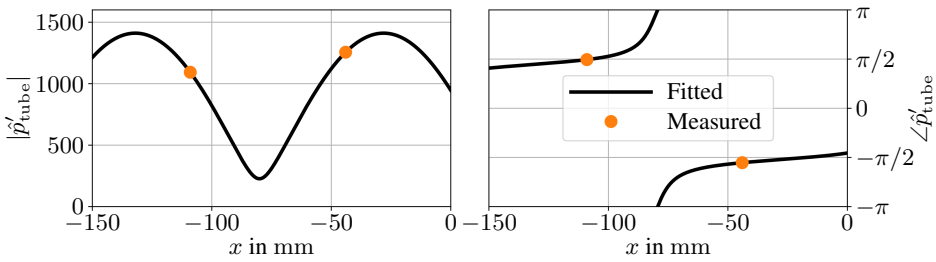

Figure 4.2: Measured pressure amplitudes and the corresponding fitted pressure mode in an injector tube. The dump plane is located at $x = 0$. The case shown here is from an injector tube excited by downstream azimuthal forcing. Note no area and swirler corrections are applied in this example.

An alternative method of obtaining the amplitudes, which also accounts for any potential time dependence, is to use the Hilbert transform in Eq. (4.5b) to obtain the value of Eq. (4.6) for each sample time t_i. Then the amplitudes with time exponents are obtained from

$$\begin{bmatrix} p'_{\text{tube,a}}(x_0, t_i) \\ p'_{\text{tube,a}}(x_1, t_i) \\ \vdots \end{bmatrix} = \begin{bmatrix} \exp(-\mathrm{i}k_+ x_0) & \exp(\mathrm{i}k_- x_0) \\ \exp(-\mathrm{i}k_+ x_1) & \exp(\mathrm{i}k_- x_1) \\ \vdots & \vdots \end{bmatrix} \begin{bmatrix} B_+(t_i)\exp(\mathrm{i}\omega t_i) \\ B_-(t_i)\exp(\mathrm{i}\omega t_i) \end{bmatrix}. \tag{4.12}$$

For the amplitudes to make physical sense it is implicitly assumed that $B_\pm$ are slowly varying compared to the fast oscillation ω. Independent of whether Eq. (4.11) or Eq. (4.12) is used to obtain the amplitudes, the pressure and the corresponding acoustic velocity at an arbitrary point in the tube are given by Eq. (4.9).

4.2.2 Contraction and expansion

The pressure and acoustic velocity can only be propagated using Eq. (4.6) and Eq. (4.9) in a tube of constant cross sectional area. However, the centrally mounted bluff body in the injector introduces a contraction before reaching the injector exit. In the case of low Mach number flows $Ma \ll 1$,the pressure and mass flow fluctuations have to be conserved across a small area change (Dowling and Stow, 2003). Assuming a smooth area change from upstream area $\mathcal{A}_\mathrm{u}$ to downstream area $\mathcal{A}_\mathrm{d}$ located at x_ac

$$\mathcal{A} = \begin{cases} \mathcal{A}_\mathrm{u} & \text{for } x < x_\mathrm{ac} \\ \mathcal{A}_\mathrm{d} & \text{for } x > x_\mathrm{ac} \end{cases}, \tag{4.13}$$

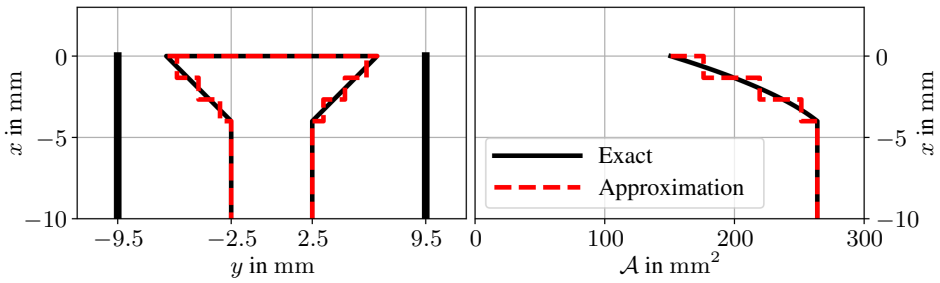

Figure 4.3: Example of how the contraction caused by the bluff body and injector geometry is approximated by 4 steps in the acoustic propagation. The approximated geometry of the bluff body is presented on the left and the cross sectional area $\mathcal{A}$ of the open part of the tube is presented on the right.

the pressure and mass flow conservation laws are expressed as

$$p'_{\mathrm{tube}}(x,t)\big|_{x=x_{\mathrm{ac}}^-} = p'_{\mathrm{tube}}(x,t)\big|_{x=x_{\mathrm{ac}}^+} , \tag{4.14a}$$

$$\mathcal{A}_{\mathrm{u}} u'_{\mathrm{tube}}(x,t)\big|_{x=x_{\mathrm{ac}}^-} = \mathcal{A}_{\mathrm{d}} u'_{\mathrm{tube}}(x,t)\big|_{x=x_{\mathrm{ac}}^+} . \tag{4.14b}$$

The bluff body represents a gradually changing cross sectional area, and not a single discrete jump as described by Eq. (4.14). The continuous area change of the bluff body can however be approximated as a series of discrete area changes. The contracting section is divided into several shorter sections, each of the same length and the same volume as the injector geometry. This is equivalent to the real continuous geometry for a series of infinitesimal area changes, but in practice a finite number of steps is usually a sufficient approximation. An example of how the continuous area change is approximated for the injector geometry described in §2.1.1 is presented in Fig. 4.3.

4.2.3 Swirler

Each injector tube has a swirler mounted downstream of the pressure measurement locations, as shown in Fig. 2.4. This represents a relatively large temporary blockage and it introduces a rotational motion to the flow around the central axis. The effect of the swirler on the acoustic mode is not trivial to quantify analytically, and the black box approach of measuring the scattering matrix is utilised instead. Following the derivation of Åbom (1991) the scattering matrix $\boldsymbol{S}$ can be defined as

$$\begin{bmatrix} B_{+,\mathrm{u}} \\ B_{-,\mathrm{d}} \end{bmatrix} = \begin{bmatrix} S_{11} & S_{12} \\ S_{21} & S_{22} \end{bmatrix} \begin{bmatrix} B_{-,\mathrm{u}} \\ B_{+,\mathrm{d}} \end{bmatrix} = \boldsymbol{S} \begin{bmatrix} B_{-,\mathrm{u}} \\ B_{+,\mathrm{d}} \end{bmatrix} , \tag{4.15}$$

where subscript u and d denote upstream and downstream of the swirler respectively.

To be able to measure the scattering matrix, at least two linearly independent states of the system have to be measured. In the case of two linearly independent states Eq. (4.15) can be rewritten as

$$\begin{bmatrix} B''_{+,\mathrm{u}} & B'''_{+,\mathrm{u}} \\ B''_{-,\mathrm{d}} & B'''_{-,\mathrm{d}} \end{bmatrix} = \boldsymbol{S} \begin{bmatrix} B''_{-,\mathrm{u}} & B'''_{-,\mathrm{u}} \\ B''_{+,\mathrm{d}} & B'''_{+,\mathrm{d}} \end{bmatrix} , \tag{4.16}$$

where the double and triple prime denotes the first and second linearly independent states respectively. The transposed scattering matrix $\boldsymbol{S}^T$ is obtained by solving the following matrix problem

$$\begin{bmatrix} B''_{-,\mathrm{u}} & B'''_{-,\mathrm{u}} \\ B''_{+,\mathrm{d}} & B'''_{+,\mathrm{d}} \end{bmatrix}^T \boldsymbol{S}^T = \begin{bmatrix} B''_{+,\mathrm{u}} & B'''_{+,\mathrm{u}} \\ B''_{-,\mathrm{d}} & B'''_{-,\mathrm{d}} \end{bmatrix}^T . \tag{4.17}$$

While the scattering matrix in Eq. (4.15) fully characterises the effect of the swirler on the acoustic mode, the expression is not convenient for the experimental setups used in this work. The equation requires one amplitude component upstream and one component downstream of the swirler to be known. However, all the pressure measurements are performed upstream of the swirler in the experiments, and only the upstream amplitudes can be obtained from those measurements. Therefore the two following matrices are introduced

$$\begin{bmatrix} B_{+,\mathrm{u}} \\ B_{-,\mathrm{u}} \end{bmatrix} = \begin{bmatrix} S_{11} & S_{12} \\ 1 & 0 \end{bmatrix} \begin{bmatrix} B_{-,\mathrm{u}} \\ B_{+,\mathrm{d}} \end{bmatrix} = \boldsymbol{T}_{\mathrm{u}} \begin{bmatrix} B_{-,\mathrm{u}} \\ B_{+,\mathrm{d}} \end{bmatrix} \tag{4.18a}$$

$$\begin{bmatrix} B_{+,\mathrm{d}} \\ B_{-,\mathrm{d}} \end{bmatrix} = \begin{bmatrix} 0 & 1 \\ S_{21} & S_{22} \end{bmatrix} \begin{bmatrix} B_{-,\mathrm{u}} \\ B_{+,\mathrm{d}} \end{bmatrix} = \boldsymbol{T}_{\mathrm{d}} \begin{bmatrix} B_{-,\mathrm{u}} \\ B_{+,\mathrm{d}} \end{bmatrix} , \tag{4.18b}$$

where $\boldsymbol{T}_{\mathrm{u}}$ and $\boldsymbol{T}_{\mathrm{d}}$ can be combined to describe the downstream amplitudes in terms of the upstream amplitudes

$$\begin{bmatrix} B_{+,\mathrm{d}} \\ B_{-,\mathrm{d}} \end{bmatrix} = \boldsymbol{T}_{\mathrm{d}} \boldsymbol{T}_{\mathrm{u}}^{-1} \begin{bmatrix} B_{+,\mathrm{u}} \\ B_{-,\mathrm{u}} \end{bmatrix} = \boldsymbol{T} \begin{bmatrix} B_{+,\mathrm{u}} \\ B_{-,\mathrm{u}} \end{bmatrix} . \tag{4.19}$$

In practice the acoustic transfer matrix $\boldsymbol{T}$ of the swirler is used to obtain the pressure and axial acoustic velocity downstream of the swirler.

The raw data for the scattering matrix calculations were kindly provided by Indlekofer et al. (2021a). The independent states required to calculate the scattering matrix were obtained by applying acoustic forcing from first upstream and then downstream of the swirler. These measurements were performed for both an open and a closed end in a constant cross section test tube, which was equipped with the

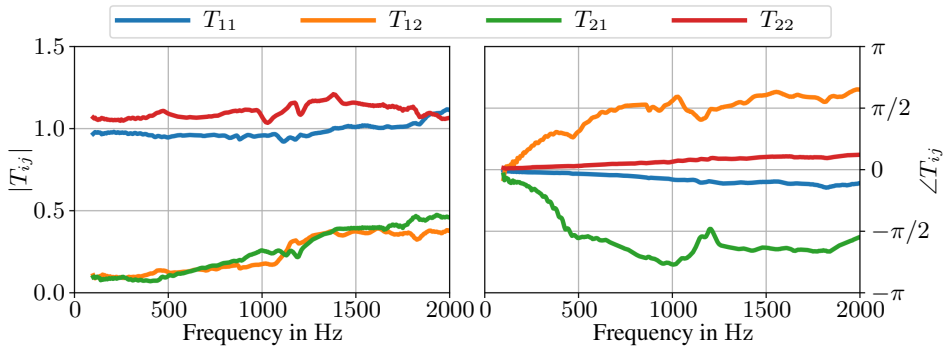

Figure 4.4: Transfer matrix $\boldsymbol{T}$ of the swirler mounted in the injector tubes. The magnitude of each component is presented on the left, and the phase is presented on the right.

swirler and several upstream and downstream microphones. The coefficients of the transfer matrix $\boldsymbol{T}$ are presented in Fig. 4.4 for the frequency range of interest in this work. The swirler is observed to have a relatively low influence on the acoustic mode up to approximately 1 kHz, as both T_{11} and T_{22} have a magnitude close to unity and low phase offset while T_{12} and T_{21} have a relatively low amplitude.

4.3 Distributed time delay model

The response of a single flame, obtained on the single sector setup in §2.2, can be characterised in terms of time delays related to the flow perturbation sources. The single sector setup has two such sources of vorticity perturbations. The swirler creates inertial wave perturbations (Komarek and Polifke, 2010; Palies et al., 2010; Albayrak et al., 2019), and additional convective perturbations are formed at the dump plane. The characteristic time delay, τ_1, of the latter is given by the ratio of the representative flame height H to the bulk flow velocity U_{bulk} at the injector exit (Kim and Santavicca, 2013a). The second time delay, τ_2, can be split into two parts: the time it takes for the perturbations to propagate a distance L from the swirler to the dump plane at velocity U_{prop}; and the propagation time from the dump plane to the flame front, which is given by the first time delay. The propagation time from the swirler to the dump plane is given by Eq. (1.5). The two

time delays can therefore be expressed as

$$\tau_1 = \frac{H}{U_{\text{bulk}}}\,, \tag{4.20a}$$

$$\tau_2 - \tau_1 = \frac{L}{U_{\text{prop}}}\,. \tag{4.20b}$$

However, it is not always trivial to correctly identify the representative length and velocity scales, as highlighted by Albayrak et al. (2019) for the velocity scale.

Another approach is to fit two distributed time delay models to the FTF to directly obtain the two relevant time scales in the problem. The model created by Æsøy et al. (2020), originally created for non-swirled flames but still featuring an upstream source of vorticity perturbations, is applied in the current work to extract the two dominant time delays. The model is given by

$$\mathrm{DTL_T}\left(\omega\right) = \exp\left(-\mathrm{i}\phi_0\right) \sum_{i=1}^{2} \left(E_i^+(\omega) + E_i^-(\omega)\right) = \sum_{i=1}^{2} \mathrm{DTL}_i\,, \tag{4.21a}$$

$$2E_i^{\pm}(\omega) = g_i \exp\left(-\frac{1}{2}(\omega \pm \beta_i)^2\sigma_i^2 - \mathrm{i}\omega\tau_i\right). \tag{4.21b}$$

where each term $E_i^{\pm}$ represents a Gaussian distribution of strength $g_i/2$ centred around frequency $\mp\beta_i$. The width of the distribution is determined by σ_i, and τ_i is the characteristic time delay corresponding to Eq. (4.20). Each of the $i = 1, 2$ components of the distributed timed delay model in Eq. (4.21) describes either a low-pass or a band-pass filter behaviour, depending mainly on the combination of β_i and σ_i. If the angular frequency β_i is sufficiently close to zero, or if the value of σ_i is sufficiently low, the model describes a low-pass filter. Otherwise it is a band-pass filter centred around $\pm\beta_i$. An example function is presented in Fig. 4.5, where the second distribution is in between a pure low-pass and pure band-pass filter.

The flame itself, and therefore the distribution belonging to the first time delay, always acts as a low-pass filter (Fleifil et al., 1996; Schuller et al., 2003). Perfectly premixed flames have a unit gain in the low frequency limit (Polifke and Lawn, 2007), which is imposed in the model by making g_1 a function of the other parameters

$$g_1 = \frac{1 - g_2 \exp\left(-\frac{1}{2}(\beta_2\sigma_2)^2\right)}{\exp\left(-\frac{1}{2}(\beta_1\sigma_1)^2\right)}\,. \tag{4.22}$$

While it is theoretically possible to express g_2 as a function of the other parameters, this is strongly discouraged due to the numerical precision in the fitting process.

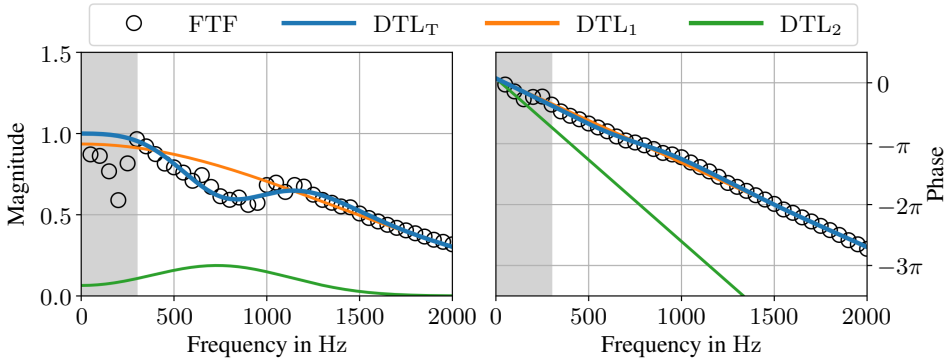

Figure 4.5: Example of distributed time delay model obtained by fitting to experimental data. The two individual components DTL_1 and DTL_2 are shown separately, in addition to the resulting total DTL_T. The fitting is performed using the experimental FTF data in the light region.

The low-pass behaviour of flames ensures the denominator of Eq. (4.22) is non-negligible. However, if g_2 is the dependent parameter, the new denominator is negligible if the second distribution describes a band-pass filter. Further details about the physical interpretation of the model can be found in Æsøy et al. (2020).

The process of obtaining the parameters of Eq. (4.21) is not trivial due to the highly nonlinear nature of the equation. As the only other application of this particular model was in Æsøy et al. (2020), the differences in both the fitting procedure and the typical length and time scales are discussed in the following. Using a nonlinear least squares solver on Eq. (4.21) was observed to be very sensitive to initial values in the search, suggesting several local minima. After the fitting, it is possible to assess whether the parameters make physical sense or not, as Æsøy et al. (2020) showed the parameters have a physical interpretation. The main approach outlined in Æsøy et al. (2020) for obtaining the parameters through successive steps of nonlinear least squares solvers was followed. However, a few additional considerations were necessary for the swirled flame response in the current work. The method used to obtain the parameters in Article I was:

- Fit only DTL_1, imposing a unit gain at zero frequency, using a nonlinear least squares solver.
- Keeping the parameters of DTL_1 fixed, the parameters of DTL_2 are found by using the differential evolution algorithm in SciPy without imposing unit gain in the low frequency limit.
- The parameters from the last two steps are used as an initial guess for a final

nonlinear least squares solver step, where all the parameters of $\mathrm{DTL_T}$ can be adjusted. The unit gain in the low frequency limit is imposed through Eq. (4.22) in the solver.

The main difference compared to Æsøy et al. (2020) is the use of the differential evolution algorithm in the second step. This is not as prone to get trapped in a local minimum in the parameter space as the least squares solver.

The gain and phase modulations in Æsøy et al. (2020) were much shorter in frequency space, resulting in better fitting conditions from having several wavelengths in the response. Then the use of a nonlinear least squares solver in each step with good initial guesses was observed to be sufficient. In the current work the second time delay is much shorter, resulting in much longer modulation wavelength in frequency space. This makes the fitting process harder due to having less than a full wavelength to fit to, as shown in the example case in Fig. 4.5. Additionally, the distributed time delay response of the swirler seems to be closer to a low-pass filter than the grub screws further upstream in Æsøy et al. (2020), further complicating the fitting procedure in terms of imposing the unit gain.

4.4 Acoustic mode in the annulus

The pressure at discrete locations on the dump plane is obtained by propagating the measured pressure following the procedure outlined in §4.2 for each of the instrumented injectors. The propagated pressures are then used to determine the azimuthal pressure mode in the annular combustion chamber. An azimuthal wave can either be described as a superposition of two plane waves rotating in opposite directions, or by using the hypercomplex quaternion formalism (Ghirardo and Bothien, 2018) mentioned in §1.5.1. Both descriptions have their own merits, and the method used for a specific purpose in the current work is chosen based on which one is beneficial for the intuitive understanding of the results. The superposition of two spinning waves formulation is discussed next, and the quaternion formalism is described in detail later in §4.4.2.

Similar to the pressure mode in the injector tubes in Eq. (4.6), the azimuthal pressure mode of order n can be described by

$$p'_{\mathrm{a}}(\theta, t) = \left[A_+ \exp\left(-\mathrm{i}n\theta\right) + A_- \exp\left(\mathrm{i}n\theta\right)\right] \exp\left(\mathrm{i}\omega t\right). \tag{4.23}$$

Here A_+ and A_- are the complex valued amplitudes of the plane waves propagating in the anti-clockwise (ACW) and clockwise (CW) direction respectively. The total pressure amplitude of the azimuthal mode is given by

$$A^{\perp} = \sqrt{|A_+|^2 + |A_-|^2}, \tag{4.24}$$

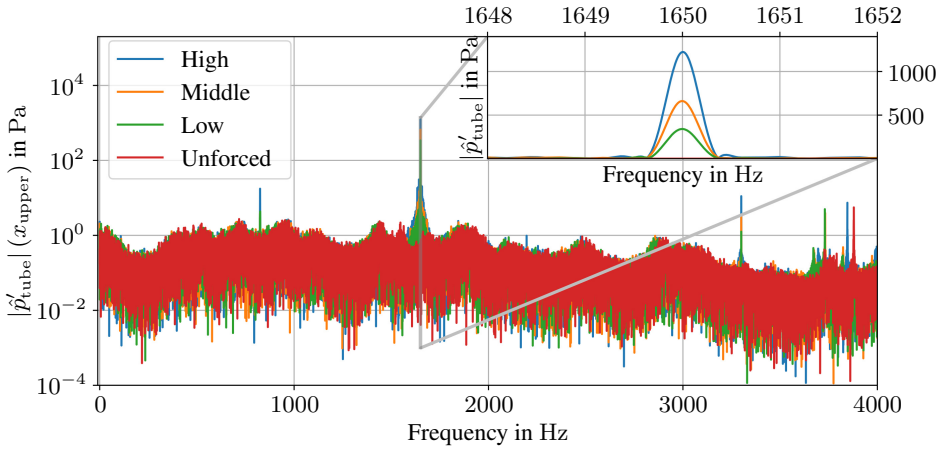

Figure 4.6: Frequency spectrum at the location of the upper microphone (x_{upper}) in an injector tube for a forced azimuthal mode in the annular combustor. The amplitudes are 1224 Pa (*High*), 661 Pa (*Middle*), and 340 Pa (*Low*) for the forced cases, with amplitude below 10 Pa for the unforced case.

which is the geometric distance in a plane where the two orthogonal axes are A_+ and A_-. The main difference between Eq. (4.6) and Eq. (4.23) are the wavenumbers, which are determined by the geometry in this case, and are part of the expression $\pm n\theta$. The dispersion relation in Eq. (4.7) still holds, but it is the frequency of the two components which might differ, and not the geometrically fixed wavenumber. The effect of having a mean azimuthal flow on the pressure mode, due to for example swirl, was investigated theoretically by Bauerheim et al. (2015); Faure-Beaulieu and Noiray (2020). However, in the current work the combustor is either acoustically forced, resulting in a single dominant frequency as illustrated in Fig. 4.6, or the combustor is equipped with non-swirling flames. In both cases there is only a single frequency in the system, and effects of frequency splitting is therefore assumed to be negligible in the current work.

Equation (4.23) describes a wide range of possible acoustic modes. Modes spinning in the ACW direction ($A_- = 0$), standing ($|A_-| = |A_+|$), spinning in the CW direction ($A_+ = 0$) and everything in between. The relation between the two amplitudes is therefore often called the nature of the mode, which can be quantified through the spin ratio (Bourgouin et al., 2013) described in Eq. (1.7).

The pressure measured at different points in the annulus for a standing and an ACW spinning mode are presented in Fig. 4.7. The spinning mode is characterised by identical responses at the different locations, but with a temporal delay equal to the azimuthal angle between the measurement locations. This is not the case for

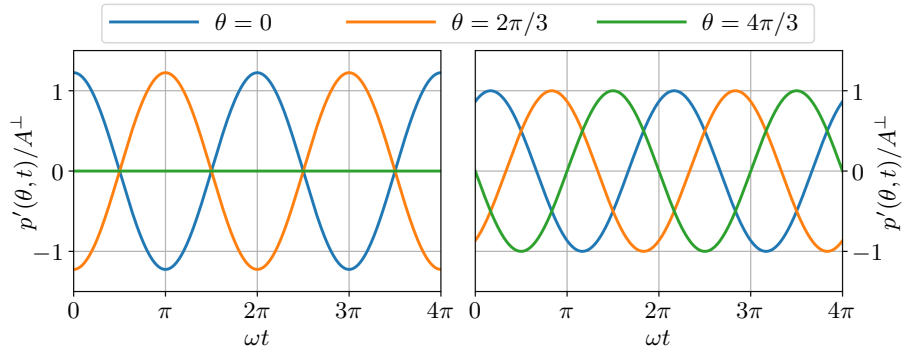

Figure 4.7: Example time series for a standing mode (*left*, $|A_+| = |A_-|$) and an ACW spinning mode (*right*, $A_- = 0$) measured at three spatial locations θ.

the standing mode, where the measured local amplitude depends on the azimuthal location. In the current example the pressure node is located at $\theta = 4\pi/3$, and the two other locations are symmetrically distributed around the node located at $\theta = \pi/3$.

4.4.1 C-indicator

Again, similar to the acoustic mode in the injector tube, the azimuthal acoustic mode in the annular combustion chamber is obtained by measuring the pressure at different unique locations in the pressure mode. The mode can be obtained by a least squares solution based on the Fourier amplitudes of the pressure measurements similar to Eq. (4.11). However, in the early parts of this work the mode was characterised through the use of the C-indicator introduced in Wolf et al. (2012). The C-indicator is given by

$$C(t) = \frac{1}{N^*} \sum_{j=1}^{N^*} p'(\theta_j, t) \exp\left(\mathrm{i}\theta_j\right), \tag{4.25}$$

where the measured, real valued pressure p' is used instead of the analytical signal p'_a or the Fourier amplitude $\hat{p}'$. There are N^* microphones in total, and the jth microphone is located at the azimuthal location θ_j. Splitting the pressure signals into short segments of only a few oscillation cycles, a nonlinear minimising function is used to obtain the complex valued amplitudes $A_\pm$ for that interval. The amplitudes $A_\pm$ are not constant in time in general, but are assumed to be slowly varying compared to the fast oscillations ω. The variations are sufficiently slow for the amplitudes to be considered constant over the fitting interval.

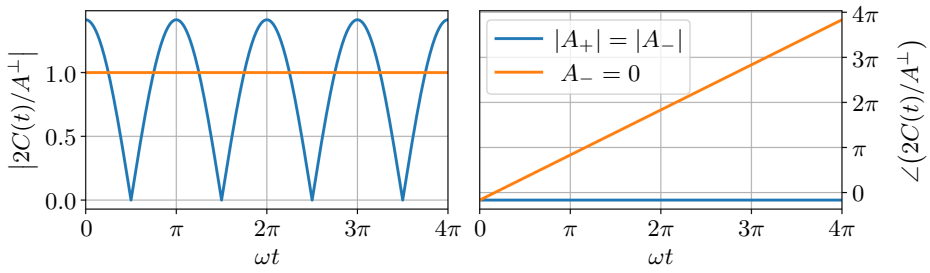

Figure 4.8: Example C-indicator time series of a standing mode ($|A_+| = |A_-|$) and an ACW spinning mode ($A_- = 0$) obtained from equidistantly distributed microphones. The C-indicator is calculated from the signals presented in Fig. 4.7.

The C-indicator works for fitting the amplitudes independent of the placement of the microphones. However, in the case of N^* equidistantly placed microphones in the azimuthal direction, which is the case in this work, the C-indicator has the special property

$$2C(t) = A_+ \exp(\mathrm{i}\omega t) + A_-^* \exp(-\mathrm{i}\omega t), \tag{4.26}$$

where A_-^* is the complex conjugate of A_-. Equation (4.26) enables the use the C-indicator to assess the nature of the mode directly. The magnitude and the phase are constantly changing at a rate $\pm\omega t$ in the case of a perfectly spinning mode, where the sign depends on the spinning direction. Standing modes have fluctuating magnitude but a constant phase, following the choice of Wolf et al. (2012) to not include the π phase change from the cyclic sign change of $C(t)$ for standing modes. This is illustrated for a perfectly standing mode and a perfectly ACW spinning mode in Fig. 4.8, corresponding to the two cases in Fig. 4.7. However, it is easier to interpret the nature of the mode from the the spin ratio in Eq. (1.7). Therefore, the C-indicator is only used for fitting the pressure mode in Eq. (4.23), and not for assessing the nature of the modes in this work. This technique was used in Article II and Article III, based on the pressure at the upper microphone location. The mode at that location and at the dump plane are only separated by a complex impedance z, which in practice only changes the amplitude and temporal phase and not the nature of the mode.

4.4.2 Quaternion formalism

Ghirardo and Bothien (2018) recently introduced the hypercomplex quaternion formalism for describing the azimuthal pressure mode, solving definition issues associated with the orthogonal description in Eq. (4.23) for modelling. In addition

to solving the modelling issues, the description is also of interest for experimentalists due to the direct inclusion of the nature of the mode. Any azimuthal mode described by the real part of Eq. (4.23) can also be described by the corresponding real valued expression in Eq. (1.8), which is repeated here for reference (Ghirardo and Bothien, 2018)

$$\begin{aligned} p'(\theta,t) =& A\cos\left(n(\theta-\theta_0)\right)\cos\left(\chi\right)\cos\left(\omega t+\varphi\right)+ \\ & A\sin\left(n(\theta-\theta_0)\right)\sin\left(\chi\right)\sin\left(\omega t+\varphi\right). \end{aligned} \tag{4.27}$$

As previously mentioned the nature of the mode is given by the nature angle χ and the azimuthal location of the anti-node of the standing component of the mode is given by the orientation angle θ_0. The nature angle is limited to the interval $-\pi/4 \leq \chi \leq \pi/4$, while the orientation angle is limited to $-\pi < \theta_0 \leq \pi$. The amplitude A is related to the amplitude $A^{\perp}$ of the orthogonal description in Eq. (4.23) through (Ghirardo and Bothien, 2018)

$$\frac{A}{\sqrt{2}} = \sqrt{|A_+|^2 + |A_-|^2} = A^{\perp}. \tag{4.28}$$

Note the factor $\sqrt{2}$ difference between the two amplitude definitions. The relation between the spin ratio SR and the nature angle χ is given by

$$\chi = \arctan\left(\mathrm{SR}\right) = \arctan\left(\frac{|A_+|-|A_-|}{|A_+|+|A_-|}\right). \tag{4.29}$$

Since the characteristic features of a given azimuthal mode are the amplitude A, the nature angle χ and the orientation angle θ_0, it is natural to describe a given mode as a point on a Poincaré sphere (Ghirardo and Bothien, 2018). The amplitude A determines the distance from the point to the origin of the sphere, and the orientation angle θ_0 is the angle in the equatorial plane relative to the reference angle of the coordinate system. Twice the nature angle (2χ) determines the angle between the equatorial plane and the point representing the pressure mode. This is shown schematically in Fig. 4.9, together with an example representing the different forced states discussed in Article IV.

The process of obtaining the state space parameters in Eq. (4.27) from measured time series is described by Ghirardo and Bothien (2018). Following the derivation of Ghirardo and Bothien (2018) the definition in Eq. (4.27) can be expressed in terms of the quaternion valued function ξ_{a}

$$2p'(\theta,t) = \exp\left(-\mathrm{i}n\theta\right)\xi_{\mathrm{a}}(t) + \mathrm{q.\,c.}, \tag{4.30}$$

where q. c. denotes the quaternion conjugate of the preceding term. The quaternion valued analytical signal ξ_{a} is defined as

$$\xi_{\mathrm{a}}(t) = \xi_1(t) + \mathrm{i}\xi_2(t) + \mathrm{j}\mathcal{H}\left[\xi_1(t)\right] + \mathrm{k}\mathcal{H}\left[\xi_2(t)\right], \tag{4.31a}$$

$$2p'(\theta,t) = \exp\left(-\mathrm{i}n\theta\right)\left[\xi_1(t) + \mathrm{i}\xi_2(t)\right] + \mathrm{c.\,c.}. \tag{4.31b}$$

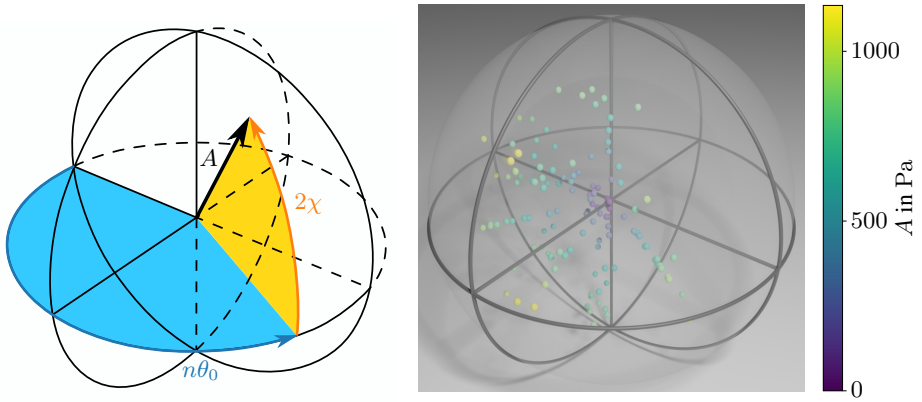

(a) Point description. (b) Forced states.

Figure 4.9: Poincaré sphere definition (a) from amplitude A, nature angle χ and orientation angle $n\theta_0$, and an example representing different forced states (b).

Here i, j and k are the three imaginary units of quaternions, c. c. is the complex conjugate of the preceding term and $\xi_1(t)$ and $\xi_2(t)$ are two real valued functions to be determined. The functions are obtained by rewriting the expression in Eq. (4.31b) as a least squares problem

$$\begin{bmatrix} \cos(n\theta_1) & \sin(n\theta_1) \\ \cos(n\theta_2) & \sin(n\theta_2) \\ \vdots & \vdots \\ \cos(n\theta_{N^*}) & \sin(n\theta_{N^*}) \end{bmatrix} \begin{bmatrix} \xi_1(t_i) \\ \xi_2(t_i) \end{bmatrix} = \begin{bmatrix} p'(\theta_1, t_i) \\ p'(\theta_2, t_i) \\ \vdots \\ p'(\theta_{N^*}, t_i) \end{bmatrix}. \tag{4.32}$$

Here N^* microphones are used, each measuring the pressure at azimuthal location θ_j. The functions ξ_1 and ξ_2 are calculated for each sample point t_i to obtain the full time series of ξ_a from Eq. (4.31a). The individual state space parameters A, χ, θ_0 and the temporal phase $\omega t + \varphi$ are then extracted from ξ_a by following the detailed step by step instructions in Appendix C in Ghirardo and Bothien (2018).

The fitting procedure described by Eq. (4.32) does not involve selecting an oscillation frequency. Therefore, the full frequency spectrum in the pressure signals on the right hand side are included when fitting the two functions ξ_1 and ξ_2. Most turbulent combustion chambers have non-negligible noise from the flow and combustion, and in some configurations higher harmonics are also present (Mazur et al., 2020; Indlekofer et al., 2021a). Therefore, the pressure signals are band-pass filtered around the frequency of interest before solving Eq. (4.32). The filter should be sufficiently wide to include the slow variation of the state space parameters, but higher harmonics have to be filtered out. The filter chosen here is a fifth order

Butterworth filter with forward and backward filtering, preserving the phase and therefore synchronisation with the camera images.

4.5 Phase averaging

The instantaneous heat release rate of the flames is significantly influenced by turbulent fluctuations, and the phase dependent dynamics of the flames are hard to discern in the instantaneous signal captured by the high speed camera. Due to the stochastic nature of the turbulent fluctuations of the heat release rate, the phase dependent dynamics can be extracted by *phase averaging* the captured heat release rate signal. The complex valued analytical signal $q_\mathrm{a} = q + \mathrm{i}\mathcal{H}[q]$ of the captured real valued heat release rate signal q is considered in the following for simplicity. The instantaneous signal can be split into three components

$$q_\mathrm{a}(\boldsymbol{x}, t) = \bar{q}(\boldsymbol{x}) + q'_\mathrm{a}(\boldsymbol{x}, t) + q'_\mathrm{s,a}(\boldsymbol{x}, t)\,, \tag{4.33}$$

where $\boldsymbol{x}$ is the spatial dependence. The temporal mean heat release rate is given by the real valued function $\bar{q}(\boldsymbol{x})$. The complex valued, phase dependent component is denoted $q'_\mathrm{a}(\boldsymbol{x}, t)$. By definition the phase dependent fluctuations have the property

$$q'_\mathrm{a}(\boldsymbol{x}, t) = q'_\mathrm{a}(\boldsymbol{x}, t + jT)\,, \tag{4.34}$$

where T is the period of oscillation and j is an integer. The turbulent fluctuations are described by the complex valued function $q'_\mathrm{s,a}$, which is defined such that

$$\lim_{N_\mathrm{im}\to\infty} \sum_{j=0}^{N_\mathrm{im}-1} q'_\mathrm{s,a}(\boldsymbol{x}, t + jT) = 0\,. \tag{4.35}$$

In practice the sum in Eq. (4.35) exhibits sufficient convergence for a finite number of samples N_im.

The phase average at reference time t_0 is then defined as

$$q'_\mathrm{a}(\boldsymbol{x}, t_0) = \sum_{j=0}^{N_\mathrm{im}-1} q_\mathrm{a}(\boldsymbol{x}, t_0 + jT) - \bar{q}(\boldsymbol{x})\,, \tag{4.36}$$

where N_im is the number of images at the same phase in the oscillation. Phase averaging should only be performed in cases where the mode is approximately constant in time. This is true for any given forced state in the current work, but for self-excited states additional conditioning on the pressure mode is required. An example of a single instantaneous sample and the corresponding phase average

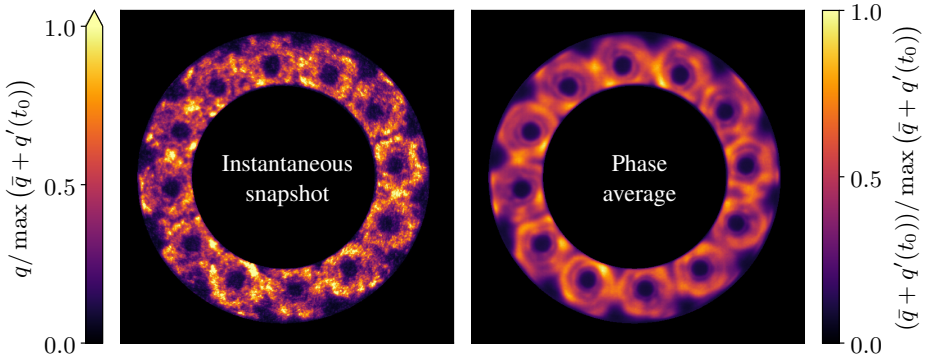

Figure 4.10: Phase average at temporal phase ωt_0 (*right*) and a snapshot of the instantaneous heat release rate at the same temporal phase (*left*). Note the explicit spatial dependence $\boldsymbol{x}$ is dropped for notational compactness in the colourbar.

is presented in Fig. 4.10, showing the stochastic turbulent fluctuations are significant. The number of images in each bin is $N_{\text{im}} \approx 550$ or more in the current work, which is sufficient to extract the phase dependent fluctuations for the studied configurations. The reference phase is chosen to be the pressure at the upper microphone location. In the annular combustor the first injector tube is used for phase reference. This required care to be taken to ensure the pressure node is never located at the first injector. The oscillation cycle is divided into M_{bin} phase bins of equal width, where each image is placed in the bin corresponding to the reference phase at the time of acquisition. After assigning each image to a phase bin, the phase average of each bin is obtained by calculating the mean value of each pixel.

4.6 Rotation averaging

The annular setup, described in §2.1, has N equidistantly spaced flames distributed in the azimuthal direction. The N flames should be identical by design, but in practice slight flame to flame differences exist. The rotationally symmetric geometry makes it a prime candidate for the use of Bloch theory (Bloch, 1929), which was introduced for solving the wave equation on a periodic lattice structure. The annulus with equidistantly spaced burner represents such a periodic setup in the azimuthal direction. Bloch theory was introduced for modelling of thermoacoustic instabilities in annular combustors by Mensah and Moeck (2015), where the computational domain was reduced to $1/N$ of the original size. Mensah and Moeck (2015) used this to calculate the response of a single injector by assuming all injectors are equal. However, Bloch theory can also be utilised for analysing experimental data,

which is the aim of the new procedure introduced in this work, defined as *rotation averaging*. By capturing the response of all N flames in the annular combustor, the response of an *average flame* is obtained by assuming all the flames are similar and performing rotation averaging, effectively averaging different phase averaged flames at the same point in the oscillation cycle.

This is of particular interest due to the effect of small asymmetries on the response of a single flame. Saurabh and Paschereit (2017, 2019) observed the response to the two different transverse forcing directions is not the same. This can be attributed to small imperfections in the manufacturing, mounting and approach flow, which are always present to some degree in practical setups. Acharya and Lieuwen (2014a, 2016, 2019) showed the response of a slightly asymmetric flame can be directly influenced by transverse oscillations, which is not the case for axisymmetric flames. The injectors in the annular combustor are designed to create axisymmetric flames from the perspective of the annulus – not the single flame, but each individual flame is not completely axisymmetric due to inevitable flame to flame differences. The flame to flame differences are likely to be distributed approximately equally around the desired symmetric flame case, assuming no systematic manufacturing, mounting or flow asymmetries. Therefore effects of flame to flame differences observed by Saurabh and Paschereit (2017, 2019) are assumed to be reduced for the average flame obtained by rotation averaging, where all the flame responses are averaged together.

The rotation averaging procedure was first introduced in Article II and applied in Article III, but the first rigorous mathematical derivation of the effect in terms of Bloch theory was presented in Article IV. The explanations in the following sections are therefore adapted from the latter paper, with some additional details to provide a more comprehensive account of this new procedure. First the rotation average of the temporal mean is discussed in §4.6.1, followed by the mathematical description for the fluctuating components in §4.6.2. Then the intuitive explanation is presented in §4.6.3, before introducing the reconstructed phase average in §4.6.4. Finally, the rotation average of the axial velocity is discussed in §4.6.5 followed by the reconstructed FDF in §4.6.6.

4.6.1 Temporal mean

The fundamental idea of rotation averaging is to average all N flames together, to obtain an average flame. The concept is most easily explained for the case of the temporal mean heat release rate $\bar{q}(r, \theta)$. The flames can be averaged together by rotating the annular geometry by an angle $2\pi/N$ around the central axis N times

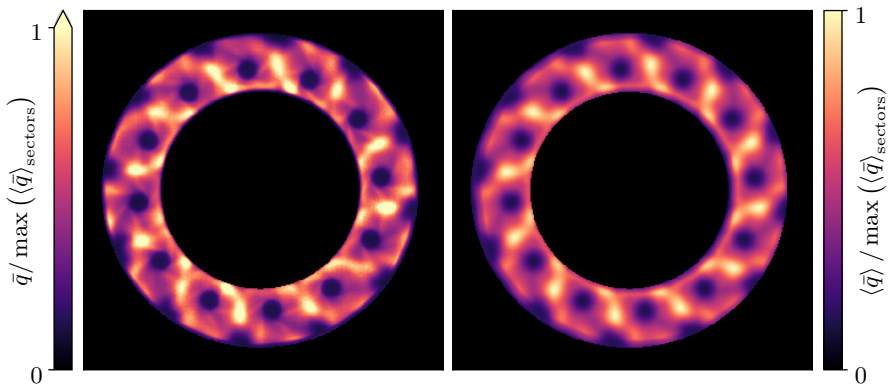

Figure 4.11: Temporal mean heat release rate (*left*) and the corresponding rotation average (*right*) for a $N = 12$ injector configuration of the annular combustor.

successively, and taking the average of all the N different rotations

$$\langle\bar{q}(r,\theta)\rangle_{\text{sectors}} = \frac{1}{N}\sum_{l=0}^{N-1}\bar{q}(r,\theta+2\pi l/N)\,. \tag{4.37}$$

Here the N fold rotational symmetry of the problem is exploited directly, and it is a straight forward averaging of each flame. The averaging reduces the spatial dependence of $\bar{q}(r,\theta)$ from the full annulus ($0 \leq \theta < 2\pi$) to a single sector ($0 \leq \theta < 2\pi/N$) for $\langle\bar{q}(r,\theta)\rangle_{\text{sectors}}$. The temporal mean heat release rates of the individual flames and of the corresponding average flame are presented in Fig. 4.11 for a $N = 12$ injector configuration. $N = 12$ copies of the average flame are shown for easier comparison. The structure of the average flame is observed to be similar to the structure of the individual flames, but there are some differences in the individual flames.

Obtaining the temporal mean of the average flame also enables the quantitative assessment of the flame to flame differences of the temporal mean heat release rate by subtracting the rotation average

$$\Delta\bar{q}(r,\theta) = \bar{q}(r,\theta) - \langle\bar{q}(r,\theta)\rangle_{\text{sectors}}\,. \tag{4.38}$$

This was performed in Article IV, where significant differences were observed within each flame. The differences were however both negative and positive within a single flame sector, resulting in low differences in the sector integrated temporal mean heat release rate.

4.6.2 Azimuthal fluctuations

The same fundamental idea of averaging all the flames together can also be used to introduce the rotation average of the fluctuating component of the heat release rate. However, the averaging operation is more complicated than for the temporal mean due to the phase dependence of the fluctuations and the degenerate nature of azimuthal modes. This is where Bloch theory (Bloch, 1929; Mensah and Moeck, 2015) is required. The base assumption is that the flames respond equally to a given fluctuation. For simplicity the only significant azimuthal component in the response is assumed to be the first azimuthal mode. This is reasonable in the current work, where the prescribed forced state is of the first azimuthal order. Additionally, the flames are assumed to only respond at the forcing frequency $f = \omega/2\pi$, which has been observed to be the dominating frequency in the pressure spectrum Fig. 4.6.

The analytical signal for the fluctuating heat release rate can then be expressed as

$$q'_{\mathrm{a}}(r,\theta,t) = \left[\psi_{-1}(r,\theta)\exp\left(-\mathrm{i}\theta\right) + \psi_{+1}(r,\theta)\exp\left(\mathrm{i}\theta\right) + \epsilon\Delta\hat{q}'_{\mathrm{a}}(r,\theta)\right]\exp\left(\mathrm{i}\omega t\right). \tag{4.39}$$

The spatially dependent amplitude of the heat release rate is described by the complex valued Bloch kernels $\psi_{\pm1}(r,\theta)$. The inclusion of two components accounts for the degeneracy of the first azimuthal mode, with ψ_{-1} describing the ACW spinning structure and the CW spinning structure described by ψ_{+1}. The flame to flame differences, which are inevitable in practical configurations, are accounted for by the last term $\epsilon\Delta\hat{q}'_{\mathrm{a}}$. This also allows for violations of the assumptions made before Eq. (4.39), making it possible to describe an arbitrary response. While it does not influence the derivations, the differences are assumed to be small, made explicit by the inclusion of $0 \leq \epsilon \ll 1$.

The Bloch kernels $\psi_{\pm1}$ are defined on a single flame sector, and are periodic in the azimuthal direction every $2\pi/N$

$$\psi_{\pm1}(r,\theta+2\pi/N) = \psi_{\pm1}(r,\theta)\,. \tag{4.40}$$

The flame to flame differences are by definition not periodic every $2\pi/N$, but are periodic every 2π

$$\Delta\hat{q}'_{\mathrm{a}}(r,\theta+2\pi) = \Delta q'_{\mathrm{a}}(r,\theta)\,, \tag{4.41}$$

due to $\theta + 2\pi$ being exactly the same azimuthal location as θ. Inspired by the rotation average of the temporal mean in Eq. (4.37), the rotation averages in the ACW $(-)$ and CW $(+)$ directions are introduced as

$$\left\langle q'_{\mathrm{a}}(r,\theta,t_0)\right\rangle^{\pm} = \frac{1}{N}\sum_{l=0}^{N-1} q'_{\mathrm{a}}(r,\theta\mp 2\pi l/N, t_0 + 2\pi l/(\omega N))\,. \tag{4.42}$$

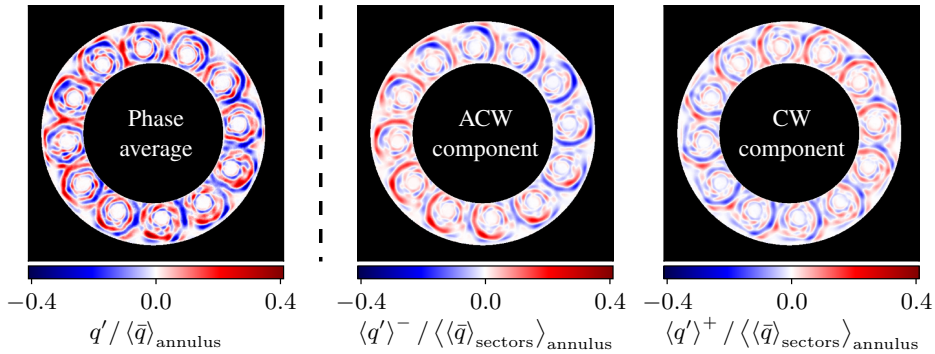

Figure 4.12: Phase average (*left*) and the corresponding ACW (*middle*) and CW (*right*) components of the rotation average for a standing mode ($\chi = 0.0$, $A \approx 710\,\mathrm{Pa}$) at arbitrary reference time t_0.

This corresponds to rotating the coordinate system by an angle $\mp 2\pi/N$ for each time step $2\pi/(\omega N)$. To perform this sum, the number of bins in the phase averaging has to be an integer multiple of the number of injectors N in the configuration. In the current work the oscillation cycle is divided into 36 equally wide phase bins, which is compatible with both $N = 12$ and $N = 18$ injector configurations. The left hand side of Eq. (4.42) will hereafter be referred to as the *rotation average component* in the ACW $(-)$ or CW $(+)$ direction.

The rotations $\theta \mp 2\pi l/N$ are the same as for the temporal mean rotation average in Eq. (4.37). However, due to the time dependence of the fluctuations, care has to be taken when choosing the temporal phase for each rotation step. The choice made in Eq. (4.42) will in the following be shown to correspond to

$$\left\langle q'_{\mathrm{a}}(r,\theta,t_0)\right\rangle^{\pm} = \psi_{\pm 1}(r,\theta)\exp\left(\pm \mathrm{i}\theta\right)\exp\left(\mathrm{i}\omega t_0\right). \tag{4.43}$$

This is equivalent to the azimuthal wave component defined by $\psi_{\pm 1}$ in Eq. (4.39), where the temporal phase ωt_0 is determined by the chosen reference time t_0. It is also trivial to generalise this approach to extract higher order azimuthal modes, but that is not relevant for the current work where the first azimuthal mode is the only significant mode. Figure 4.12 shows an example of how Eq. (4.42) splits the heat release rate fluctuations of a standing pressure mode into the two spinning components according to Eq. (4.43).

To prove that Eq. (4.42) and Eq. (4.43) are equivalent, the flame to flame differences $\Delta\hat{q}'_{\mathrm{a}}$ are expressed as

$$\Delta\hat{q}'_{\mathrm{a}}(r,\theta,t) = \sum_{b=-\infty}^{\infty} \psi''_b(r,\theta)\exp\left(\mathrm{i}b\theta\right), \tag{4.44}$$

Here $\psi''_b(r,\theta)\exp(\mathrm{i}b\theta)$ is an azimuthal wave of order b, and the sum is performed over all possible Bloch wavenumbers b. The Bloch wave kernels ψ''_b are again N fold rotationally symmetric

$$\psi''_b(r,\theta+2\pi/N)=\psi''_b(r,\theta)\,. \tag{4.45}$$

The expression in Eq. (4.44) is valid for an arbitrary response since the the Bloch wave functions are linearly independent and all possible wave numbers b are included. The sum also includes $b=\pm1$, but all components with wavenumbers $b=\pm1$ are *by definition* part of the $\psi_{\pm1}$ terms in Eq. (4.39). Therefore, $\psi''_{\pm1}=0$ and the sum in Eq. (4.44) can be expressed as

$$\Delta\hat{q}'_\mathrm{a}(r,\theta,t)=\sum_{b\neq\pm1}\psi''_b(r,\theta)\exp(\mathrm{i}b\theta)\,, \tag{4.46}$$

without loss of generality of Eq. (4.39). The Bloch wave components of the first azimuthal order are rewritten to

$$\begin{aligned}
&\psi_{\pm1}(r,\theta)\exp(\pm\mathrm{i}\theta)\exp(\mathrm{i}\omega t)\\
&=\frac{1}{N}\sum_{l=0}^{N-1}\psi_{\pm1}(r,\theta)\exp(\pm\mathrm{i}\theta)\exp(\mathrm{i}\omega t)\exp(\mathrm{i}(1-1)2\pi l/N)\\
&=\frac{1}{N}\sum_{l=0}^{N-1}\psi_{\pm1}(r,\theta\mp2\pi l/N)\exp(\pm\mathrm{i}(\theta\mp2\pi l/N))\exp(\mathrm{i}\omega(t+2\pi l/(\omega N)))\,,
\end{aligned} \tag{4.47}$$

where the periodicity $\psi_{\pm1}(r,\theta)=\psi_{\pm1}(r,\theta\mp2\pi l/N)$ is exploited in the last step. Inserting Eq. (4.46) into the rotation average definition in Eq. (4.42) and taking advantage of the rewrite in Eq. (4.47) yields the equivalence of the rotation average components and the azimuthal Bloch waves shown in Eq. (4.43). This requires exploiting the N fold rotational symmetry of the Bloch kernels $\psi_{\pm1}$ and ψ''_b, as well as recognising the following sum property

$$\frac{1}{N}\sum_{l=0}^{N-1}\exp(\mathrm{i}m2\pi l/N)=\begin{cases}0 & \text{for } m\neq0\\ 1 & \text{for } m=0\end{cases}\,. \tag{4.48}$$

While the derivation of this result relied on the analytical, complex valued heat release rate signals, it is worth noting that it also applies to the real valued heat release rate captured by the cameras. All the operations required to calculate the rotation average in Eq. (4.42) are summation, rotation and rescaling by a constant factor, which are all linear operations. Therefore, the real and complex parts of the

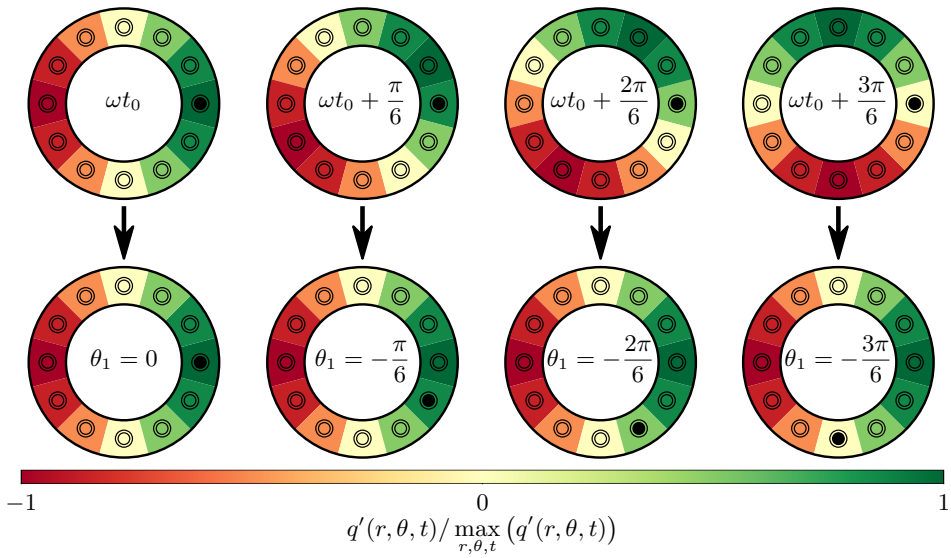

Figure 4.13: Illustration of using the ACW rotation average on a purely ACW mode, showing the phase average at different points in the cycle both before (*top*) and after (*bottom*) the rotation. The injector located at θ_1 in the original coordinate system is highlighted by the filled inner circle.

analytical signal can be treated separately, and the real part of the analytical signal is the measured heat release rate signal. In practice the rotation averaging is only performed on the real valued image data, and the imaginary part is obtained from spectral analysis afterwards if desired.

4.6.3 Alternative description of rotational averaging

The rotation averaging process can alternatively be explained in slightly more intuitive terms. Assume the total heat release pattern is a superposition of two patterns rotating in opposite directions. Then each component will propagate around the annulus in the time $2\pi/\omega$, which is the period of oscillation. Due to the symmetry of having N equidistantly spaced injectors in the annulus, each of the patterns should travel the same distance for each time step $2\pi/(\omega N)$, and the azimuthal distance is as such $2\pi/N$.

Considering the response of just an ACW propagating component, for each time step $2\pi/(\omega N)$ the pattern propagates an azimuthal distance $2\pi/N$ in the ACW direction. By rotating the combustion chamber (or the overhead images) an azimuthal distance $2\pi/N$ in the opposite, CW direction for each step, the pattern is effectively frozen in space. This is illustrated for a simple and purely ACW

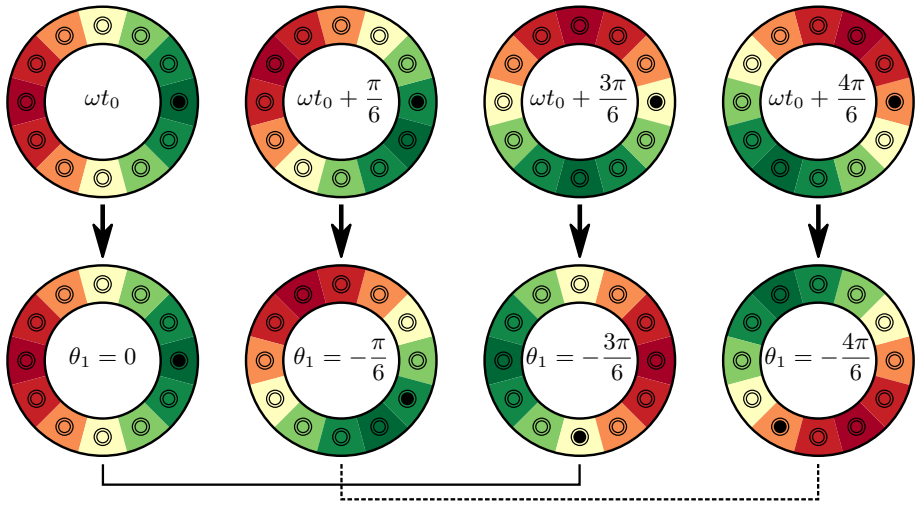

Figure 4.14: Illustration of using the ACW rotation average on a purely CW mode, showing the phase average at different points in the cycle both before (*top*) and after (*bottom*) the rotation. The injector located at θ_1 is highlighted by the filled inner circle. Colourbar is the same as in Fig. 4.13.

spinning pattern in Fig. 4.13. Each of the N injectors is located at a new injector location for each of the N steps, as illustrated by the different locations θ_1 of the first injector in Fig. 4.13. Therefore, averaging these N rotated combustor images together averages all the flames together for the same phase in the ACW propagating heat release rate pattern. This is the basic idea of the rotation average. Additionally, any CW component in this example would rotated twice as fast compared to when the phase averages are not rotated. This is illustrated in Fig. 4.14 for selected points in the phase average of a purely CW mode. By grouping the N points in the phase averaged series in pairs, where the temporal phase difference between the two averages in each pair is separated by $\pi/2$, it is observed the rotation average is zero, as expected from the mathematical derivation. The pairings are illustrated by the solid and dashed lines in Fig. 4.14. The cancellation still holds for odd number of injectors N, but the explanation is not as intuitive.

In practice this is the implementation used in the current work, where actual rotation of the heat release rate images captured from directly downstream of the annular combustor is used. For a low number of injectors N, the time resolution might not be satisfactory using this approach with only N time steps. However, this is improved by splitting the phase average into an integer multiple of the number of injectors N and treating it as multiple time series, each with N samples

separated by a time $2\pi/(\omega N)$. Each of these time series are used to obtain rotation averages with slightly different temporal phase, which in turn can be used to create a reconstruction, described in the following subsection, with finer time resolution.

4.6.4 Reconstruction of the phase average

According to Eq. (4.43) the rotation average components equal the azimuthal Bloch wave components in the given directions, which describes the response of the average flame to perturbations in that direction. This can be used to reconstruct the total heat release rate signal for a combustor consisting of only average flames. The rotation averaging process merges space and time, and the reconstructed response is obtained by reversing this process, separating space and time again. The reconstructed response at time $t_l = t_0 + l2\pi/(\omega N)$ is defined as

$$q_a'^{,\mathrm{rec}}(r,\theta,t_l) = \left\langle q_a'(r,\theta+2\pi l/N,t_0)\right\rangle^{+} + \left\langle q_a'(r,\theta-2\pi l/N,t_0)\right\rangle^{-} . \quad (4.49)$$

Inserting Eq. (4.43) into the right hand side and gathering the $2\pi l/N$ terms in the time exponent yields

$$q_{\mathrm{a}}'^{,\mathrm{rec}}(r,\theta,t_l) = \left[\psi_{-1}(r,\theta)\exp\left(-\mathrm{i}\theta\right) + \psi_{+1}(r,\theta)\exp\left(\mathrm{i}\theta\right)\right]\exp\left(\mathrm{i}\omega t_l\right). \quad (4.50)$$

This is equivalent to the definition of the heat release rate fluctuations in Eq. (4.39) without the flame to flame differences $\epsilon\Delta\hat{q}_{\mathrm{a}}'(r,\theta)$. Similar to the rotation average definitions this is shown for the analytical description, but it also holds for the real and imaginary parts separately as only linear operations are required. Figure 4.15 shows the reconstructed phase average at a given phase of a standing pressure mode based on the rotation average components in Fig. 4.12.

Similar to the reconstruction in Eq. (4.49), the time evolution of just one of the spinning components can be obtained by rotation

$$\left\langle q_a'(r,\theta,t_l)\right\rangle^{\pm} = \left\langle q_a'(r,\theta\pm 2\pi l/N,t_0)\right\rangle^{\pm} . \quad (4.51)$$

This also demonstrates how the concept of temporal phase and space is combined into a single image. For a single rotation average component a rotation is equivalent to a change in temporal phase, and a change in temporal phase is equivalent to a rotation. The rotations are always restricted to discrete values that are a multiple of $2\pi/N$ to keep the injector locations constant. Another interpretation of this is that a single rotation average component image, as shown in Fig. 4.12, represents the heat release rate response of the average flame for N discrete temporal phases at once.

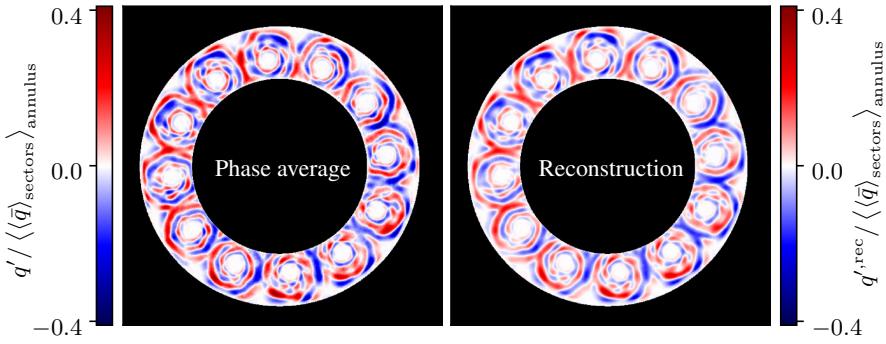

Figure 4.15: Phase average at arbitrary time t_0 (*left*) and the corresponding reconstruction (*right*) based on rotation averaging for a standing pressure mode ($\chi = 0.0$, $A \approx 710\,\text{Pa}$).

4.6.5 Azimuthal axial velocity components

The axial velocity in the injector located at azimuthal location θ_j is related to the local pressure fluctuations through a geometry specific impedance $z(\omega)$, as mentioned in Eq. (1.4). The azimuthal pressure modes of interest in this work are of the first azimuthal order and are given by either the orthogonal description in Eq. (4.23) or the quaternion formalism in Eq. (4.27). Each flame sector spans an angle of $\pi/6$ or less of the full annulus in the current configurations, and the injector itself even less. Therefore, the azimuthal wavelength of 2π is large compared to the span of the injector openings. This enables the pressure at the injector centred at $\theta = \theta_j$ to be approximated as the pressure in the centre of the injector. For a given impedance $z(\omega)$ the Fourier amplitude of the axial velocity at the injector is given by

$$\begin{aligned} \hat{u}'_{\text{axial}}(\theta_j) &= z\left[A_+ \exp\left(-\mathrm{i}\theta_j\right) + A_- \exp\left(\mathrm{i}\theta_j\right)\right] , \\ &= \psi^u_{-1} \exp\left(-\mathrm{i}\theta_j\right) + \psi^u_{+1} \exp\left(\mathrm{i}\theta_j\right) , \end{aligned} \tag{4.52}$$

where the orthogonal pressure description in Eq. (4.23) is used for the first azimuthal mode $n = 1$. This describes the axial acoustic velocity perturbations as two azimuthally spinning components propagating in opposite directions, a concept which is denoted *azimuthal axial velocity components* hereafter.

It is important to note the sign convention change in Eq. (4.52)

$$\psi^u_{\pm 1} = z A_{\mp} \,. \tag{4.53}$$

While not ideal, it is considered the lesser evil, as it allows the notation to be consistent with previous Bloch theory work (Mensah and Moeck, 2015) and the

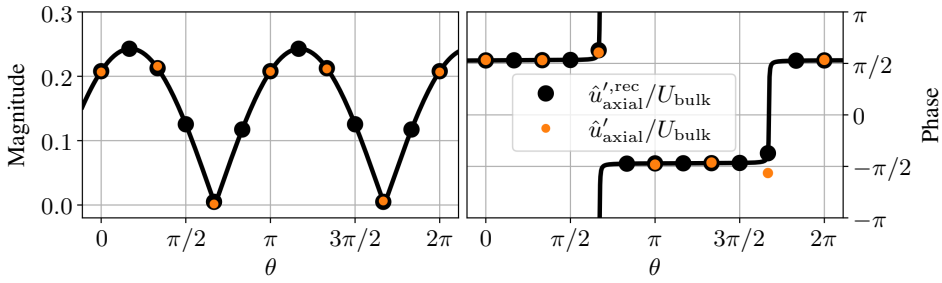

Figure 4.16: Experimentally determined axial velocity for a standing mode in the annular combustor with $N = 12$ injectors, of which $N^* = 6$ are instrumented. The reconstructed axial velocity in all $N = 12$ injectors is presented in black markers, with the solid line representing the interpolation between injector locations.

derivation in §4.6.2 while also being consistent with the sign convention in previous pressure mode descriptions (Wolf et al., 2012; Worth and Dawson, 2013a; Bourgouin et al., 2013). Equation (4.52) has a similar form to the Fourier amplitude of the Bloch theory description of the heat release rate in Eq. (4.39), and as such it is interesting to split the response into the two separate components.

Similar rotation averaging operations as Eq. (4.42) are introduced for the azimuthal axial velocity components as

$$\left\langle \hat{u}'_{\mathrm{axial}}(\theta_j) \right\rangle^{\pm} = \frac{1}{N^*} \sum_{l=0}^{N^*-1} \hat{u}'_{\mathrm{axial}}(\theta_j \mp 2\pi l/N^*) \exp\left(\mathrm{i}2\pi l/N^*\right). \tag{4.54}$$

Here N^* is the number of instrumented injectors, which are assumed to be equidistantly distributed at locations $\theta_j = 2\pi j/N^*$. In the current work only some of the injectors are instrumented, with either $N^* = 3$ in Article II, Article III, and Article V or $N^* = 6$ in Article IV. Since the pressure mode is relatively well behaved and understood compared to heat release rate modes in such configurations, this does not introduce significant uncertainty in the average response. Inserting Eq. (4.52) into Eq. (4.54) yields

$$\left\langle \hat{u}'_{\mathrm{axial}}(\theta_j) \right\rangle^{\pm} = \psi^u_{\pm 1} \exp\left(\pm \mathrm{i}n\theta_j\right), \tag{4.55}$$

after a similar derivation to the one performed in §4.6.2. Similar to Eq. (4.49) the reconstructed velocity is defined as

$$\hat{u}'^{,\mathrm{rec}}_{\mathrm{axial}}(\theta_j) = \left\langle \hat{u}'_{\mathrm{axial}}(\theta_j) \right\rangle^{-} + \left\langle \hat{u}'_{\mathrm{axial}}(\theta_j) \right\rangle^{+} \tag{4.56}$$

This does not provide the same value in averaging together the different flames in Eq. (4.39) due to the well behaved acoustic mode and clear spatial separation of

injectors. However, it does provide additional value in that the Fourier amplitude of the acoustic axial velocity can be calculated for *all* the injector tubes, and not only the instrumented ones. The experimentally determined velocity and the corresponding reconstruction is presented in Fig. 4.16 for the same standing mode as in Fig. 4.12 and Figure 4.15, showing excellent agreement between experimentally obtained and reconstructed values.

The following notational simplification is introduced to be more consistent with the notation for the integrated heat release rate of the jth sector

$$\left\langle \hat{u}'_{\text{axial}} \right\rangle_j^{\pm} = \left\langle \hat{u}'_{\text{axial}}(\theta_j) \right\rangle^{\pm} , \tag{4.57a}$$

$$\hat{u}'^{,\text{rec}}_{\text{axial},j} = \hat{u}'^{,\text{rec}}_{\text{axial}}(\theta_j) . \tag{4.57b}$$

Here θ_j is the centre location of the jth injector, and the velocity signal with subscript j is the reference acoustic axial velocity for the corresponding flame sector.

4.6.6 Reconstructed Flame Describing Function

Both the reconstructed heat release rate fluctuations and the reconstructed acoustic axial acoustic velocity are introduced in the preceding sections. These are now used to define the reconstructed FDF, which is the FDF of the average flame for different positions in the pressure mode. The reconstructed FDF for the jth flame is defined as

$$\text{FDF}_j^{\text{rec}} \left(\left| \hat{u}'^{,\text{rec}}_{\text{axial},j} \right| \right) = \frac{\left\langle \hat{q}'^{,\text{rec}} \right\rangle_j \,/\, \left\langle \left\langle \bar{q} \right\rangle_{\text{sectors}} \right\rangle_j}{\hat{u}'^{,\text{rec}}_{\text{axial},j} / U_{\text{bulk}}} , \tag{4.58}$$

where $\langle \bar{q} \rangle_{\text{sectors}}$ is the rotation averaged temporal mean heat release rate. The rotation averaged temporal mean heat release rate is chosen to ensure no flame to flame differences are included in the reconstructed FDF definition. Note the hat on $\hat{q}'^{,\text{rec}}$ in Eq. (4.58), which is the Fourier amplitude of the reconstructed analytical signal $q'^{,\text{rec}}_{\text{a}}$. The reconstructed FDFs based on the experimentally determined FDF data in Fig. 4.1 are presented in Fig. 4.17. The trends are observed to be the same in both figures, but slightly highlighted in the reconstructed version due to the increased number of points.

All of the quantities in Eq. (4.58) are defined to be independent of any flame to flame differences. However, in practice there might be small differences between the different sectors. This is believed to be mostly influenced by the mask definitions for the sector average operations ($\langle (\cdot) \rangle_j$). The annular geometry suggest that a coordinate system defined using cylindrical coordinates would be optimal, but the camera captures pixel data on a square grid. Defining the mask for each single flame sector in the annular burner is therefore done on a square grid, even though they are defined by radial lines and lines of constant radius. The effect of this is

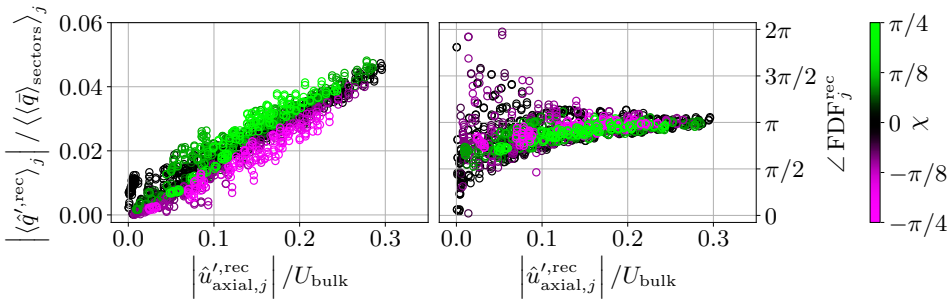

Figure 4.17: Example of the reconstructed FDF calculated from the experimentally obtained FDF values at frequency $f = 1650\,\mathrm{Hz}$ presented in Fig. 4.1. The reconstructed heat release rate magnitude is presented on the left and the phase of the reconstructed FDFs is presented on the right. All injectors are represented by a point for each forced state. The interpretation of the figure is presented in Article IV.

all the masks are not perfectly identical in the number of included pixels, which can lead to small differences. Additionally, there might be small differences in the masks caused by imperfect centring. However, for a single annular combustor configuration the same masks are used for all the different forced states. Therefore the effect of mask differences is reduced when setting up spinning modes, where all the flames should be subjected to the same pressure amplitudes and all the responses should be the same. They are also reduced in the case of mixed and standing pressure modes by repeating the mode for different orientation angles θ_0. The differences can have a small impact when a single forced state is considered, but the trends should be independent of the mask imperfections when full data sets are considered.

4.7 Azimuthal Flame Describing Functions

Now that each component of both the heat release rate and the azimuthal axial acoustic velocity perturbations are known, it is natural to define the *Azimuthal Flame Describing Function*

$$\mathrm{FDF}^{\pm}\left(\left|\langle\hat{u}'_{\mathrm{axial}}\rangle^{\pm}\right|\right) = \frac{1}{N}\sum_{j=0}^{N-1}\frac{\left\langle\langle\hat{q}'\rangle^{\pm}\right\rangle_j / \langle\langle\bar{q}\rangle_{\mathrm{sectors}}\rangle_j}{\langle\hat{u}'_{\mathrm{axial}}\rangle^{\pm}_j / U_{\mathrm{bulk}}}\,. \tag{4.59}$$

The magnitude of azimuthal axial acoustic velocity perturbations $\langle\hat{u}'_{\mathrm{axial}}\rangle^{\pm}_j$ for a given direction is the same for all injectors j by definition, which is why the subscript j is dropped on the left hand side. However, as previously mentioned, there

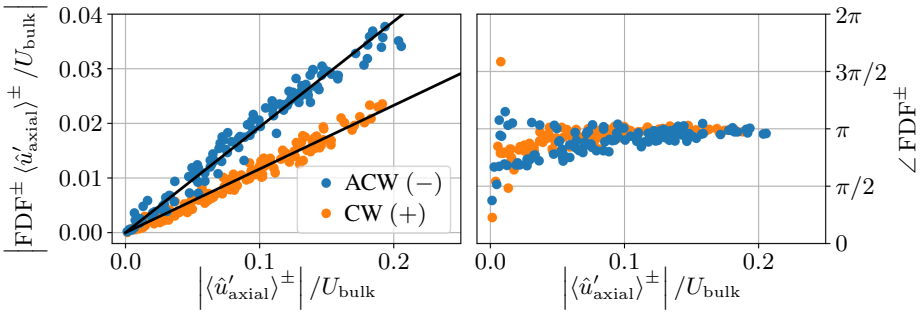

Figure 4.18: Example of the two Azimuthal FDF components obtained experimentally in an annular combustor with swirl. The heat release rate magnitude is presented on the left and the phase of the Azimuthal FDF is presented on the right. The solid lines on the left are the linear interpolation of each component.

are some differences introduced by differences in masks separating the different flames. Therefore the Azimuthal FDF values in Eq. (4.59) are defined as the average over all injectors j. It is worth noting there are only two Azimuthal FDF values in Eq. (4.59) for a given forced state, the ACW $(-)$ component and the CW $(+)$ component. This is in contrast to the N different values in the more conventional FDF in Eq. (4.2). This makes it easier to extract the global trends of the response to a given forced state, due to having a single fixed perturbation amplitude and no flame to flame differences.

The Azimuthal FDF describes the response of the average flame to the azimuthal axial velocity perturbation component in a given direction. This makes it possible to quantify how the response in the ACW direction to the ACW component of the azimuthal axial velocity perturbations compare to the response in the CW direction to the CW component. As shown in Fig. 4.18, the response to the same perturbation level in the two directions are not the same in the swirled flame configuration studied in this work. Comparing this to the conventional FDF in Fig. 4.1 and the corresponding reconstruction in Fig. 4.17, the difference in response is much clearer in the Azimuthal FDF in Fig. 4.18. Therefore the Azimuthal FDF is preferred over the conventional FDF for extracting the global features of the heat release rate response to azimuthal pressure modes. The in-depth explanation of this, and further discussion of the interpretation of Fig. 4.18, are found in Article IV.

4.7.1 Azimuthal heat release rate mode

Another advantage of introducing the Azimuthal FDF is the possibility of describing a heat release rate mode based on the sector integrated values, similar to the pressure mode in Eq. (4.23). The Fourier amplitude of the sector integrated average heat release rate response is defined as

$$\frac{\langle \hat{q}'^{,\mathrm{rec}} \rangle_j}{\langle \langle \bar{q} \rangle_{\mathrm{sectors}} \rangle_j} = \mathrm{FDF}^+ \left(\left| \langle \hat{u}'_{\mathrm{axial}} \rangle^+ \right| \right) \frac{\langle \hat{u}'_{\mathrm{axial}} \rangle_j^+}{U_{\mathrm{bulk}}} + \mathrm{FDF}^- \left(\left| \langle \hat{u}'_{\mathrm{axial}} \rangle^- \right| \right) \frac{\langle \hat{u}'_{\mathrm{axial}} \rangle_j^-}{U_{\mathrm{bulk}}} \tag{4.60}$$

Here the Azimuthal FDFs ($\mathrm{FDF}^{\pm}$) can either be given by the two values from a specific forced state, or from the fitted general values presented as the solid black lines in Fig. 4.18. According to Eq. (4.55) the azimuthal axial acoustic velocity perturbations in injector j can be expressed in terms of the perturbations of injector $j = 0$

$$\langle \hat{u}'_{\mathrm{axial}} \rangle_j^{\pm} = \psi_{\pm 1}^u \exp\left(\pm \mathrm{i}\theta_j\right) = \langle \hat{u}'_{\mathrm{axial}} \rangle_{j=0}^{\pm} \exp\left(\pm \mathrm{i}\theta_j\right), \tag{4.61}$$

where $\theta_j = 2\pi j/N$ is the centre location of the jth injector. The expression in Eq. (4.60) therefore describes the sector integrated heat release rate as the sum of two plane waves propagating in opposite directions

$$\frac{\langle q_{\mathrm{a}}^{\prime,\mathrm{rec}} \rangle_j}{\langle \langle \bar{q} \rangle_{\mathrm{sectors}} \rangle_j} = \left[\mathcal{Q}^+ \exp\left(\mathrm{i}\theta_j\right) + \mathcal{Q}^- \exp\left(-\mathrm{i}\theta_j\right) \right] \exp\left(\mathrm{i}\omega t\right) \tag{4.62}$$

Note the absence of the hat and introduction of subscript a in $q_{\mathrm{a}}^{\prime,\mathrm{rec}}$ due to the introduction of the term $\exp\left(\mathrm{i}\omega t\right)$. The complex valued amplitudes $\mathcal{Q}^{\pm}$ are given by

$$\mathcal{Q}^{\pm} = \mathrm{FDF}^{\pm} \left(\left| \langle \hat{u}'_{\mathrm{axial}} \rangle^{\pm} \right| \right) \frac{\langle \hat{u}'_{\mathrm{axial}} \rangle_{j=0}^{\pm}}{U_{\mathrm{bulk}}}. \tag{4.63}$$

Equation (4.62) is of the exact same form as Eq. (4.23) for $n = 1$, but the difference in sign convention between the two definitions should be noted. Here $+$ and $-$ corresponds to CW and ACW component respectively, opposite of Eq. (4.23). The pressure expression in Eq. (4.23) is denoted the pressure mode, and similarly the heat release rate expression in Eq. (4.62) will hereafter be denoted the *heat release rate mode*.

Similar to the nature angle of the azimuthal pressure mode, the nature angle for the heat release rate mode is defined as

$$\chi_q = \arctan\left(\frac{|\mathcal{Q}^-| - |\mathcal{Q}^+|}{|\mathcal{Q}^-| + |\mathcal{Q}^+|} \right). \tag{4.64}$$

The values of χ_q have the same interpretation as for χ, with perfectly spinning modes for $\chi_q = \pm\pi/4$ and standing modes for $\chi_q = 0$. The most interesting

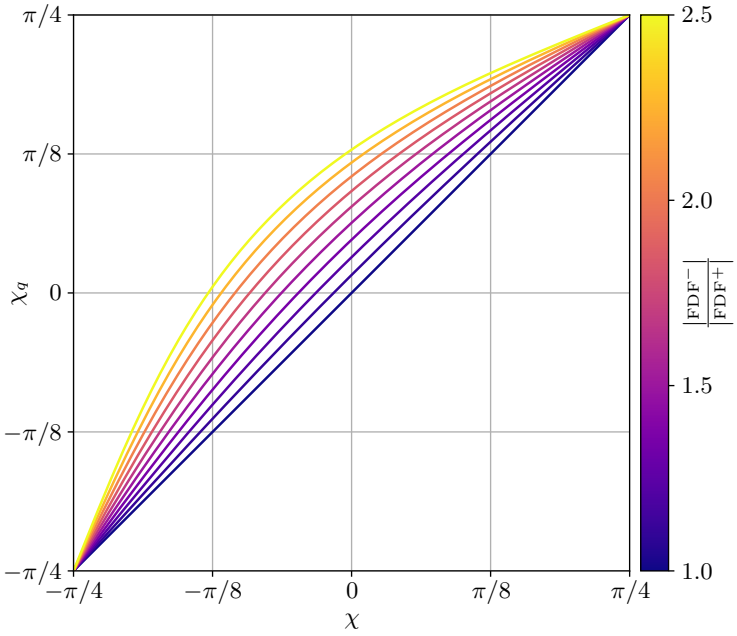

Figure 4.19: Nature angle of the pressure mode χ and the heat release rate χ_q modes for select values of the ratio of the ACW and CW Azimuthal FDF magnitude. All the examples are for cases with $\left|\mathrm{FDF}^-\right| \geq |\mathrm{FDF}|^+$. A magnitude ratio less than unity results in $\chi_q \leq \chi$.

feature of the definition in Eq. (4.64) is that the nature angle of the heat release rate χ_q is not necessarily the same as the nature angle of the pressure mode χ. Inserting Eq. (4.52), Eq. (4.55) and Eq. (4.63) into Eq. (4.64) yields the following expression for the nature angle of the heat release rate mode

$$\chi_q = \arctan\left(\frac{\left|\mathrm{FDF}^-\right||A_+| - \left|\mathrm{FDF}^+\right||A_-|}{\left|\mathrm{FDF}^-\right||A_+| + \left|\mathrm{FDF}^+\right||A_-|}\right). \tag{4.65}$$

Note the explicit velocity amplitude dependence $\left|\langle\hat{u}'_{\mathrm{axial}}\rangle^{\pm}\right|$ of the Azimuthal FDFs ($\mathrm{FDF}^{\pm}$) is dropped for notational compactness, but should be included in the calculations if required.

The nature angle χ_q in Eq. (4.65) is in general *not* equal to the nature angle of the pressure mode χ defined in Eq. (4.29). For purely spinning pressure modes $\chi = \pm\pi/4$ the two nature angles are equal by definition, due to only perturbing one of the spinning modes. Otherwise the response is dependent on the magnitude ratio of the two Azimuthal FDF components $\left|\mathrm{FDF}^-\right| / \left|\mathrm{FDF}^+\right|$. The only case where χ_q and χ are equal for all values of χ is when both directions have an equal magnitude response to a given perturbation level $\left|\mathrm{FDF}^-\right| / \left|\mathrm{FDF}^+\right|$. The difference in nature angle is illustrated in Fig. 4.19 for a logarithmic range of Azimuthal FDF magnitude ratios. The example shows $\chi_q \geq \chi$ when the ACW component of the Azimuthal FDF has a larger magnitude than the CW component. If the CW component has a larger magnitude than the ACW component, the nature angle of the heat release rate mode would be lower than the pressure mode ($\chi_q \leq \chi$). The results presented in Article IV demonstrate this difference in the two nature angles.

4.7.2 Processing steps to obtain Azimuthal FDF

There are relatively many steps required to obtain the Azimuthal FDF based on the camera images and using the rotation averaging, and most of the steps should be performed in a specific order. These steps are summarised in the process diagram in Fig. 4.20.

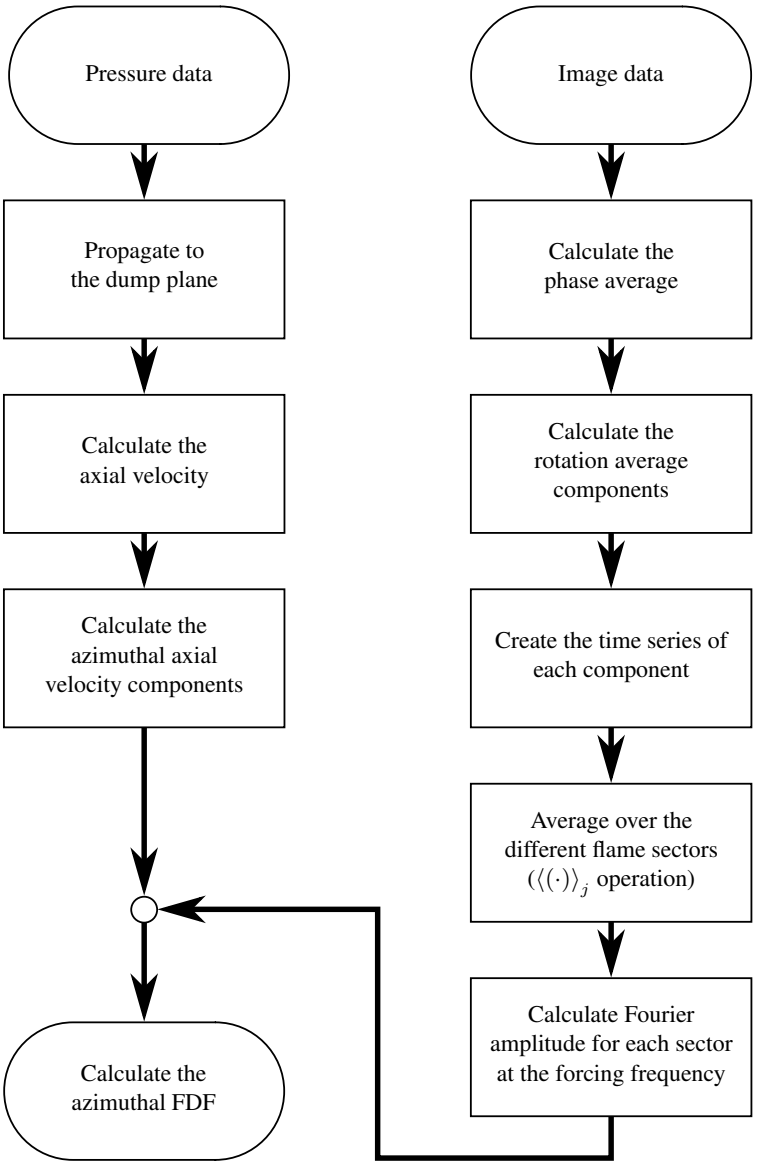

Figure 4.20: Process diagram of how to calculate the Azimuthal FDF from the sampled data. Note this assumes the image and pressure data are synchronised before the first step.

Chapter 5

Summary of research articles

This thesis contains five research articles, one concentrating on the characterisation of an isolated flame subjected to axial velocity perturbations and four focusing on the response of an annular combustor to azimuthal pressure modes. The research goals set out in the introduction are addressed in these articles, which are included at the end of this thesis. In the following a short summary of the content and novel contributions of each article is presented.

Article I

Flame transfer functions and dynamics of a closely confined premixed bluff body stabilized flame with swirl.
Håkon T. Nygård, Nicholas A. Worth (2021). *Journal of Engineering for Gas Turbines and Power*, 143(4):041011.

Article I addresses research goal i) from the introduction. A single flame setup made to resemble the geometry of a single sector in the annular combustor is characterised through the Flame Transfer Function, obtained by applying axial acoustic forcing. The response is obtained for a wide range of operating conditions as well as frequencies. This makes it a valuable reference case for the other articles, which focus on the response to azimuthal pressure modes in annular combustion chambers. Additionally, the relevant time delays in the problem are extracted through the use of distributed time delay models, further characterising the response. The response of the flame was observed to depend on the effective confinement for the lower frequency range. The dip phenomenon typically observed in swirling flames was suppressed for sufficiently high relative confinement. The effect was however observed to be small for the higher frequency range observed in the annular combustor.

Article II

Flame dynamics of azimuthal forced spinning and standing modes in an annular combustor.
Håkon T. Nygård, Marek Mazur, James R. Dawson, Nicholas A. Worth (2019). *Proceedings of the Combustion Institute*, 37(4):5113–5120.

Article II is the first step in properly addressing research goal ii) and iii) in the introduction. In this article the azimuthally forced response of an annular combustor with swirl is presented for the first time for different spin ratios. An anti-clockwise spinning, a clockwise spinning and a standing mode were investigated for a $N = 18$ injector configuration of the annular combustor, extending previous forced data which was restricted to standing modes. A number of differences in the spatial structure of the heat release rate perturbations were observed for the different modes, and most interestingly it was concluded that the amplitude might depend on the spin ratio of the mode. Additionally, the rotation averaging technique was introduced for the first time for thermoacoustic instabilities.

Article III

Characteristics of self-excited spinning azimuthal modes in an annular combustor with turbulent premixed bluff-body flames.
Marek Mazur, Håkon T. Nygård, James R. Dawson, Nicholas A. Worth (2019). *Proceedings of the Combustion Institute*, 37(4):5129–5136.

Article III is related to research goal iii) in the introduction. The annular combustor with $N = 12$ injectors is studied in a self-excited configuration where all the swirlers have been removed. The stability map and modal dynamics are presented for a range of operating conditions. Most operating conditions were observed to exhibit both anti-clockwise and clockwise modes, which is not the case for the swirled configurations. Additionally, the spatial structure of the heat release rate oscillations are examined in detail for each of the spinning directions by performing the rotation average. The two directions are observed to result in a very similar response, but mirrored around the radial plane intersecting the injector centres. This is in contrast to the broken reflectional symmetry of the swirled configurations used in *Article II*, *Article IV* and *Article V*. It also suggest the response amplitude is most likely not dependent on the nature of the azimuthal mode for this unswirled configuration, which is part of research goal iii).

Article IV

Azimuthal flame response and symmetry breaking in a forced annular combustor.
Håkon T. Nygård, Giulio Ghirardo, Nicholas A. Worth (2021). *Under consideration for publication in Combustion and Flame*.

Article IV is the second, and last, step in addressing research goal ii) and iii) in the introduction. The technique used in *Article II* to force three different pressure modes is improved to be able to force an arbitrary azimuthal mode of the first order up to a finite amplitude limit imposed by the speakers. This fulfils the objective set out in research goal ii). The studied annular combustor configuration consists of $N = 12$ injectors, all equipped with a swirler imposing anti-clockwise swirl when viewed from downstream. A total of 123 different forced states for the current configuration are presented, and used to characterise the heat release rate response to the different pressure modes. It is shown conclusively that the response depends on the nature of the pressure mode for a given forcing amplitude for this configuration with non-negligible annulus width and co-swirling flames. The response in the anti-clockwise direction was observed to be higher than the response in the clockwise direction for the same perturbation amplitude. To be able to show this, the rotation averaging is explained in terms of Bloch theory, and the concept of the Azimuthal Flame Describing Function is introduced. This also allowed some interesting phenomenon observed in the conventional Flame Describing Function to be explained, and was shown to result in a difference in mode nature for the pressure and heat release rate modes.

Article V

Symmetry breaking modelling for azimuthal combustion dynamics.
Giulio Ghirardo, Håkon T. Nygård, Alexis Cuquel, Nicholas A. Worth (2021). *Proceedings of the Combustion Institute*, 38(4):5953–5962.

Article V addresses research goal iii) in the introduction by examining the effect of a spinning state dependence of the gain response on the self-excited pressure mode. Analysis of the pressure mode is presented for a case with small flame to flame differences, and numerical simulations are presented for a case where the flames respond stronger to the anti-clockwise component than the clockwise one. This was compared to self-excited experimental results, showing good agreement. Small flame to flame differences were observed to result in a preferred mode orientation. Additionally, it was shown that the pressure mode always became anti-clockwise spinning for a realistic noise level in the combustion chamber. The clockwise mode was still an attractor, but the solution escaped quickly relative to

the experimental time scale for the given level of noise, explaining why only the anti-clockwise mode was observed in the experimental data. This article was based on the findings in *Article II* related to research goal iii), and is the first observation of the effect of a nature angle dependence in the heat release rate amplitude in a simulation.

Chapter 6

Conclusions

This thesis set out to improve the current understanding of the flame response in annular combustors to azimuthal pressure modes. Due to the immense cost and complexity of running full scale tests for development of new gas turbine engines, it is not feasible to perform parametric studies experimentally. A promising approach is to use the experimentally determined response of a single flame to axially forced acoustic velocity perturbations in numerical models instead. However, how applicable these functions are to model annular combustors where the azimuthal pressure modes are common is currently unknown. To improve this, the current work has characterised the response of an annular combustor, as well as the response of an isolated flame subjected to axial acoustic forcing, acting as a reference case for the conventional approach. The main conclusions in relation to the research goals set out in the introduction are summarised in the following:

i) *Article I* presents the response of a single flame to axially forced acoustic velocity perturbations over a range of equivalence ratios, inlet velocities and frequencies. The enclosure of the flame is made to resemble one sector in the annular combustor, and acts as a reference case for the response to azimuthal pressure perturbations in the true annular combustion chamber.

ii) *Article II* was the first step in addressing the second research goal of being able to force an arbitrary azimuthal mode of the first order in the combustion chamber. For the first time the response of both an anti-clockwise and a clockwise spinning mode at the same operating condition was presented, as well as a standing mode, which was first achieved by Worth et al. (2017). Then the technique was refined further in *Article IV*, where a total of 123 different forced states were presented, spanning the whole range of nature angles, orientation angles and amplitudes of the mode. This represents for the first time good control of an arbitrary forced azimuthal pressure mode of the first order

in an annular combustion chamber.

iii) *Article II* showed for the first time that the response to the anti-clockwise and clockwise spinning pressure modes in the annular combustor might not be the same for a case with co-swirling flames. The anti-clockwise direction was observed to have a higher heat release rate response compared to a clockwise pressure mode of similar amplitude. When the swirl was removed, as presented in *Article III*, no significant differences were observed, and the heat release rate oscillation pattern was observed to have a reflectional symmetry around the injectors. This was not the case for the swirled cases in *Article II*, suggesting the swirl might influence the response in the two different spinning directions. In *Article IV* this was quantified through the introduction of the Azimuthal Flame Describing Function, showing conclusively that the heat release rate response to the two different spinning directions are not the same for the annular combustor geometry with co-swirling flames. The Azimuthal Flame Describing Function was also shown to be able to quantify the difference in the nature of the pressure mode and the heat release rate mode, suggesting it would be a useful tool for modelling purposes. The effect of a different response in the two directions was studied in the numerical study in *Article V*, based on the findings in *Article II* and therefore without the Azimuthal Flame Describing Function. It was shown that the difference in response resulted in a double well potential, with the solution showing a strong preference for the spinning direction with the higher heat release rate response. The lower amplitude solution was still an attractor, but due to the level of noise in the combustion chamber, the solution escapes to the higher response direction in a relatively short time.

To be able to fulfil the research goals, as described above, two novel techniques were introduced. The first one is the rotation averaging based on Bloch theory, which was itself only recently introduced in the field of thermoacoustics for modelling purposes. In this thesis, Bloch theory was utilised to decompose the heat release rate pattern into two components spinning in opposite directions while also extracting the response of an average flame, removing flame to flame differences. This was used in *Article II-IV* and indirectly in *Article V*. The technique also makes it possible to extract the response of both an anti-clockwise and a clockwise mode from a single standing mode, and could potentially be used to extract similar information in high fidelity large eddy simulations. The rotation averaging made it natural to introduce the Azimuthal Flame Describing Function (*Article IV*), which describes the response to the two different spinning directions separately. This allows for an arbitrary recombination to interpolate between measured forced states, making it possible to obtain the response for an arbitrary azimuthal pressure mode

based on the information extracted from just standing modes.

6.1 Future outlook

There are several interesting directions in which the work conducted in this thesis can be extended in the future. The difference in response to the two spinning directions in an annular combustor with swirlers is first observed and quantified in this study. However, it is performed on a single combustion chamber geometry in terms of annulus thickness relative the mean radius. It would be interesting to study the effect of different thickness combustors on the quantitative difference in response, as it is expected to disappear in the limit of a very thin annulus compared to the mean radius. Additionally, the influence of the swirl number and inlet velocity on the response could be tested. In short, it would be of great interest to study how the difference in response scales with different parameters.

Additionally, the new Azimuthal Flame Describing Functions could be incorporated into low-order models, allowing for a nature angle dependence on the heat release rate. A similar approach was used in *Article V* before the introduction of the new concept, but it would be interesting to implement the full functions in the models as it includes some additional features. Of particular interest is the potential effect of having a non-zero response at the pressure node for a standing pressure mode, even when the node is centred at one injector, which was not captured in *Article V*.

Bibliography

Åbom, M. (1991). Measurement of the scattering-matrix of acoustical two-ports. *Mechanical Systems and Signal Processing*, 5(2):89 – 104.

Acharya, V. and Lieuwen, T. (2014a). Response of non-axisymmetric premixed, swirl flames to helical disturbances. In *Proceedings of the ASME Turbo Expo 2014: Turbine Technical Conference and Exposition*, volume 4B: Combustion, Fuels and Emissions. V04BT04A052. ASME.

Acharya, V. and Lieuwen, T. (2016). Premixed flame response to helical disturbances: Mean flame non-axisymmetry effects. *Combustion and Flame*, 165:188 – 197.

Acharya, V., Shreekrishna, Shin, D.-H., and Lieuwen, T. (2012). Swirl effects on harmonically excited, premixed flame kinematics. *Combustion and Flame*, 159(3):1139 – 1150.

Acharya, V. S. and Lieuwen, T. C. (2014b). Role of azimuthal flow fluctuations on flow dynamics and global flame response of axisymmetric swirling flames. In *52nd Aerospace Sciences Meeting*.

Acharya, V. S. and Lieuwen, T. C. (2019). Premixed flame response to high-frequency transverse acoustic modes: Mean flame asymmetry effects. In *AIAA Scitech 2019 Forum*.

Æsøy, E., Aguilar, J. G., Wiseman, S., Bothien, M. R., Worth, N. A., and Dawson, J. R. (2020). Scaling and prediction of transfer functions in lean premixed H2/CH4-flames. *Combustion and Flame*, 215:269 – 282.

Albayrak, A., Juniper, M. P., and Polifke, W. (2019). Propagation speed of inertial waves in cylindrical swirling flows. *Journal of Fluid Mechanics*, 879:85120.

Allison, P. M., de Oliveira, P. M., and Mastorakos, E. (2017). Forced response of flames in a swirling, bluff-body stabilized annular combustor. In *AIAA SciTech Forum-55th AIAA Aerospace Sciences Meeting*.

Balachandran, R., Ayoola, B., Kaminski, C., Dowling, A., and Mastorakos, E. (2005). Experimental investigation of the nonlinear response of turbulent premixed flames to imposed inlet velocity oscillations. *Combustion and Flame*, 143(1):37 – 55.

Bauerheim, M., Cazalens, M., and Poinsot, T. (2015). A theoretical study of mean azimuthal flow and asymmetry effects on thermo-acoustic modes in annular combustors. *Proceedings of the Combustion Institute*, 35(3):3219 – 3227.

Bauerheim, M., Parmentier, J.-F., Salas, P., Nicoud, F., and Poinsot, T. (2014). An analytical model for azimuthal thermoacoustic modes in an annular chamber fed by an annular plenum. *Combustion and Flame*, 161(5):1374 – 1389.

Bloch, F. (1929). Über die quantenmechanik der elektronen in kristallgittern. *Zeitschrift für physik*, 52(7-8):555–600.

Bloxsidge, G. J., Dowling, A. P., and Langhorne, P. J. (1988). Reheat buzz: an acoustically coupled combustion instability. Part 2. Theory. *Journal of Fluid Mechanics*, 193:445473.

Blumenthal, R. S., Subramanian, P., Sujith, R. I., and Polifke, W. (2013). Novel perspectives on the dynamics of premixed flames. *Combustion and Flame*, 160(7):1215 – 1224.

Bothien, M. R., Ciani, A., Wood, J. P., and Fruechtel, G. (2019). Toward decarbonized power generation with gas turbines by using sequential combustion for burning hydrogen. *Journal of Engineering for Gas Turbines and Power*, 141(12).

Boudy, F., Durox, D., Schuller, T., Jomaas, G., and Candel, S. (2011). Describing function analysis of limit cycles in a multiple flame combustor. *Journal of Engineering for Gas Turbines and Power*, 133(6). 061502.

Bourgouin, J.-F., Durox, D., Moeck, J. P., Schuller, T., and Candel, S. (2013). Self-sustained instabilities in an annular combustor coupled by azimuthal and longitudinal acoustic modes. In *Proceedings of the ASME Turbo Expo 2013: Turbine Technical Conference and Exposition*, volume 1B: Combustion, Fuels and Emissions. V01BT04A007. ASME.

Bourgouin, J.-F., Durox, D., Moeck, J. P., Schuller, T., and Candel, S. (2014). Characterization and modeling of a spinning thermoacoustic instability in an annular combustor equipped with multiple matrix injectors. *Journal of Engineering for Gas Turbines and Power*, 137(2). 021503.

Bourgouin, J. F., Durox, D., Moeck, J. P., Schuller, T., and Candel, S. (2015). A new pattern of instability observed in an annular combustor: The slanted mode. *Proceedings of the Combustion Institute*, 35(3):3237 – 3244.

Candel, S. (2002). Combustion dynamics and control: Progress and challenges. *Proceedings of the Combustion Institute*, 29(1):1 – 28.

Chen, J. H. (2011). Petascale direct numerical simulation of turbulent combustion-fundamental insights towards predictive models. *Proceedings of the Combustion Institute*, 33(1):99 – 123.

Chen, J. H., Choudhary, A., de Supinski, B., DeVries, M., Hawkes, E. R., Klasky, S., Liao, W. K., Ma, K. L., Mellor-Crummey, J., Podhorszki, N., Sankaran, R., Shende, S., and Yoo, C. S. (2009). Terascale direct numerical simulations of turbulent combustion using S3D. *Computational Science & Discovery*, 2(1):015001.

Crocco, L. (1951). Aspects of combustion stability in liquid propellant rocket motors Part I: Fundamentals. Low frequency instability with monopropellants. *Journal of the American Rocket Society*, 21(6):163–178.

Cuquel, A., Durox, D., and Schuller, T. (2013). Scaling the flame transfer function of confined premixed conical flames. *Proceedings of the Combustion Institute*, 34(1):1007 – 1014.

Dawson, J. R. and Worth, N. A. (2014). Flame dynamics and unsteady heat release rate of self-excited azimuthal modes in an annular combustor. *Combustion and Flame*, 161(10):2565 – 2578.

Dawson, J. R. and Worth, N. A. (2015). The effect of baffles on self-excited azimuthal modes in an annular combustor. *Proceedings of the Combustion Institute*, 35(3):3283 – 3290.

Docquier, N. and Candel, S. (2002). Combustion control and sensors: a review. *Progress in Energy and Combustion Science*, 28(2):107 – 150.

Dowling, A. P. (1997). Nonlinear self-excited oscillations of a ducted flame. *Journal of Fluid Mechanics*, 346:271–290.

Dowling, A. P. (1999). A kinematic model of a ducted flame. *Journal of Fluid Mechanics*, 394:5172.

Dowling, A. P. and Stow, S. R. (2003). Acoustic analysis of gas turbine combustors. *Journal of Propulsion and Power*, 19:5:751–764.

Ducruix, S., Durox, D., and Candel, S. (2000). Theoretical and experimental determinations of the transfer function of a laminar premixed flame. *Proceedings of the Combustion Institute*, 28(1):765 – 773.

Faure-Beaulieu, A. and Noiray, N. (2020). Symmetry breaking of azimuthal waves: Slow-flow dynamics on the Bloch sphere. *Physical Review Fluids*, 5(2):023201.

Fleifil, M., Annaswamy, A. M., Ghoneim, Z. A., and Ghoniem, A. F. (1996). Response of a laminar premixed flame to flow oscillations: A kinematic model and thermoacoustic instability results. *Combustion and Flame*, 106(4):487 – 510.

Fureby, C. (2009). LES of a multi-burner annular gas turbine combustor. *Flow, Turbulence and Combustion*, 84(3):543–564.

Gatti, M., Gaudron, R., Mirat, C., and Schuller, T. (2017). Effects of the injector design on the transfer function of premixed swirling flames. In *Proceedings of the ASME Turbo Expo 2017: Turbomachinery Technical Conference and Exposition*, volume 4A: Combustion, Fuels and Emissions. V04AT04A054. ASME.

Gatti, M., Gaudron, R., Mirat, C., Zimmer, L., and Schuller, T. (2018). A comparison of the transfer functions and flow fields of flames with increasing swirl number. In *Proceedings of the ASME Turbo Expo 2018: Turbomachinery Technical Conference and Exposition*, volume 4B: Combustion, Fuels, and Emissions. V04BT04A003. ASME.

Gatti, M., Gaudron, R., Mirat, C., Zimmer, L., and Schuller, T. (2019). Impact of swirl and bluff-body on the transfer function of premixed flames. *Proceedings of the Combustion Institute*, 37(4):5197 – 5204.

Gaudron, R., Gatti, M., Mirat, C., and Schuller, T. (2019). Flame describing functions of a confined premixed swirled combustor with upstream and downstream forcing. *Journal of Engineering for Gas Turbines and Power*, 141(5):051016.

Gelbert, G., Moeck, J. P., Paschereit, C. O., and King, R. (2012). Feedback control of unstable thermoacoustic modes in an annular Rijke tube. *Control Engineering Practice*, 20(8):770 – 782.

Ghirardo, G. and Bothien, M. R. (2018). Quaternion structure of azimuthal instabilities. *Physical Review Fluids*, 3(11):113202.

Ghirardo, G. and Gant, F. (2019). Background noise pushes azimuthal instabilities away from spinning states. *arXiv preprint arXiv:1904.00213*.

Ghirardo, G. and Gant, F. (2021). Averaging of thermoacoustic azimuthal instabilities. *Journal of Sound and Vibration*, 490:115732.

Ghirardo, G. and Juniper, M. P. (2013). Azimuthal instabilities in annular combustors: standing and spinning modes. *Proceedings of the Royal Society A: Mathematical, Physical and Engineering Sciences*, 469(2157):20130232.

Ghirardo, G., Juniper, M. P., and Moeck, J. P. (2015). Stability criteria for standing and spinning waves in annular combustors. In *Proceedings of the ASME Turbo Expo 2015: Turbine Technical Conference and Exposition*, volume 4B: Combustion, Fuels and Emissions. V04BT04A005. ASME.

Haeringer, M. and Polifke, W. (2019). Time-domain Bloch boundary conditions for efficient simulation of thermoacoustic limit cycles in (can-)annular combustors. *Journal of Engineering for Gas Turbines and Power*, 141(12):121005.

Han, X. and Morgans, A. S. (2015). Simulation of the flame describing function of a turbulent premixed flame using an open-source LES solver. *Combustion and Flame*, 162(5):1778 – 1792.

Hardalupas, Y. and Orain, M. (2004). Local measurements of the time-dependent heat release rate and equivalence ratio using chemiluminescent emission from a flame. *Combustion and Flame*, 139(3):188 – 207.

Hauser, M., Lorenz, M., and Sattelmayer, T. (2011). Influence of transversal acoustic excitation of the burner approach flow on the flame structure. *Journal of Engineering for Gas Turbines and Power*, 133(4):041501.

Hemchandra, S. and Lieuwen, T. (2010). Local consumption speed of turbulent premixed flames An analysis of "memory effects". *Combustion and Flame*, 157(5):955–965.

Hemchandra, S., Peters, N., and Lieuwen, T. (2011). Heat release response of acoustically forced turbulent premixed flames – role of kinematic restoration. *Proceedings of the Combustion Institute*, 33(1):1609–1617.

Higgins, B., McQuay, M. Q., Lacas, F., Rolon, J. C., Darabiha, N., and Candel, S. (2001). Systematic measurements of OH chemiluminescence for fuel-lean, high-pressure, premixed, laminar flames. *Fuel*, 80(1):67 – 74.

Hirsch, C., Fanaca, D., Reddy, P., Polifke, W., and Sattelmayer, T. (2005). Influence of the swirler design on the flame transfer function of premixed flames. In *Proceedings of the ASME Turbo Expo 2005: Power for Land, Sea, and Air*, volume 2: Turbo Expo 2005, pages 151–160. ASME.

Humbert, S. C., Gensini, F., Andreini, A., Paschereit, C. O., and Orchini, A. (2020a). Nonlinear analysis of self-sustained oscillations in an annular combustor model with electroacoustic feedback. *Proceedings of the Combustion Institute*.

Humbert, S. C., Moeck, J., Orchini, A., and Paschereit, C. O. (2020b). Effect of an azimuthal mean flow on the structure and stability of thermoacoustic modes in an annular combustor model with electroacoustic feedback. *Journal of Engineering for Gas Turbines and Power*.

Hummel, T., Berger, F., Schuermans, B., and Sattelmayer, T. (2016). Theory and modeling of non-degenerate transversal thermoacoustic limit cycle oscillations. In *Thermoacoustic Instabilities in Gas Turbines and Rocket Engines: Industry meets Academia*, number GTRE-038.

Indlekofer, T., Ahn, B., Kwah, Y. H., Wiseman, S., Mazur, M., Dawson, J. R., and Worth, N. A. (2021a). The effect of hydrogen addition on the amplitude and harmonic response of azimuthal instabilities in a pressurized annular combustor. *Combustion and Flame*, 228:375–387.

Indlekofer, T., Faure-Beaulieu, A., Noiray, N., and Dawson, J. (2021b). The effect of dynamic operating conditions on the thermoacoustic response of hydrogen rich flames in an annular combustor. *Combustion and Flame*, 223:284 – 294.

Kim, K. T. and Santavicca, D. A. (2013a). Generalization of turbulent swirl flame transfer functions in gas turbine combustors. *Combustion Science and Technology*, 185(7):999–1015.

Kim, K. T. and Santavicca, D. A. (2013b). Interference mechanisms of acoustic/convective disturbances in a swirl-stabilized lean-premixed combustor. *Combustion and Flame*, 160(8):1441 – 1457.

Komarek, T. and Polifke, W. (2010). Impact of Swirl Fluctuations on the Flame Response of a Perfectly Premixed Swirl Burner. *Journal of Engineering for Gas Turbines and Power*, 132(6):061503.

Kopitz, J., Huber, A., Sattelmayer, T., and Polifke, W. (2005). Thermoacoustic stability analysis of an annular combustion chamber with acoustic low order modeling and validation against experiment. In *Proceedings of the ASME Turbo Expo 2005: Power for Land, Sea, and Air*, volume 2: Turbo Expo 2005, pages 583–593. ASME.

Krebs, W., Flohr, P., Prade, B., and Hoffmann, S. (2002). Thermoacoustic stability chart for high-intensity gas turbine systems. *Combustion Science and Technology*, 174(7):99–128.

Krediet, H. J., Beck, C. H., Krebs, W., Schimek, S., Paschereit, C. O., and Kok, J. B. W. (2012). Identification of the flame describing function of a premixed swirl flame from LES. *Combustion Science and Technology*, 184(7-8):888–900.

Kunze, K., Hirsch, C., and Sattelmayer, T. (2004). Transfer function measurements on a swirl stabilized premix burner in an annular combustion chamber. In *Proceedings of the ASME Turbo Expo 2004: Power for Land, Sea, and Air*, volume 1: Turbo Expo 2004, pages 21–29. ASME.

Laera, D., Schuller, T., Prieur, K., Durox, D., Camporeale, S. M., and Candel, S. (2017). Flame describing function analysis of spinning and standing modes in an annular combustor and comparison with experiments. *Combustion and Flame*, 184:136–152.

Langhorne, P. J. (1988). Reheat buzz: an acoustically coupled combustion instability. Part 1. Experiment. *Journal of Fluid Mechanics*, 193:417443.

Lee, D.-H. and Lieuwen, T. C. (2003). Premixed flame kinematics in a longitudinal acoustic field. *Journal of Propulsion and Power*, 19(5):837–846.

Lespinasse, F., Baillot, F., and Boushaki, T. (2013). Responses of V-flames placed in an HF transverse acoustic field from a velocity to pressure antinode. *Comptes Rendus Mécanique*, 341(1 - 2):110 – 120.

Lieuwen, T., McDonell, V., Santavicca, D., and Sattelmayer, T. (2008). Burner development and operability issues associated with steady flowing syngas fired combustors. *Combustion Science and Technology*, 180(6):1169–1192.

Mazur, M., Kwah, Y. H., Indlekofer, T., Dawson, J. R., and Worth, N. A. (2020). Self-excited longitudinal and azimuthal modes in a pressurised annular combustor. *Proceedings of the Combustion Institute*.

Mensah, G. A. and Moeck, J. P. (2015). Efficient computation of thermoacoustic modes in annular combustion chambers based on Bloch-wave theory. In *Proceedings of the ASME Turbo Expo 2015: Turbine Technical Conference and Exposition*, volume 4B: Combustion, Fuels and Emissions. V04BT04A036. ASME.

Merk, H. J. (1957). Analysis of heat-driven oscillations of gas flows: I. general considerations. *Applied Scientific Research, Section A*, 6(4):317–336.

Moeck, J. P., Paul, M., and Paschereit, C. O. (2010). Thermoacoustic instabilities in an annular Rijke tube. In *Proceedings of the ASME Turbo Expo 2010: Power for Land, Sea, and Air*, volume 2: Combustion, Fuels and Emissions, Parts A and B, pages 1219–1232. ASME.

Noiray, N., Bothien, M., and Schuermans, B. (2011). Investigation of azimuthal staging concepts in annular gas turbines. *Combustion Theory and Modelling*, 15(5):585–606.

Noiray, N., Durox, D., Schuller, T., and Candel, S. (2008). A unified framework for nonlinear combustion instability analysis based on the flame describing function. *Journal of Fluid Mechanics*, 615:139–167.

O'Connor, J. and Acharya, V. (2013). Development of a flame transfer function framework for transversely forced flames. In *Proceedings of the ASME Turbo Expo 2013: Turbine Technical Conference and Exposition*, volume 1B: Combustion, Fuels and Emissions. V01BT04A064. ASME.

O'Connor, J., Acharya, V., and Lieuwen, T. (2015). Transverse combustion instabilities: Acoustic, fluid mechanic, and flame processes. *Progress in Energy and Combustion Science*, 49:1 – 39.

O'Connor, J. and Lieuwen, T. (2011). Disturbance field characteristics of a transversely excited burner. *Combustion Science and Technology*, 183(5):427–443.

O'Connor, J. and Lieuwen, T. (2012). Recirculation zone dynamics of a transversely excited swirl flow and flame. *Physics of Fluids*, 24(7):075107.

Oefelein, J. C. and Yang, V. (1993). Comprehensive review of liquid-propellant combustion instabilities in F-1 engines. *Journal of Propulsion and Power*, 9(5):657–677.

Palies, P., Durox, D., Schuller, T., and Candel, S. (2010). The combined dynamics of swirler and turbulent premixed swirling flames. *Combustion and Flame*, 157(9):1698 – 1717.

Palies, P., Durox, D., Schuller, T., and Candel, S. (2011). Acoustic-convective mode conversion in an aerofoil cascade. *Journal of Fluid Mechanics*, 672:545569.

Palies, P., Ilak, M., and Cheng, R. (2017). Transient and limit cycle combustion dynamics analysis of turbulent premixed swirling flames. *Journal of Fluid Mechanics*, 830:681707.

Paschereit, C., Schuermans, B., and Monkewitz, P. (2006). Non-linear combustion instabilities in annular gas-turbine combustors. In *44th AIAA Aerospace Sciences Meeting and Exhibit*.

Paschereit, C. O., Schuermans, B., Polifke, W., and Mattson, O. (2002). Measurement of transfer matrices and source terms of premixed flames. *Journal of Engineering for Gas Turbines and Power*, 124(2):239–247.

Poinsot, T. (2017). Prediction and control of combustion instabilities in real engines. *Proceedings of the Combustion Institute*, 36(1):1 – 28.

Polifke, W. (2020). Modeling and analysis of premixed flame dynamics by means of distributed time delays. *Progress in Energy and Combustion Science*, 79:100845.

Polifke, W. and Lawn, C. (2007). On the low-frequency limit of flame transfer functions. *Combustion and Flame*, 151(3):437 – 451.

Preetham, Hemchandra, S., and Lieuwen, T. (2008). Dynamics of laminar premixed flames forced by harmonic velocity disturbances. *Journal of Propulsion and Power*, 24(6):1390–1402.

Preetham, S. H. and Lieuwen, T. C. (2007). Response of turbulent premixed flames to harmonic acoustic forcing. *Proceedings of the Combustion Institute*, 31(1):1427–1434.

Prieur, K., Durox, D., Schuller, T., and Candel, S. (2017). A hysteresis phenomenon leading to spinning or standing azimuthal instabilities in an annular combustor. *Combustion and Flame*, 175:283 – 291. Special Issue in Honor of Norbert Peters.

Raun, R. L., Beckstead, M. W., Finlinson, J. C., and Brooks, K. P. (1993). A review of Rijke tubes, Rijke burners and related devices. *Progress in Energy and Combustion Science*, 19(4):313 – 364.

Rayleigh (1878). The explanation of certain acoustical phenomena. *Nature*, 18:319–321.

Rijke, P. L. (1859). Notiz über eine neue Art, die in einer an beiden Enden offenen Röhre enthaltene Luft in Schwingungen zu versetzen. *Annalen der Physik*, 183(6):339–343.

Roy, A., Singh, S., Nair, A., Chaudhuri, S., and Sujith, R. I. (2020). Flame dynamics during intermittency and secondary bifurcation to longitudinal thermoacoustic instability in a swirl-stabilized annular combustor. *Proceedings of the Combustion Institute*.

Sattelmayer, T. (2003). Influence of the combustor aerodynamics on combustion instabilities from equivalence ratio fluctuations. *Journal of Engineering for Gas Turbines and Power*, 125(1):11–19.

Saurabh, A. and Paschereit, C. O. (2013). Combustion instability in a swirl flow combustor with transverse extensions. In *Proceedings of the ASME Turbo Expo 2013: Turbine Technical Conference and Exposition*, volume 1B: Combustion, Fuels and Emissions. V01BT04A057. ASME.

Saurabh, A. and Paschereit, C. O. (2017). Dynamics of premixed swirl flames under the influence of transverse acoustic fluctuations. *Combustion and Flame*, 182:298 – 312.

Saurabh, A. and Paschereit, C. O. (2019). Premixed flame dynamics in response to two-dimensional acoustic forcing. *Combustion Science and Technology*, 191(7):1184–1200.

Saurabh, A., Steinert, R., Moeck, J. P., and Paschereit, C. O. (2014). Swirl flame response to traveling acoustic waves. In *Proceedings of the ASME Turbo Expo 2014: Turbine Technical Conference and Exposition*, volume 4B: Combustion, Fuels and Emissions. V04BT04A043. ASME.

Schimek, S., Gke, S., Schrdinger, C., and Paschereit, C. O. (2012). Flame transfer function measurements with CH4 and H2 fuel mixtures at ultra wet conditions in a swirl stabilized premixed combustor. In *Proceedings of the ASME Turbo Expo 2012: Turbine Technical Conference and Exposition*, volume 2: Combustion, Fuels and Emissions, Parts A and B, pages 1335–1344. ASME.

Schimmer, H. and Vortmeyer, D. (1977). Acoustical oscillation in a combustion system with a flat flame. *Combustion and Flame*, 28:17 – 24.

Schuermans, B., Bellucci, V., Guethe, F., Meili, F., Flohr, P., and Paschereit, C. O. (2004). A detailed analysis of thermoacoustic interaction mechanisms in a turbulent premixed flame. In *Proceedings of the ASME Turbo Expo 2004: Power for Land, Sea, and Air*, volume 1: Turbo Expo 2004, pages 539–551. ASME.

Schuller, T., Durox, D., and Candel, S. (2003). A unified model for the prediction of laminar flame transfer functions: comparisons between conical and V-flame dynamics. *Combustion and Flame*, 134(1):21 – 34.

Schuller, T., Poinsot, T., and Candel, S. (2020). Dynamics and control of premixed combustion systems based on flame transfer and describing functions. *Journal of Fluid Mechanics*, 894:P1.

Seume, J. R., Vortmeyer, N., Krause, W., Hermann, J., Hantschk, C.-C., Zangl, P., Gleis, S., Vortmeyer, D., and Orthmann, A. (1988). Application of active combustion instability control to a heavy duty gas turbine. *Journal of Engineering for Gas Turbines and Power*, 120(4):721–726.

Seybert, A. F. and Ross, D. F. (1977). Experimental determination of acoustic properties using a two-microphone random-excitation technique. *The Journal of the Acoustical Society of America*, 61(5):1362–1370.

Shin, D.-H. and Lieuwen, T. (2012). Flame wrinkle destruction processes in harmonically forced, laminar premixed flames. *Combustion and Flame*, 159(11):3312–3322.

Shin, D.-H. and Lieuwen, T. (2013). Flame wrinkle destruction processes in harmonically forced, turbulent premixed flames. *Journal of Fluid Mechanics*, 721:484513.

Silva, C. F., Nicoud, F., Schuller, T., Durox, D., and Candel, S. (2013). Combining a Helmholtz solver with the flame describing function to assess combustion instability in a premixed swirled combustor. *Combustion and Flame*, 160(9):1743 – 1754.

Staffelbach, G., Gicquel, L. Y. M., Boudier, G., and Poinsot, T. (2009). Large Eddy Simulation of self excited azimuthal modes in annular combustors. *Proceedings of the Combustion Institute*, 32(2):2909 – 2916.

Stow, S. R. and Dowling, A. P. (2004). Low-order modelling of thermoacoustic limit cycles. In *Proceedings of the ASME Turbo Expo 2004: Power for Land, Sea, and Air*, volume 1: Turbo Expo 2004, pages 775–786. ASME.

Straub, D. L. and Richards, G. A. (1999). Effect of axial swirl vane location on combustion dynamics. In *Proceedings of the ASME 1999 International Gas Turbine and Aeroengine Congress and Exhibition*, volume 2: Coal, Biomass and Alternative Fuels; Combustion and Fuels; Oil and Gas Applications; Cycle Innovations. V002T02A014. ASME.

Tay Wo Chong, L., Bomberg, S., Ulhaq, A., Komarek, T., and Polifke, W. (2011). Comparative validation study on identification of premixed flame transfer function. *Journal of Engineering for Gas Turbines and Power*, 134(2):021502.

Tay Wo Chong, L., Komarek, T., Kaess, R., Föller, S., and Polifke, W. (2010). Identification of flame transfer functions from LES of a premixed swirl burner. In *Proceedings of the ASME Turbo Expo 2010: Power for Land, Sea and Air*, volume 2: Combustion, Fuels and Emissions, Parts A and B, pages 623–635. ASME.

Valera-Medina, A., Xiao, H., Owen-Jones, M., David, W. I. F., and Bowen, P. J. (2018). Ammonia for power. *Progress in Energy and Combustion Science*, 69:63 – 102.

Vignat, G., Durox, D., Renaud, A., and Candel, S. (2019). High Amplitude Combustion Instabilities in an Annular Combustor Inducing Pressure Field Deformation and Flame Blow Off. *Journal of Engineering for Gas Turbines and Power*, 142(1):011016.

Vignat, G., Durox, D., Schuller, T., and Candel, S. (2020). Combustion dynamics of annular systems. *Combustion Science and Technology*, 192(7):1358–1388.

von Saldern, J., Orchini, A., and Moeck, J. (2020). Analysis of thermoacoustic modes in can-annular combustors using effective Bloch-type boundary conditions. *Journal of Engineering for Gas Turbines and Power*.

Wiseman, S., Rieth, M., Gruber, A., Dawson, J. R., and Chen, J. H. (2020). A comparison of the blow-out behavior of turbulent premixed ammonia/hydrogen/nitrogen-air and methaneair flames. *Proceedings of the Combustion Institute*.

Wolf, P., Staffelbach, G., Gicquel, L. Y. M., Müller, J.-D., and Poinsot, T. (2012). Acoustic and Large Eddy Simulation studies of azimuthal modes in annular combustion chambers. *Combustion and Flame*, 159(11):3398–3413.

Worth, N. A. and Dawson, J. R. (2012). Cinematographic OH-PLIF measurements of two interacting turbulent premixed flames with and without acoustic forcing. *Combustion and Flame*, 159(3):1109–1126.

Worth, N. A. and Dawson, J. R. (2013a). Modal dynamics of self-excited azimuthal instabilities in an annular combustion chamber. *Combustion and Flame*, 160(11):2476 – 2489.

Worth, N. A. and Dawson, J. R. (2013b). Self-excited circumferential instabilities in a model annular gas turbine combustor: Global flame dynamics. *Proceedings of the Combustion Institute*, 34(2):3127 – 3134.

Worth, N. A. and Dawson, J. R. (2017). Effect of equivalence ratio on the modal dynamics of azimuthal combustion instabilities. *Proceedings of the Combustion Institute*, 36(3):3743 – 3751.

Worth, N. A., Dawson, J. R., Sidey, J. A., and Mastorakos, E. (2017). Azimuthally forced flames in an annular combustor. *Proceedings of the Combustion Institute*, 36(3):3783 – 3790.

Xia, Y., Laera, D., Jones, W. P., and Morgans, A. S. (2019). Numerical prediction of the flame describing function and thermoacoustic limit cycle for a pressurised gas turbine combustor. *Combustion Science and Technology*, 191(5-6):979–1002.

Yang, D., Laera, D., and Morgans, A. S. (2019). A systematic study of nonlinear coupling of thermoacoustic modes in annular combustors. *Journal of Sound and Vibration*, 456:137 – 161.

Zhang, H., Zhang, X., and Zhu, M. (2011). Experimental investigation of thermoacoustic instabilities for a model combustor with varying fuel components. *Journal of Engineering for Gas Turbines and Power*, 134(3).

ARTICLE I

Flame transfer functions and dynamics of a closely confined premixed bluff body stabilised flame with swirl

Håkon T. Nygård and Nicholas A. Worth

Published in
Journal of Engineering for Gas Turbines and Power

Flame Transfer Functions and Dynamics of a Closely Confined Premixed Bluff Body Stabilized Flame With Swirl

Håkon T. Nygård[1]
Department of Energy and Process Engineering,
Norwegian University of
Science and Technology,
Trondheim 7491, Norway
e-mail: hakon.t.nygard@ntnu.no

Nicholas A. Worth
Department of Energy and Process Engineering,
Norwegian University of
Science and Technology,
Trondheim 7491, Norway

The flame transfer function (FTF) and flame dynamics of a highly swirled, closely confined, premixed flame is studied over a wide range of equivalence ratios and bulk velocities at a fixed perturbation level at the dump plane. The operating conditions are varied to examine the ratio of flame height to velocity in scaling the FTF. The enclosure geometry is kept constant, resulting in strong flame-wall interactions for some operating conditions due to varying flame height. The resulting effect on the FTF due to changes in the "effective flame confinement" can therefore be studied. For sufficiently high equivalence ratio, and the resulting sufficiently small effective confinement, modulations of the FTF are observed due to interference of the perturbations created at the swirler and at the dump plane. The small length scales and high velocities result in modulations centered at high frequencies and spanning a wide range of frequencies compared to previous studies of similar phenomena. A critical point was reached for increasing effective confinement, where the modulations are suppressed. This is linked to a temporal shift in the heat release rate where the flame impinges on the combustion chamber walls. The shift reduced the expected level of interference, demonstrating effective confinement is important for the FTF response. Additionally, a distributed time lag (DTL) model with two time lags is successfully applied to the FTFs, providing a simple method to capture the two dominant time scales in the problem, recreate the FTF, and examine the effect of effective confinement. [DOI: 10.1115/1.4049513]

Introduction

The occurrence of thermoacoustic instabilities is an issue which may restrict fuel and operational flexibility in gas turbine engines, hindering the development of low emission systems. Such instabilities arise due to the unsteady interaction and growth of heat release rate and pressure oscillations inside the combustor, which can reach damaging levels [1], and therefore must be eliminated during design.

A common framework to predict such instabilities during the design phase relies on accurate knowledge of the magnitude and delay of a flame's heat release rate oscillations, in response to reference input oscillations over a range of frequencies and amplitudes. Such response functions are denoted as flame transfer functions (FTF) which are valid for low and moderate oscillation amplitudes, where the response is assumed to be linear, or flame defining functions if these also capture high amplitude and specifically the nonlinear response of the flame. When known, these functions can be used in low-order network [2–4] or more involved Helmholtz [5] solvers to predict the system stability. The potential utility of this approach, in reducing the significant complexity associated with the reacting flow to a simple response function, has resulted in considerable effort in understanding the behavior, scaling, and generality of such functions [6–11].

In particular, a number of recent studies have focused on understanding the presence of multiple time scales in the response, due to vorticity oscillations generated both at the injector lip and further upstream from the swirler geometry [7–9], or from nonuniform mixtures and therefore equivalence ratio oscillations [6]. In this study, the response of a closely confined premixed swirling flame will be investigated, and therefore in terms of multiple time scales, it is interesting to review previous studies which have examined interference effects from an upstream swirler.

Previous studies have focused on the effect of the location of an axial swirler [7,12,13], the difference between axial and tangential inlet swirler [10], the influence of swirl number [9], or the geometry of the injector [14]. A common feature of all of these studies is the effective *interference* which can be introduced under certain conditions, resulting from the interaction between velocity oscillations generated at the combustor inlet and the upstream convective vorticity oscillations generated at the swirler. The interference can result in modulations in the gain and phase of the transfer function, with the variation in gain manifesting as a characteristic minima or *dip*. Some of these physical interference phenomena were described in a series of papers by Palies et al., demonstrating convective oscillations modulate the swirl number, which can interfere either constructively or destructively with the vorticity oscillations generated at the inlet [8,15]. Gatti et al. [14] showed two vortex shedding locations are required to generate interference by using an upstream swirler and a bluff body at the combustion chamber inlet. Recently, Æsøy et al. [16] made this more explicit, by showing the interference could be generated by replacing the swirler with round cylinders (grub screws). The presence of multiple sources of vortex shedding can be modeled through the inclusion of multiple time scales, and thus multiple Strouhal numbers. Kim and Santavicca [6] show that a combination of Strouhal number scalings is most effective for collapsing the flame response in the presence of multiple time delays. This use of multiple scaling parameters is similarly taken by Sattelmayer [17] with multiple distributed time lags (DTLs). This approach has been used successfully, for example, by Schuermans et al. [18] and Schimek et al. [11] who use two DTLs to model both equivalence ratio and acoustic oscillations.

Another geometric parameter of relevance in this study is the confinement ratio of the combustor. Several studies have shown that changing the confinement of the flame results in flame shape changes, which in turn affects the FTF [19–21]. More recently, De

[1]Corresponding author.

Manuscript received October 9, 2020; final manuscript received October 14, 2020; published online February 26, 2021. Editor: Jerzy T. Sawicki.

Rosa et al. [22] studied the effect of changing confinement in a configuration featuring multiple time delays, finding that confinement can have significant influence in modulating the transfer function response. The frequency scaling could be somewhat captured by basing the time delay on the flame height, allowing a scaling of the minima. However, a significant change was also observed in the FTF gain at low frequencies, which was linked to the increasingly noncompact behavior of the more closely confined and therefore elongated flame.

The aim of this study is to characterize the response of a perfectly premixed swirling bluff body stabilized flame, confined within a square enclosure. The injector geometry under investigation is almost identical to the one used in a number of previous studies of self-excited thermoacoustic instabilities in annular enclosures [23,24]. Therefore, it is of interest to define the response function for this injector to permit stability predictions to be made for this annular configuration, and this is likely useful in terms of modeling practically relevant annular systems. Additionally, the characteristic geometric features of this particular configuration result in a number of interesting features in the response, as a result of both multiple response time delays, the relatively close confinement, and asymmetry effects. Therefore, a further aim of this study is to examine the response with reference to these influences, and assess the performance of a multiple delay model in accurately capturing these. In particular, the influence of the relative confinement on the dip behavior typically associated with swirling flames will be highlighted.

Experimental Setup and Methods

The setup used for the experiments is shown in Fig. 1. The reactants, air and ethylene, were mixed in the supply lines and the mixture is considered perfectly premixed when injected into the plenum. After entering the plenum, the reactants pass through a honeycomb flow straightener. Above the flow straightener, two horn drivers (Adastra HD60) are mounted diametrically opposite each other. These are driven in phase to create flow perturbations

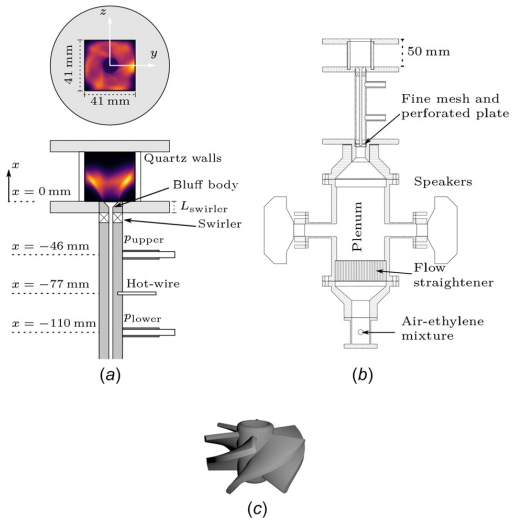

Fig. 1 Experimental setup with key dimensions and equipment with top view in (*a*), the full setup in (*b*), and a 3D model of the swirler in (*c*). Cameras were aligned with the *z*-axis, with the top view achieved by a 45 deg mirror mounted directly above the flame. The photomultiplier tube is aligned with the *y*-axis: (*a*) Close side and top view, (*b*) full setup view, and (*c*) swirler.

that result in velocity fluctuations at the burner dump plane. The flow passes through a conic contraction before entering the injection tube.

The injection tube geometry is exactly the same as that used in previous investigations of combustion instabilities in annular chambers [25] (and almost identical to Refs. [23] and [24]), shown in detail in Fig. 1(*a*). The injector tube has a length of 145mm, and a bluff body with a swirler is mounted in the center. The bluff body has a final diameter $d_{bb} = 13$mm and half angle 45 deg and is mounted on a rod of diameter 5mm. The swirler, shown in detail in Fig. 1(*c*), produces an anticlockwise swirl when observed from downstream, and the trailing edge of the swirler is oriented at an angle $\alpha = 60$ deg. The axial distance from the trailing edge of the swirler vanes to the dump plane is $L_{swirler} = 10$mm. Based on geometric considerations, the swirl number will be $S_{geometry} = 1.22$ right after the swirler [23], but is reduced at the exit due to the contraction. The swirl number has been measured to be approximately $S_{exp} = 0.65$ in an unconfined configuration 10mm downstream of the injector exit.

At the dump plane, the injector exit has a diameter $d_{exit} = 19$mm, giving a blockage ratio of 47%. The combustion chamber side walls are made of quartz for optical access and form a square enclosure of dimensions $41 \times 41 \times 50$mm. The width and breadth of the combustion chamber are chosen to be consistent with the distance between the inner and outer wall of the annular burner setup in Refs. [23–25]. Square enclosure geometry was selected over cylindrical geometry in order to more closely resemble the annular confinement using a simple geometric design suitable for a single flame.

In order to generate the acoustic forcing, an excitation signal was created with an Aim-TTi TGA1244 signal generator and amplified by a TQX PRO1000 amplifier before being sent to the horn drivers. To characterize the excitation the inlet tube is equipped with two pressure ports, which are 46 mm and 110 mm upstream of the dump plane, respectively. Each port is equipped with a Kulite XCS-093-0.35D pressure transducer flush mounted with the inner wall, and the signal from these transducers is amplified using a Fylde FE-579-TA bridge amplifier. The two-microphone method [26] was used to relate pressure fluctuations to velocity fluctuations. To aid the reconstruction of the acoustic perturbations, especially for low forcing frequencies, a Dantec 55P11 hotwire was inserted in the injector pipe approximately 77 mm upstream of the dump plane.

A Phantom v2012 high-speed camera with a LaVision intensified relay optics unit and a Hamamatsu photomultiplier (*H11902-113*) and amplifier (*C7169*) are used to measure the local and global OH* chemiluminescence, respectively. Both are equipped with identical bandpass filters centered at 310nm, with a full width half maximum of 10nm. The camera is equipped with a Cerco 2178 UV lens. Images were acquired over a period of 1s at a sampling rate of 10kHz. The images from the side and top views have resolutions of 11.4 pixel/mm and 8.3 pixel/mm, respectively.

The photomultiplier signal is logged together with the pressure and forcing reference signal using NI-9234 24-bit DAQ (Austin, TX) cards at a sampling frequency $f_s = 51.2$kHz. A constant sample length of 10 s was used in order to capture the response at each condition. A range of operating conditions were investigated, varying both the equivalence ratio, $\Phi = 0.6 - 1.0$, and the bulk inlet velocity, $U_b = 12 - 20$ m/s. This allowed us to investigate the flame response over a similar range of operating conditions to previous instability studies in annular geometry [23,24].

Theoretical Approach

Flame Transfer Function. The aim of this study is to characterize and understand the flame response to inlet velocity oscillations. We approach this using the well-known framework of the flame transfer function [7,8,14,24–29]. The flame transfer function can be defined in frequency space as

$$\mathrm{FTF}(\omega) = \frac{\langle \dot{q}' \rangle / \overline{\langle \dot{Q} \rangle}}{u'/U_\mathrm{b}} \tag{1}$$

where $\langle \dot{q}' \rangle$ and u' are the respective amplitudes of the global heat release rate fluctuations and acoustic velocity perturbations in frequency space, and $\overline{\langle \dot{Q} \rangle}$ and U_b are the mean heat release rate and the mean axial bulk exit velocity, respectively. The heat release rate is assumed to be directly proportional to the OH* chemiluminescence signal due to the use of a perfectly premixed air-fuel mixture [29], and the effect of heat losses to the wall are neglected. The frequency space amplitudes of the heat release rate oscillations in Eq. (1) are computed by dividing the recorded signal into 40 segments with 50% overlap and evaluating the cross power spectral density with the forcing signal to reduce the effect of background noise. Additionally, Hann windowing was employed to reduce finite signal length effects.

The two microphone method is used to evaluate the velocity oscillation amplitude [26]. In a long narrow tube with a mean flow, the pressure mode is assumed to be two one-dimensional plane waves propagating in opposite lengthwise direction. Mathematically, this is expressed as $p(x,t) = (A_+ e^{-\mathrm{i}k_+ x} + A_- e^{\mathrm{i}k_- x}) e^{\mathrm{i}\omega_0 t}$, where subscript + and – denote downstream and upstream propagating components, respectively. $A_\pm$ are complex amplitudes, $k_\pm$ are the corresponding wave numbers, x is the location along the tube, ω_0 is the dominant angular frequency in the signal and t is the time. The wave numbers are related by $k_\pm = k_0/(1 \pm M)$ where k_0 is the wave number in the absence of a mean flow, and M is the mean flow Mach number.

The acoustic velocity perturbation corresponding to the pressure fluctuations is [26]

$$u(x,t) = \left(A_+ e^{-\mathrm{i}k_+ x} - A_- e^{\mathrm{i}k_- x}\right) \frac{e^{\mathrm{i}\omega_0 t}}{\rho c} \tag{2}$$

Here, ρ is the mean fluid density and c is the mean speed of sound in the injector tube. $A_\pm$ can be calculated by the two microphones in the injector only, but the direct velocity fluctuation measurements in the tube are also used to make a least squares solution of $A_\pm$, in order to reduce uncertainty.

The flame response was characterized over a wide range of excitation frequencies, $f_0 = 50 - 2000$ Hz, in steps of 50 Hz, in order to cover a typical Strouhal number range [8]. In comparison with previous studies [6–9], the frequencies of interest in this study are relatively high, due to the small physical size of the inlet and combustor geometry, and the high velocities used in previous studies of this injector configuration in annular chambers [23,24]. The acoustic excitation was adjusted at each frequency of interest in order to maintain a constant amplitude of $u'/U_\mathrm{b} = 0.05 \pm 0.01$, permitting evaluation of the linear response at the chosen operating conditions for the frequencies of interest.

In the current investigation, the flame response will be described in terms of the acoustic velocity perturbations evaluated at a reference location corresponding to the combustor inlet or dump plane. The dump plane is chosen as the reference location due to the acoustic mode which is setup in the injector tube, which causes the acoustic velocity oscillations at the combustor inlet to dominate the FTF, if the convective perturbations from the swirler are neglected. As this location is directly downstream of the swirler, additional convective perturbations may be present in the total velocity oscillations at the combustor inlet, which are not taken into account through this definition, which is based solely on the upstream measurement of pressure. However, this definition is chosen to be suitable for direct input into low-order models, allowing the swirler and flame response to be lumped together in a single response function. It should also be noted that due to the close proximity of the swirler to the exit plane, if the reference location for the acoustic velocity perturbations was instead chosen to be just upstream of the swirler, very similar gain and phase values would be observed for the majority of frequencies of interest.

Distributed Time Lag Models. Another aim of this work is to examine if the flame transfer function can be accurately described using a DTL approach, which permits the flame response to be modeled as series of time delays which have different characteristic gains, phases and delays. The application of such a model in this study provides additional insight into the response of the system through the fitted model constants of interest and also allows the transfer functions reported here to be accurately reconstructed for deployment in low-order models.

In this study, the distributed time lag expression introduced by Æsøy et al. [16] for nonswirling flames will be used. The total distribution $\mathrm{DTL_T}$ is given by

$$\mathrm{DTL_T}(\omega) = \exp(-\mathrm{i}\phi_0) \sum_{i=1}^{2} \left(E_i^+(\omega) + E_i^-(\omega)\right) \tag{3}$$

$$E_i^\pm = \frac{g_i}{2} \exp\left[-\frac{1}{2}(\omega \pm \beta_i)^2 \sigma_i^2 - \mathrm{i}\omega\tau_i\right] \tag{4}$$

where ϕ_0 is a phase common to all the components of the distribution. This formulation corresponds to a Gaussian Impulse Response with a cosine modulation in the time domain, allowing for excess gain for a single time delay distribution. In Eq. (4) the maximum value of each Gaussian is given by $g_i/2$, β_i is the angular frequency of the modulation term, σ_i determines the width of the Gaussian and τ_i is the characteristic delay between the acoustic perturbation and the heat release rate response. $E_i^\pm$ corresponds to a Gaussian distribution centered at $\mp\beta_i$, making the magnitude of each distribution, DTL_i, symmetric around $\omega = 0$.

Equation (3) can describe any phenomenon where there are two distinct time scales, τ_1 and τ_2, in the problem. In the first DTL, representing the FTF without modulations caused by the swirler, β_1 corresponds to the frequency of maximum excess gain (gain above unity), which in combination with σ_1 gives the cutoff frequency of the low-pass behavior of the FTFs. The time delay τ_1 represents the convection time from the dump plane to the flame. The interpretation of the second DTL model is slightly different, where β_2 is the preferred frequency of the formation of convective perturbations by the swirler. σ_2 determines the width of the frequency range where the swirler produces significant perturbations, and depending on the value of β_2 and σ_2 it can either be a low-pass or a bandpass behavior. The associated time delay τ_2 is the total convective time from perturbation is created at the swirler until it reaches the flame.

According to theory, there is a unit gain in the low frequency limit [30], introducing the constraint

$$|\mathrm{DTL_T}(\omega = 0)| = 1 \tag{5}$$

on Eq. (3). In practice, this is imposed by letting g_1 be a function, $g_1(g_2, \beta_1, \sigma_1, \beta_2, \sigma_2)$, of the other parameters. It would also be possible to express g_2 as a function, but g_1 is preferred for numerical reasons. Another physical constraint in the low frequency limit is the phase of the FTF should be zero, but this constraint is relaxed by the introduction of ϕ_0 in Eq. (3). This is done to account for any phase discrepancy created by the acoustic mode reconstruction due to uncertainty in the position and the finite size of the microphones. Additionally, it improves the overall fitting of the large range of function parameters, by reducing the effective weighting of the overall regression on this phase condition.

A modulation in the flame response is captured by the two components, $i = 1, 2$, causing positive and negative interference. The wavelength in frequency space of the modulation is controlled by the inverse of the difference in time delays, $\lambda = 1/\tau_3 = 1/(\tau_2 - \tau_1)$. The phase difference at the dump plane for low Mach number flows is given by $\Delta\phi \approx 2\pi f L_\mathrm{swirler}/U'_\mathrm{bt}$ [13,31], where $L_\mathrm{swirler}/U'_\mathrm{bt}$ is the mean convective time delay between the swirler trailing edge and the dump plane. The first minima in FTF gain is expected at $\Delta\phi = \pi$, meaning the

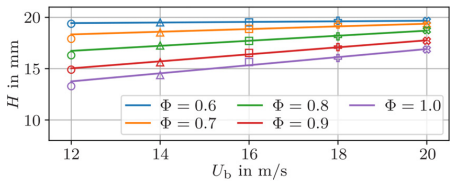

Fig. 2 Vertical flame height over a range of equivalence ratios, Φ, and bulk exit velocities, U_b. Measured flame heights are represented by markers, and the solid lines represent linear regressions. (Color online).

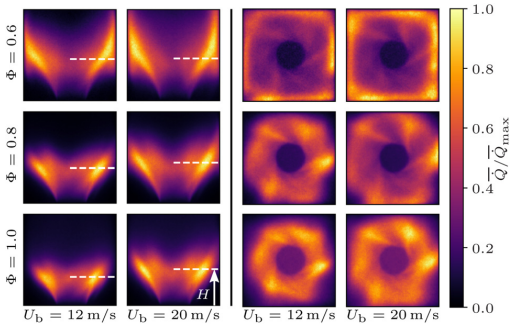

Fig. 3 Side (*left*) and top (*right*) view of average unforced flame shape with equivalence ratio Φ (*vertical axis*) and bulk inlet velocity U_b (*horizontal axis*). Distributions are cropped at the combustion chamber extremities. The white dashed line in the side views indicates the measured vertical flame height *H*. (Color online).

wavelength in frequency space, λ, is determined solely by the distance between the two sources of time delays and the convective velocity for low Mach number flows. The larger the difference in time delays, the sharper the modulations will appear in the FTF, in other words the dip will be narrower and affect a smaller range of frequencies.

Results and Discussion

Unforced Flames. An important scaling parameter for response is the flame height H, defined as the streamwise location of the maximum cross-stream integrated heat release rate of the unforced flames, and is shown for all operating conditions in Fig. 2. Assuming negligible changes to the turbulent flame speed for increasing bulk velocity in the studied interval, the flame height is expected to scale linearly with bulk velocity at a fixed equivalence ratio [29]. The solid lines in Fig. 2 are linear regressions based on the different bulk velocities, showing good agreement between measured and expected behavior. For increasing bulk velocity, the flames elongate due to the decreasing ratio of flame speed to bulk velocity, while for increasing equivalence ratio the flames shorten due to the increase in flame speed.

A selection of flame shapes are shown through line of sight integrated images from the side and top of the flame in Fig. 3. For all operating conditions, the flame structure resembles that of a V-flame, but with some flame elements stabilized in the outer shear layer. The side view shows the same flame height trends observed in Fig. 2, with increasing flame height when either increasing the bulk velocity or decreasing the equivalence ratio. When $\Phi = 0.6$, the flame attaches to the side walls of the combustion chamber, which is also clearly seen from the top view. This causes an underestimation of the flame height due to the spatial redistribution of heat release rate, as seen in the side views in Fig. 3.

The other operating conditions in Fig. 3 show less flame wall interaction. However, a secondary inner structure can be observed inside the main reaction zone from the side views. This can be further examined from the top views, where a clear six-fold rotational symmetry is observed. This is caused by the close proximity of the six vane swirler to the dump plane combined with the relatively large blockage presented by the swirler. Despite the very thin vanes (thickness of 1mm), the high inclination angle of $\alpha = 60$ deg results in a relatively high blockage, producing notable wakes, which are likely causing the secondary structure. Such features associated with this geometry have been observed previously [23], but can be viewed here in higher resolution.

Flame Transfer Function Scaling. Flame transfer functions for all operating conditions are presented in Fig. 4. Adopting a similar scaling to a number of previous investigations [6,32,33], the gain and phase are plotted against a Strouhal number, $St_l = fH/U_b$. The FTF gain for all cases exhibits a low-pass filter behavior which is well documented for acoustically perturbed flames [6,29,34] for Strouhal numbers $St_l \gtrsim 1$, showing a reasonable collapse in both gain and phase for constant Φ, but less agreement as equivalence ratio is varied. However, despite modest variations in gain and phase, at high St_l similar cutoff behavior is observed. The onset of cutoff occurs at slightly lower values of St_l for $\Phi = 0.6$, but this is most likely caused by an underestimation of flame height due to wall attachment of the flame, shown in Fig. 3. This observation is further supported by the steeper evolution of the phase compared to the other equivalence ratios. Plotting the transfer function variation with St_l is equivalent to scaling the response with the dominant time scale, explaining the almost linear slopes of the phase. It is noted that when $St_l \gtrsim 1.5$ the slope of the $\Phi = 0.6$ drastically changes shape. This coincides

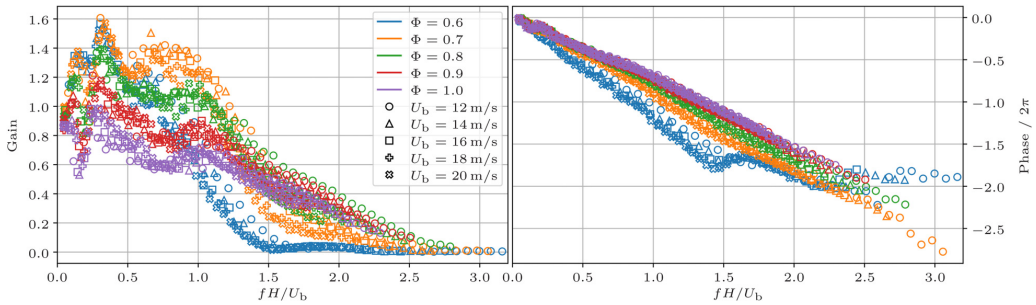

Fig. 4 Flame response in terms of the flame transfer function gain (*left*) and phase (*right*) for all cases, normalized by Strouhal number St_l. Colors and symbols are consistent with those used previously in Fig. 2 for flame height. (Color online).

with a very low gain value, meaning measurement noise and any potential extra time delays may result in a major change in the phase.

In contrast, however, at low St_1 the transfer function gain does not collapse and is observed instead to significantly decrease with increasing equivalence ratio, creating a local minima or dip at $St_1 \approx 0.75$ when $\Phi \geq 0.8$. Similar dip features have been observed in previous studies of highly swirling flames [6–9], which are attributed to the interference between convective and acoustic velocity perturbations at the dump plane [8]. The presence of multiple time scales associated with such interference phenomena can also be observed through the subtle changes of the phase slope in Fig. 4 for the high equivalence ratio cases.

It is noted that there are some non-negligible modulations for very low Strouhal numbers ($St_1 < 0.3$), but these will later be shown to likely stem from a source of convective perturbations upstream of the swirler due to the wavelength λ in frequency space. However, the main focus of this study will relate to the suppression of the expected dip caused by the swirler for decreasing equivalence ratio. For a given inlet velocity, the hydrodynamic and acoustic response in the inlet duct should be approximately the same for all equivalence ratios due to the same bulk velocity and negligible changes in density. Therefore, the absence of interference at $St_1 \approx 0.75$ for some equivalence ratios is somewhat unexpected and will be studied further in the flame dynamics section.

Alternative Strouhal Number Scaling. The St_1 scaling in Fig. 4 is designed to collapse the cutoff frequency of the FTF, but the location of the minima clearly observed for $\Phi \geq 0.8$ is expected to scale with another Strouhal number. This Strouhal number is based on the convective time from the swirler to the dump plane of the induced perturbations and is given by $St_3 = fL_{swirler}/U'_{bt}$, with the rescaled FTFs in Fig. 5. In this scaling, it is assumed the convective time from the swirler to the dump plane is proportional to the time it takes for a disturbance to travel, at the local bulk velocity U_{bt} (which varies with cross-sectional area). Recently, it has been shown by Albayrak et al. [35] that the propagation speed of the perturbation created at the swirler is significantly faster than U_{bt} due to its inertial wave nature. Therefore the propagation speed in St_3 is estimated to be $U'_{bt} = 1.5U_{bt}$ based on the theoretical dip location $St_3 = 1/2$ and visual inspection of Fig. 5. Using this scaling, the length of the modulation should be unity and the frequency location of the dips collapse as shown in the figure. While the dip frequency locations collapse reasonably well for the previous St_1 scaling shown in Fig. 4, this is due to the flame heights' weak dependence on the inlet velocity for a given equivalence ratio.

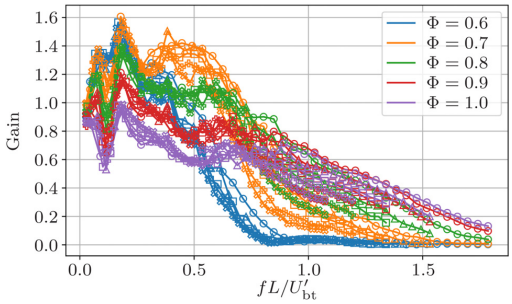

Fig. 5 Flame response in terms of the flame transfer function gain (*left*) and phase (*right*) for all cases, normalized by Strouhal number St_3. Colors and symbols are the same as presented in Fig. 4. (Color online).

The modulations at the lowest Strouhal numbers $St_3 \lesssim 0.2$ interestingly also collapse well. The much shorter wavelength in frequency space of these suggests a source of convective vorticity oscillations upstream of the swirler. A likely source of the extra convective perturbations is the grub screws used upstream to center the bluff body, the same source as described in detail in Ref. [16]. The visual effect of these low Strouhal number perturbations on the flame is very subtle even in the absence of swirl, and therefore in the presence of additional perturbations induced by the swirl vanes, it was decided not to examine the effect of these further.

The similarity of the time scales represented by the two Strouhal numbers St_1 and St_3, with τ_1 in the range $0.85 - 1.62$ ms, and τ_3 in the range $0.53 - 0.89$ ms, results in several interesting features. One prominent feature is the frequency location of the dip being located close the cutoff region, and in some cases extending all the way until cutoff starts to dominate. This results in the local maximum following the dip not being present in all cases. Compared to previous studies [8,14], the location of measured maximum interference is very high, in the range $0.5 - 0.9$ kHz, and the width of the dip in frequency space is much broader.

Distributed Time Lag Models. Examining the gain and phase of the flame response over the range of presented cases shows that the response can either be dominated by the time lag based on the flame height, or a significant interference with the convective perturbations created at the swirler can introduce an additional time scale. Therefore, to confirm this, and to gain additional insight into these characteristic values a distributed time delay model [17] is employed, with either a single or a pair of time delays used.

The DTL model described in the theory section is applied to the measurements in this study, and the reconstructed functions for each case are shown in Fig. 6. In this study, the potential third convective time lag is not considered, and therefore the range used for the parameter fitting starts at $f_0 = 300$ Hz and will not capture the first sharper dip by design. For presentation clarity, a

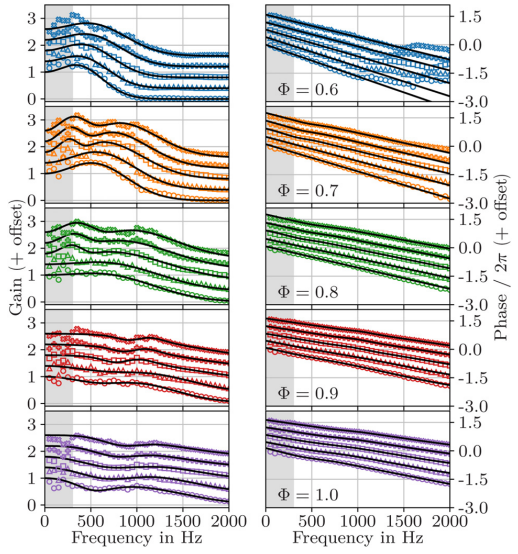

Fig. 6 FTFs and fitted distributed time delay model, with one ($\Phi = 0.6$ and $U_b = 12-14$ m/s for $\Phi = 0.7-0.8$) or two (otherwise) time delays. The colors and markers are the same Fig. 4. Both the phase and gain curves are offset by 0.4 for each increase in velocity to aid readability. (Color online).

positive offset of 0.4 has been added to both gain and phase for increasing velocity in order to separate the functions, and these are plotted now against frequency to allow a compact presentation of all 25 cases. The parameters presented can be found in Appendix A (Table 1).

Corresponding to previous observations, a single DTL is used when $\Phi = 0.6$ for all velocities, and for $\Phi = 0.7 - 0.8$ when $U_b = 12 - 14\,\mathrm{m/s}$. For the single time delay cases with $\Phi = 0.7 - 0.8$ the width and amplitude of the dip is too small and the location is too close to the 300 Hz cutoff point to fit the model well, but the single delay captures the main features well. For all other cases, two delays are used to capture the features of the transfer function. The close agreement between measurements and the fitted model for all cases indicates that this modeling approach is appropriate, including the use of only a single time delay for the low equivalence ratio cases with $\Phi = 0.6$.

To study the reconstruction further, the aforementioned coefficients are graphically presented in Fig. 7. First the time delays are examined, which are shown on the bottom row. There is good agreement between the fitted time delays and the theoretical values from the Strouhal number scaling. The first time delay τ_1 scales with the ratio of flame height H to the bulk velocity, while the second time delay τ_2 is a sum of τ_1 and the convective time from the swirler to the dump plane. This implies that the shorter time delays due to the dispersive inertial wave nature of the convective perturbations from the swirler are automatically accounted for in the fitted model values of τ_2, and therefore the fitted time delay is the one best characterizing the actual time delay. For τ_1 it is observed that the high equivalence ratio cases, which correspond to short flame heights, overestimate the time delay, suggesting the definition of the time delay is slightly incorrect for these cases. It is also observed that as the flame length increases, the time scale is underestimated. This may be explained by the underestimation of the flame height H observed previously, when the flame begins to interact with the wall. It also shows the model, which was originally proposed for unswirled flames [16], is capable of recreating the response well with a very simple expression suitable for modeling and based on the assumption of two distinctive time scales in the problem.

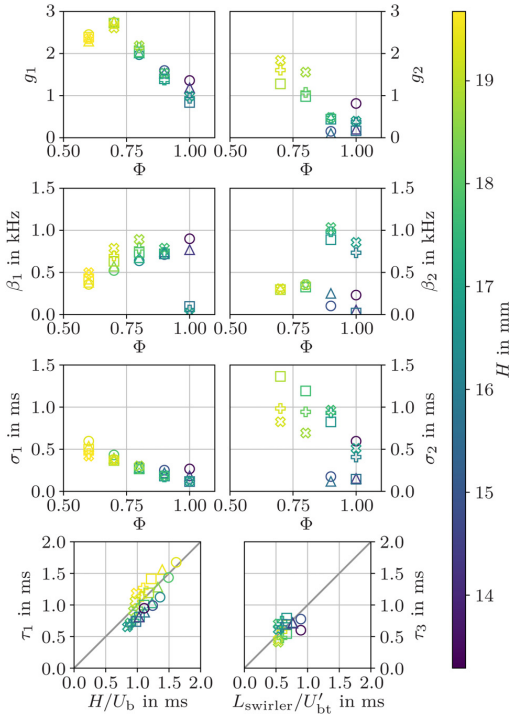

Fig. 7 Parameters for DTL$_1$ (*left*) and DTL$_2$ (*right*) for all operating conditions. $g_{1,2}$, $\beta_{1,2}$ and $\sigma_{1,2}$ are plotted against equivalence ratio and the time delays $\tau_{1,3}$ are plotted against the respective Strouhal number time delays. The color indicates the flame height *H*, and the symbols indicate the same velocities as in previous figures. (Color online).

In terms of the other model parameters, the first DTL distribution is also observed to always behave as a low-pass filter, in line with the expected behavior of a perfectly premixed flame. Observing g_1, β_1, and σ_1 in Fig. 7, there are clear trends for the evolution of the parameters for the first DTL as a function of equivalence ratio. As the equivalence ratio is increased both the location β_1 of the maximum gain and the width σ_1^{-1} increases, resulting in a simultaneous decrease in the gain g_1 due to the symmetry of Eq. (3).

However, the other model parameters for the second DTL do not show such clear trends, due to the under-constrained fitting and the much lower amplitude of the phenomenon. This causes the interpretation of the swirler behavior to not be physically consistent across all cases, despite the models ability to accurately describe the transfer function in the region of interest $f_0 = 300 - 2000\,\mathrm{Hz}$. The second DTL is observed to either be a bandpass filter centered at a high frequency, $\beta_2 > 700$ Hz, or a bandpass to low-pass filter with finite amplitude at zero frequency, $\beta_2 \lesssim 350\,\mathrm{Hz}$. It is important to note that while the correct time delay τ_2 is reliably captured, the type of filter is not consistent across all cases.

Phase Averaged Flame Dynamics. In order to further understand the spatial location, magnitude, and phase of the heat release rate oscillations, the phase averaged heat release rate distribution is presented for two operating conditions at select frequencies. Two extremes are chosen in terms of the peak magnitude of the FTF response, with the $\Phi = 0.7$, $U_b = 18\,\mathrm{m/s}$ case presented in Fig. 8, and the $\Phi = 1.0$, $U_b = 12\,\mathrm{m/s}$ case presented in Fig. 9. The frequencies presented correspond to a location before the expected local minimum, a frequency close to expected local minimum of the dip and a third higher frequency. For the $\Phi = 0.7$ case the highest frequency is well into the cutoff range, while it is at the local maximum after the dip for $\Phi = 1.0$. The forcing amplitude is adjusted to $u'/U_b = 0.1$ to better highlight the flame dynamics.

For the selected forcing frequencies, the weighted phase representation [36] of the first Fourier mode of the phase average (*left*) and five points in the phase averaged cycle are presented from both the side and top views (*center*). In the weighted phase representation, the brightness and color are determined by the fluctuation magnitude and phase, respectively, on a pixel by pixel basis. On the right-hand side, the integrated response of the first Fourier mode is plotted over two periods to show the timing of the heat release rate in the streamwise direction, which is a similar metric to the phase averaged representation presented in fig. 14 in Ref. [8]. The complex amplitude $\tilde{\dot{q}}'_y(x)$ is found by first integrating the heat release rate in the transverse direction (y-direction in Fig. 1(*a*)), and then taking the discrete Fourier transform of the integrated heat release rate at the forcing frequency f_0. The presented time series of the first Fourier mode is then given by $\Re(\tilde{\dot{q}}'_y e^{i2\pi t/T})$ normalized by the mean spatially integrated heat release rate. The time series are plotted against downstream distance, x, in order to create contour maps of the first Fourier mode, in which streaked regions represent the convection of high and low oscillations in space and time. The mean value along a horizontal cut represents the quantity $\langle q' \rangle / \overline{\langle \dot{Q} \rangle}$ in Eq. (1).

Considering initially the low equivalence ratio case ($\Phi = 0.7$, $U_b = 18\mathrm{m/s}$) in Fig. 8, for each forcing frequency the

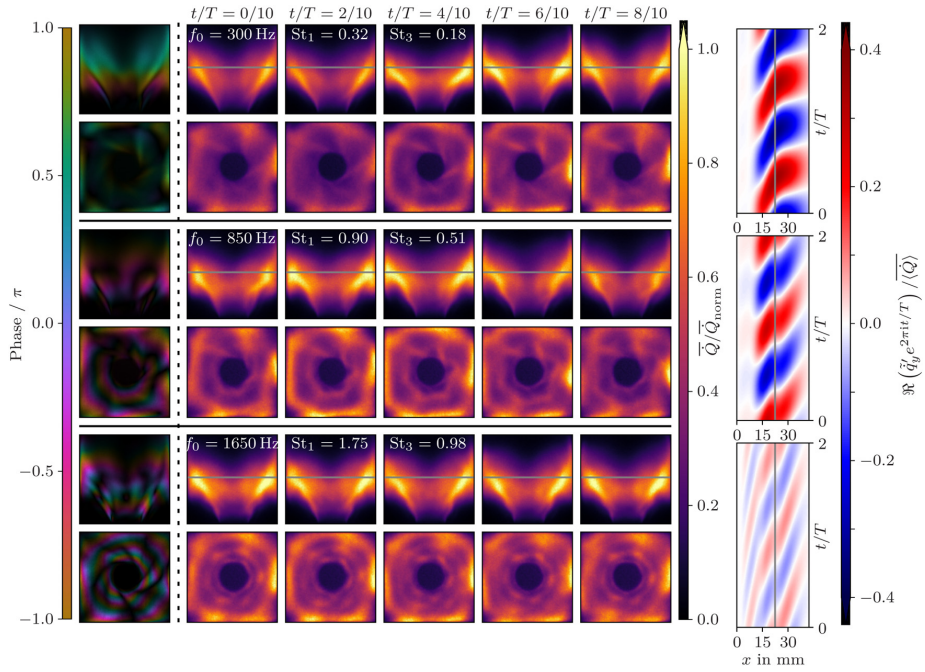

Fig. 8 Weighted phase (*left*), phase averages (*center*), and the time evolution of the cross integrated first Fourier mode (*right*) for different forcing frequencies, f_0. The weighted phase plots and the phase averages are presented from both the side and top view. All operating conditions are at a bulk velocity $U_b = 18$ m/s and equivalence ratio $\Phi = 0.7$. $\overline{\dot{Q}}_{\mathrm{norm}} = 0.9\overline{\dot{Q}}_{\mathrm{max}}$ to slightly saturate the plots for viewing clarity. (Color online).

phase averaged motion of the flame in response to the velocity oscillations can be observed. The side view shows the flame front oscillating as perturbations convect along it, rolling up the flame brush at the tip. During the cycle, the flame tip remains attached to the combustion chamber walls. The top view confirms that flame wall interactions are present throughout the cycle, but also provides insight into the asymmetry of the heat release structure. This view shows fluctuations traveling along the flame front as hexagonal ring structures, with this patternation due to the close proximity of the swirler to the dump plane. The number of ring structures increase with frequency as the wavelength of the convective perturbation decreases. The effect of this can also be observed in the side view, with the flame oscillating less for the highest frequency.

The features observed in the phase averaged distributions can be described more compactly through the weighted phase plots shown on the left-hand side of Fig. 8. The two lower frequency cases, $f_0 = 300$ Hz and $f_0 = 850$ Hz, experience most heat release rate oscillations in the upper part of the flame, close to the walls. Furthermore, the range of phase angles present for the two lower frequencies are restricted to a span of approximately half a period, indicating that no significant destructive interference is occurring in these cases. In contrast, the highest frequency case, $f_0 = 1650$ Hz, contains similar magnitude oscillations at all downstream locations. Together with the shorter convective disturbance wavelength at the higher frequency, this results in a wider range of oscillation phases. The presence of significant amplitude oscillations at phase angles separated by a full period in this case provides the destructive interference consistent with the response in the cutoff region.

While the weighted phase plots provide a useful way to compactly represent the structure of the oscillations in heat release rate, in order to further understand the interference between convective perturbations it is instructive to examine first Fourier mode contour plots on the right-hand side of Fig. 8. Due to the normalized time axis, the inclination angle of the streaked blue and red regions (which represent the convection of positive and negative heat release rate oscillations) with respect to the horizontal is controlled by both the advection velocity along the flame and the frequency. For a fixed inlet velocity and equivalence ratio, the advection velocity is expected to remain relatively constant, resulting in a monotonically increasing streak angle with frequency.

Frequency $f_0 = 850$ Hz in Fig. 8 corresponds to a case where significant destructive interference may be expected ($\mathrm{St}_3 \approx 0.5$), but as shown in Fig. 4, this is not observed for equivalence ratio $\Phi = 0.7$. A crucial observation from the first Fourier mode plot in Fig. 8 is the occurrence of a significant temporal shift in the streaks at a downstream location $x \approx 22$ mm, which is marked with a gray line. This temporal shift manifests in the contour plots as a sharp decrease in the inclination angle of the streaked regions at this downstream location. Such a temporal shift increases the magnitude of the heat release oscillations, by reducing the expected level of interference. This can be understood by considering the average heat release rate oscillations along any horizontal cut in the first Fourier mode plot. The sharp decrease in streak angle results in less cancelation of heat release rate oscillations. Therefore, the absence of the expected minima at $\mathrm{St}_3 \approx 0.5$ is likely caused by this temporal shift resulting in less interference.

In the absence of confinement, it is reasonable to assume the convective velocity along the flame should vary gradually with downstream location. Therefore, it is interesting to compare the downstream location of the clear shift in the Fourier mode timing to the phase averaged representation in the center of Fig. 8, also marked with gray lines. The downstream location of the shift corresponds to approximately the mean height of the flame-wall

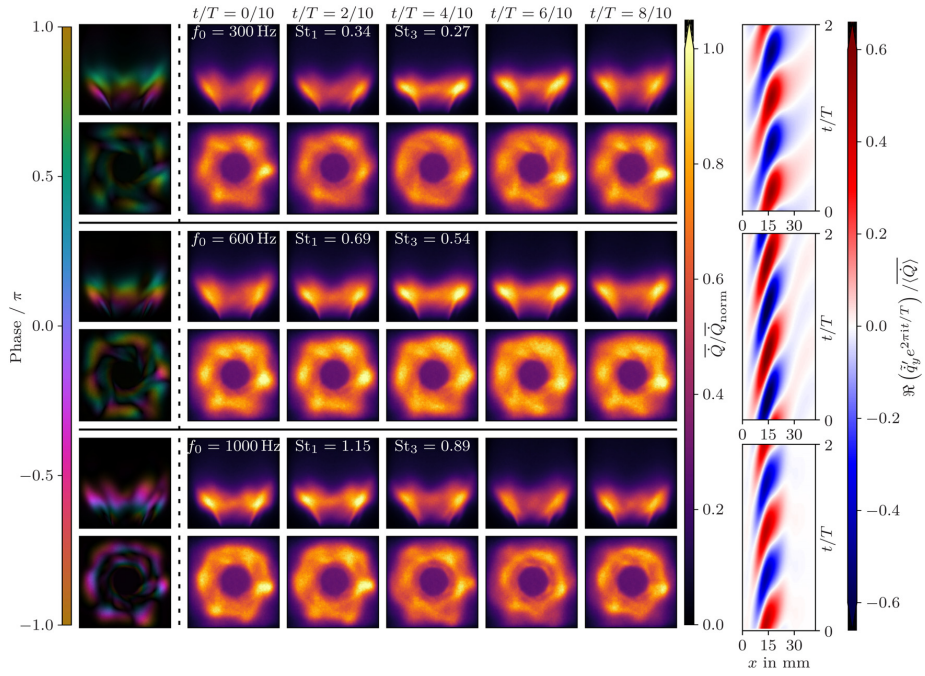

Fig. 9 Weighted phase (*left*), phase averages (*center*) and the time evolution of the cross integrated first Fourier mode (*right*) for different forcing frequencies, f_0. The weighted phase plots and the phase averages are presented from both the side and top view. All operating conditions are at a bulk velocity $U_b = 12$ m/s and equivalence ratio $\Phi = 1.0$. $\overline{\dot{Q}}_{\mathrm{norm}} = 0.9\overline{\dot{Q}}_{\mathrm{max}}$ to slightly saturate the plots for viewing clarity. (Color online).

impingement during the cycle, suggesting that the flame confinement is the main cause of the change in streak angle, and consequently the suppression of interference. Therefore, the presence of confinement explains the absence of the dip feature for this equivalence ratio case. Returning to the Fourier mode distribution, the decrease in streak angle suggests the suppression is realized through a modification of the convective velocity. Furthermore, as the intensity of the heat release rate oscillations are similar before and after this location, it appears that neither quenching nor a modification of the flame-vortex interaction due to the presence of the wall is the dominant mechanism for the interference suppression.

Figure 9 shows the same metrics as Fig. 8 for a case with significant interference observed in the FTF gain ($\Phi = 1.0$ and $U_b = 12$ m/s). An important difference in comparison with Fig. 8 is the flame is significantly shorter, and hence, does not interact strongly with the wall, as seen from the phase averaged cycle. Therefore, despite the use of the same enclosure geometry, through the variation of operating conditions, the effective confinement is reduced. At $f_0 = 300$ Hz more fluctuations close to the flame base are visible in the $\Phi = 1.0$ case in comparison with the lower equivalence ratio, giving a wider range of phases. However, the top view shows the high-magnitude oscillations occur in the upper section of the flame, with a narrow range of phases dominating, similar to the $\Phi = 0.7$ case.

It is interesting to contrast this response with the weighted phase plots from the $f_0 = 600$ Hz case, which corresponds to the local FTF interference minima. At this higher frequency, a relatively wide range of phases can be seen from the side and now also from the top view, demonstrating the presence of multiple disturbances on the flame at the same instances, and therefore the cancelation of integrated heat release rate oscillations. This can be clearly observed in the cross integrated Fourier modes where regions of positive and negative heat release rate oscillation are simultaneously present. Crucially, in this case the temporal shift of the streaks only occurs after the peak heat release rate oscillations occur, and thus a greater amount of cancelation is present, resulting in the observation of the expected local FTF minimum at the frequency predicted by theory. Therefore, the absence of close wall confinement due to the shorter flame height allows destructive interference to occur in this case.

Comparing cases corresponding to the local FTF maximum at $f_0 = 1000$ Hz to the local FTF minimum at $f_0 = 600$ Hz, a narrower range of phases in the weighted phase plot is observed for the former. This is also shown in the cross integrated Fourier mode plot in which a lower response is observed both toward the flame base and toward the top of the flame. Therefore, as oscillations at this frequency result in heat release rate oscillations at a narrower range of heights, less interference is observed, corresponding to the local maxima in the transfer function.

Conclusion

The FTF of a closely confined, swirling flame have been investigated experimentally for a wide range of operating conditions. The FTFs are shown to exhibit characteristic low-pass behavior and collapse reasonably well when plotted nondimensionally against a Strouhal number based on the flame height and bulk flow velocity. Further to this, at high equivalence ratios $\Phi \geq 0.8$ the FTF is observed to have characteristic modulations in both the gain and phase typically associated with highly swirling flames. These are caused by the interference between convective perturbations from the swirler interacting with the perturbations at the injector exit. This is confirmed by scaling the FTFs against a second Strouhal number based on the upstream swirler location and the convective velocity in the inlet pipe. Due to the small length

scales and relatively high velocity in the studied configuration, the frequency of the dip in the gain is relatively high compared to other studies, and it spans a much wider range of frequencies, which is consistent with the current understanding of the phenomenon.

However, in contrast to previous studies, at the lower equivalence ratios $\Phi \leq 0.7$ the expected modulations due to convective perturbations from the swirler are shown to be suppressed. By examining the flame structure and dynamics, it is shown that at lower equivalence ratios (and higher velocities) the flames are longer and therefore interact significantly with the walls. This increase in effective confinement results in a temporal shift in the heat release distribution at the downstream location where the flame impinges on the wall during the oscillation cycle. The temporal shift reduces the interference between convective perturbations from the swirler and from the injector exit for a given frequency due to an increase in convective velocity, which increases the FTF gain compared to the higher equivalence ratios with smaller effective confinements. This demonstrates the response is not only dependent on the hydrodynamic and acoustic oscillations at the inlet, but also on the downstream effective confinement.

Finally, to gain additional insight into the time scales of the problem a DTL model with two distinct time scales is applied to the FTFs. The model is shown to accurately capture the time delays as well as providing a simple expression for recreating and interpolating the FTF. The extracted time delays correctly capture the fact that the convective time delay from the swirler to dump plane is faster than the local bulk velocity, due to the inertial wave nature of the perturbations, as well as demonstrating the difficulty in defining the flame height for flames attached to the combustion chamber walls.

Funding Data

- European Research Council (ERC) under the European Union's Horizon 2020 (Grant No. 677931 TAIAC; Funder ID: 10.13039/100010663).

Appendix A

The coefficients for all the DTL models presented in Fig. 6 are presented in Table 1. As discussed the fitting does not account for the effect possibly caused by a third convective time lag in the model, and is therefore not applicable to recreate that behavior. The quality of the fit can be checked in Fig. 6.

Table 1 Coefficients used for creating the modeled FTFs as shown in Fig. 6

Φ	U_b in m/s	H in mm	g_1	$\beta_1/(2\pi)$ in Hz	σ_1 in ms	τ_1 in ms	g_2	$\beta_2/(2\pi)$ in Hz	σ_2 in ms	τ_2 in ms	ϕ_0
0.6	12	19.4	2.450	358	0.596	1.675	N/A	N/A	N/A	N/A	0.000
0.6	14	19.5	2.294	382	0.537	1.560	N/A	N/A	N/A	N/A	−0.006
0.6	16	19.5	2.389	420	0.500	1.414	N/A	N/A	N/A	N/A	0.017
0.6	18	19.7	2.354	464	0.449	1.269	N/A	N/A	N/A	N/A	0.129
0.6	20	19.7	2.356	498	0.418	1.187	N/A	N/A	N/A	N/A	0.078
0.7	12	17.9	2.737	523	0.432	1.434	N/A	N/A	N/A	N/A	−0.674
0.7	14	18.5	2.751	573	0.395	1.282	N/A	N/A	N/A	N/A	−0.614
0.7	16	18.9	2.722	632	0.366	1.192	1.279	296	1.365	1.875	−0.839
0.7	18	19.3	2.713	695	0.375	1.136	1.605	300	0.984	1.711	−0.963
0.7	20	19.3	2.609	787	0.371	1.059	1.837	307	0.826	1.508	−1.026
0.8	12	16.3	1.972	638	0.291	1.123	N/A	N/A	N/A	N/A	−0.474
0.8	14	17.3	2.013	674	0.279	1.032	N/A	N/A	N/A	N/A	−0.424
0.8	16	17.7	2.039	738	0.266	0.998	0.979	326	1.192	1.546	−0.716
0.8	18	18.2	2.142	785	0.270	0.942	1.076	354	0.944	1.420	−0.759
0.8	20	18.8	2.186	892	0.302	0.906	1.558	352	0.693	1.317	−1.031
0.9	12	14.9	1.597	712	0.251	0.990	0.152	102	0.175	1.766	−0.502
0.9	14	15.6	1.532	746	0.220	0.885	0.102	251	0.118	1.606	−0.331
0.9	16	16.5	1.400	720	0.181	0.810	0.440	889	0.825	1.602	−0.159
0.9	18	17.1	1.370	738	0.171	0.749	0.471	983	0.932	1.493	−0.139
0.9	20	17.7	1.537	788	0.187	0.714	0.480	1033	0.964	1.415	−0.168
1.0	12	13.3	1.360	900	0.266	0.947	0.813	231	0.595	1.547	−0.903
1.0	14	14.4	1.185	770	0.184	0.809	0.201	54	0.153	1.521	−0.379
1.0	16	15.6	0.838	96	0.116	0.737	0.164	18	0.144	1.428	−0.258
1.0	18	16.0	0.936	54	0.120	0.692	0.375	734	0.407	1.339	−0.229
1.0	20	16.9	0.991	13	0.121	0.654	0.395	857	0.510	1.266	−0.190

Note some of the parameters are not qualitatively consistent, which is as previously discussed due to the under-constrained fitting caused by the similar time scales and data range used. However, these coefficients give a quantitatively good fit for recreating the FTFs when $f_0 \geq 300$ Hz, allowing these to be applied in low-order models.

References

[1] Lieuwen, T. C., 2005, "Combustion Instabilities in Gas Turbine Engines," Progress in Astronautics Aeronautics, American Institute of Aeronautics & Astronautics.
[2] Dowling, A. P., 1997, "Nonlinear Self-Excited Oscillations of a Ducted Flame," J. Fluid Mech., **346**, pp. 271–290.
[3] Stow, S. R., and Dowling, A. P., 2004, "Low-Order Modelling of Thermoacoustic Limit Cycles," ASME Paper No. GT2004-54245.
[4] Noiray, N., Durox, D., Schuller, T., and Candel, S., 2008, "A Unified Framework for Nonlinear Combustion Instability Analysis Based on the Flame Describing Function," J. Fluid Mech., **615**, pp. 139–167.
[5] Nicoud, F., Benoit, L., Sensiau, C., and Poinsot, T., 2007, "Acoustic Modes in Combustors With Complex Impedances and Multidimensional Active Flames," AIAA J., **45**(2), pp. 426–441.
[6] Kim, K. T., and Santavicca, D., 2013, "Generalization of Turbulent Swirl Flame Transfer Functions in Gas Turbine Combustors," Combust. Sci. Technol., **185**(7), pp. 999–1015.
[7] Komarek, T., and Polifke, W., 2010, "Impact of Swirl Fluctuations on the Flame Response of a Perfectly Premixed Swirl Burner," ASME J. Eng. Gas Turbines Power, **132**(6), p. 061503.
[8] Palies, P., Durox, D., Schuller, T., and Candel, S., 2010, "The Combined Dynamics of Swirler and Turbulent Premixed Swirling Flames," Combust. Flame, **157**(9), pp. 1698–1717.
[9] Gatti, M., Gaudron, R., Mirat, C., Zimmer, L., and Schuller, T., 2018, "A Comparison of the Transfer Functions and Flow Fields of Flames With Increasing Swirl Number," ASME Paper No. GT2018-76105.
[10] Hirsch, C., Fanaca, D., Reddy, P., Polifke, W., and Sattelmayer, T., 2005, "Influence of the Swirler Design on the Flame Transfer Function of Premixed Flames," ASME Paper No. GT2005-68195.

[11] Schimek, S., Göke, S., Schrödinger, C., and Paschereit, C. O., 2012, "Flame Transfer Function Measurements With CH_4 and H_2 Fuel Mixtures at Ultra Wet Conditions in a Swirl Stabilized Premixed Combustor," ASME Paper No. GT2012-69788.
[12] Straub, D. L., and Richards, G. A., 1999, "Effect of Axial Swirl Vane Location on Combustion Dynamics," ASME Paper No. 99-GT-109.
[13] Kim, K. T., and Santavicca, D. A., 2013, "Interference Mechanisms of Acoustic/Convective Disturbances in a Swirl-Stabilized Lean-Premixed Combustor," Combust. Flame, **160**(8), pp. 1441–1457.
[14] Gatti, M., Gaudron, R., Mirat, C., and Schuller, T., 2017, "Effects of the Injector Design on the Transfer Function of Premixed Swirling Flames," ASME Paper No. GT2017-63874.
[15] Palies, P., Ilak, M., and Cheng, R., 2017, "Transient and Limit Cycle Combustion Dynamics Analysis of Turbulent Premixed Swirling Flames," J. Fluid Mech., **830**, pp. 681–707.
[16] Æsøy, E., Aguilar, J. G., Wiseman, S., Bothien, M. R., Worth, N. A., and Dawson, J. R., 2020, "Scaling and Prediction of Transfer Functions in Lean Premixed H_2/CH_4-Flames," Combust. Flame, **215**, pp. 269–282.
[17] Sattelmayer, T., 2003, "Influence of the Combustor Aerodynamics on Combustion Instabilities From Equivalence Ratio Fluctuations," ASME J. Eng. Gas Turbines Power, **125**(1), pp. 11–19.
[18] Schuermans, B., Bellucci, V., Guethe, F., Meili, F., Flohr, P., and Paschereit, C. O., 2004, "A Detailed Analysis of Thermoacoustic Interaction Mechanisms in a Turbulent Premixed Flame," ASME Paper No. GT2004-53831.
[19] Cuquel, A., Durox, D., and Schuller, T., 2013, "Scaling the Flame Transfer Function of Confined Premixed Conical Flames," Proc. Combust. Inst., **34**(1), pp. 1007–1014.
[20] Birbaud, A.-L., Durox, D., Ducruix, S., and Candel, S., 2007, "Dynamics of Confined Premixed Flames Submitted to Upstream Acoustic Modulations," Proc. Combust. Inst., **31**(1), pp. 1257–1265.
[21] Fu, Y., Cai, J., Jeng, S.-M., and Mongia, H., 2005, "Confinement Effects on the Swirling Flow of a Counter-Rotating Swirl Cup," ASME Paper No. GT2005-68622.
[22] De Rosa, A. J., Peluso, S. J., Quay, B. D., and Santavicca, D. A., 2016, "The Effect of Confinement on the Structure and Dynamic Response of Lean-Premixed, Swirl-Stabilized Flames," ASME J. Eng. Gas Turbines Power, **138**(6), p. 061507.
[23] Worth, N. A., and Dawson, J. R., 2013, "Self-Excited Circumferential Instabilities in a Model Annular Gas Turbine Combustor: Global Flame Dynamics," Proc. Combust. Inst., **34**(2), pp. 3127–3134.
[24] Worth, N. A., and Dawson, J. R., 2017, "Effect of Equivalence Ratio on the Modal Dynamics of Azimuthal Combustion Instabilities," Proc. Combust. Inst., **36**(3), pp. 3743–3751.
[25] Nygård, H. T., Mazur, M., Dawson, J. R., and Worth, N. A., 2019, "Flame Dynamics of Azimuthal Forced Spinning and Standing Modes in an Annular Combustor," Proc. Combust. Inst., **37**(4), pp. 5113–5120.
[26] Seybert, A. F., and Ross, D. F., 1977, "Experimental Determination of Acoustic Properties Using a Two-Microphone Random-Excitation Technique," J. Acoust. Soc. Am., **61**(5), pp. 1362–1370.
[27] Dowling, A. P., 1999, "A Kinematic Model of a Ducted Flame," J. Fluid Mech., **394**, pp. 51–72.
[28] Ducruix, S., Durox, D., and Candel, S., 2000, "Theoretical and Experimental Determinations of the Transfer Function of a Laminar Premixed Flame," Proc. Combust. Inst., **28**(1), pp. 765–773.
[29] Schuller, T., Durox, D., and Candel, S., 2003, "A Unified Model for the Prediction of Laminar Flame Transfer Functions: Comparisons Between Conical and V-Flame Dynamics," Combust. Flame, **134**(1–2), pp. 21–34.
[30] Polifke, W., and Lawn, C., 2007, "On the Low-Frequency Limit of Flame Transfer Functions," Combust. Flame, **151**(3), pp. 437–451.
[31] Palies, P., Durox, D., Schuller, T., and Candel, S., 2011, "Acoustic–Convective Mode Conversion in an Aerofoil Cascade," J. Fluid Mech., **672**, pp. 545–569.
[32] Fleifil, M., Annaswamy, A. M., Ghoneim, Z., and Ghoniem, A. F., 1996, "Response of a Laminar Premixed Flame to Flow Oscillations: A Kinematic Model and Thermoacoustic Instability Results," Combust. Flame, **106**(4), pp. 487–510.
[33] Wang, H., Law, C. K., and Lieuwen, T., 2009, "Linear Response of Stretch-Affected Premixed Flames to Flow Oscillations," Combust. Flame, **156**(4), pp. 889–895.
[34] Baillot, F., Durox, D., and Prud'homme, R., 1992, "Experimental and Theoretical Study of a Premixed Vibrating Flame," Combust. Flame, **88**(2), pp. 149–168.
[35] Albayrak, A., Juniper, M. P., and Polifke, W., 2019, "Propagation Speed of Inertial Waves in Cylindrical Swirling Flows," J. Fluid Mech., **879**, pp. 85–120.
[36] Hauser, M., Lorenz, M., and Sattelmayer, T., 2011, "Influence of Transversal Acoustic Excitation of the Burner Approach Flow on the Flame Structure," ASME J. Eng. Gas Turbines Power, **133**(4), p. 041501.

ARTICLE II

Flame dynamics of azimuthal forced spinning and standing modes in an annular combustor

Håkon T. Nygård, Marek Mazur, James R. Dawson,
and Nicholas A. Worth

Published in
Proceedings of the Combustion Institute

Available online at www.sciencedirect.com

ScienceDirect

Proceedings of the Combustion Institute 37 (2019) 5113–5120

Proceedings of the Combustion Institute

www.elsevier.com/locate/proci

Flame dynamics of azimuthal forced spinning and standing modes in an annular combustor

Håkon T. Nygård*, Marek Mazur, James R. Dawson, Nicholas A. Worth

Department of Energy and Process Engineering, Norwegian University of Science and Technology, Trondheim N-7491, Norway

Received 30 November 2017; accepted 20 August 2018
Available online 8 September 2018

Abstract

Azimuthal forcing has been applied to flames in a laboratory scale annular combustor in order to accurately control the azimuthal mode of excitation. A new forcing configuration permitted not only the pressure amplitude, but also the spin ratio and mode orientation to be accurately controlled, in order to generate standing modes and for the first time strong spinning modes in both a clockwise (CW) and anti-clockwise (ACW) direction. The phase averaged heat release dynamics of these modes was compared and a number of differences observed depending on the direction of pressure wave propagation, demonstrating characteristic ACW and CW heat release patterns. A new spin compensating averaging method was then introduced to analyse the flame dynamics, and it was shown that through the application of this method the dynamics of standing wave oscillations could be decomposed to recover the characteristic ACW and CW heat release responses. The global heat release response was also assessed during strongly spinning modes, and the magnitude of the response was shown to depend strongly on the direction of propagation, demonstrating the importance of the local swirl direction on the global heat release response, with important implications for the modelling of such flows.

Keywords: Gas turbines; Azimuthal modes; Combustion instabilities; Acoustic forcing; Flame dynamics

1. Introduction

The issue of thermoacoustic instability can arise during the development of new gas turbine engines, or when operating existing engines in new regimes, for example in order to reduce emissions or increase fuel flexibility. Damaging levels of pressure and heat release oscillations can occur during these instabilities, and therefore there is a need to eliminate these at the design stage, motivating the need for a greater understanding of the phenomenon.

A number of recent studies have focused on the advent of such instabilities in annular geometry [1–4], where the excitation of azimuthal modes results in flame responses which are no longer solely controlled by the magnitude and frequency of pressure oscillations, but also by characteristics

* Corresponding author.
E-mail address: hakon.t.nygard@ntnu.no (H.T. Nygård).

https://doi.org/10.1016/j.proci.2018.08.034

of the acoustic mode, such as the standing wave ratio (commonly referred to as the spin ratio [2]) and the orientation of the mode relative to flames. Previous studies in annular geometry have recently identified well defined modal preferences for different oscillation types, where changes to the chamber geometry, equivalence ratio and bulk flow velocities can result in significant changes to the modal dynamics observed [5–9]. To further complicate matters, recent studies have also shown that these modal characteristics may vary with time, leading to rapid switching between predominantly spinning and standing states [3,5,10,11] and rapid changes in orientation [8]. It has been shown in recent studies [12–14] that a small breaking in symmetry can greatly influence which mode is dominating. For example, in [12] non-uniformities in the heat release and pressure coupling resulted in a preference for spinning modes for weak non-uniformities and standing modes for sufficiently large non-uniformities. Furthermore, in [13] it was found the standing mode is related to either combustors that are non-rotationally symmetric, weak flame response at low amplitudes and strong response at large amplitudes or other physical mechanisms such as a mean azimuthal flow affecting the flame response. Symmetry breaking was found to promote standing modes in [14], while the addition of a mean azimuthal flow promote spinning modes.

Azimuthal pressure waves can induce local transverse velocity oscillations which can affect the flame dynamics and the spatial distribution of the heat release rate [15,16]. Therefore, in order to fully quantify the heat release response of an annular combustor there is a need to understand and ultimately predict the dynamic response of each flame to different modes of excitation. A greater knowledge of the flame response to different modes of oscillation may help us to construct models of the heat release response, which when integrated in low order network models [17–19] or as part of more involved Helmholtz calculations [20] represent both a viable and promising method of predicting system stability. Such flame describing functions (FDF) have previously been calculated experimentally [2,11], or numerically through either high fidelity simulations [21] or flame front modelling [22,23]. However, the prediction of such functions, particularly with lower order approaches, is still far from resolved, and a greater understanding of the flame dynamics should be considered invaluable to the further development of these methods. Furthermore, a better phenomenological understanding may also help us to understand how and why mode switching occurs in annular chambers, and help us to draw links between underlying flow behaviour and the modal dynamics in such systems.

Rapid mode switching in annular chambers makes isolating and studying the flame dynamics in annular configurations very challenging. Studies of self-excited instabilities are forced to rely on conditional averaging which reduces the amount of available data at each condition, but more crucially may only cover a small subset of the possible range of azimuthal mode characteristics. One way to address this issue is to prescribe the mode of excitation through the application of acoustic forcing. Recently transverse acoustic forcing has been applied in order to investigate the flame response to the orientation of pressure disturbances [24–26]. More recently, acoustic forcing of azimuthal modes in annular chambers have been undertaken, first in an annular chamber fitted with electrically heated Rijke tubes [27] and then later in annular combustor [28].

The present paper seeks to further our understanding of the flame dynamics in annular chambers through the application of azimuthal forcing to a laboratory scale annular combustor. When operated in a self-excited state, the current combustor exhibits a strong preference for anticlockwise (ACW) spinning modes [5], making the study of self-excited spinning modes in the clockwise (CW) direction almost impossible. Azimuthal forcing has been used to generate and analyse for the first time strong spinning modes in both directions for a reacting flow setup and relate the structure and dynamics of these oscillations to standing wave oscillations. Studying the heat release distribution and flame dynamics for a prescribed mode of excitation will eventually help predicting the growth rate and amplitude of the limit cycle of the instabilities. The ability to study modes of excitation which do not naturally occur allow important observations on the dynamics of spinning modes to be made, and for the first time give us the ability to accurately quantify these.

2. Experimental methods

2.1. Annular combustor and data acquisition

The annular combustor used in this study is described in detail in [1]. In the current study it is operated with a premixed air-ethylene mixture at an equivalence ratio of $\phi = 0.75$ and a bulk exit velocity of approximately 20ms^{-1} at the injector exit. Operation at this equivalence ratio ensures the flow is not self-excited, resulting in better modal control. In the current configuration, as shown in Fig. 1, the combustor consists of a cylindrical plenum chamber ($D_\text{p} = 212\text{mm}$, $L_\text{p} = 200\text{mm}$) with honeycomb flow straightener and grids to condition the flow. A hemispherical body ($D_\text{h} = 140\text{mm}$) aids flow distribution to each burner. 18 injectors ($d_\text{exit} = 18\text{mm}$) are equally spaced around a circle of diameter $d_\text{c} = 170\text{mm}$, and each features a centrally located bluff body ($d_\text{bb} = 13\text{mm}$). Each bluff

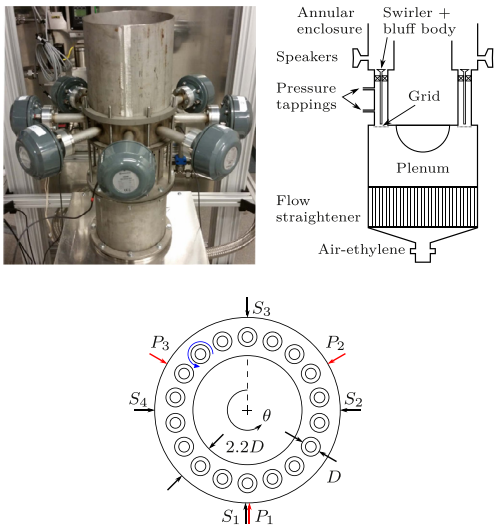

Fig. 1. Annular combustor with forcing array. *left top* combustor image (every other speaker used for forcing); *right top* schematic side view; *bottom* schematic top view. S_i and P_k mark the angular positions of speakers and transducers. S_1 and P_1 are located at $\theta = 180^\circ$, with 90° between each speaker used and 120° between each transducer. Direction of swirl is indicated by the blue arrow. (For interpretation of the references to colour in this figure legend, the reader is referred to the web version of this article.)

body features a six vane, $\alpha = 60^\circ$ anti-clockwise swirler mounted 10mm upstream measured from the dump plane to the swirler trailing edge. The annular chamber consists of inner and outer cylinders of diameter $D_\mathrm{i} = 129$mm and $D_\mathrm{o} = 212$mm, which extend 130mm and 300mm downstream of the dump plane respectively.

Three Kulite XCS-093-05D pressure transducers are mounted flush with the inner wall of the injector tubes 45mm below the dump plane at the angular locations marked by P_k in Fig. 1. The transducer signals are amplified by a Fylde FE-579-TA bridge amplifier, before being logged using NI-9234 24-bit DAQ cards with sampling frequency $f_\mathrm{trans} = 51.2$kHz. The heat release fluctuations are recorded through OH^* chemiluminescence using a Photron SA1.1 CMOS camera with a LaVision Intensified Relay Optics unit and a Cerco 2178 UV lens equipped with a D20-VG0035942 filter (centre wavelength 310nm, full width half maximum 10nm). The camera was operated with sampling frequency $f_\mathrm{cam} = 10$kHz at a 768×768 pixels resolution (resulting in a spatial resolution of 3.2 pixels/mm) and a total of 19,410 images were recorded.

2.2. Mode determination

Assuming the acoustic mode in the combustor is a superposition of two counter rotating 1D plane waves with wavelength corresponding to the unwrapped length of the combustor, the complex pressure fluctuations can be expressed as $p(\theta_k, t) = \left[A_+ e^{\mathrm{i}(\theta_k - \nu_\theta t/R)} + A_- e^{\mathrm{i}(-\theta_k + \nu_\theta t/R)}\right] e^{\mathrm{i}\omega_0 t}$. A_+ and A_- are the amplitudes of the ACW and CW rotating waves respectively, where θ_k is the angle of the kth sensor, as defined in Fig. 1, ω_0 is the forcing angular frequency and ν_θ/R is the angular velocity of the nodal line if there is a standing wave component. The pressure fluctuation amplitude of any given mode is given by $\left[A_+^2 + A_-^2\right]^{1/2}$. The pressure measured from each pressure transducer is the real part of the complex pressure, $p_\mathrm{meas} = \mathrm{Re}\{p\}$. To determine all the unknowns in the equation, a nonlinear least squares fit is applied to the indicator $C(t) = \frac{1}{N}\sum_{k=1}^{N} \mathrm{Re}\left\{p(\theta_k, t) e^{\mathrm{i}\theta_k}\right\}$, which was introduced in [10]. To differentiate between predominantly spinning and standing modes, the spin ratio $SR = (|A_+| - |A_-|)/(|A_+| + |A_-|)$ is used [2], with the following scheme applied to classify modes which are predominantly spinning in either the CW ($SR < -1/3$) or ACW ($SR > 1/3$) directions, or otherwise standing. The value of $\pm 1/3$ corresponds to the largest pressure amplitude of the two travelling waves being twice the lowest and is chosen to be consistent with previous work [29].

2.3. Forcing setup

The forcing array, shown in Fig. 1, consists of eight 120mm long standoff tubes, mounted at a height of 35mm above the dump plane and spaced equidistantly around the chamber. Each standoff tube has a horn driver (Adastra HD60 16Ω) mounted at the end, with diametrically opposite drivers forced in anti-phase forming a speaker pair. A multi channel waveform generator Aim-TTI TGA1244 was used to create synchronised forcing outputs which were amplified using QTX PRO 1000 amplifiers. In the present investigation the two speaker pairs indicated in Fig. 1, and thus only every other horn driver, are used to set up the acoustic modes, simplifying the setup process while still giving good control. Given ideal geometry and speaker response, if all forcing amplitudes were equal, zero phase delay would be used to produce standing modes, while a phase delay of $\pm 90\circ$ would be used to produce spinning modes. In practice the amplitude and phase delay between the speakers were adjusted carefully to achieve the desired amplitude response, and mode type and orientation.

2.4. Spin compensating rotational averaging

Forcing different azimuthal modes in the presence of a turbulent reacting flow has been shown

to lead to stochastic fluctuations in the pressure response and spin ratio [28] when compared to cold flow conditions. Therefore, in order to investigate the phase averaged component of the heat release that is moving at a constant rate in a given direction, a new rotational averaging method is introduced in the current paper.

As in previous work, initially the phase averaged normalised heat release fluctuation $\tilde{Q}_n = ((\tilde{Q} - \overline{Q})/\langle \overline{Q} \rangle)$ is calculated based on the pressure signals. Here $\tilde{Q}_n = \tilde{Q}_n(r, \theta, \tau/T)$, where τ/T is the normalised position in the phase averaged cycle, $Q = Q(r, \theta, t)$ is the spatial distribution of OH* intensity captured by the camera, and $\tilde{Q} = \tilde{Q}(r, \theta, \tau/T)$ is its phase average, $\overline{Q} = \overline{Q}(r, \theta)$ is the temporal mean and $\langle \overline{Q} \rangle$ is the spatial and temporal mean. Phase averaging is highly applicable given the typical self-excited response in the current combustor is dominated by oscillations at a single frequency [5], as are the forced oscillations.

For a general case using N burners one forcing cycle is divided into a total of N time steps for phase averaging. In order to isolate the spinning component in a given direction the jth phase average distribution is rotated by an angle $2\pi j/N$ in the opposite direction to the prescribed direction of interest. Since N time steps are used the burners will overlap after the rotation, and the transformation effectively freezes the propagation of any spinning component in the prescribed direction. This is done under the assumption of heat release patterns moving at the same constant speed in both directions. The assumption can be made due to the induced bulk swirl being at least two orders of magnitude lower than the speed of sound, making a negligible difference in propagation speed for the two plane waves. The average of the N rotated distributions is then calculated according to Eq. (1), producing a single spatial spin compensated distribution, $\overline{Q}^{\mathrm{x}}_{\mathrm{rot}} = f(r, \theta)$.

$$\overline{Q}^{\mathrm{x}}_{\mathrm{rot}} = \frac{1}{N} \sum_{j=0}^{N-1} \mathrm{Rot}_{\beta_j} \left\{ \left[\frac{\tilde{Q} - \overline{Q}}{\langle \overline{Q} \rangle} \right]_j \right\}, \tag{1}$$

where x is either the ACW or the CW component, j is the phase average time step and Rot_{β_j} is a rotation of β_j around the center of the annulus. The angle is calculated as $\beta_j = \pm \frac{2\pi}{N} j$, where positive and negative signs are used for CW and ACW components respectively.

The summation of these rotated images effectively averages the heat release distribution of each of the N flames at the same point in the cycle, in the direction of rotation. Oscillations travelling in the opposite direction are effectively cancelled, making the method invaluable for isolating and studying the effect of spinning waves travelling in different directions around the annulus. The method also offers an advantage in that slight variations in heat release from flame to flame are also averaged out, providing a clearer description of the mean flame response to acoustic waves and retaining finer structural details of the heat release rate.

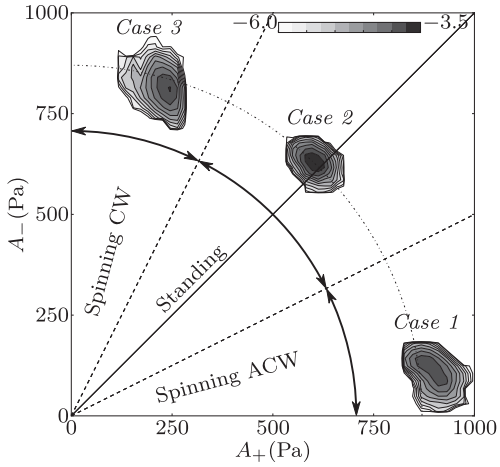

Fig. 2. Joint PDF of A_+ and A_- for three different cases, all using forcing frequency $f_0 = 1690$Hz. Dashed lines indicate $SR = \pm 1/3$ and the solid line is $SR = 0$. Case 1: $\overline{SR} = 0.9$; Case 2: $\overline{SR} = 0.0$; Case 3: $\overline{SR} = -0.6$. Intensity contours describe base 10 exponentials.

In the rest of the paper $\overline{Q}^{\mathrm{ACW}}_{\mathrm{rot}}$ and $\overline{Q}^{\mathrm{CW}}_{\mathrm{rot}}$ will be used to describe the spin compensated averages of the normalised phase average heat release oscillations in the ACW and CW directions respectively.

3. Results and discussion

3.1. Acoustically forced modes

Azimuthal acoustic forcing was applied in order to investigate the flame dynamics of the following three different oscillation modes: *Case 1.* Strongly spinning in the ACW direction; *Case 2.* Predominantly Standing; *Case 3.* Strongly spinning in the CW direction. In order to assess the pressure response of these forced cases Fig. 2 shows the joint probability density function (JPDF) of the two counter rotating waves A_+ and A_-. The centre of the JPDF distributions for the three cases shows that the application of acoustic forcing is sufficient to exercise good control over the mode of oscillation, and generate as desired distinct standing and spinning modal responses. Although a high level of sensitivity to forcing parameters resulted in a larger spin ratio in the ACW direction in comparison with the CW direction, it should be noted that both cases can be considered strongly spinning, with a ratio between ACW and CW travelling waves of over 4 times. All cases have approximately the same mean pressure fluctuation amplitude, meaning the acous-

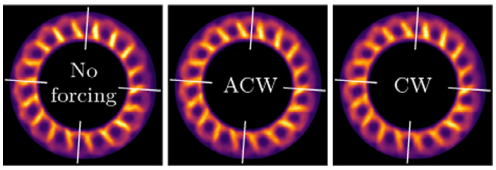

Fig. 3. Mean flame structure for the no forcing case (left), and the ACW spinning (middle) and the CW spinnning (right) forced modes. The white lines represent the location of the speakers used for forcing.

tic energy fed into the system is of similar magnitude for all cases. This amplitude was selected to be similar to previously observed self-excited modes observed in the combustor [5]. Finally it should be noted that while the size of the probability distributions for all cases is significantly smaller than those observed during the study of self-excited instabilities, the finite size of these still indicates the presence of some unsteady mode switching, which is consistent with previous work [28].

3.2. Mean flame structure

The mean OH^* chemiluminescence of unforced and spinning mode cases is shown in Fig. 3. As seen in previous investigations, the regions of highest heat release are observed between adjacent flames. While the heat release distribution is strongly asymmetric around each flame, there is rotational symmetry from flame to flame. Comparison between unforced and spinning mode cases shows no significant qualitative differences in the distributions, suggesting the forcing does not significantly affect the mean flame structure, which is consistent with previous investigations [28].

3.3. Flame dynamics of azimuthally forced modes

The flame dynamics of the acoustically forced modes have been studied through snapshots of the phase average heat release distribution and through the application of the new spin compensating average procedure described in §2.4. Figure 4 shows snapshots of the phase average heat release oscillations at a single location in the pressure cycle in the left column for all three forced cases. In the two middle columns the spin compensated distributions in both directions for the same cases are shown with zoomed in versions of selected cases in the rightmost column.

Observing the snapshot for the strong ACW mode, *Case 1* in the left column of Fig. 4, the heat release oscillations are qualitatively similar to those observed during self-excited instabilities [1]. The largest fluctuations are appearing close to the outer radial wall in a large band-like structure which spans almost half the annulus, and large oscillations are also produced in the interacting region between adjacent flames. Such structures have been linked previously to the formation of coherent vortical structures in the shear layers as a response to the pressure oscillations in the chamber [15]. The close agreement with previous results suggests the acoustic forcing of spinning waves produces a similar flame response to self-excited fluctuations.

While the use of acoustic forcing allows good control over the spin ratio, increasing the amount of data used for phase averaging and therefore the clarity of the imaging, the use of spin compensating averaging further improves clarity, and also allows the decomposition of oscillations to be investigated. Comparing the two centre images for the upper and lower rows in Fig. 4, the averaged component traveling in the direction of forcing is shown to dominate over the component in the counter direction (Strong oscillations are therefore observed in $\overline{Q}_{\mathrm{rot}}^{\mathrm{ACW}}$ and $\overline{Q}_{\mathrm{rot}}^{\mathrm{CW}}$ for the ACW and CW spinning cases respectively). The residual oscillations observed in the counter direction averages may arise due to the imperfect spinning waves generated in the present study (as seen in Fig. 2) or non uniformity between burners. The heat release structure of both ACW and CW components is similar to the phase averaged snapshots, but the averaging procedure removes burner to burner differences, making observations of the structure much clearer, highlighting the difference between the cases. Allowing the entire phase average cycle to be collapsed onto one image also allows a more straightforward comparison of the magnitude of the response, and a slight decrease in oscillation amplitude of the most intense structure is observed for the CW spinning case.

It is interesting to contrast the response in *Case 1* featuring a strong ACW mode with that of *Case 3* which features a strong CW spinning wave. The CW case occurs rarely when the combustor is self-excited [5], and therefore the use of acoustic forcing presents the only viable method of studying the flame response. Comparing the zoomed in views in Fig. 4 of the two spinning modes the main features are quite similar, but with a number of subtle differences. The flame response to the CW spinning wave is again very asymmetric, with the largest heat release oscillations observed close to the outer wall and between adjacent flames. However, the structures appear to be more isolated in comparison with the linked structure produced by the ACW spinning wave, with breaks visible between adjacent flames. Furthermore, the largest heat release oscillations are observed to move from the outer radial wall to the interacting region between adjacent flames and more activity is also observed close to the inner wall, representing a spatial shift in the centre of heat release in the radial direction. Another difference that can be observed is the presence of linked structure between the bluff body and the interacting region for the CW case that is much weaker for the ACW case (black squares in zoomed

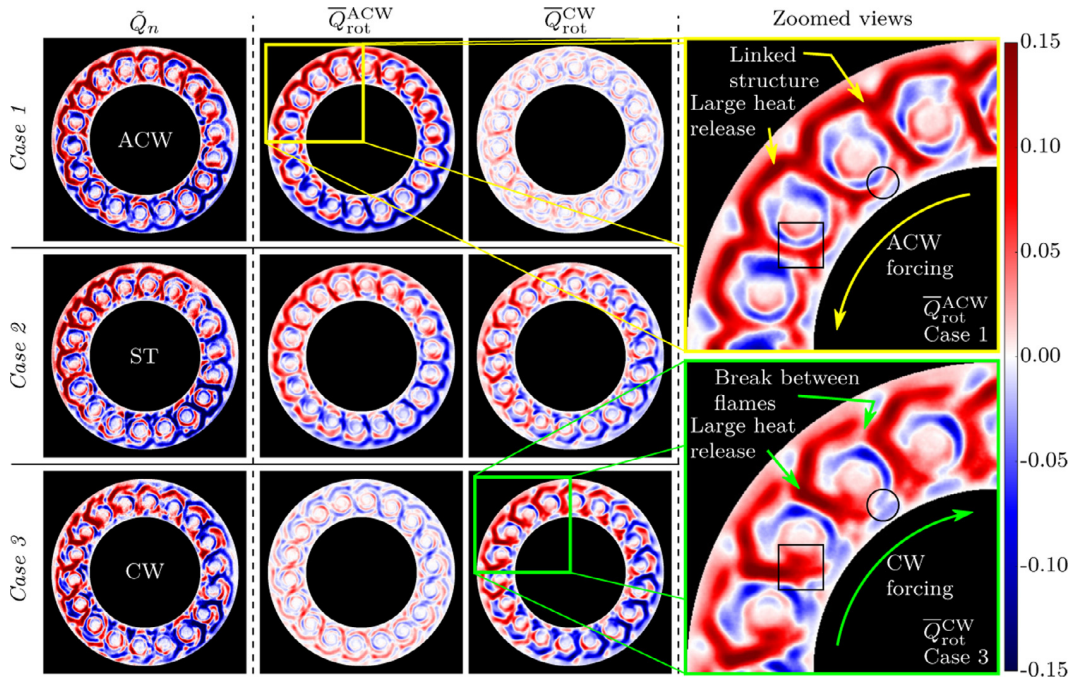

Fig. 4. Snapshot of phase average in left column, with the spin compensating average in both directions in the two middle columns. Each row represents one forcing case and for ease of comparison the regions of maximum heat release have been aligned. Top: Strong ACW forcing (*Case 1*); middle: Standing mode (*Case 2*); bottom: Strong CW forcing (*Case 3*). The right column is annoted and highlighted zoomed in views of two of the most interesting cases of the spin compensated average. The colour bar is valid for the whole figure. (Colour online).

views in Fig. 4). In the CW case heat release rate along the inner part of the wall is also in phase and connected with the heat release around the bluff body closest to the inner annular wall, while for the ACW case there is a clear division between them (black circles in zoomed views in Fig. 4). The major difference between the two spinning cases is the direction of forcing in relation to the direction of swirl. For the ACW case the acoustic forcing is in the flow direction induced by the swirlers along the outer wall, while for the CW case the forcing is in the opposite direction. The direction of the acoustic wave relative to the local swirl direction is observed therefore to have a significant effect on the flame dynamics when flames are closely confined in annular geometry.

The same spin compensating averaging procedure was also applied to the standing wave in *Case 2*, shown in the middle row (two centre images) in Fig. 4. In this case the heat release oscillations in both $\overline{Q}^{ACW}_{rot}$ and $\overline{Q}^{CW}_{rot}$ have similar magnitudes, and observation of the spatial distributions shows strong similarities with the corresponding spinning waves in *Case 1* and *Case 3* respectively. The oscillation magnitudes of these components are lower in comparison with the spinning cases, as the vector sum of pressure fluctuation amplitudes was kept constant between cases. The observation of the ability to decompose the heat release distribution during a standing wave oscillation into its constituent spinning wave components may be invaluable in further understanding the dynamics of such systems in cases where the full range of responses cannot be measured directly, and in the modelling of such responses.

3.4. Integrated heat release response

It is also useful to examine the global heat release response of each flame which is a parameter widely used in low order models. A 20° wide kernel positioned at each burner centre is used to evaluate the mean heat release over an oscillation cycle. The integration is performed on the spin compensated averages in the direction of forcing in order to evaluate the average burner behaviour for this dominant component. The sector kernel is also further divided into inner and outer regions in order to understand the local distribution of heat release between cases. The results for the two forced spinning modes are shown in Fig. 5 together with sinusoidal fitted curves, and for ease of comparison the phase of the cycles is normalised to the global integrated heat release.

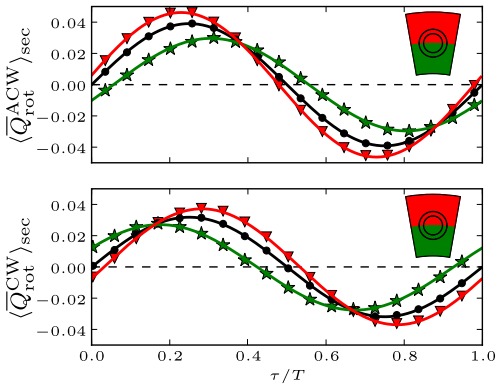

Fig. 5. Sector averaged heat release oscillations for *top* ACW and *bottom* CW spinning modes. Averages shown from inner (green line, star markers) and outer (red line, triangle marker) regions, and the total response (black line, circular markers). The markers represent measurements while the solid lines are fitted sine curves. To aid interpretation, the phase of the total heat release (black lines) for the two cases have been aligned. (For interpretation of the references to colour in this figure legend, the reader is referred to the web version of this article.)

It is interesting to examine the phase and magnitude of the inner and outer heat release oscillations. For *Case 1* for an ACW spinning mode the inner heat release oscillation is observed to lag the outer, with a phase difference of $\Delta t/T \approx 0.08$. In comparison in *Case 3* for a CW spinning mode the phase lag is inverted, and now the outer oscillation lags the inner. Significantly for this case the phase lag also increased to $\Delta t/T \approx 0.11$.

Moreover, the oscillation amplitude of the inner and outer regions are $|\langle \overline{Q}^{ACW}_{rot} \rangle_{inner}| = 0.030$ and $|\langle \overline{Q}^{ACW}_{rot} \rangle_{outer}| = 0.046$ respectively during an ACW spinning mode. In comparison for the CW spinning mode the amplitudes are $|\langle \overline{Q}^{CW}_{rot} \rangle_{inner}| = 0.027$ and $|\langle \overline{Q}^{CW}_{rot} \rangle_{outer}| = 0.037$. This quantifies the observation in the previous section that the heat release magnitude decreases and appears to shift radially inward. The amplitude ratio between outer and inner regions decreases slightly from $|\langle \overline{Q}^{ACW}_{rot} \rangle_{outer}|/|\langle \overline{Q}^{ACW}_{rot} \rangle_{inner}| = 1.6$ for the ACW case to $|\langle \overline{Q}^{CW}_{rot} \rangle_{outer}|/|\langle \overline{Q}^{CW}_{rot} \rangle_{inner}| = 1.4$ for the CW case, conforming broadly to spatial reorganisation of heat release observed previously [5].

The combination of increased phase lag and decreased oscillation amplitude for the CW spinning case results in an amplitude difference of around 23% for the total integrated heat release response in comparison with the ACW case. Given the slight differences in the pressure response amplitudes (shown in Fig. 2) and the spin ratios this difference may not be purely due to differences in the spinning mode orientation. To eliminate these influences a similar analysis was performed using the decomposed standing wave of case 2, ensuring the similarity of both components in terms of spin ratio and pressure response magnitude. While not included graphically for brevity, a similar difference of 35% was calculated for the total heat release response. The similarity of this adds to the qualitative evidence presented in Section 3.3 which suggests that standing waves can be decomposed into their spinning components, although further evidence will be sought in future work. Therefore, given that the main difference between cases is the orientation of swirl relative to the incoming pressure wave, the directionality of the spinning mode appears in this case to be significant. This result has important implications for low order models which use the integrated heat release response, and suggest that different flame responses may need to be defined in order to characterise CW and ACW spinning modes.

Finally it is worth observing that the sinusoidal curves fit the measurements very closely, demonstrating that sinusoidal forcing of a spinning mode results in a traveling heat release fluctuation that is also sinusoidal. While the rotational averaging assumes that the heat release rate fluctuation is azimuthally periodic, and identical burner response, it does not impose a sinusoidal response. The observed behaviour provides a further indication for how the heat release field can be linearly manipulated for the cases in the present study.

4. Conclusions

In the present study azimuthal forcing has been applied to generate for the first time well controlled spinning and standing waves in a lab scale annular combustor, allowing the flame dynamics of modes with different spin ratios to be investigated with much greater precision than previously possible. A close agreement between the dynamics of ACW spinning waves in forced and previous self-excited experiments was observed. However, a number of differences were observed between these ACW cases and the flame dynamics occurring during CW spinning waves, including the redistribution of heat release in the annulus. Observation of the integrated heat release oscillations indicated a shift from outer to inner annulus depending on direction of the spinning wave. These changes were attributed to the symmetry breaking effect of the locally swirling flow at each flame. Finally through the introduction of a novel averaging method it was shown that the heat release dynamics during a standing mode could be decomposed into ACW and CW spinning components, offering a new way of understanding the dynamics of such systems.

Acknowledgements

The authors gratefully acknowledge financial support from the European Research Council (ERC): Grant agreement 677931 TAIAC.

References

[1] N.A. Worth, J.R. Dawson, *Proc. Combust. Inst.* 34 (2) (2013) 3127–3134, doi:10.1016/j.proci.2012.05.061.

[2] J.-F. Bourgouin, D. Durox, J. Moeck, T. Schuller, S. Candel, in: Proceedings of the ASME Conference, 2013. GT2013-95010.

[3] G. Ghirardo, M.P. Juniper, *Proc. Royal Soc. A* 469 (2157) (2013), doi:10.1098/rspa.2013.0232.

[4] G. Staffelbach, L. Gicquel, G. Boudier, T. Poinsot, *Proc. Combust. Inst.* 32 (2) (2009) 2909–2916.

[5] N.A. Worth, J.R. Dawson, *Combust. Flame* 160 (11) (2013) 2476–2489, doi:10.1016/j.combustflame.2013.04.031.

[6] D. Laera, T. Schuller, K. Prieur, D. Durox, S.M. Camporeale, S. Candel, *Combust. Flame* 184 (2017) 136–152.

[7] K. Prieur, D. Durox, T. Schuller, S. Candel, *Combust. Flame* 175 (2017) 283–291.

[8] N.A. Worth, J.R. Dawson, *Proc. Combust. Inst.* 36 (3) (2017) 3743–3751.

[9] K. Prieur, D. Durox, T. Schuller, S. Candel, *J. Eng. Gas Turb. Power* 140 (3) (2018) 031503, doi:10.1115/1.4037824.

[10] P. Wolf, G. Staffelbach, L.Y. Gicquel, J.-D. Müller, T. Poinsot, *Combust. Flame* 159 (11) (2012) 3398–3413, doi:10.1016/j.combustflame.2012.06.016.

[11] N. Noiray, B. Schuermans, *Proc. Royal Soc. A* 469 (2151) (2013), doi:10.1098/rspa.2012.0535.

[12] N. Noiray, M. Bothien, B. Schuermans, *Combust. Theor. Model.* 15 (5) (2011) 585–606, doi:10.1080/13647830.2011.552636.

[13] G. Ghirardo, M.P. Juniper, J.P. Moeck, in: Proceedings of the ASME Conference, 2015. GT2015-43127.

[14] M. Bauerheim, M. Cazalens, T. Poinsot, *Proc. Combust. Inst.* 35 (3) (2015) 3219–3227, doi:10.1016/j.proci.2014.05.053.

[15] J.R. Dawson, N.A. Worth, *Combust. Flame* 161 (10) (2014) 2565–2578.

[16] V. Acharya, T. Lieuwen, *Combust. Flame* 165 (2016) 188–197, doi:10.1016/j.combustflame.2015.12.003.

[17] A.P. Dowling, *J. Fluid Mech.* 346 (1997) 271–290.

[18] S.R. Stow, A.P. Dowling, *Proceedings of the ASME Conference* (2004) 775–786. GT2004-41669.

[19] N. Noiray, D. Durox, T. Schuller, S. Candel, *J. Fluid Mech.* 615 (2008) 139–167, doi:10.1017/S0022112008003613.

[20] F. Nicoud, L. Benoit, C. Sensiau, T. Poinsot, *AIAA Journal* 45 (2) (2007) 426–441.

[21] X. Han, J. Li, A.S. Morgans, *Combust. Flame* 162 (10) (2015) 3632–3647.

[22] A. Cuquel, D. Durox, T. Schuller, in: Seventh Mediterranean Combustion Symposium, Sardinia, Italy, September, 2011, pp. 11–15.

[23] P. Palies, T. Schuller, D. Durox, S. Candel, *Proc. Combust. Inst.* 33 (2) (2011) 2967–2974.

[24] J. O'Connor, T. Lieuwen, *Combust. Sci. Technol.* 183 (2011) 427–443. 17.

[25] M. Hauser, M. Lorenz, T. Sattelmayer, *J. Eng. Gas Turb. Power* 133 (4) (2011) 041501, doi:10.1115/1.4002175.

[26] A. Saurabh, C.O. Paschereit, *Combust. Flame* 182 (2017) 298–312.

[27] G. Gelbert, J.P. Moeck, C.O. Paschereit, R. King, *Control Eng. Pract.* 20 (8) (2012) 770–782.

[28] N.A. Worth, J.R. Dawson, J.A. Sidey, E. Mastorakos, *Proc. Combust. Inst.* 36 (3) (2017) 3783–3790.

[29] J.R. Dawson, N.A. Worth, *Proc. Combust. Inst.* 35 (3) (2015) 3283–3290.

ARTICLE III

Characteristics of self-excited spinning azimuthal modes in an annular combustor with turbulent premixed bluff-body flames

Marek Mazur, Håkon T. Nygård, James R. Dawson, and Nicholas A. Worth

Published in
Proceedings of the Combustion Institute

Available online at www.sciencedirect.com

ScienceDirect

Proceedings of the Combustion Institute 37 (2019) 5129–5136

Proceedings of the Combustion Institute

www.elsevier.com/locate/proci

Characteristics of self-excited spinning azimuthal modes in an annular combustor with turbulent premixed bluff-body flames

Marek Mazur*, Håkon T. Nygård, James R. Dawson, Nicholas A. Worth

Department of Energy and Process Engineering, Norwegian University of Science and Technology, N-7491 Trondheim, Norway, Kolbjørn Hejes v 1B, Trondheim 7491, Norway

Received 30 November 2017; accepted 16 July 2018
Available online 23 August 2018

Abstract

In this paper we investigate self-excited azimuthal modes in an annular combustor with turbulent premixed bluff-body stabilised flames. Previous studies have shown that both swirl and equivalence ratio influence modal dynamics, i.e. the time-varying nature of the modes. However, self-excited azimuthal modes have not yet been investigated in turbulent flames without bulk swirl, which do not generate any preferential flow in either azimuthal direction, and may therefore lead to different behaviour. Joint probability density functions of the instability amplitudes at various flowrates and equivalence ratios showed a strong bi-modal response favouring both ACW and CW spinning states not previously observed. Operating conditions leading to a bi-modal response provide a unique opportunity to investigate whether the structure of the global fluctuating heat release rate of self-excited spinning modes in both directions exhibit similar dynamics and structure. This was investigated using high-speed OH* chemiluminescence images of the annular combustor and a new rotational averaging method was applied which decomposes the spinning components of the global fluctuating heat release rate. The new rotational averaging, which differs from standard phase-averaging, produces spatial averages in a frame of reference moving with the spinning wave. The results show that the structure of the fluctuating heat release rate for spinning modes is highly asymmetric as characterised by large, crescent shaped regions of high OH* intensity, located on the far side of each flame, relative to the direction of the azimuthally propagating pressure wave. In comparison with interacting swirling flames, these results indicate that the previously observed radial asymmetry of OH* fluctuations may be introduced through advection by local swirl.

Keywords: Flame dynamics; Combustion instability; Annular combustor; Azimuthal modes; Modal dynamics

* Corresponding author.
E-mail address: marek.mazur@ntnu.no (M. Mazur).

https://doi.org/10.1016/j.proci.2018.07.080

1. Introduction

Thermoacoustic instabilities remain a crucial impediment in the design and operation of low emission combustors in aeroengines and gas turbines for power generation. Many gas turbines use annular combustor geometries which give rise to self-excited azimuthal modes [6].

Recent studies have provided new insight into azimuthal modes and have shown that due to azimuthal symmetry, self-excited instabilities in these systems give rise to more complex behaviour [1,2,4,7–10] compared with longitudinal modes in isolated single flame systems. Depending on the burner geometry, equivalence ratio and bulk velocity, the system can excite specific azimuthal modes or exhibit modal dynamics. Other investigations in annular combustors with turbulent swirling flames give rise to modal dynamics where, at a given operating point, the excited mode exhibits time-varying phase and amplitude, switching back and forth between spinning, standing and mixed modes [1–4,8,10]. In theoretical studies it was suggested, that this mode switching is related to the asymmetries in the heat release rate or flow [11–13].

So far, the occurrence of modal dynamics has only been observed in annular combustors equipped with turbulent swirling flames. Identical swirling injectors imparts mean azimuthal flow patterns which has an influence on the modal dynamics [3]. Bauerheim et al. [18] developed an analytical model demonstrating that changing the burner geometry breaks the azimuthal symmetry and promotes standing waves but the addition of even a small level bulk swirl promotes spinning modes. Bourgouin et al. [14] modified the annular combustor presented in Bourgouin et al. [2] by replacing swirling injectors with laminar matrix burners thereby removing any mean azimuthal flow components but demonstrated that spinning modes could be excited. Using the same configuration, Prieur et al. [17] showed that spinning, standing or slanted azimuthal modes were self-excited depending on the operating point but at certain conditions mode selection was very sensitive as hysteresis effects were observed. To date, the effect of turbulent premixed flames without swirl on the modal dynamics of self-excited azimuthal modes have yet to be investigated. Based on the limited information available, we are interested in knowing whether the absence of swirl and bulk azimuthal flow will result in a suppression of modal dynamics or, if modal dynamics occur, will they exhibit any statistical modal preference.

The aim of the present investigation is twofold: (i) to demonstrate the occurrence of self-excited azimuthal modes in an annular combustor equipped with bluff-body stabilised turbulent premixed flames without swirl and characterise their modal response for a range of operating conditions and, (ii) take advantage of the absence of swirl to better understand the fundamental response of the global fluctuating heat release rate in terms of its structure and dynamics when undergoing self-excited spinning modes. Insight into the modal response of turbulent premixed flames without swirl and associated structure dynamics of the heat release rate are required to gain a more complete understanding of combustion instabilities in annular combustors.

2. Experimental methods

2.1. Annular combustor

The experiments were carried out in an atmospheric annular combustor developed previously [3–5]. Figure 1 shows a 3D model of the annular combustor. It consists of a plenum, which is fed by premixed ethylene-air mixtures, and contains a grid and a honeycomb for flow conditioning and a hemispherical body in the upper part of the plenum is used to divide the flow. The reactants are fed into the combustor through 12 injector tubes of diameter = 18.5 mm, fitted with a flush-mounted bluff body with a blockage ratio of 50%. A top view of the 12 bluff bodies is shown to the right of Fig. 1. The annular combustion chamber has an inner wall of diameter $D_i = 127$ mm and outer wall diameter $D_o = 212$ mm. The length of the inner and outer walls, $L_i = 130$ mm and $L_o = 300$ mm respectively, are mismatched to obtain self-excited instabilities as reported in [2–4]. Stability maps were obtained by varying the bulk exit velocity U_b, (calculated at the dump plane from the volumetric flow rate), in 0.6 m/s steps between $U_b = 17.7 - 21.1$ m/s. The equivalence ratio, ϕ, was varied in steps of 0.05 between $\phi = 0.7 - 1.0$. The power therefore varied between $82 - 194$ kW.

2.2. Experimental measurements

Pressure and OH* chemiluminescence measurements were obtained simultaneously. Dynamic pressures were measured by pairs of pressure sensors located upstream of the combustion chamber as shown in Fig. 1 at circumferential positions *p1, p2* and *p3*. The Kulite pressure sensors, model XCS-093s with a measurement sensitivity of 4.2857×10^{-3} mV/Pa, were connected to Fylde FE-579-TA bridge amplifiers and measurements were recorded with a sampling frequency of 51.2 kHz for a duration of 10 s, giving a frequency resolution of 0.1 Hz. Each measurement was repeated a total of 4 times across a range of inlet velocities, and for $U_b = 19.9$ m/s case, each measurement was repeated 40 times in order to report statistically resolved distributions of the modal preference. Between measurements the rig was reignited to ensure independence, removing the possibility of hysteresis. A wall mounted thermocouple ensured that

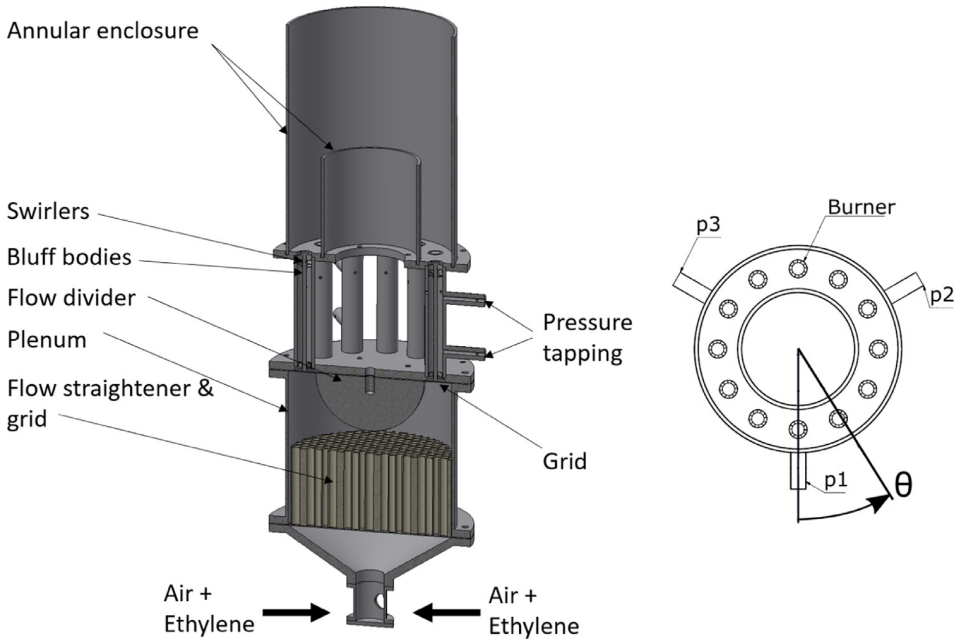

Fig. 1. Left: 3D model of the annular combustor with labels describing the main geometrical features. Right: Top view of the annular combustor showing the burner spacing and circumferential locations of the pressure measurements.

the combustor temperature was in the same range during each measurement. It should be noted that the JPDF distributions show little change varying the number of independent samples between 4 and 40, and can therefore be considered resolved for the current combustor setup.

To measure the structure of the fluctuating heat release rate around the annulus, high speed OH* chemiluminescence images were obtained from above using an air cooled mirror (As shown in [3]). A Phantom V2012 camera equipped with a LaVision IRO unit and a UV filter (model: D20-VG0035942) with a center wavelength of 310 nm and a full width at half maximum of 10 nm was used. A total of 120,000 images (full camera memory) was acquired at a sampling frequency of 10 kHz and using an array of 768 × 768 pixels, giving a spatial resolution of 0.31 mm/pixel. Triggering and measurements were recorded using a 24 bit NI Compact DAQ system, model 9174.

2.3. Analysis of the pressure data

To evaluate the self-excited modes the procedure described in previous papers was used [3,5,8,10]. Measurement positions of the pressure sensors, *p1*, *p2* and *p3*, were separated by $\theta = 120^\circ$ as shown in Fig. 1. We assume the modes correspond to a superposition of one-dimensional plane waves according to: $p(\theta_k, t) = [A_+ e^{i(\theta_k - vt/R)} + A_- e^{i(-\theta_k + vt/R)}]e^{i\omega_0 t}$ where A_+ and A_- are the amplitudes of anti-clockwise (ACW) and clockwise (CW) waves respectively, ω is the angular frequency, and $v_\theta t/R$ is a lumped parameter that defines the angular velocity of the nodal line when both A_+ and $A_- > 0$.

The measured pressure is the real part of the complex pressure, $p_{meas} = Re(p)$. A least-squares fit over 6 cycles is used to evaluate the amplitudes A_+ and A_-, as well as the lumped parameter $\theta_P = v_\theta t/R$. The amplitude of the pressure fluctuations of any given mode is given by $[A_+^2 + A_-^2]^{1/2}$. A_+ and A_- are also used to calculate the spin ratio (SR) defined by Bourgouin et al. [2]: $SR = (|A_+| - |A_-|)/(|A_+| + |A_-|)$, where a $SR = \pm 1$ correspond to perfect spinning modes in the ACW and CW directions respectively, a $SR = 0$ corresponds to a standing wave and intermediate values are mixed modes.

2.4. Rotational averaging method for OH*

Due to the time-varying nature of the modes, conditional averaging is required for investigating the structure of the OH* fluctuations for different modes. OH* images are conditioned on the SR evaluated from the pressure time-series data. Since the SR varies in time, we must resort to choosing suitable thresholds of the SR to classify the modes into spinning and standing. In the present work OH* images are conditioned using the following thresholds and then phase-averaged [3,5,8]: $SR > 1/3$ are classified as ACW spinning modes, $SR < -1/3$ are classified as CW spinning modes, intermediate values are classed as standing modes $-1/3 < SR <$

1/3. The large imaging data set allowed a minimum of 500 images to be used at each phase angle even after conditional averaging to ensure convergence. In this paper we focus on spinning modes and are particularly interested in determining whether the structure of the OH* fluctuations is affected by the spin direction as found in swirling flames [3]. It is reasonable to expect that in the absence of swirl and bulk azimuthal flow the structure of the OH* fluctuations should be similar for modes spinning in either direction.

Since perfect spinning modes rarely occur and due to the presence of mode switching (described in 3.4), conditionally averaged spinning modes are more accurately described as mixed modes with a dominant spin direction. Consequently, the OH* response from underlying mixed mode contaminates the structure of the phase averaged OH*. However, we can extract the pure spinning response of the OH* fluctuations by employing a novel rotational averaging procedure.

This method takes advantage of previous observations that the global fluctuating OH* responds at the resonant frequency, does not exhibit harmonics, is approximately sinusoidal, and that in spinning modes the dynamic response of all flames is the same but with an offset in phase determined by the burner distance and resonant frequency [4]. The basic premise of the method is to conduct a spatial averaging in a frame of reference moving with the spinning wave in either direction.

We first assemble normalised phase averages: $\tilde{Q}_n = (\tilde{Q} - \overline{Q})/\langle\overline{Q}\rangle$, where $\tilde{Q} = \tilde{Q}(r, \theta, t)$ is the spatial distribution of OH* intensity captured by the camera, $\overline{Q} = \overline{Q}(r, \theta)$ is the time-averaged mean and $\langle\overline{Q}\rangle$ is the spatially ensembled time-average evaluated over the whole annulus. Therefore, $\tilde{Q}_n = \tilde{Q}_n(r, \theta, \tau/T)$, where τ/T is the normalised position in the phase averaged cycle.

For the general case of N burners, the normalised forcing cycle is divided into N time-steps for phase averaging ($N = 12$ herein). In order to isolate the spinning component in a given direction, the jth phase average field is rotated by an angle $\beta = 2\pi j/N$ against the given spin direction effectively *freezing* the spinning mode. The average of the N rotations distributions is then calculated according to Eq. 1, producing a single spatial spin compensated distribution, $\overline{Q}^{x}_{rot} = f(r, \theta)$. A schematic of the method is shown in Fig. 2.

$$\overline{Q}^{x}_{rot} = \frac{1}{N}\sum_{j=0}^{N-1} \mathrm{Rot}_{\beta_j}\left\{\left[\frac{\tilde{Q} - \overline{Q}}{\langle\overline{Q}\rangle}\right]_j\right\}, \qquad (1)$$

where x is either the ACW or the CW component, j is the phase average time step and Rot_{β_j} is a rotation of β_j around the center of the annulus. The angle is calculated as $\beta_j = \pm\frac{2\pi}{N}j$, where positive and negative signs are used for CW and ACW components respectively.

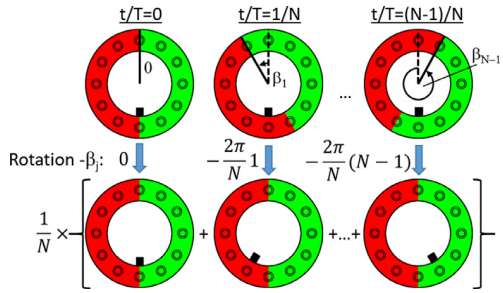

Fig. 2. Schematic of the rotational averaging method. The sector rotations, β_j, depicted in the figure are in the ACW direction as would be applied to an ACW spinning mode.

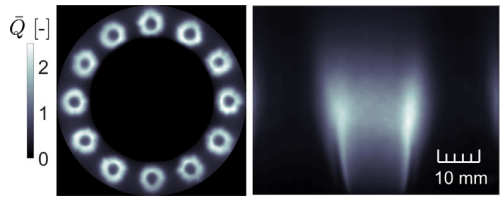

Fig. 3. Left: Overhead image of the mean OH*. Right: Side image of the mean OH*.

The method effectively decomposes OH* distribution into harmonic components by cancelling OH* fluctuations driven by pressure waves travelling in the opposite direction. An additional advantage is that small variations in the flames are also averaged out, providing a clearer description of the unsteady flame response to acoustic waves.

3. Results

3.1. Mean flame structure

Figure 3 shows the mean OH* chemiluminescence imaged from above and a picture from the side of one of the turbulent bluff-body flames. Compared with swirling flames reported in previous investigations [3–5], these flames are longer, more radially compact and remain isolated around the annulus as shown by the concentric OH* structure of all 12 flames. The flame is stabilised along the inner shear layer at the bluff body edge although a second lifted flame front is stabilised in the outer shear layer. It was previously observed that for the 12 burner swirling flame configuration the tops of the flame brushes were in close proximity to both neighbouring flames and the combustor walls [4].

3.2. Frequency and amplitude response

The frequencies of the self-excited azimuthal modes for different U_b and different values of ϕ are

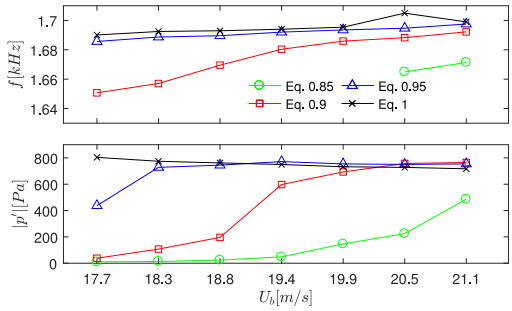

Fig. 4. Effect of ϕ and U_b on the self-excited instability frequency (top) and amplitude (bottom).

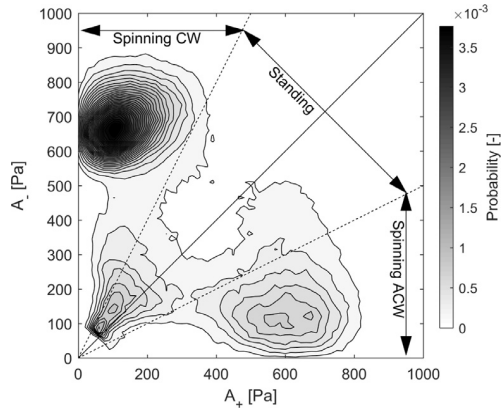

Fig. 5. Joint PDF of A_+ and A_- for all ϕ at $U_b = 19.9$ m/s. Dashed lines from origin denote thresholded boundary of predominantly spinning and standing modes.

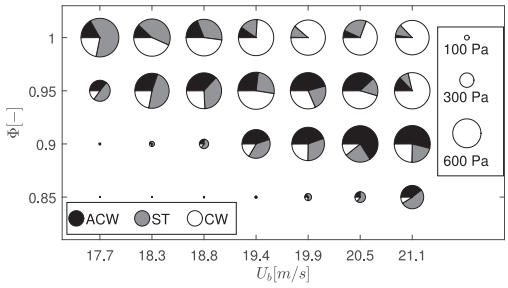

Fig. 6. Stability map showing modal content at each operating point. Note: circle diameter scales with the magnitude of the pressure fluctuations.

plotted in Fig. 4. The instability frequency of the first azimuthal mode lies between 1650 and 1710 Hz depending on the operating conditions. Overall the trends show that the instability frequency increases approximately linearly with increasing power and with increasing flame speed (increasing ϕ) as observed previously [3]. However, in the absence of swirl, the instability frequencies are approximately 50 Hz lower. The frequency difference equates to an approximate reduction in the mean gas temperature of $\Delta T \approx 115$K indicating that the temperature profile in the combustor is modified by the change in the flame shape compared with swirling flames.

Figure 4 (bottom) shows the stability map in terms of the mean pressure amplitude of the response in terms of ϕ and U_b. It shows that, in general, high amplitude instabilities are excited at richer equivalence ratios and higher thermal loads. It is interesting to note that there appears to be a well defined maximum pressure amplitude response, which may result from saturation of the instability at high amplitudes.

3.3. Mode characterisation

Figure 5 plots the joint probability density function (PDF) of A_+ and A_- for all ϕ at $U_b = 19.9$m/s. The joint PDF shows that the modal response is stochastic at low instability amplitudes, and bi-modal at higher amplitudes, with a statistical preference for CW spinning waves. This distribution is distinctly different to that observed in swirling flames, which did not exhibit a bi-modal response [3,4,8], but shows remarkably close agreement with theory of Schuermans et al. [12] who suggested a transition from standing to spinning waves when the amplitude of an instability increases. The high probability of exciting spinning modes in either direction can be attributed to the absence of swirl or mean azimuthal flow. We conjecture that the higher probability of exciting CW, as opposed to ACW, spinning modes is likely to arise from imperfections in geometric azimuthal symmetry or small flow non-uniformities as suggested by Sensiau [19].

We note some general similarities to the results of Prieur et al. [17], who found that initial conditions determined the direction of self-excited spinning modes. The present findings appear to support this finding, albeit with the addition of bi-modal dynamics, which may be driven by the fully turbulent flow in the current configuration [1].

Figure 6 shows a stability map that also includes the modal content at each operating point. The diameter of the circles scale with the amplitude of the pressure fluctuations and are divided into pie graphs which show the proportion of predominantly spinning (in both directions) and standing modes according to the definition in Section 2.4. It is interesting to note that only the cases close to the onset boundary of high amplitude instabilities appear to show stochastic behaviour and a predominantly standing behaviour, but at higher ϕ and U_b conditions spinning modes are observed more frequently. The small fractions of predominantly standing waves that are observed during bi-modal behaviour occur mainly during the switching transition between CW and ACW states.

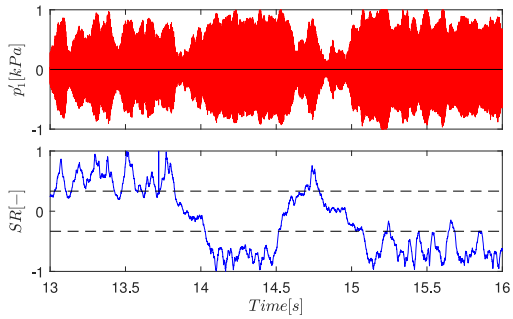

Fig. 7. Top: Pressure time-series showing modal dynamics. Bottom: Time-series of the spin ratio SR evaluated from the pressure data. Dashed lines correspond to thresholds use to classify modes: $SR > 1/3$ are classified as ACW spinning modes, $SR < -1/3$ are classified as CW spinning modes intermediate values are classed as standing modes.

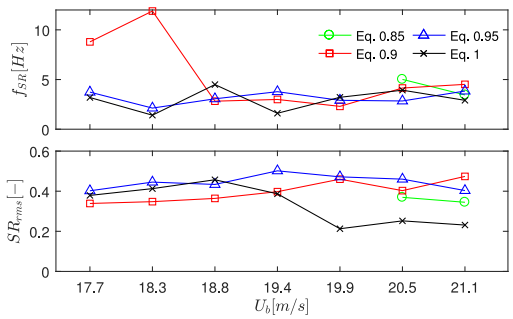

Fig. 8. Top: Frequency of the spin ratio time-series for different values of U_b and ϕ. Bottom: *r.m.s* fluctuations of the SR time-series for different values of U_b and ϕ.

3.4. Modal dynamics

We now consider the time-varying nature of the self-excited modes in more detail. Figure 7 (top) shows a typical pressure time-series recorded at location *p1* for the case where $\phi = 0.95$ and $U = 19.9$ m/s. Figure 7 (bottom) shows the time-series of the SR evaluated from the pressure time-series. The pressure time series shows low frequency modulations, relative to the instability frequency, of the amplitude envelope which is characteristic feature of mode switching. The mode switching is quantified by the SR time-series which shows that the mode of oscillation is constantly oscillating experiencing low amplitude oscillations in spin ratio. The mode can also be observed to periodically switch from strongly spinning in the ACW to the CW direction and vice versa, passing through predominantly standing modes during each switch. Excursions of the SR above the top dashed line and below the bottom dashed line are classified as spinning modes whereas points in-between are classified as predominantly standing. The observed low frequency switching of the SR and the low frequency modulations of the pressure time series are qualitatively similar, however their time-scales are orders of magnitude longer than the instability.

Figure 8 plots the low frequency modulation of the SR (top) and the *r.m.s* of the SR modulations (bottom), evaluated using a similar approach to [8]. The frequency range of the mode switching in terms of SR is between $2 - 11$ Hz, but overall mode switching occurs at a relatively constant frequency of around 4 Hz and appears to be independent of both ϕ and U_b. The slow time-scale of the mode-switching is of the order of the convective velocities but the mechanism that drives this low frequency behaviour is at present not understood. It should also be noted that this behaviour is notably different from swirling flames where the oscillation frequency was observed to increase with ϕ [8].

Figure 8 (bottom) shows that the magnitude of the spin ratio fluctuations remains relatively constant at $SR_{rms} \approx 0.3 - 0.5$ for the majority of cases. It is only the $\phi = 1$ cases which show a reduction in the rms value with increasing U_b. This occurs when the periodic switching from CW to ACW modes occurs less often, and the mode appears to settle in a preferred state.

3.5. Fluctuating heat release rate

In this section we consider the periodic structure of the fluctuating heat release rate obtained from high speed OH* imaging using phase averages as well as a new rotational averaging procedure described earlier in Section 2.4. We are particularly interested in understanding how the spatial structure and dynamics of the global fluctuating heat release rate of isolated turbulent flames respond to spinning waves and whether the response is the same in both spin directions. We conjecture that in the absence of swirl and bulk azimuthal flow the structure of the OH* fluctuations should be similar.

Figure 9 shows 6 non-dimensional time-steps, t/T, of the standard phase averaged images of the fluctuating component of the heat release rate for an ACW mode where $\phi = 0.95$ and $U = 19.9$ m/s. At $t/T = 0$ we see peak values of the OH* fluctuations, shown in red, in the bottom right hand quadrant and negative OH* fluctuations (mean is set to zero), shown in blue, diametrically opposite. This structure rotates around the annulus over the duration of the cycle. The turbulent bluff body flames have a low cone angle which means that a stable flame appears as a concentric region of peak OH* chemiluminescence as shown in Fig. 3. The phase averaged images of the ACW spinning mode in Fig. 9 show that the regions of maximum and minimum OH* form crescent shaped structures on opposite sides of the flame. As an observer sitting on the bluff body and looking inwards, the larger

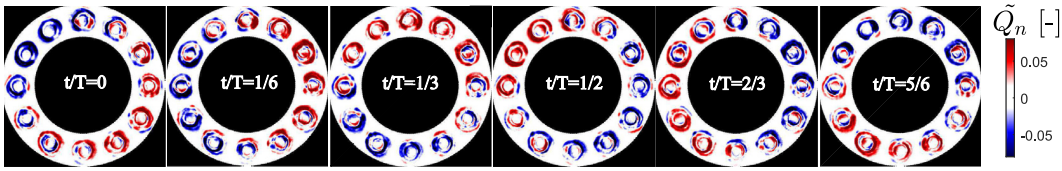

Fig. 9. Phase averaged overhead OH* chemiluminescence conditioned for spinning ACW at $\phi = 0.95$ and $U = 19.9$ m/s.

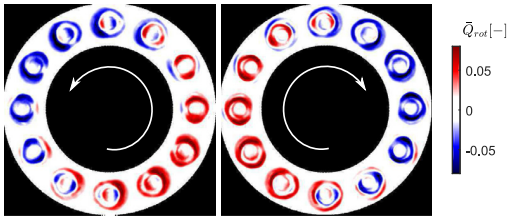

Fig. 10. Rotating average of the phase averaged overhead OH* chemiluminescence conditioned for spinning $\overline{Q}_{\mathrm{rot}}^{\mathrm{ACW}}$ (left) and $\overline{Q}_{\mathrm{rot}}^{\mathrm{CW}}$ (right). $\phi = 0.95$, $U = 19.9$ m/s.

crescent shaped regions of maximum OH* appear on the right hand side of the flame relative to the spinning wave, whereas the minimum OH* crescents appear on the left hand side. These features are particularly clear in $t/T = 1/6$ and 1/3.

Since near perfect spinning modes rarely occur, as shown in the joint PDF in Fig. 6 and the SR time-series in Fig. 8, the OH* responses from mixed mode components are present in the structure of the phase averaged OH*. However, we can extract the harmonic component of the OH* fluctuations produced by the spinning wave by employing the novel rotational averaging procedure described earlier.

The result of the rotational averaging procedure carried out for both CW and ACW spinning modes is shown in Fig. 10 as $\overline{Q}_{\mathrm{rot}}^{\mathrm{ACW}}$ (left) and $\overline{Q}_{\mathrm{rot}}^{\mathrm{CW}}$ (right). Despite minor differences in response amplitude, spin ratio and convergence the same features can be readily observed during both ACW and CW modes. Looking at the ACW mode, we see that the maximum and minimum OH* fluctuations show asymmetric ring like structures which spread radially outwards from the centre of each burner. The formation of these structures can be attributed to both the axial oscillation of the flow rate into the combustor and the transverse velocity oscillation resulting from the spinning pressure wave. Although the formation mechanism is generally similar to that of swirling flames (for example see ref. [5]), the response of the flames in the current configuration has a number of important differences.

Firstly, the absence of swirl reduces the spreading rate resulting in flames which are fully isolated from each other. Secondly, the fluctuating OH* structures, which are correlated to the roll-up of vortex structures on the shear layers, do not rotate locally around each bluff body as they advect downstream as found in swirling flames [3,5]. Both of these features make it more straightforward to unambiguously investigate the heat release rate response. The ring like fluctuating OH* structures are clearly asymmetric in terms of width and oscillation magnitude, with larger oscillations present on the sides of the flame aligned in the azimuthal direction. Moreover, the largest magnitude oscillation is observed on the side of the flame facing away from the incoming pressure wave. This is the opposite side of the flame in comparison with the response of swirling flames in [5], and may result from either vorticity cancellation [15], shear sheltering, or the absence of axially propagating vorticity waves [16] which may change the timing of the flame sheet dynamics although without access to the velocity field this remains a conjecture. While the source of the oscillation asymmetry remains uncertain, the fact that the largest asymmetries are aligned with the azimuthal direction suggest that the radial asymmetry observed in swirling flames [5] may be simply a result of these structures rotating locally around each bluff body as they advect downstream. This provides a possible explanation for the different spatial distribution of the fluctuating OH* structures around the annulus observed in previous studies [3].

It is also worth noting that at a number of points in the cycle (for example the flame at 7 o' clock on the CW mode image), multiple oscillations appear to be present simultaneously, with inner and outer ring or crescent like structures. For the inner set of structures, the orientation of the maximum and minimum values of the crescent shaped regions are on occasion reversed in comparison with the outer set. This structure is consistent with occurrence of transverse fluctuations giving rise to *flapping* motions of the flame brush, producing a staggered arrangement of azimuthally plane-symmetric structures rather than axisymmetric structures.

4. Conclusion

In this paper we have demonstrated experimentally that self-excited azimuthal modes can be excited in an annular combustor using turbulent bluff body flames without swirl, enabling us to better understand the time-varying nature of azimuthal

modes and the structure of the fluctuating heat release rate. Simultaneous pressure measurements and high speed OH^* chemiluminescence were obtained for a range of operating conditions and showed that self-excited instabilities occur over a wide range of conditions. Stability maps and joint probability density functions of the instability amplitudes show that azimuthal modes are stochastic at low equivalence ratios showing similar probabilities for spinning, standing and mixed modes, but exhibit bimodal behaviour at higher equivalence ratios and velocities, preferring instead spinning modes. These features are significantly different to the behaviour of self-excited azimuthal modes with turbulent swirling flames. A new rotational averaging method to extract the harmonic components of the fluctuating heat release rate was presented and used to process high speed OH^* images and analyse the structure of the OH^* fluctuations for spinning modes. It was found that the structure of the fluctuating heat release rate of spinning modes is highly asymmetric and characterised by crescent shaped regions of peak OH^* that are preferentially oriented according to the direction of spin and are observed on approximately half of the flames around the annulus. The same structure is observed in both spin directions but with opposite handedness.

Acknowledgements

This work was funded by the European Research Council (ERC) under the European Union's Horizon 2020 research and innovation programme (grant agreement no 677931 TAIAC). We also thank the technical staff of NTNU EPT for their support.

References

[1] N. Noiray, B. Schuermans, *Proc. R. Soc. A Math. Phys. Eng. Sci.* 469 (2012).
[2] J.F. Bourgouin, D. Durox, J.P. Moeck, T. Schuller, S. Candel, *Self-Sustained Instabilities in an Annular Combustor Coupled by Azimuthal and Longitudinal Acoustic Modes* (2013), doi:10.1115/GT2013-95010.
[3] N.A. Worth, J.R. Dawson, *Proc. Combust. Inst.* 34 (2013) 3127–3134.
[4] N.A. Worth, J.R. Dawson, *Combust. Flame* 160 (2012) 2476–2489.
[5] J.R. Dawson, N.A. Worth, *Combust. Flame* 161 (2014) 2565–2578.
[6] W. Krebs, P. Flohr, B. Prade, S. Hoffmann, *Comb. Sc. Tech.* 174 (2002) 99–128.
[7] G. Ghirardo, M.P. Juniper, *Proc. R. Soc. A Math. Phys. Eng. Sci.* 469 (2013).
[8] N.A. Worth, J.R. Dawson, *Proc. Combust. Inst.* 36 (2017) 3743–3751.
[9] N.A. Worth, J.R. Dawson, J.A.M. Sidey, E.M. Mastorakos, *Proc. Combust. Inst.* 36 (2017) 3783–3790.
[10] P. Wolf, G. Staffelbach, L.Y.M. Gicquel, J.D. Müller, T. Poinsot, *Combust. Flame* 159 (2012) 3398–3413.
[11] B. Schuermans, V. Bellucci, C.O. Paschereit, *Non-Linear Combustion Instabilities in Annular Gas-Turbine Combustors*, American Institute of Aeronautics and Astronautics, 2006, doi:10.1115/GT2013-95010.
[12] B. Schuermans, V. Bellucci, C.O. Paschereit, *Thermoacoustic Modeling and Control of Multi Burner Combustion Systems* (2003), doi:10.1115/GT2003-38688.
[13] M.R. Bothien, N. Noiray, B. Schuermans, *J. Eng. Gas Turbines Power* 137 (2015) 061505.
[14] J.F. Bourgouin, D. Durox, J.P. Moeck, T. Schuller, S. Candel, *J. Eng. Gas Turbines Power* 137 (2015) 021503.
[15] R. Sau, K. Mahesh, *JFM* 604 (2008) 389–409.
[16] P. Palies, D. Durox, T. Schuller, S. Candel, *Combust. Flame* 157:9 (2010) 1698–1717.
[17] K. Prieur, D. Durox, T. Schuller, S. Candel, *Combust. Flame* 175 (2017) 283–291.
[18] M. Bauerheim, M. Cazalens, T. Poinsot, *Proc. Combust. Inst.* 35 (2015) 3219–3227.
[19] C. Sensiau, F. Nicoud, T. Poinsot, *Int. J. Aeroacoust.* 8 (1) (2009) 57–67.

ARTICLE IV

Azimuthal Flame Response and Symmetry Breaking in a Forced Annular Combustor

Håkon T. Nygård, Giulio Ghirardo, and Nicholas A. Worth

Under review for
Combustion and Flame

This article is awaiting publication and is therefore not included.

ARTICLE V

Symmetry breaking modelling for azimuthal combustion dynamics

Giulio Ghirardo, Håkon T. Nygård, Alexis Cuquel, and Nicholas A. Worth

Published in
Proceedings of the Combustion Institute

Available online at www.sciencedirect.com

ScienceDirect

Proceedings of the Combustion Institute 38 (2021) 5953–5962

Proceedings of the Combustion Institute

www.elsevier.com/locate/proci

Symmetry breaking modelling for azimuthal combustion dynamics

Giulio Ghirardo [a,*], Håkon T. Nygård [b], Alexis Cuquel [a], Nicholas A. Worth [b]

[a] *Ansaldo Energia Switzerland, Haselstrasse 18, Baden 5401, Switzerland*
[b] *Department of Energy and Process Engineering, Norwegian University of Science and Technology, Trondheim N-7491, Norway*

Received 7 November 2019; accepted 15 May 2020
Available online 14 July 2020

Abstract

Annular combustors can exhibit azimuthal thermoacoustic instabilities, which can rotate as a spinning wave at the speed of sound in the azimuthal direction, oscillate as a standing wave with pressure nodes fixed in space, or be a linear combination of these. These oscillations happen if a positive feedback loop between acoustics and the response of the flames to the acoustics in the annulus occurs. This paper discusses how two different explicit symmetry breaking mechanisms affect the dynamics of these waves. We first show how small differences between the flame responses lead to one strong topological change in the dynamical system phase space, making the system prefer orientation angles at two azimuthal locations, one opposite of the other in the annulus, as found in the experiments. This symmetry breaking is modelled by directly perturbing the flame responses around the annulus with some scatter, to represent the effect of manufacturing tolerances of the burners. We then consider recent experimental evidence that the heat release rate of the flames depends on the spinning direction (clockwise or anticlockwise) when the system is spinning. In particular we model one experiment in which the flame response is found to be stronger when the wave rotates in the anticlockwise direction. We show that the statistics of the resulting model are qualitatively very similar to the experimental results showing a preference for spinning states in the anticlockwise direction.

Keywords: Azimuthal instabilities; Thermoacoustics; Heat release rate response models; Low-order models; Symmetry breaking

1. Introduction

Azimuthal instabilities are typical of symmetrical combustion systems, either as unwanted acoustic oscillations, like in annular combustors [1], or as part of the combustion concept, as in rotating

* Corresponding author.
E-mail address: giulio.ghirardo@ansaldoenergia.com (G. Ghirardo).

https://doi.org/10.1016/j.proci.2020.05.018

detonating combustion [2]. A common approach in the modelling of these instabilities assumes that the flame responds, by means of the acoustic admittance of the system upstream of the flames, to the local value of acoustic pressure[1] at the flame position [1]. Under this assumption, in the fully symmetric case one proves in absence of noise that spinning solutions always exist as stable periodic attractors, and that when standing periodic solutions exist the N_{2n} criterion can be used to ascertain their stability [5]. This is in agreement with the experiments for both spinning [5] and standing solutions [6]. In presence of noise, as is typical of many industrial applications and of turbulent flames, one proves that the system state is driven away from spinning solutions, also in agreement with the experiments [7].

The first part of this paper lifts the assumption of full symmetry, and investigates how a slight loss of discrete symmetry affects the system. This has been previously studied theoretically in the deterministic case, for a simple cubic flame response, and for a homogeneous heat release distribution along the annulus [8]. We will lift all these assumptions except fixing a certain flame response, and show how the pressure antinodes of the azimuthal instability are pushed towards two azimuthal orientations in the annulus, as found in the experiment.

The second part of the paper considers recent advances in the response of the flame to also the azimuthal acoustic velocity. Theoretical works have shown that the nonlinear response of the flame to azimuthal velocity fluctuations can affect the dynamics of the solution [9] and push the system towards standing states. Later experimental works have confirmed this effect, which originates either by a loss of mirror symmetry of the flame [10,11] or by the complex interaction of neigbouring flames [12] or by both. This paper models this effect and shows how we can recover a statistical preference of the acoustic field for anticlockwise solutions as in the experiment.

We review from the literature the governing equations and the experiment in Section 2. We then discuss the baseline, reference axisymmetric case in Section 3. We consider the first symmetry breaking mechanism, related to manufacturing imperfections, in Section 4, and the second mechanism in Section 5. We draw the conclusions in Section 6.

2. The model

In this section we briefly recall the features of interest of the experiment and recapitulate the governing equations from the literature. We study a laboratory annular combustor with bluff-body swirling flames that has been discussed in detail in [14–16]. In the following we will consider a variant of this setup with $M = 18$ burners, as sketched in Fig. 1 and described recently in [12], operated at an equivalence ratio of 0.75 and a bulk flow velocity U_b =20m/s at the burner exit. At this condition, a top view of the measured mean chemiluminescence is presented in Fig. 2, at which the system exhibits thermoacoustic pulsations of azimuthal order $n = 1$ at a frequency of approximately 1.7 kHz. The acoustic pressure field in the annular combustor, at the cross-section just downstream of the burners can be written as [13]:

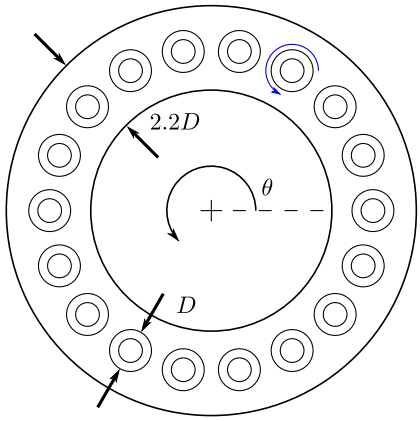

Fig. 1. View of the annular rig from the top. The acoustic pressure field depends in this plane on the azimuthal angle θ and on the time t. The $M = 18$ burners, sketched with two concentric circles, are located at equispaced azimuthal angles $\theta_m = 2\pi m/M$, $m = 0, \dots, M-1$.

$$p(t,\theta) = A\cos(n(\theta-\theta_0))\cos(\chi)\cos(\omega t+\varphi) + A\sin(n(\theta-\theta_0))\sin(\chi)\sin(\omega t+\varphi) \quad (1)$$

where θ is the azimuthal coordinate defined in Fig. 1, the three variables (A, $n\theta_0$, χ) depend on the time t and are described in Fig. 3, and φ also depends on time and is the temporal phase of the instability. The resulting governing equations are obtained by substituting the ansatz (1) into the fluctuating mass and momentum conservation equations [7]:

$$\begin{aligned}(\ln A)' + (n\theta_0' + \varphi'\sin(2\chi))i + \varphi'\cos(2\chi)j - \chi' k = \\ + \frac{1}{2}\frac{1}{2\pi}\int_0^{2\pi}\left(e^{i2n(\theta-\theta_0)}e^{k\chi} + e^{-k\chi}\right)Q_\theta(A_p(\theta))d\theta\, e^{k\chi} \\ + \left(-\frac{\omega}{2} + \frac{\omega_0^2}{2\omega}\right)e^{-k\chi}je^{k\chi} + \frac{\sigma^2}{4A^2}(1+\tan(2\chi)k) \\ + \frac{\sigma}{\sqrt{2}A}\mu \end{aligned} \quad (2)$$

and are described in the rest of this section. Eq. (2) is quaternion-valued, so that i, j, k are distinct imaginary units [7,17]. The left hand side of (2) describes the evolution of the four variables

[1] See [3,4] for works where it is instead the azimuthal velocity that drives the flames.

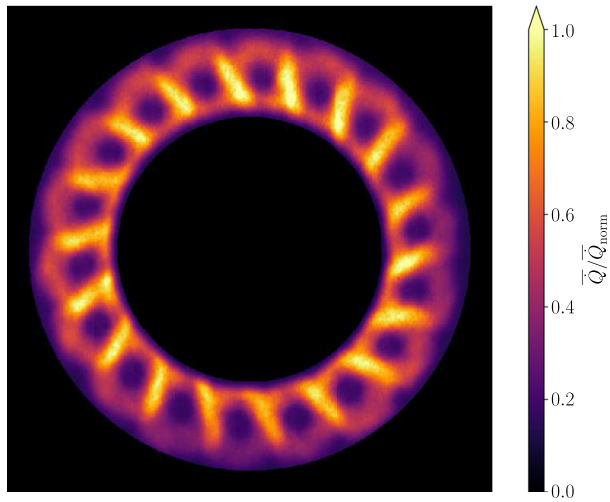

Fig. 2. Mean normalized chemiluminescence from the top. The $M = 18$ darker round regions correspond to the bluff-bodies of the burners.

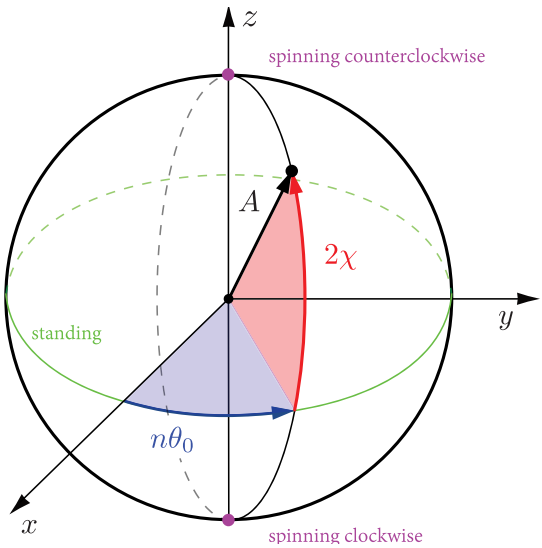

Fig. 3. Poincaré sphere representation of an azimuthal instability of order n, presented in (1). The radius A describes the amplitude of acoustic oscillation, the nature angle 2χ describes whether the system is spinning (at the poles) or standing (on the equator) and the angle $n\theta_0$ describes the location of the pressure antinode of the standing component of the instability [13].

of interest $\{A,\ n\theta_0,\ \chi,\ \varphi\}$ as a function of time. The real part describes the the evolution of the amplitude A, the imaginary i and j units encode spatial and temporal phase, while k encodes the nature angle χ. The right hand side describes the vector field that the four variables follow, which will be presented in the figures later. In particular the second line in (2) is the contribution over the annulus of Q_θ, which is the projection of the describing functions of the flames and of the acoustic losses on the azimuthal mode [18]:

$$Q_\theta(A_p) = 2\pi\, Q_{\theta,\mathrm{flames}}(A_p) - M\alpha \tag{3}$$

where the last term describes the acoustic damping of the system, assumed linear, by means of the coefficient α. In the simplest cases the flame responds to the axial acoustic velocity measured just upstream of the flame position. It is possible to express such velocity as function of the acoustic pressure in the combustion chamber by mean of the acoustic impedance of the whole system just

upstream of the flame [5,19]. As a consequence, the response of the flames $Q_{\theta,\text{flames}}$ depends on the local amplitude $A_p(\theta)$ of acoustic pressure at the azimuthal location θ [1], which can be calculated as

$$A_p(\theta) \equiv A\sqrt{\begin{matrix}\cos^2\left[n(\theta-\theta_0)\right]\cos^2(\chi)\\ +\sin^2\left[n(\theta-\theta_0)\right]\sin^2(\chi)\end{matrix}} \tag{4}$$

Exploiting the fact that each flame is acoustically compact, we can rewrite $Q_{\theta,\text{flames}}$ as:

$$Q_{\theta,\text{flames}}(A_p) = \sum_{m=0}^{M-1} Q_m(A_p(\theta))\delta(\theta-\theta_m) \tag{5}$$

where $\delta(x)$ is the Dirac distribution, and θ_m is the location of the mth burner as presented in Fig. 1, and the projected flame responses $Q_m = Q_{m,r} + jQ_{m,j}$ may be different from one another, and are assumed here to be real-valued for simplicity, as in many other studies [1,18,20]. Under these assumptions the thermoacoustic oscillation frequency ω matches the natural oscillation frequency ω_0 and the first term in the last row of (2) cancels out. Ending the analysis of (2), the last two terms on the third line depend on the intensity σ of the background noise. These terms arise because of the random HRR fluctuations of the turbulent flame [21,22] and are modelled here as stochastic [23], with μ being a quaternion-valued additive white gaussian noise process. A detailed description of the model (2) and its derivation can be found in [7].

3. Baseline: the axisymmetric case with a simple nonlinear saturation in absence of noise

Because the describing functions of the flames are not available, we choose a simple saturation model with monotonic response for the axisymmetric case. In particular we constrain the flame response such that in the linear regime it is equal to a linear effective gain β_m:

$$Q_m(A_p(\theta_m)) = \beta_m e^{-A_p(\theta_m)} \tag{6}$$

where for the axisymmetric case the flames have the same constant effective gain $\beta_m = \beta_{\text{sym}}$. Since the flame transfer functions of the flames are not known, we fix first the linear growth rate of the system azimuthal instability to the value of $\nu_0/\omega_0 = 0.16$ in absence of acoustic damping, on the high end of common values in the literature discussed in [19]. The resulting value of the effective gains $\beta_m = \beta_{\text{sym}}$, equal for all the flames in this symmetric case, can then be calculated as $\beta_{\text{sym}}/\omega_0 = (2\nu_0/\omega_0)/(\pi M)$. We then add a level of acoustic damping α equal to $\beta_m/5$. The flame strength and the acoustic damping are kept fixed in the following, are common tunable parameters in low-order models for azimuthal instabilities and are typically identified in applications. Most of the following results have been tested also for different values, and should apply as long as $\beta_{\text{sym}} > \alpha$ to make the system linearly unstable.

The three variables $\{A, n\theta_0, 2\chi\}$ are the spherical coordinate of a point in Fig. 3, which describes the system trajectory as function of time t, driven by the vector field described by the right hand side of (2). This three-dimensional vector field is hard to present as a whole, therefore we present next two projections of this vector field on two planes: the equatorial plane of the sphere in Fig. 3, and on one vertical plane passing through both poles. We present on the two rows of Fig. 4 these two projections for the axisymmetric case of this section, in absence of noise, as discussed next. On each row, in the first frame, the component of the vector field pushing the system state in the radial direction is presented, so that in red regions the state is driven outwards towards infinity, and in blue regions the state is driven towards the origin. In the second frame, the component of the vector field acting in the tangential direction is presented, so that red regions push the system counterclockwise and blue regions clockwise. In the third frame, the same information is presented in terms of the streamlines in the plane. Repellors in the plane are marked with empty circles and attractors in the plane are marked with filled circles. The same structure of this Figure is used later in Figs. 6, 9, 10, and the axes of the frames share the same radius limit at $A = 3.2$, so that they can be compared. In all these frames the azimuthal coordinate starts at three o'clock as in Fig. 1, and in the vertical cuts only the right half is presented, because in this plane it is always symmetric. In the equatorial plane of Fig. 4 we observe how the streamlines are almost parallel to radii passing through the origin, which is due to the azimuthal component of the field being significantly weaker than its radial counterpart. This will play a role when we perturb the symmetry in the next section. In the vertical plane, we observe that for this specific choice of flame saturation the spinning solution is an attractor of the system. This is not always the case, because also standing solutions can exist and be attractors, depending on how the flame saturates in the nonlinear regime [5]. In these figures, higher values of the flame effective gain β push the solutions further away from the origin. Similarly, higher values of the acoustic damping α push the system towards the origin.

4. The effect of a small loss of rotational symmetry

Due to small manufacturing scatter, small differences in the mass-flow rates of air and fuel are expected between the flames. In thermoacoustics, these differences affect the flame response. One way to account for this is to perturb to the effective flame gains β_m, $m = 0, \ldots, M-1$ some additive white gaussian noise scalars with a small standard deviation, here chosen equal to 1/10th of the base-

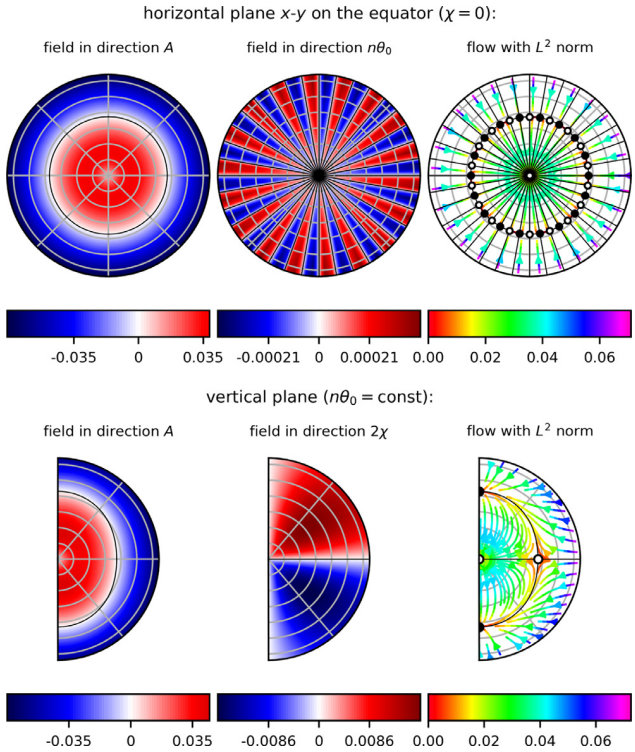

Fig. 4. Axisymmetric case for an annular combustor with $M = 18$ burners exhibiting an azimuthal mode of order $n = 1$. All the symbols are introduced in Fig. 3. In the top 3 frames, a cut on the equator plane of Fig. 3 is presented. In the bottom 3 frames a cut passing through the north and south poles of the sphere of Fig. 3 is presented. On each row the first frame presents the component of the vector field in the radial direction A, the second frame presents the component in the tangential direction, and the last frame presents the streamlines of the resulting 2D vector field. In the first two columns the contour levels where the components are zero are presented with black lines. These two sets of black lines are reported also in the third column, where their intersections are the fixed points of the system. We draw with a filled circle fixed points that are attractors in the plane, and with an empty circle points that are either saddles or repellors.

line value β_{sym}. One realization of the resulting slightly asymmetric pattern is presented in Fig. 5 and is considered next. Of the pattern, only the mean value β_{sym} and the $2n$-azimuthal component have an effect on the system dynamics,[2] so that their sum is presented in the Fig. 5 with red markers as an equivalent pattern. The $2n = 2$ locations where this equivalent pattern is maximum are presented in Fig. 5 at $\theta = \theta^{(2n)} \approx 3\pi/4$ and at $\theta = \theta^{(2n)} + \pi$. The resulting vector field is presented in Fig. 6. The dynamics in the equatorial plane are quite different from the axisymmetric case of Fig. 4: only 4 fixed points survive, and of these 2 are saddles and 2 are attractors in the plane. The 2 attractors are azimuthally located approximately at the angle $\theta^{(2n)}$ corresponding to to the $2n$ maxima of the linear coefficients of Fig. 5 just described.

This result matches qualitatively the experimental evidence presented in Fig. 7, and past evidence from the literature: Fig. 10 of Worth and Dawson [14], a similar pdf of the orientation angle presented by Ghirardo and Bothien [13] in their Fig. 6 after the addition of the dampers, and Fig. 6 of Bourgouin et al. [24]. In all four cases there are two azimuthal locations (actually one location, and the same location rotated by π) where the antinode of the standing component of the pressure field is more likely to be found. These results apply regardless of whether the system is noisy or not, i.e regardless of the intensity σ of the background noise. Technically this is the case because from the equations this strong change in the topology of the deterministic vector field in the equatorial plane does not depend on σ.

Of the many vertical planes, we present in Fig. 6 the cut at the angle $n\theta_0 = \theta^{(2n)}$. In this vertical

[2] this can be observed in the governing Eq. (2) and discussed in [7] in the general nonlinear case and in [8] for the linear term.

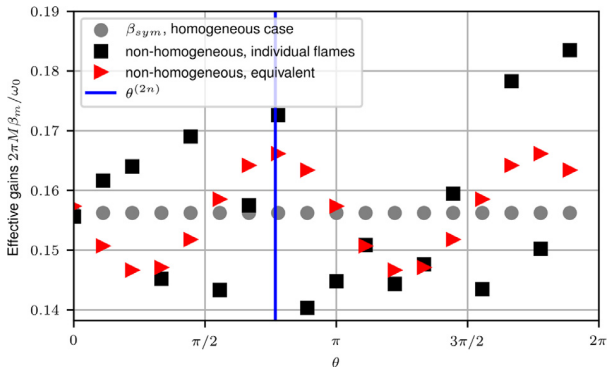

Fig. 5. Burner to burner scatter can affect the response of the flames in an annular combustor. These slight changes can affect the effective gains of the flames, presented with black squares, which depart from the baseline symmetric value, presented with gray circles..

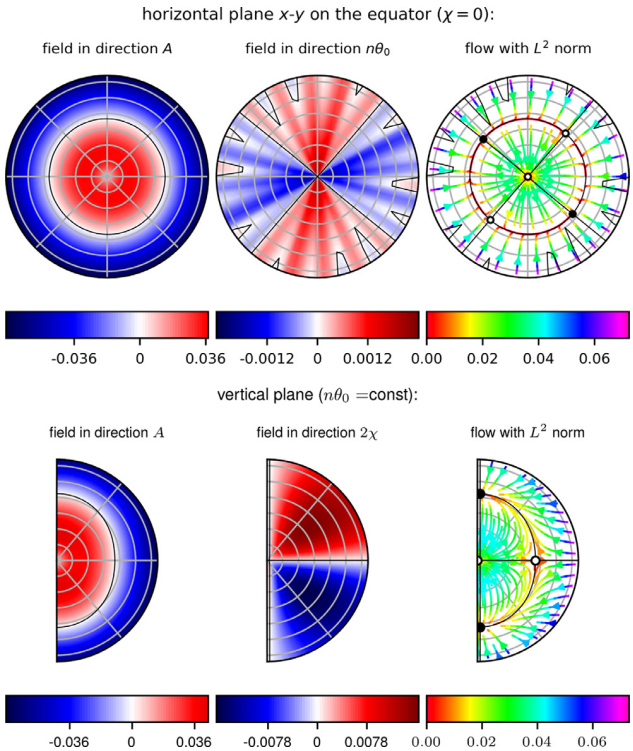

Fig. 6. Effect of a small loss of rotational symmetry on an annular combustor with $M = 18$ burners exhibiting an azimuthal mode of order $n = 1$. All the symbols are introduced in Fig. 3, and the structure of the plot is the same of Fig. 4. The loss of symmetry considered here is modelled as some random scatter in the response of the flames, as presented in Fig. 5. In comparison to the axisymmetric case of Fig. 4, there are now just 4 fixed points in the xy plane, of which two are repellors and two are attractors in the plane. The vertical plane is very similar to the axisymmetric case.

plane the solutions that were perfectly spinning in the axisymmetric case of Fig. 4 are now pushed slightly off from the poles, but still spinning to a very good approximation, consistently with [8]. We also find that the vector field is very close to the axisymmetric case, suggesting that existing theoretical results and the N_{2n} stability criteria for standing solutions [5] derived for perfectly symmetric configurations are robust against small asymmetries like this one.

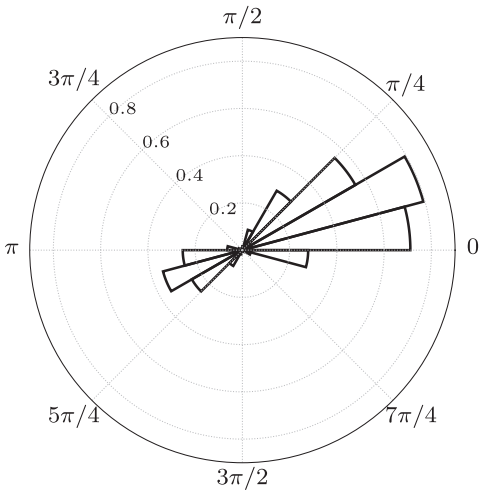

Fig. 7. Probability density function of the orientation angle $n\theta_0$ for the self excited case. The system lingers in the vicinity of two preferred orientations, one opposite of the other.

5. The effect of the nature angle on the HRR response

Saurabh et al. [10,11] force a single flame with simultaneous axial and transverse excitation as in annular combustors. They show that the gain and the phase of the flame response to a spinning wave can significantly depend on whether the spinning wave rotates clockwise or anticlockwise in the annulus. They attribute this to a loss of reflection symmetry on a plane orthogonal to the direction of the spinning wave passing through the burner axis. Nygård et al. [12] force the annular combustor of Fig. 1 with loudspeakers so that the acoustic field is to a good approximation spinning clockwise or anticlockwise. They measure the integrated HRR and show that it differs between the two cases, as rediscussed here in Fig. 8. We can model this in the equations, by making the effective gains of the flames β_m depend on the nature angle χ. We propose to write:

$$\beta_m = \beta_{\text{sym}}[1 + \gamma \sin(2\chi)] \tag{7}$$

to model the experimental evidence that when the system is spinning anticlockwise (2χ close to $\pi/2$) the HRR response is larger than when the system is spinning clockwise (2χ close to $-\pi/2$). The coefficient γ models the strength of this effect. For this analysis the effect of (7) on the HRR is linear in the amplitude of oscillation A, because γ directly perturbs the gains β_m, and we fix $\gamma = 0.14$ to match the experimental evidence that the HRR for the clockwise forced case is 23% smaller than the one for the anticlockwise forced case, as presented in Fig. 8. The resulting flow and discussion are presented in Fig. 9. In comparison to the baseline case of Fig. 4, the spinning solution in the northern hemisphere has moved to a larger amplitude, and the spinning solution in the southern hemisphere has moved to smaller amplitudes. To match the noisy experimental data, the background noise is now switched on in the model by tuning $\sigma = 0.09$, affecting the flow as in Fig. 10. Noise pushes the two attractors away from the poles, as proved by [7]. The value of σ is chosen to match the statistics of the experiment. We run a simulation starting from an anticlockwise initial condition, and present in Fig. 11 a comparison with the experimental data. We observe how the two probability density functions qualitatively agree, have a similar width and tail to the lower values, but the simulation peaks at a location closer to the north pole at $\pi/2$. Regarding the effect of the noise intensity σ, we mention that in the numerical model it is possible to shift the position of

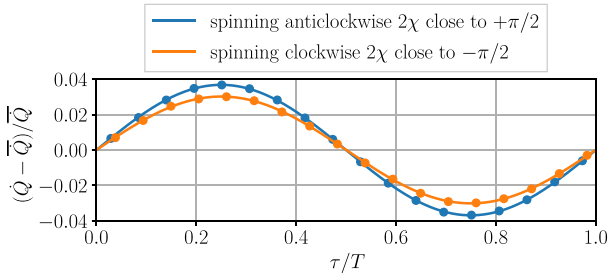

Fig. 8. Loudspeakers were connected to the walls of the combustion chamber by means of ducts designed to damp the thermoacoustic instability. The resulting linearly stable system was then forced with the loudspeakers to push the system state to a spinning wave, first in the anticlockwise direction and then in the clockwise direction, approximately at the same level of acoustic amplitude. One period of the fluctuating HRR $\dot{Q} - \overline{\dot{Q}}$ of one burner representative of all others is then reconstructed for the two cases, normalized by the mean HRR $\overline{\dot{Q}}$. The timeseries of the two cases have been adjusted to start at zero because it was not possible to synchronize them with the occurrence of the acoustic pressure maximum at the same burner position. Of the two states, the flame response is larger when the system is spinning anticlockwise. More information can be found in [12].

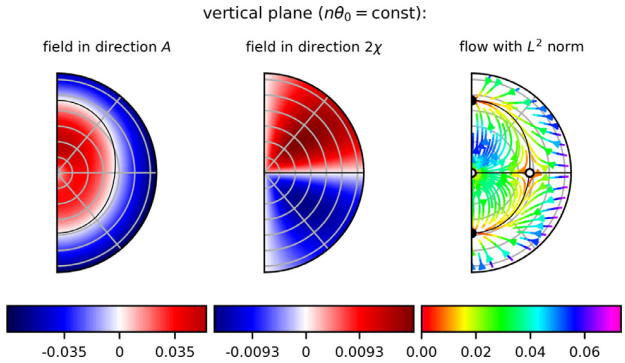

Fig. 9. Effect on the system dynamics of the dependence of the HRR on the nature angle, for $\gamma = 0.14$. Only the vertical plane is presented because the equatorial cut matches exactly the axisymmetric case of Fig. 4. The addition of noise is considered next in Fig. 10

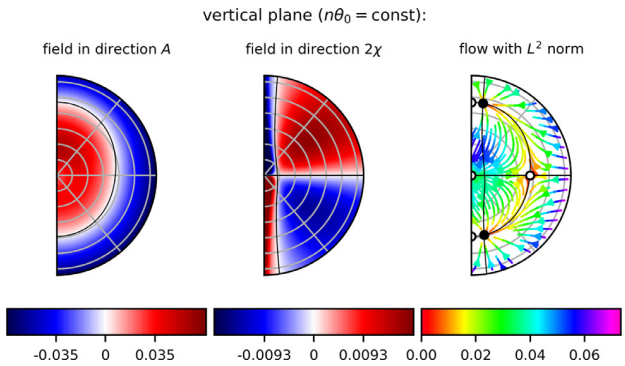

Fig. 10. Same as in Fig. 9, with the same limits on the colormaps, but now accounting also for the effect of the background noise σ, set here to 0.09. Simulation results of this case are presented in Fig. 11.

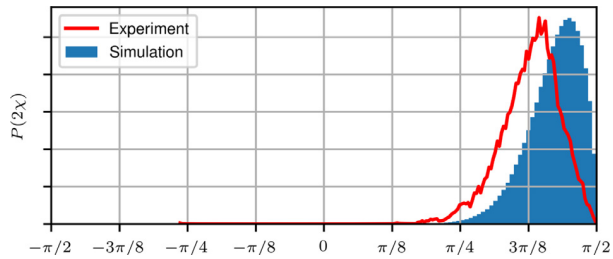

Fig. 11. Comparison between simulations and experiments of the statistics of the nature angle 2χ. The experimental data refers to the self-excited case, ran at the same operating conditions of Fig. 8 but without loudpspeakers. Both histograms describe approximately 52′000 periods of acoustic oscillations.

the maximum while maintaining the solution in the northern hemisphere by increasing both the noise intensity σ and the coefficient γ, or both σ and the linear growth rate of the system ν_0 introduced in Section 3. We did not attempt a systematic optimization study in the space $\{\nu_0, \sigma, \gamma\}$ to improve this result. Other plausible reasons for the maximum pdf peak shift include a partial loss of symmetry as discussed in Section 4, which is not accounted for in this section but hinted at by the experimental result of Fig. 7, and the nonlinear saturation of the flame responses, which is at the moment unknown and modelled according to (6).

Another matter of interest is the fact that there exist two distinct attractors in Fig. 10. We find numerically that a point initialized close to the anticlockwise solution does not escape the northern hemisphere in the same time span measured in the

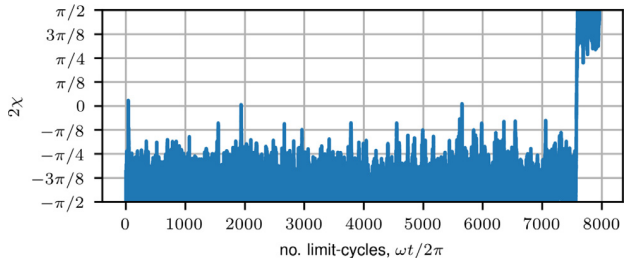

Fig. 12. From an initial condition in the southern hemisphere close to the clockwise spinning solution, the system escapes to the north hemisphere in this specific simulation after about 7′500 periods, which is about 4.7 s for the experiment considered.

experiment. Similarly, we find that a point initialized close to the clockwise solution escapes the southern hemisphere after a time that is small compared to the observation time of the experiment, as presented in Fig. 12. Both observations are typical of systems with a double well potential, where one well is deeper than the other. The double well is then called asymmetric, and the asymmetry is described in our case by the coefficient γ introduced in (7). The solution in the deeper well is the anticlockwise solution, which is more likely to be observed in the model and that is observed in the experiment, while in the shallower well we find the clockwise solution, which is not observed in the experiment. The two probabilities of escaping from one basin to the other are different.

6. Conclusions

We model an annular combustor with $M = 18$ burners, with a simple flame saturation model that neglects the HRR not in phase with the acoustic pressure. We show how a small loss of rotational symmetry pushes the pressure antinodes of the first order azimuthal instability towards two preferential azimuthal locations, one location and the same location rotated by π, as found in two different laboratory experiments and in one industrial scale engine.

We then model recent experimental evidence showing that the heat release response depends on the direction of the spinning wave, i.e. on the nature angle 2χ. For the annular experiment considered, the HRR is found to be larger for a wave rotating in anticlockwise direction than in clockwise direction. We model this effect and find that it pushes the anticlockwise solution to larger amplitudes and the clockwise solution to smaller amplitudes, while mantaining both solutions as attractors in the deterministic case, i.e in absence of background noise. When noise is considered, we present numerical evidence of how it is possible that the system escapes from the basin of attraction of the clockwise solution because of the noise, and that this can happen in a matter of seconds, and then easily go undetected in the experiment. We present numerical evidence that it is harder for the system to escape from the basin of attraction of the anticlockwise solution, which is the only one measured in the experiments. A comparison of the statistics of the nature angle 2χ between model and experiment shows a good qualitative agreement.

Declaration of Competing Interest

None.

Acknowledgments

This work is partially supported by the European Research Council under the EU Horizon 2020 research and innovation programme (grant no 677931 TAIAC)

References

[1] B. Schuermans, C.O. Paschereit, P. Monkewitz, in: 44th AIAA Aerospace Sciences Meeting and Exhibit. Paper no. AIAA-2006-0549, American Institute of Aeronautics and Astronautics, Reno (NV), U.S.A., 2006, pp. 1–12.

[2] M.D. Bohon, R. Bluemner, C.O. Paschereit, E.J. Gutmark, *Exp. Therm. Fluid Sci.* 102 (October 2018) (2019) 28–37.

[3] P.G. Mehta, G. Hagen, A. Banaszuk, *SIAM J. Appl. Dyn. Syst.* 6 (3) (2007) 549–575.

[4] J. Cohen, G. Hagen, A. Banaszuk, S. Becz, P. Mehta, in: 49th AIAA Aerospace Sciences Meeting including the New Horizons Forum and Aerospace Exposition, 732, American Institute of Aeronautics and Astronautics, Reston, Virigina, 2011, pp. 1–225.

[5] G. Ghirardo, M.P. Juniper, J.P. Moeck, *J. Fluid Mech.* 805 (2016) 52–87.

[6] D. Laera, T. Schuller, K. Prieur, D. Durox, S.M. Camporeale, S. Candel, *Combust. Flame* 184 (2017) 136–152.

[7] G. Ghirardo, F. Gant, Background noise pushes azimuthal instabilities away from spinning states, arXiv:1904.00213v1 (2019) 1–4.

[8] N. Noiray, M.R. Bothien, B. Schuermans, *Combust. Theory Model.* 15 (5) (2011) 585–606.
[9] G. Ghirardo, M.P. Juniper, *Proceedings of the Royal Society A: Mathematical, Physical and Engineering Sciences* 469 (2013) 1–16.
[10] A. Saurabh, C.O. Paschereit, *Combust. Flame* 182 (2017) 298–312.
[11] A. Saurabh, C.O. Paschereit, *Combust. Sci. Technol.* 191 (7) (2019) 1184–1200.
[12] H.T. Nygård, M. Mazur, J.R. Dawson, N.A. Worth, *Proc. Combust. Inst.* 37 (4) (2018) 1–8.
[13] G. Ghirardo, M.R. Bothien, *Phys. Rev. Fluids* 3 (11) (2018) 113202.
[14] N.A. Worth, J.R. Dawson, *Combust. Flame* 160 (2013) 2476–2489.
[15] N.A. Worth, J.R. Dawson, *Proc. Combust. Inst.* 34 (2) (2013) 3127–3134.
[16] N.A. Worth, J.R. Dawson, *Proc. Combust. Inst.* 36 (3) (2017) 3743–3751.
[17] C. Doran, A. Lasenby, *Geometric Algebra for Physicists*, Cambridge University Press, Cambridge, 2003.
[18] G. Ghirardo, F. Boudy, M.R. Bothien, *J. Fluid Mech.* 844 (2018) 216–246.
[19] G. Ghirardo, M.P. Juniper, M.R. Bothien, *Combust. Flame* 187 (2017) 165–184.
[20] N. Noiray, B. Schuermans, *Proce. R. Soc. A* 469 (20120535) (2013) 1–15.
[21] W.C. Strahle, *J. Sound Vib.* 23 (1) (1972) 113–125.
[22] R. Rajaram, T. Lieuwen, *J. Fluid Mech.* 637 (2009) 357–385.
[23] T. Lieuwen, *J. Sound Vib.* 260 (1) (2003) 3–17.
[24] J.-F. Bourgouin, D. Durox, J.P. Moeck, T. Schuller, S. Candel, *J. Eng. Gas Turb. Power* 137 (2015).